

al-Farabi Kazakh National University

UDC: 542.943(043)

On manuscript rights

ANAS HOUBI

**Creating and Studying New Composite Materials for Microwave Absorption in the
Range of 8.8-12 GHz**

8D07104 – Chemical technology of inorganic substances

Dissertation submitted in partial fulfillment of the requirements for the degree of Doctor
of Philosophy (Ph.D.)
(final version)

Scientific supervisors:

Doctor of Technical Sciences, Professor, National
Center on Complex Processing of Mineral Raw
Materials,
Zharmenov Abdurassul Aldashevich;

Doctor of Physical Chemistry, Professor, Higher
Institute for Applied Sciences and Technology,
Yomen Atassi

Republic of Kazakhstan
Almaty, 2023

CONTENTS

LIST OF ABBREVIATION.....	5
INTRODUCTION.....	6
1 LITERATURE REVIEW	10
1.1 Significance of microwave absorbing materials	10
1.2 Microwaves	11
1.3 Mechanisms of EM wave absorption	11
1.4 Microwave absorption materials	12
1.4.1 Ferrites.....	13
1.4.2 Carbonyl iron powder (CIP).....	16
1.4.3 Conductive polymers (CPs)	16
1.4.4 Carbonaceous substances	17
1.5 Composite absorbent materials with graded impedance	17
1.6 Characteristics of an ideal microwave absorption material	17
1.7 Absorbent ferrites nanoparticles for microwave	18
1.8 Incorporation of CPs with ferrite nanoparticles to absorb microwaves.....	20
1.9 MA behavior of carbon-based nanomaterials	21
2 PRACTICAL PART	24
2.1 Chemical, raw and commercial materials	24
Continuation of Table 3	25
2.2 Tools and equipment used for sample preparation.....	25
2.3 Characterization devices.....	26
2.4 Sample preparation.....	29
2.4.1 Preparation of ferrite powders.....	29
2.4.2 Preparation of microwave composites	35
2.4.3 Preparation of hybrid composites.....	38
2.5 Statistical processing of experimental data	42
3 RESULTS AND DISCUSSION.....	43

3.1 Results and discussion of the preparation of ferrite powders by the ceramic sintering technique	43
3.1.1 XRD patterns.....	43
3.1.2 FTIR spectra of ferrite samples.....	45
3.1.3 Morphology investigations for spinel and hexagonal ferrites	45
3.1.4 EDX analysis for spinel and hexagonal ferrites.....	47
3.1.5 Microwave absorption properties of ferrite samples prepared by the ceramic sintering technique	48
3.2 Results and discussion of the preparation of ferrite powders by citrate precursor technique	56
3.2.1 X-ray diffraction of ferrite samples.....	56
3.2.2 FTIR spectra of ferrite samples.....	58
3.2.3 Morphology investigations for spinel ferrite sample	58
3.2.4 EDX analysis for spinel ferrite sample	58
3.2.5 Microwave absorption properties of ferrite samples prepared by citrate precursor technique	61
3.3 Results and discussion of the preparation of ferrite powders by self-combustion technique	63
3.3.1 X-ray diffraction of ferrite samples.....	63
3.3.2 FTIR spectra of ferrite samples.....	65
3.3.3 Morphology investigations for spinel ferrite sample	67
3.3.4 EDX analysis for spinel ferrite sample	67
3.3.5 Microwave absorption properties of ferrite samples prepared by the self-combustion technique	68
3.4 Results and discussion of microwave composites.....	70
3.4.1 X-ray diffraction of CB, AC, C and CI samples	70
3.4.2 FTIR spectra of CB, AC, C and CI samples	72
3.4.3 Microwave absorption properties of ferrite composites	72
3.5 Results and discussion of the preparation of Hybrid composites	83

3.5.1	X-ray diffraction of PANI-based composites	83
3.5.2	FTIR spectra of PANI-based composites.....	85
3.5.3	Morphology investigations of PANI-based composites	86
3.5.4	EDX analysis of PANI-based composites	90
3.5.5	TGA analysis of PANI-based composites	93
3.5.6	Microwave absorption properties of PANI-based composites	95
	CONCLUSION.....	107
	REFERENCES.....	109

LIST OF ABBREVIATION

SE_A	- Absorption shielding
Z_0	- Air impedance
AC	- Activated carbon
BW	- Bandwidth
CB	- Carbon black
CNTs	- Carbon nanotubes
CI	- Carbonyl iron
ϵ_r	- Complex relative permittivity
μ_r	- Complex relative permeability
EDX	- Energy-dispersive X-ray spectroscopy
EMI	- Electromagnetic interference
F	- Ferrite
FTIR	- Fourier Transform IR
Hf	- Hexagonal ferrite
ϵ''	- Imaginary part of permittivity
μ''	- Imaginary part of permeability
p_{in}	- Incident electromagnetic waves
LP	- Loading percentage
f_m	- Matching frequency
Z	- Matching impedance characteristic
Z_1	- Material impedance
MA	- Microwave absorption
RL_{min}	- Minimal reflection loss
SE_{max}	- Maximum shielding efficiency
MAMs	- Microwave absorption materials
PANI	- Polyaniline
PVA	- Polyvinyl alcohol
RAMs	- Radar absorbing materials
SE_R	- Reflection shielding
p_{ref}	- Reflected power
ϵ'	- Real part of permittivity
μ'	- Real part of permeability
SEM	- Scanning electron microscope
SF	- Spinel ferrite
SD	- Surface density
TGA	- Thermogravimetric analysis
p_T	- Transmitted power
XRD	- X-ray diffractometer

INTRODUCTION

General description of the work. The current thesis consists of 3 chapters. The first chapter presents the theoretical part literature review on microwave absorbers. The second chapter contains an experimental part that describes the experimental procedures and the equipment that was used for the synthesis. The third chapter is devoted to describing for results and discussion. The prepared samples are structurally characterized using XRD, FTIR, TGA, and EDX. SEM is utilized to define the morphology of the powders. The prepared samples are functionally characterized by utilizing the horn antenna connected to an oscilloscope. In the first stage of the current work, spinel and hexagonal ferrites were prepared by the ceramic sintering method. The effect of ferrite type, substitution with metal ions, the concentration of metal ions, and loading percentage of ferrite in the host matrix on electromagnetic interference (EMI) and microwave absorption (MA) properties were studied. The best result obtained at this stage was by using $\text{Ni}^{3+}_{0.25}\text{Ni}^{2+}_{0.375}\text{Zn}^{2+}_{0.25}\text{Fe}_2\text{O}_4$. In the second stage of the current work, the effect of the preparation method, calcination temperature, molar ratio of metal ions to citrate acid, and solution of polyvinyl alcohol (PVA) on EMI and MA properties were investigated. The best result was obtained by using the $\text{Ni}_{0.5}\text{Zn}_{0.5}\text{Fe}_2\text{O}_4$ nanoparticles with a loading percentage of 60% at a constant calcination temperature of 650°C prepared by the citrate precursor method. It was figured out from the above-mentioned studies that the defects of these prepared absorbers are that they have a limited absorption bandwidth under -10 dB ($\text{BW}_{-10\text{ dB}}$) and high loading percentage. This necessitated working to decrease the loading percentage and increase the absorption $\text{BW}_{-10\text{ dB}}$ of the absorbers to cover most of the frequency band of 8.8–12.0 GHz by incorporating magnetic loss and dielectric loss materials. As a result, MA composites were prepared. The effect of composite type, weight ratios of composites, spinel ferrite type used within the composite, and absorbent layer thickness on EMI and MA properties were investigated. The results showed that the absorption $\text{BW}_{-10\text{ dB}}$ increased from 1.1 GHz to 3.2 GHz and the loading percentage decreased from 65% to 45% compared with the aforementioned studies. To enhance the RL (reflection loss) value and obtain 99.9% absorption (attenuation) to the microwave with improving shielding efficiency (SE) and surface density (SD). This required working on using conductive polymers such as polyaniline (PANI). According to that, hybrid composites were prepared. The effect of hybrid composite type, loading percentage, and weight ratios of PANI/F composite on EMI and MA properties were investigated. The results showed at this stage of the research that the RL and SE improved by obtaining 99.9% absorption to the microwave and decreasing the loading percentage from 45% to 25% which means obtaining lightweight absorbers with distinguished properties. The prepared composites are promising candidates for applications such as EMI shielding and stealth technology.

Actuality of the theme. EMI is a well-known critical problem in radar and antenna systems and electronic devices [1,2]. EMI is an unwanted Electromagnetic (EM) wave that works as a noise that disturbs the natural operation of electronic devices. This noise arises from electronic devices that release EM waves, such as mobile phones, wireless devices, television/computer

screens and cordless microphones in halls. Generally, EMI would be regarded as an unwanted result of modern technology that has dangerous effects on human health, intelligent devices, telecommunication devices, and military industries. Consequently, the effective disposal of EM waves from EMI is so important for public protection security and electronic safety [3–8]. The development of radar or microwave absorbing materials technology has had a great impact on the military field. Radar absorbing materials (RAMs) are significant tools in electronic warfare, as they can be used to hide targets and protect them from radar detection [9,10]. EM shielding materials and RAMs have been produced by international companies at high prices. In this regard, the relevance of the research topic of the doctoral dissertation is paving the way for putting the methodology and scientific bases for the manufacture of MAMs in the laboratory with the required international quality. As well as competing with commercial absorbers mentioned in the literature in terms of weight, reflection loss, absorption bandwidth, and shielding efficiency.

Purpose of the work: to design novel microwave absorbers by appropriately incorporating magnetic loss and dielectric loss components in order to fulfill the requirements of lightweight and wide band microwave absorbers working at the suitable microwave band with improved shielding efficiency.

Tasks of the work:

1. Revealing the effect of ferrite type, substitution with metal ions, the concentration of metal ions, the molar ratio of metal ions to citrate acid, and the PVA concentration on the reflection loss, absorption bandwidth, and shielding efficiency.
2. Detecting the synergistic effect of incorporation of dielectric loss and magnetic loss materials on the reflection loss, surface density, absorption bandwidth, and shielding efficiency.
3. Revealing the effect of the loading percentage of hybrid composite in the host matrix, and weight ratios of PANI/Ni³⁺_{0.25}Ni²⁺_{0.375}Zn²⁺_{0.25}Fe₂O₄, and PANI/BaNiZnFe₁₆O₂₇ on the EMI shielding and MA properties.
4. Figuring out the effect of the combination of soft and hard ferrites with coating with polyaniline on the RL_{min}, BW_{-10 dB}, SD and SE_{max}.

The main provisions for the defense of the thesis:

- Increasing the metal ions to citrate acid and PVA concentration in the ferrite leads the RL attenuation peaks of samples to shift to lower frequencies. This allows the position of the f_m to be controlled.
- The synergistic incorporation of magnetic loss and dielectric loss materials leads to decreasing the loading percentage of the absorber in the host matrix, increasing the absorption BW_{-10 dB}, and enhancing the SE_{max} of the absorbers to cover most of the frequency band of 8.8–12.0 GHz.
- Detecting that the RL attenuation peaks of hybrid composites moved to higher frequencies by increasing the PANI in the hybrid composites. These results lead to the possibility to control the absorption BW_{-10 dB}, RL_{min}, and f_m of the absorbers.

- Enhancing the RL value and obtaining 99.9% absorption to the microwave with improving SE and SD by adding carbon black (CB) and carbonyl iron (CI) to the hybrid composites.

The object of the research is to create microwave absorbers that are characterized by low surface density and strong reflection loss with broad absorption bandwidth at the range of 8.8–12.0 GHz by adjusting different fabrication parameters.

The subject of research is obtaining microwave absorbers prepared by different physical and chemical methods. Evaluating the characteristics of the absorbers by measuring RL, SE, absorption $BW_{-10\text{ dB}}$ and SD.

The scientific novelty of the research results obtained is ascertained by the fact that for the first time:

- Creating novel microwave absorbing composites based on carbonaceous materials and PANI operating between the frequency range of 8.8–12.0 GHz, which are lightweight with good reflection loss and wide bandwidth under -10 dB with high shielding efficiency by tuning the different parameters of the fabrication and properly combining magnetic loss and dielectric loss components in order to meet the requirements of lightweight and broadband microwave absorbers.
- A low loading percentage of PANI/ $\text{Ni}^{3+}_{0.25}\text{Ni}^{2+}_{0.375}\text{Zn}^{2+}_{0.25}\text{Fe}_2\text{O}_4$ composite in the host matrix of 25% was reached, which is one of the lowest published loading percentages globally.
- Novel microwave absorbing composite based on a combination of soft ferrite ($\text{Ni}^{3+}_{0.25}\text{Ni}^{2+}_{0.375}\text{Zn}^{2+}_{0.25}\text{Fe}_2\text{O}_4$) and hard ferrite ($\text{BaNiZnFe}_{16}\text{O}_{27}$) incorporated with CB, namely ($\text{Ni}^{3+}_{0.25}\text{Ni}^{2+}_{0.375}\text{Zn}^{2+}_{0.25}\text{Fe}_2\text{O}_4/\text{BaNiZnFe}_{16}\text{O}_{27}/\text{CB}$) with coating with PANI was designed. This absorber can exceed the -10 dB threshold and cover the entire frequency band of 8.8–12.0 GHz with a loading percentage of 30%.

Research methods. The prepared samples were structurally characterized using XRD, FTIR, TGA, and EDX. SEM was utilized to define the morphology of the powders. Finally, the prepared samples were functionally characterized utilizing the horn antenna connected to an oscilloscope.

Theoretical significance: The results of the dissertation research expanded the known knowledge in the field of producing EMI shielding materials and MAMs to suppress EMI and improve the effectiveness of electronic devices.

The practical significance. The current research provides a methodology for tailoring the design of microwave absorbers by tuning the different parameters of the fabrication and properly combining magnetic loss and dielectric loss components in order to meet the requirements of lightweight and broadband microwave absorbers at the appropriate microwave band with optimized reflection loss.

In this respect, novel microwave absorbing composites based on carbonaceous materials and polyaniline operating between the frequency range of 8.8–12.0 GHz, which are lightweight with strong RL and wide $BW_{-10\text{ dB}}$ with high SE. Furthermore, one of the prepared microwave

absorbers (PANI/spinel ferrite (SF)/hexagonal ferrite (HF)/CB) can attenuate 99.9% of the microwave with a loading percentage of 30%.

Relation to the plan of state research programs. This dissertational work was carried out without any framework.

The personal contribution of the author of the work consists of the collection, processing and analysis of literature data on the topic of the thesis, direct planning and implementation of the experimental part. The applicant took part in the analysis, interpretation and presentation of the obtained research results and their discussion, as well as in the preparation of scientific articles.

Approbation of thesis

The materials of the thesis were reported and discussed at various international conferences:

- International Scientific Conference of Students and Young Scientists "CHEMICAL PHYSICS AND PHYSICAL CHEMISTRY" (Al-Farabi Kazakh National University, Almaty, Kazakhstan, 6-8 April 2021).
- 11th INTERNATIONAL BEREMZHANOV CONGRESS ON CHEMISTRY AND CHEMICAL TECHNOLOGY "FUNDAMENTAL AND APPLIED MATERIALS SCIENCE", Almaty, Kazakhstan, 19-20 November 2021.
- YOUTH CHEMISTRY CONFERENCE (Nazarbayev University, Astana, Kazakhstan, November 20, 2021).
- International Scientific Conference of Students and Young Scientists "CHEMICAL PHYSICS AND PHYSICAL CHEMISTRY" (Al-Farabi Kazakh National University, Almaty, Kazakhstan, 6-8 April 2022).

Publications

The main research results on the topic of the dissertation are presented in 10 published works, including:

- One scientific article, published in a journal has an impact factor according to the Scopus database.
- Two scientific articles, published in a journal indexing to the Web of Science database.
- One scientific article, published in a journal recommended by the Committee for Control in the Sphere of Education and Science of the Ministry of Education and Science of the Republic of Kazakhstan.
- Four abstracts at international conferences.
- Two scientific articles at international journals.

Volume and structure of the thesis. The thesis consists of an introduction, 3 chapters, conclusion and list of references. The work is presented on 117 pages, contains 82 figures, 40 tables, and 121 bibliographical references.

1 LITERATURE REVIEW

1.1 Significance of microwave absorbing materials

Smart devices, nowadays, are inspiring the infinite vitality and possibilities of intelligent life, such as self-power electromagnetic nanogenerators and microsensors, smart windows, thermally-driven EM absorbers, interstellar energy deliverers, and so on. The accelerated progress of the smart era is connected with the backing of smart devices. Particularly, with the coming of the 5G era or future 6G or 7G era, smart EM devices in high-frequency are getting growing consideration because of the absolute supremacy in long-range, wireless, and great-speed response, etc [11]. They allow connecting the countries with each other with stunning unusual convenience (Figure 1). The increased growth of these devices and telecommunication systems, operating at high frequencies (MHz and GHz), raises the issue of electromagnetic interference (EMI) that affects the proper performance of those devices. The lifetime of telecommunication systems can be increased by efficient EMI shielding using appropriate absorbing materials. Moreover, the harmful nature of high-frequency waves to human health is considered a serious environmental issue that needs to be addressed by lowering the level of electromagnetic pollution. Microwave absorbing materials constitute an elegant way to mitigate the aforementioned problem on the basis of wave attenuation and wave impedance matching ensuring low reflection. Microwave absorbing materials are also promising for military applications, such as stealth technology. Their use in camouflage is due to their ability to reduce radar cross-section by attenuating the reflection.

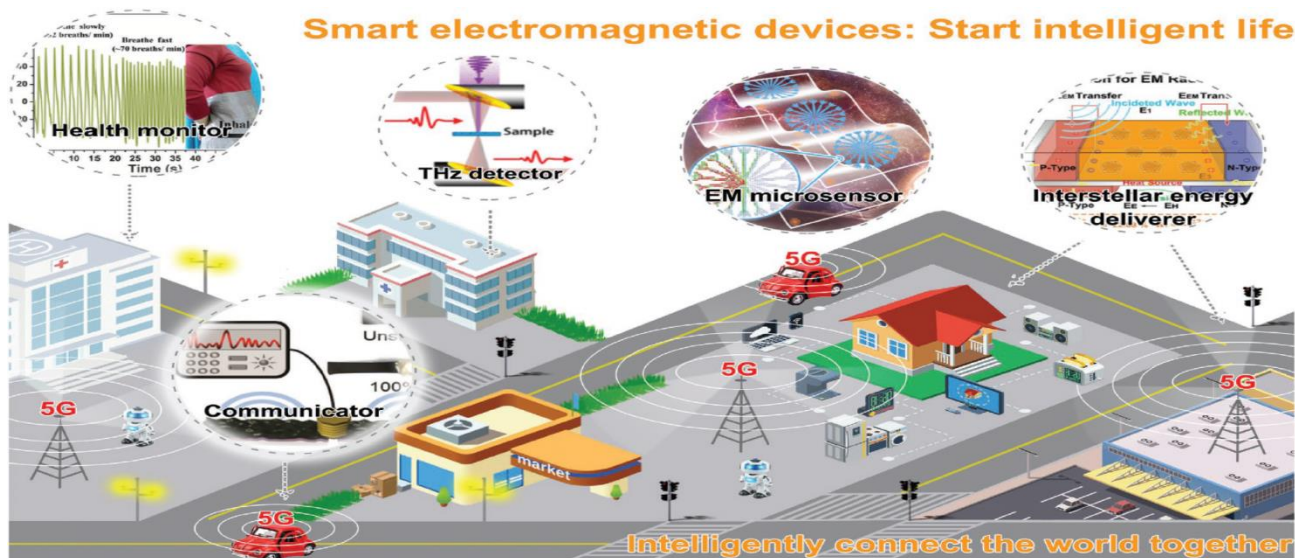


Figure 1 – Schematic illustration for intelligent life, including smart home, smart hospital, smart shopping, smart factory, etc., showing that in the future, we can employ smart EM devices (e.g. EM monitor (top 1), detector (top 2), microsensor (top 3), communicator (bottom) and energy deliverer (top 4), and 1–4 is from left to right) to bring all aspects of our livelihoods together and create smarter lifestyles with more convenience [11]

1.2 Microwaves

Microwaves are EM waves ranging from about 0.3 GHz to 300 GHz with corresponding wavelengths ranging from 1 m to 1 mm [12]. EM waves have two perpendicular components, the electric and the magnetic field. Microwaves are used in the following applications:

- 1) Antennas.
- 2) Radars.
- 3) Telecommunications.
- 4) Satellites.
- 5) Industrial applications.

The frequency bands of microwaves are shown in Table 1.

Table 1 – Frequency bands of microwaves [13]

Frequency bands	f (GHz)	λ (cm)
L-band	1.0-2.0	15.0-30.0
S-band	2.0-4.0	7.5-15.0
C-band	4.0-8.0	3.75-7.5
X-band	8.0-12.0	2.5-3.75
Ku-band	12.0-18.0	1.67-2.5

1.3 Mechanisms of EM wave absorption

Microwave absorption and electromagnetic interference shielding are two general approaches to resisting the interference of incident electromagnetic waves. They are usually estimated via various analysis models due to their distinct interests. For a EMI shielding model, the significant point is to attenuate the transmitted power of the EM waves.

The incident wave undergoes reflection, transmission, and absorption. The reaction of the EM power with the substance's electronic and molecular structure generates heat inside the substance because of power squandering, which turns the incident EM wave into heat or other shapes of power [14]. The electromagnetic shielding efficiency (SE) is measured in terms of a reduction in the income power/field size upon transition across the shield. SE can be expressed in the following equation:

$$SE = R + T + M \quad (1)$$

Where R, T, and M are the reflection loss, the absorption loss, and the multiple reflection loss, respectively [15].

In this state, elevated reflectivity is so convenient to the shielding efficiency, and almost all incoming waves have reflected on the surface of shielding substances. The physical importance of RL in electromagnetic interference shielding is the variation between the primary incoming waves and those waves entering the shielding substances (Figure 2). For the model of microwave

absorption (MA) (Figure 2), though, a mineral substance is put to reflect the transmission waves. As a consequence, the transmission waves are constantly negligible in MA. Here, RL indicates the variation between the primary incident and the final reflected waves.

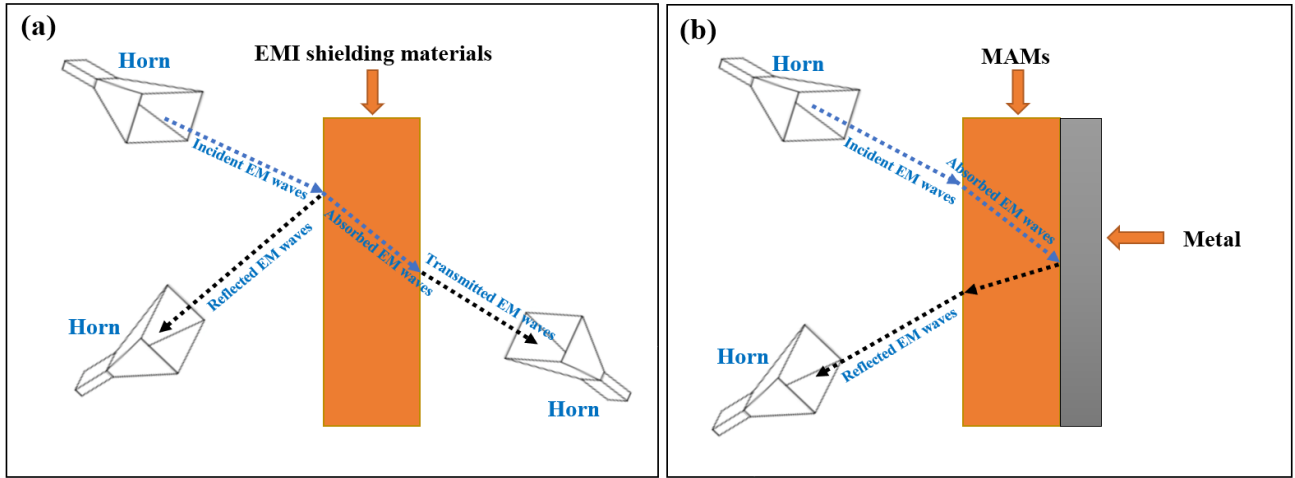


Figure 2 – Diagram of the estimated models of (a) electromagnetic interference shielding and (b) microwave absorption [16]

In order to get effective electromagnetic wave absorption, there should be material impedance (Z_1) close/equal to air impedance (Z_0), and the electromagnetic wave should be quickly attenuated inside the substance [17]. The model's impedance matching characteristic (Z) can be determined as shown in equation (2).

$$Z = \frac{Z_1}{Z_0} \quad (2)$$

The EM characteristics of a substance, i.e., the complex relative permittivity (ϵ_r) and permeability (μ_r) are defined by equations (3 and 4) [12,18–20].

$$\epsilon_r = \epsilon' - i\epsilon'' \quad (3)$$

$$\mu_r = \mu' - i\mu'' \quad (4)$$

The real part of permittivity and permeability (ϵ' and μ') describes the ability to store the energy in the pattern. In contrast, the imaginary parts (ϵ'' and μ'') describe the energy loss of the electric and magnetic [21–23].

1.4 Microwave absorption materials

Many materials can be used to absorb microwaves, and they are generally divided into three main types:

1. Magnetic loss materials: These materials have high complex relative permeability. Many magnetic materials can absorb microwaves. The most important of these are ferrites and carbonyl iron.

2. Dielectric loss materials: These materials have high complex relative permittivity. Many dielectric materials can absorb microwaves, such as conductive polymers (e.g., polyaniline, polypyrrole) and carbonaceous materials (e.g., carbon black, activated carbon, carbon fibers, graphene), which have played a significant role in high-frequency EM wave absorption.

3. Hybrid materials: Hybrid materials are composites made via the incorporation of organic and inorganic components, such as composite materials with a nano ferrite core and a conducting polymer shell.

1.4.1 Ferrites

Ferrites are magnetic ceramic materials, the main component of which is iron (III) oxide, in addition to other metallic elements (Ba, Mn, Co, Cu, Ni) [24].

1.4.1.1 Classification of ferrites according to their crystal structure

According to the crystal structure, ferrites can be divided mainly into three main sections:

(a) Spinel ferrites

The metal cations in this type of ferrite are located in a cubic structure. The spinel lattice comprises an arrangement of close-packed oxygen ions, where 32 oxygen ions shape the unit cell. These ions are located in a face-centered cubic arrangement (FCC), leaving two types of spaces between the ions through which metal cations can be located, which are as follows:

1. Tetrahedral sites: These sites are surrounded by 4 oxygen ions.
2. Octahedral sites: These sites are surrounded by 6 oxygen ions.

In the unit cell, there are 64 tetrahedral sites and 32 octahedral sites, but metal cations can occupy 8 tetrahedral sites and 16 octahedral sites [25].

(b) Hexagonal ferrites

They are ferrites consisting of magnetic iron oxides with a hexagonal structure. This type of ferrite has several general formulas indicated by letters such as (M, U, Y, etc.), the most important of which is $MFe_{12}O_{19}$, where M is elements such as barium, lead, or cobalt. Table 2 shows the most important structures of ferrites with a hexagonal structure. This type of ferrite is used as a permanent magnet, which is used at very high frequencies. The lattice of these ferrites is similar to spinel ferrite, with oxygen ions distributed according to the specific patterns.

Table 2 – Types of hexaferrite

Hexaferrite type	Chemical formula
M	$MFe_{12}O_{19}$
Y	$M_2Me_2Fe_{12}O_{22}$
W	$MMe_2Fe_{16}O_{27}$
Z	$M_3Me_2Fe_{24}O_{41}$
X	$M_2Me_2Fe_{28}O_{46}$
U	$M_4Me_2Fe_{36}O_{60}$

(c) Garnet ferrites

This ferrite type has the general formula $3M_2O_3 \cdot 5Fe_2O_3$, where M is a trivalent metal ion (Yttrium, Gadolinium, Samarium, etc.). These ferrites have a cubic crystal structure where the divalent cations are located in the tetrahedral sites and the trivalent cations in the octahedral and hexahedral sites [25].

1.4.1.2 Classification of ferrites according to magnetic properties

According to their magnetic properties, ferrites can be classified into soft and hard.

a) Soft ferrites

Ferrites with spinel and garnet crystal structures are soft magnetic materials characterized by a low coercivity field, such as NiZn ferrite and MnZn ferrite.

b) Hard ferrites

This ferrite type is characterized by high coercivity and remanent magnetization, such as hexagonal ferrites [26].

1.4.1.3 Applications of ferrites

Magnetic materials are characterized by their high resistance, low cost, easy manufacturing methods, and super magnetic properties. Ferrites are widely used in many applications such as radar, magnetic shielding, microwave absorption, audio, telecommunications, power transformer cores, amplifiers, small motor cores, magnetic sensors, automobiles, etc.

1.4.1.4 Methods of preparing ferrites

The preparation method is considerably significant to acquiring the desired outcome where properties of different types of nano ferrites change, particularly with varying ways of preparation. For instance, the size and form of particles determine the properties of nano ferrites, which are managed by the preparation method. Nano ferrites can be fabricated via different methods as follows:

1. Ceramic sintering method.
2. Co-Precipitation method.
3. Hydrothermal method.

4. Sol-gel method.
5. Microemulsions method.

1.4.1.4.1 Ceramic sintering method

This method involves mixing the raw materials (metallic oxides or carbonates) using a ball mill. The prepared ferrites are sintered in the temperature range (900–1250 °C). Co-Precipitation method

This method is considered one of the most essential for preparing ferrite nanomaterials. It especially depends on preparing an aqueous solution based on suitable initial materials to form the ferrite, adding a convenient sedimentation factor until a convenient pH is reached, and a precipitate is obtained, followed by a filtration and drying process, and heat treatment to obtain the nano ferrite powder. Among the most significant initial materials used in this method: are metal chlorides, metal nitrate, metal sulfate as sources of mineral cations, ammonium hydroxide, and sodium hydroxide as sedimentation agents [27–30].

1.4.1.4.2 Hydrothermal method

An ideal thermal technique includes various steps for getting nano ferrites and their composites. These synthesis methodologies involve hydrothermal, microwave-aided hydrothermal (MAH), colloid mill or mechano-hydrothermal, combustion, and thermal decomposition techniques. Nano-particles acquired from the thermal process on the decay of organometallic precursors usually submit symmetric shape and size dispensation. Chemical reactions occur in the hydrothermal method of initial materials (mineral salts) within an aqueous medium under certain conditions of temperature and pressure. The preparation process occurs in special reactors through which the interaction conditions can be controlled to crystallize the ferrite material directly from the solution [31–34].

1.4.1.4.3 Sol-Gel method

The sol-gel technique can be defined as forming a relatively stable solid phase at a specific temperature starting from the liquid phase. The main reactions in this method are the hydrolysis phase, where the acids and bases are used as catalysts, and the condensation phase. In this phase, the molecules resulting from hydrolysis are linked together to form a three-dimensional structure. The essential primary materials used in this technique are chlorides and nitrates of metals [35–37]. On the other hand, it is necessary to carefully control the variables of the sol-gel method to obtain a homogeneous final product and good magnetic and radar absorption properties, the most important of which are: purity, quality of raw materials, reaction temperature, stirring quality (mechanical, ultrasound, and magnetism), and finally the pH value.

1.4.1.4.4 Microemulsion method

The microemulsion technique is used for attaining more concern in essential as well as manufacturing research due to its unique characteristics. We mention some of them, like

thermodynamic stability, sizeable interfacial area, and capability to get dissolvable in immiscible liquids. The microemulsion technique includes three segments, water, oil, and surfactant. During blending organometal antecedents, a precipitate is formed. This technique controls particle characteristics like homogeneity, geometry, morphology, and particle size. These particles are used in magnetic recording and microelectronic devices [38]. Table 3 shows the advantages and disadvantages of the microemulsion technique.

1.4.1.5 Factors impacting characteristics of nano ferrites

The difference in nano ferrites properties can be adjusted by dominating the various preparation factors, such as the components, annealing temperature, and pH value.

1.4.2 Carbonyl iron powder (CIP)

CIP is a type of magnetic loss material of EM waves. CIP has a low electrical conductivity, high saturation magnetization, and Curie temperature. However, the increased density and insufficient stability restrain their practical uses.

1.4.2.1 Applications of carbonyl iron powder

CIP is widely used in many applications such as radar, magnetic shielding, radar absorption, stealth jets, drones, vehicles, telecommunications, power transformer cores, amplifiers, small motor cores, magnetic sensors, vehicles, etc.

1.4.3 Conductive polymers (CPs)

CPs are organic polymers that conduct electricity, usually indicated as “synthetic metals” because of their capability to integrate polymers' chemical and mechanical characteristics with the electrical characteristics of metals and semiconductors. CPs combine moderate conductivity, ease of fabrication, low cost, corrosion resistance, low density compared to metals, and the ability to absorb electromagnetic waves [39,40].

1.4.3.1 Polyaniline

PANI is one of the most studied conductive polymers due to its ease of fabrication and good electrical conductivity. PANI consists of monomer units built from reduced (y) and oxidized ($1-y$) blocks: where $0 \leq y \leq 1$. The redox state of the polymer is defined by the value of y , which may vary continuously from zero to unity. Figure 3 shows the general chemical formula of polyaniline [41].

1.4.3.2 Applications of conductive polymers

CPs seem to be one of the few substances qualified to show dynamic MA conduct, called “smart stealth substances”, because of the reversible electrical characteristics of CPs. Their benefit can also be expanded to high-tech fields such as space, military defense, navigation/communication control, or as a RAM in solar cells, computers, biosensors, etc.

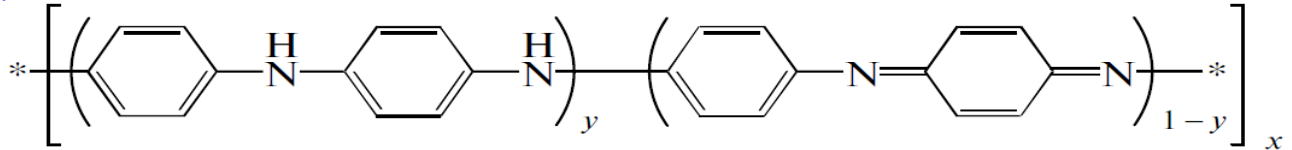


Figure 3 – General chemical formula of polyaniline [41]

1.4.4 Carbonaceous substances

Carbon is considered the 4th most existing chemical element in the world by mass. It is the element that earth selected as a base for the environment under the circumstances conformable to Earth's. Pure carbon has many forms involving diamond, graphite, graphene, buckminsterfullerene, nanotube, etc.

1.4.4.1 Carbon black

CB is a shape of paracrystalline carbon that has a high surface area to volume ratio, albeit lower than that of activated carbon. CB has been used for electronics, RAMs, photocopiers, laser printer toners, and paints.

1.4.4.2 Activated carbon

AC has small and low-volume pores that increase the surface area for adsorption or chemical reactions. AC has been used for air purification, water purification, medicine, sewage treatment, and RAMs.

1.4.4.3 Graphite

C is a crystalline form of the element carbon. It consists of weakly bound layers of graphene stacked into a hexagonal structure. C occurs naturally and is the most stable form of carbon under standard conditions. Graphite has been used in batteries, solar panels, electrodes, and RAMs.

1.5 Composite absorbent materials with graded impedance

Absorption is achieved by gradually decreasing the impedance starting from the dielectric layer, whose impedance is close to the impedance value of air, to secure the entry of most of the incident waves into the material and reduce reflection. Then the absorbent layers are graded with increasing impedance.

1.6 Characteristics of an ideal microwave absorption material

MAMs should be lightweight, prepared in various shapes, waterproof, chemically resistant, have good mechanical and physical properties, be easy to prepare, low cost, have a wide absorption field, and are strong absorption [42].

1.7 Absorbent ferrites nanoparticles for microwave

The researchers designed the absorbent ferrites of the EM waves to use them in civilian and military applications. According to this, the $\text{Ni}_{0.7}\text{Zn}_{0.3}\text{Y}_x\text{Fe}_{2-x}\text{O}_4$ was successfully prepared by Chen et al. The sol-gel technique synthesized the absorbents. The results displayed that the RL_{\min} peaks of absorbents shifted to lower frequencies (f_m) with the increasing absorbent thickness (t_m), as shown in Figure 4 [43]. This case may be determined by the $\lambda/4$ cancellation model, as indicated in formula (5) [44–46].

$$t_m = \frac{nc}{4f_m\sqrt{|\mu_r||\epsilon_r|}} \quad (n = 1, 3, 5, \dots) \quad (5)$$

Where c is the velocity of light.

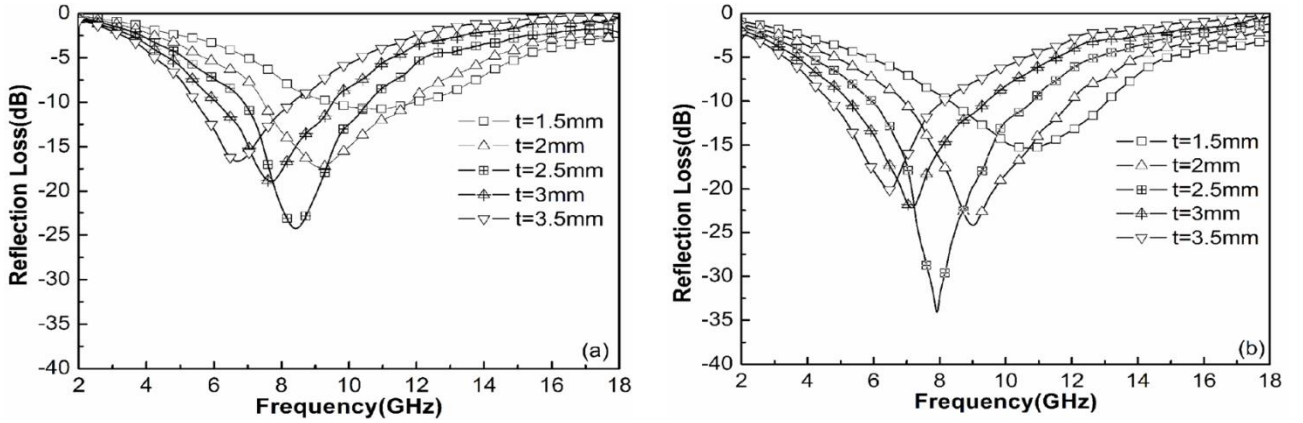


Figure 4 – RL curves of $\text{Ni}_{0.7}\text{Zn}_{0.3}\text{Y}_x\text{Fe}_{2-x}\text{O}_4$ ferrite ($x = 0$, (a); $x = 0.2$, (b)) at different thicknesses [43]

The $\text{Cu}_{0.2}\text{Ni}_{0.4}\text{Zn}_{0.4}\text{Fe}_2\text{O}_4$ was studied by Gregori et al. The absorbents were prepared by the citrate precursor. The absorbents were synthesized by dispersing $\text{Cu}_{0.2}\text{Ni}_{0.4}\text{Zn}_{0.4}\text{Fe}_2\text{O}_4$ powder within the wax matrix of 80 % w/w. The results displayed that $\text{BW}_{-10\text{ dB}}$ for the absorbent reached 2.4 GHz [47]. Malas et al. prepared the $\text{Cu}_{0.2}\text{Ni}_{0.4}\text{Zn}_{0.4}\text{Fe}_2\text{O}_4$, too but with a different technique, which was the co-sedimentation technique. The absorbents were synthesized by dispersing ferrite nanoparticles within the ER matrix of 30 % w/w. The results displayed that $\text{BW}_{-10\text{ dB}}$ for the absorbent reached 4.1 GHz [48]. The changes in MA characteristics were observed with the variation of the synthesis method. Zhang et al. designed the $\text{Ni}_x\text{Co}_{1-x}\text{Fe}_2\text{O}_4$ ($x = 0.5, 0.8$) by ball milling. The RL_{\min} of -35.5 dB at 11.5 GHz and the absorption $\text{BW}_{-10\text{ dB}}$ of 3.2 GHz for 2.5 mm thickness were noticed for $\text{Ni}_{0.8}\text{Co}_{0.2}\text{Fe}_2\text{O}_4$. On the other hand, the RL of -30.6 dB at 11.9 GHz and the absorption $\text{BW}_{-10\text{ dB}}$ of 3.4 GHz for 2.5 mm thickness were noticed for $\text{Ni}_{0.5}\text{Co}_{0.5}\text{Fe}_2\text{O}_4$ [49], where the changes in MA characteristics were noticed with the variation of the compound composition, as cited above.

However, other scholars have investigated the impact of substitution operation with a number of cations and substitution rates on ferrite. According to this, the $[\text{Ni}_{0.4}\text{Cu}_{0.2}\text{Zn}_{0.4}](\text{Nd}_x\text{Y}_x\text{Fe}_{2-2x})\text{O}_4$ ($0.0 \leq x \leq 0.05$) was designed by Chen et al. The absorbents were synthesized by the citrate sol-gel technique [50]. The results displayed that the RL_{\min} peaks of absorbents shifted to higher frequencies by increasing the substitution with several cations on ferrite. Zubar et al. designed the $\text{Ni}_{0.4}\text{Cu}_{0.2}\text{Zn}_{0.4}\text{Tb}_x\text{Fe}_{2-x}\text{O}_4$ ($0.0 \leq x \leq 0.10$) by sonochemical method. The outcomes exhibited that the substitutions rate significantly influences MA properties, as shown in Figure 5 [51]. Kostishyn et al. designed the $\text{Ni}_{0.4}\text{Cu}_{0.2}\text{Zn}_{0.4}\text{Eu}_x\text{Fe}_{2-x}\text{O}_4$ ($0.0 \leq x \leq 0.10$) by sol-gel method. The effect of Eu^{3+} ion substitution on the MA properties was studied [52]. The results displayed that the RL_{\min} peaks of absorbents shifted to higher frequencies with increasing the Eu^{3+} contents. Trukhanov et al. designed the $[\text{Ni}_{0.5}\text{Co}_{0.5}](\text{Dy}_x\text{Fe}_{2-x})\text{O}_4$ ($x \leq 0.08$) by citrate gel technique. The effect of Dy^{3+} ion substitution on the MA properties was studied [53]. The results displayed that the RL_{\min} peaks of absorbents shifted to higher frequencies with increasing the Dy^{3+} contents. From these researches, it was noted that the unsubstituted ferrites were known for their poor capability to absorb EM waves, which required the study of the impact of the cations substituted and cations content in ferrite through which the MA properties were enhanced. On the other hand, other researchers have investigated the impact of doped on MA properties. Garg et al. studied the impact of Nd^{3+} doping on the MA properties of barium hexaferrite. The results displayed that RL_{\min} was -33.17 dB at 9.5 GHz for a thickness of 2.2 mm and the absorbing $\text{BW}_{-10\text{ dB}}$ was 2.94 GHz for $\text{BaNd}_{0.04}\text{Fe}_{11.96}\text{O}_{19}$ [54]. Ghasemi et al. studied the Mn–Co–Sn doped on barium ferrite. The barium ferrite was synthesized by the sol-gel method. The results displayed that by changing the substituted elements in barium ferrite, the absorbing $\text{BW}_{-10\text{ dB}}$ reached 8 GHz with unique RL_{\min} [55]. These investigations illustrated the substantial impact of the synthesis technique, the kind of ferrite, the influence of the cations substituted and cations content in absorbent ferrite, the absorbent ferrite thickness, and the impact of elements doping on MA properties of absorbent ferrite.

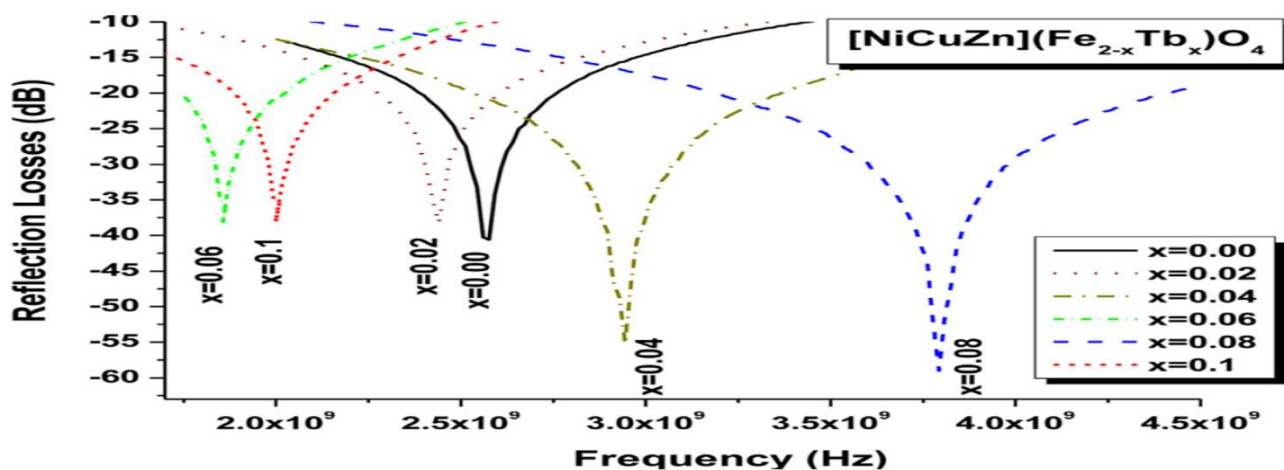


Figure 5 – RL as a function of the EM wave frequency of $\text{Ni}_{0.4}\text{Cu}_{0.2}\text{Zn}_{0.4}\text{Tb}_x\text{Fe}_{2-x}\text{O}_4$ ($0.0 \leq x \leq 0.10$) [51]

1.8 Incorporation of CPs with ferrite nanoparticles to absorb microwaves

Spinel and hexagonal ferrites have been well-known for their integral MA characteristics [56,57]. However, these ferrites are restrained because of high density, lower dielectric loss, and limited absorption band, which makes use of these ferrites inefficient, particularly when wideband absorption is required [58,59]. To find solutions for these shortcomings, dielectric loss materials are added, such as polyaniline, polypyrrole, carbon nanotubes, carbon black, etc. The results have shown the synergistic impact of combining magnetic loss and dielectric loss material together [60]. Many researchers have conducted studies of the MA characteristics of ferrite nanoparticles containing CPs. Researchers have tried to enhance the absorption $BW_{-10\text{dB}}$ by designing nanocomposites with a construction (core/shell). The magnetic core is coated with CPs shell [61,62]. According to this, PANI/NiZn ferrite nanocomposites in the frequency range of 2–40 GHz were designed by Ting et al. [63]. The 67% w/w of the nanocomposites was dispersed in an ER matrix. The outcomes showed that by rising PANI content in NiZn ferrite, a wide absorption $BW_{-10\text{ dB}}$ could be acquired. Li et al. investigated the MA properties of PANI/NiZn ferrite nanorods. The 70% w/w of the nanorods was dispersed in a paraffin wax matrix. The MA properties were studied in the frequency range of 2-18 GHz. The results displayed that RL_{min} was -27.5 dB at 6.2 GHz for a thickness of 2 mm, and the absorption $BW_{-10\text{ dB}}$ was 3 GHz [64]. Yang et al. investigated the MA properties of PANI/NiZn ferrite nanocomposites. The nanocomposites were synthesized by in-situ polymerization. The 75% w/w of the nanocomposites was dispersed in a paraffin wax matrix. The molar ratios of PANI/NiZn ferrite nanocomposites were 3:1, 2:1, 1:1, 1:2, and 1:3. The results displayed that RL_{min} was -41 dB at 12.8 GHz for a thickness of 2.6 mm and the absorption $BW_{-10\text{ dB}}$ was 5 GHz for PANI/NiZn (1:2) as shown in Figure 6 [65]. Xie et al. synthesized NiZn ferrite/PANI nanocomposites by hydrothermal technique. The MA properties were studied in the 2–18 GHz range. The results displayed that RL_{min} was -17 dB at 11.1 GHz and the absorption $BW_{-10\text{ dB}}$ was 5 GHz [66]. Ma et al. have reported the MA properties of PANI/ $\text{Co}_{0.5}\text{Zn}_{0.5}\text{Fe}_2\text{O}_4$ nanocomposite. The MA properties were studied in the 8.2–26.5 GHz range. The absorbers were synthesized by in-situ polymerization technique. They found that the absorbers had broadband, and minimal reflection loss, where the results indicated that the absorber had a RL_{min} of -39.9 dB at 22.4 GHz and the absorption $BW_{-10\text{ dB}}$ was 5 GHz for 2 mm thickness [67]. However, in various cases, the PANI/F nanocomposites can be incorporated with carbon materials as well, e.g. core-shell F/GO/PANI [68], $\text{Fe}_3\text{O}_4@\text{C}@\text{PANI}$ [[69], F/G/PANI [70], and so on. These nanocomposites can possess special MA performance due to the connection absorbent mechanism in each part. From the above of these studies, we can summarize that the PANI-based nanocomposites are the premium RL of PANI-based nanocomposites produced essentially from the impacts of conduction, magnetic, and dielectric losses. Where combining PANI and other waste substances can improve the absorption $BW_{-10\text{ dB}}$ and enhance the RL values. The EM wave attenuation performance of PANI-based nanocomposites can also be developed by adjusting their architectures.

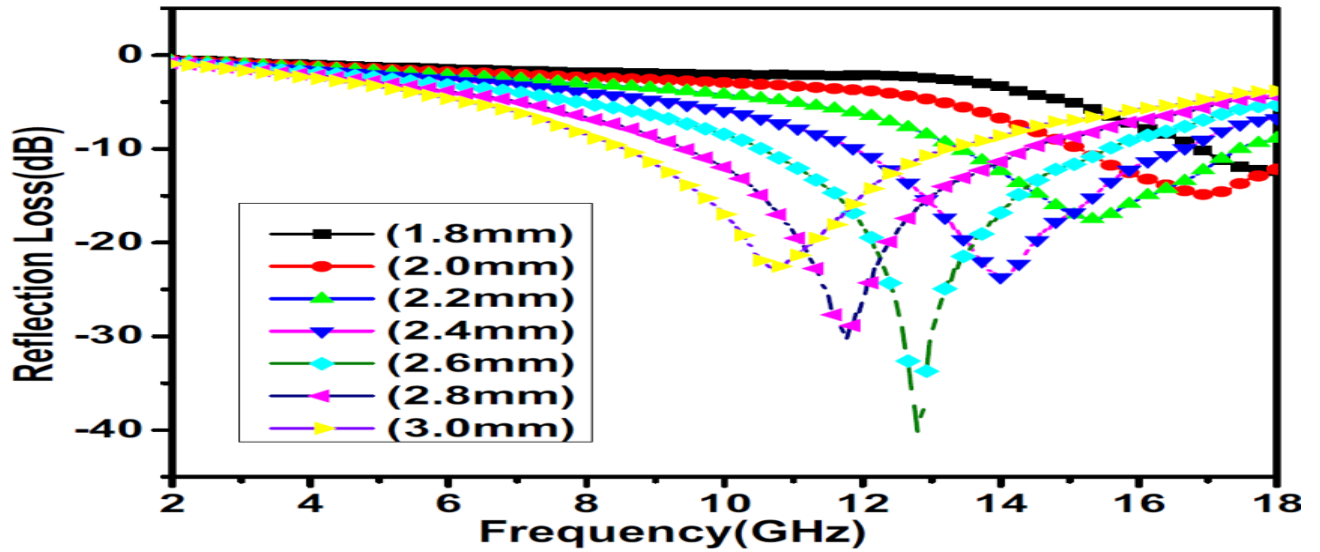


Figure 6 – RL as a function of the EM wave frequency of PANI/NiZn (1:2) nanocomposites with different thicknesses [65]

1.9 MA behavior of carbon-based nanomaterials

These days, new carbon nanomaterials are showing and presenting excellent microwave-absorbing characteristics. CNS-based substances have attracted significant attention for microwave absorption lately because of the unique structure and the characteristics of the physical and chemical of carbon, for example, high permittivity, high specified surface region, unique electronic conductivity, huge interface, etc. [71,72]. Accordingly, carbon nanomaterials are usually created to fit the requirements of elevated-effective microwave attenuation substances. When ferrites are incorporated with CB, the MA properties of the resultant absorber are expected to improve. According to this, CB/ $Zn_{0.8}Ni_{0.2}Fe_2O_4$ nanocomposites dispersed in a silicon dioxide matrix were prepared by Dan et al. [73]. The results of $Zn_{0.8}Ni_{0.2}Fe_2O_4$ nanoparticles range of 0–1.75 wt% and different coating thicknesses (1–2.5 mm) on MA behavior in the frequency range of 8–12 GHz have been studied. The results referred that a model of 1.5 wt% $Zn_{0.8}Ni_{0.2}Fe_2O_4$ nanoparticles displayed the highest MA at 10 GHz. Higher coating thicknesses (1–2.5 mm) displayed a bigger MA and reached a RL_{min} of 2 mm thickness. On the other hand, Chakradhary et al. [74] designed strontium ferrite epoxy (SrF) NC and CB-loaded (CBSrF) NC. The RL_{min} for the SrF NC is -25.19 dB at 13.32 GHz for 10.5 mm thickness, whereas for (CBSrF) NC the RL_{min} is -31.15 dB at 10.32 GHz for 9.5 mm thickness. Therefore, the CB-loaded (SrF) NC displays higher attenuation efficiency than the (SrF) NC. On the other hand, Peng et al. prepared a collection of CNTs filled with Fe, which induced a rise in the reaction with EM radiation from the absorber substance. The amount of normal carbon permeability exceeds 1. The outcome of this conjugation was that the amount of RL was -24.8 dB at 10.9 GHz for a thickness of 1.2mm, and the absorption (BW)_{-10 dB} was 16.0 GHz [75]. Zhu et al. prepared the carbon nanotubes/iron nanowires compounds and the maximum reflection loss (RL_m) of the compounds was -22.73 dB [76]. The carbon nanotubes/cobalt

nanoparticles compounds were manufactured and the symmetric cobalt nanoparticles were well scattered on the carbon nanotubes surface [77]. The RL_m of the compounds was -36.5 dB. Several magnetic metal alloy compounds, like rod-like FeCo/CNTs were studied [78]. The RL_m of FeCo/CNTs compounds was -46.5 dB at 12.56 GHz and the active absorption $(BW)_{-10dB}$ reached 3.92 GHz. The RL_m of carbon nanotubes/ carbonyl iron particle compounds was -33.3 dB at 11.4 GHz.

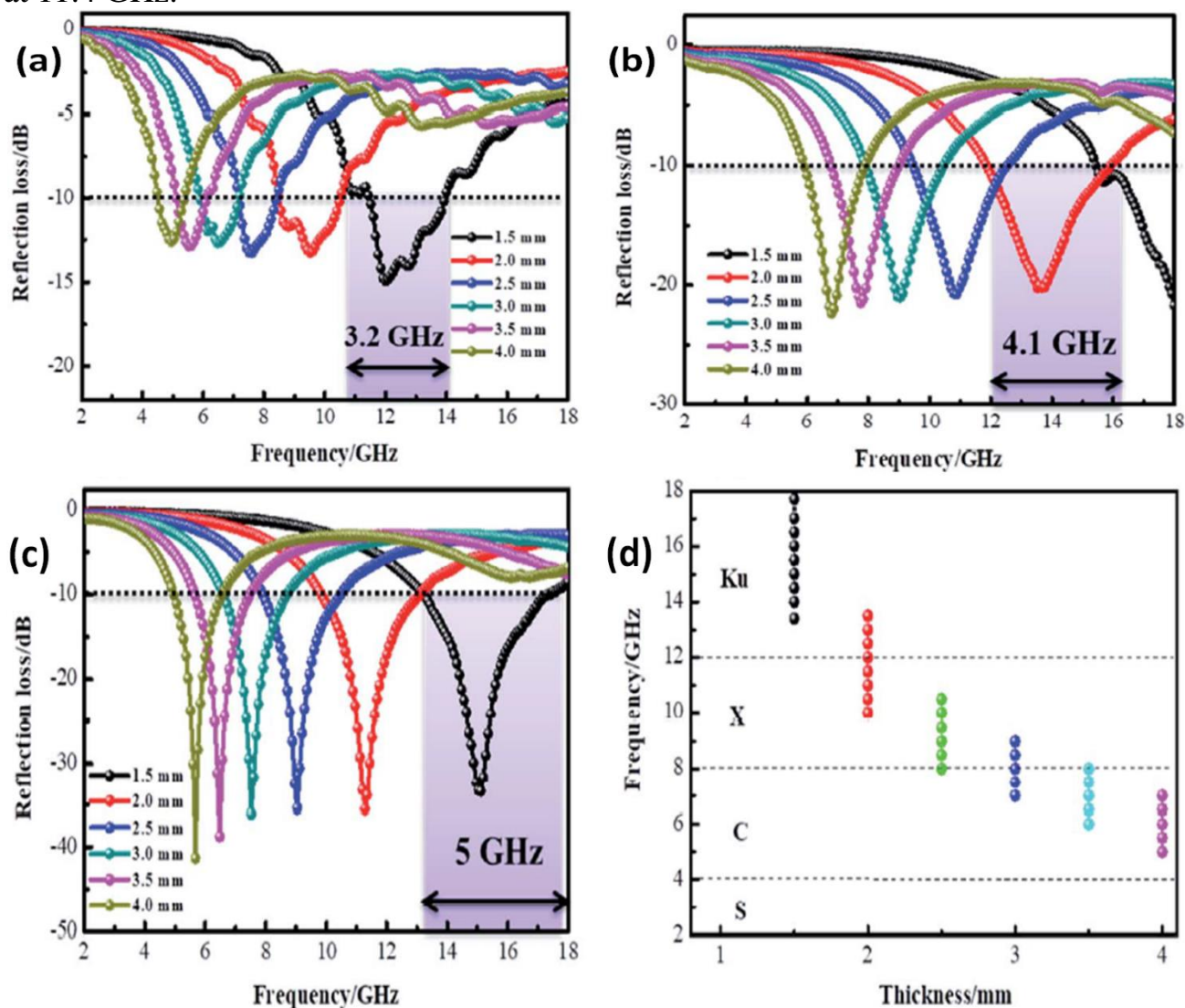


Figure 7 – RL shapes for carbon fiber (a), carbon fiber@cobalt iron oxide (b) and carbon fiber@cobalt iron oxide@manganese(IV) oxide composites (c) at different thicknesses the efficient absorption $(BW)_{-10dB}$ of carbon fiber@cobalt iron oxide@manganese(IV) oxide composite (d) [56]

On the other hand, many scientists have studied the impact of CF on ferrite. For example, Hou et al. [79] studied carbon fiber@cobalt iron oxide and carbon fiber@cobalt iron oxide@manganese(IV) oxide composites by the sol-gel method. Carbon fiber@cobalt iron

oxide@manganese(iv) oxide composite exhibits excellent MA performance due to reasonable EM matching, and its RL_m value equals -34 dB with a sample thickness of 1.5 mm. Figure 7 illustrates RL shapes of carbon fiber (a), carbon fiber@cobalt iron oxide (b), and carbon fiber@cobalt iron oxide@manganese(iv) oxide composites (c) at different thicknesses, the efficient absorption BW of carbon fiber@cobalt iron oxide@manganese(iv) oxide composite (d) [56]. Figure 7 shows that the RL attenuation peaks of samples moved to lower frequencies with increasing sample thickness. This phenomenon may be defined by the quarter-wavelength ($\lambda/4$) cancellation model, as shown in equation (5). The insert of impurities into the carbon fibers scope in several states created diversities in the magnetic reaction to EM wave via the nanomaterial, [80] for example, by ferromagnetism, [81] although some cases, like the Fe_3O_4 /mineral-coated by carbon fibers, [82] the examined substance only showed perversion in response to the electronic reaction of the substance, appearing in an essential electronic loss role compared to a small magnetic loss [82].

From the above of these studies, we can summarize that the carbon-based nanocomposites are the premium reflection loss of carbon-based nanocomposites produced from the impacts of conduction, magnetic, and dielectric losses. Combining carbon and other waste substances can improve the absorption $BW_{-10\text{ dB}}$ and enhance the RL values. Carbon-based nanocomposites' electromagnetic wave attenuation performance can be developed by adjusting their architectures.

2 PRACTICAL PART

2.1 Chemical, raw and commercial materials

Ferrites were prepared in this research by different methods (physical and chemical), starting from metal oxides (physical method) and metal salts (chemical methods: citrate precursor, self-combustion). The preparation of the composite (PANI/SF, PANI/HF, PANI/CI, PANI/CB, etc.) required different chemicals (monomers, oxidizers, and various chemicals). Table 3 shows the specifications of the chemicals used to accomplish this research.

Table 3 – Chemicals used in laboratory work and their specifications

Chemicals	Formula	molar mass (g/mole)	Purity (%)	Melting point (°C)	Appearance	Source
1	2	3	4	5	6	7
Iron(III) oxide	Fe ₂ O ₃	159.69	98.7	1565	Solid	Mosreactive company
Zinc(II) oxide	ZnO	81.380	78.3	1975	Solid	
Nickel(II) oxide	NiO	74.6928	77.6	1955	Solid	
Nickel(III) oxide	Ni ₂ O ₃	165.390	77.2	600	Solid	
Copper(II) oxide	CuO	79.545	78.5	1326	Solid	
Manganese(I) oxide	MnO	70.937	80.7	1945	Solid	
Paraffin wax	–	–	Commercial	–	Solid	Market
Iron(III) nitrate nonahydrate	Fe(NO ₃) ₃ ·9H ₂ O	403.95	98.3	47	Solid	Trading company ant
Nickel(II) nitrate hexahydrate	Ni(NO ₃) ₂ ·6H ₂ O	290.81	98.3	56	Solid	
Zinc nitrate hexahydrate	Zn(NO ₃) ₂ ·6H ₂ O	297.5	98.7	36.4	Solid	

Continuation of Table 3

1	2	3	4	5	6	7
Sucrose	$C_{12}H_{22}O_{11}$	342.3	Commercial	–	Solid	Market
Sodium dodecyl sulfate (SDS)	$C_{12}H_{25}NaO_4S$	288.38	92.2 %	206	Solid	Trading company ant
Ethanol	C_2H_5OH	46.07	Commercial	–	Liquid	Market
Hydrochloric acid	HCl 37%	36.46	Commercial	–	Liquid	Market
Aniline	$C_6H_5NH_2$	93.13	99.5 %	–	Solid	Sigma Aldrich Company
Ammonium persulfate (APS)	$(NH_4)_2S_2O_8$	228.20	95.3 %	–	Solid	Trading company ant
Citric acid	$C_6H_8O_7$	192.12	99.0 %	–	Solid	Sigma
Ammonium hydroxide	NH_4OH	35.05	99.8 %	–	Liquid	Commercial
Carbonyl iron	CI		99.6 %	1538	Solid	Cabot Norit Company
Carbon black	CB	12.011	99.5 %	3550	Solid	
Activated carbon	AC	12.011	Commercial	3500	Solid	Market
Graphite	C	12.011	Commercial	3652	Solid	Market

2.2 Tools and equipment used for sample preparation

Table 4 shows the laboratory's tools and equipment used to prepare microwave absorbers.

Table 4 – Tools and equipment used for sample preparation

Tool/Equipment	Manufacture Company
Sensitive scale	Hochoice electronic
Sieve shaker	Fritsch
Ball mill	Fritsch
Glassware	–
Homogenizer	Fritsch
Vacuum pump	jinteng
Büchner funnel	–
Digital magnetic hot plate stirrer	CAPPRondo
Heat treatment oven	GIMA
Digital pH meter	Benchtop
Dryer	Henan Touch

2.3 Characterization devices

The prepared samples were structurally characterized using XRD, FTIR, TGA, and EDX. A powder X-ray diffractometer (XRD, Rigaku Miniflex 600, Cu-K α) was used to define the crystal structures of the powders. The X-ray diffraction patterns of the prepared samples were recorded at $2\theta = 10 - 90^\circ$. Fourier Transform IR (FTIR) spectra of the prepared samples were recorded on a Perkin Elmer 65 FTIR spectrometer in the 400–4000 cm^{-1} . Thermogravimetric analysis (TGA) curve of the prepared samples were recorded on a thermal analyzer (NETZSCH 449F3A-0372-M) under a nitrogen atmosphere, from room temperature to 1000°C under a constant heating rate of 10 °C/min. Energy-dispersive X-ray spectroscopy (EDX, Quanta 200 3D) was used to know the chemical composition of some of the prepared samples. A scanning electron microscope (SEM, FEI Quanta 200 3D) was utilized to define the morphology of some of the prepared powders. The prepared samples were functionally characterized using the horn antenna connected to an oscilloscope (AKTAKOM ADS-2221M).

The samples' microwave absorption and electromagnetic interference shielding properties were estimated with the free-space technique. A microwave generator generates EM waves at the X-band frequency, where a microwave generator is connected by a WR90 waveguide instrument (IEC Standard R100, X Band). EM waves are detected by using a waveguide microwave detector circuit (Figure 8), which is attached to the pyramidal horn antenna. The measurement results in this method are verified by using a reference sample, which is an aluminum plate with previously known microwave properties. The incident EM waves (p_{in}) are measured by the pyramidal horn antenna connected to an oscilloscope (Figure 9), then the prepared sample perpendicularly is placed between a microwave generator and the pyramidal horn antenna to measure the transmitted power of the EM waves (p_T) by an oscilloscope. As a result, SE can be calculated for the EMI shielding by applying the equation (6) [83]:

$$SE (dB) = SE_R + SE_A + SE_M = 10 \log \frac{p_{in}}{p_T} \quad (6)$$

It is significant to note that the multiple reflection loss (SE_M) can be ignored if the absorption shielding (SE_A) of EMI shielding material is higher than 10 dB and equation (7) then can be rewritten as [83]:

$$SE (dB) = SE_R + SE_A = 10 \log \frac{p_{in}}{p_T} \quad (7)$$

In addition to that, the reflected power of the EM waves (p_{ref}) is measured when the EM waves are incident on the sample surface at an angle of 45° by an oscilloscope. As a result, the shielding by reflection (SE_R) can be calculated for the EMI shielding by applying equation (8).

$$SE_R (dB) = -10 \log(1 - R) = -10 \log \left(1 - \frac{p_{ref}}{p_{in}} \right) \quad (8)$$

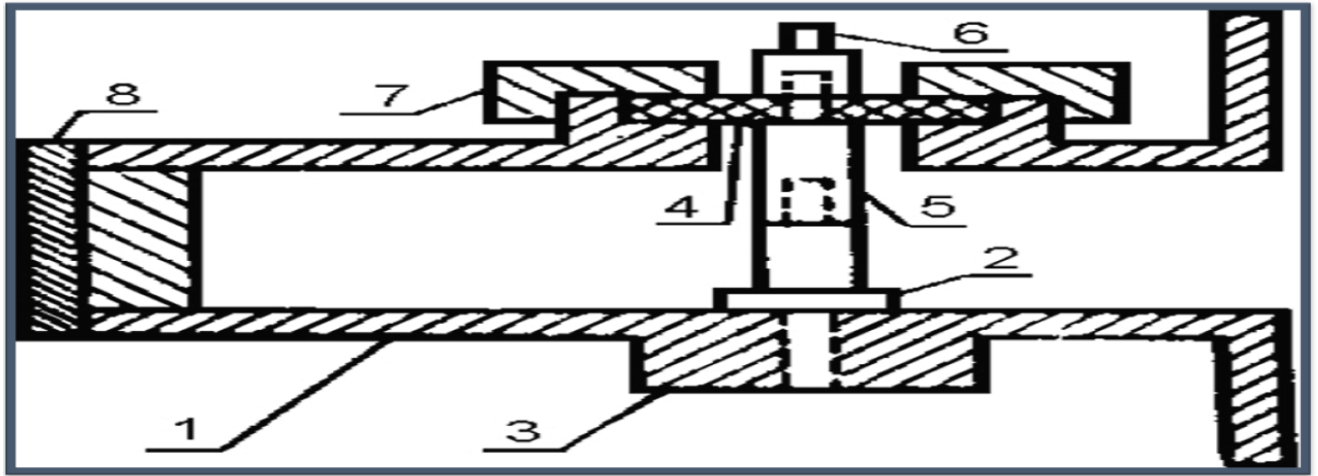


Figure 8 – Waveguide microwave detector circuit consists of: (1) waveguide segment, (2) cathode of the microwave diode, (3) bronze bushing, (4) dielectric sleeve, (5) rod, (6) output terminal signal, (7) coupling nut and (8) piston

Finally, the shielding by absorption (SE_A) is calculated by equation (9) [84,85]:

$$SE_A (dB) = -10 \log \left(\frac{T}{1 - R} \right) = -10 \log \left(\frac{p_T}{p_{in} - p_{ref}} \right) \quad (9)$$

For the microwave absorption method, the prepared sample is placed on the metal plate at an angle of 45° to measure the reflected power of the EM waves (p_{ref}) by an oscilloscope, as shown in Figure 10. As a result, the RL can be calculated by applying the equation (10) [84,85]:

$$Rl (dB) = 10 \log \frac{p_{in}}{p_{ref}} \quad (10)$$

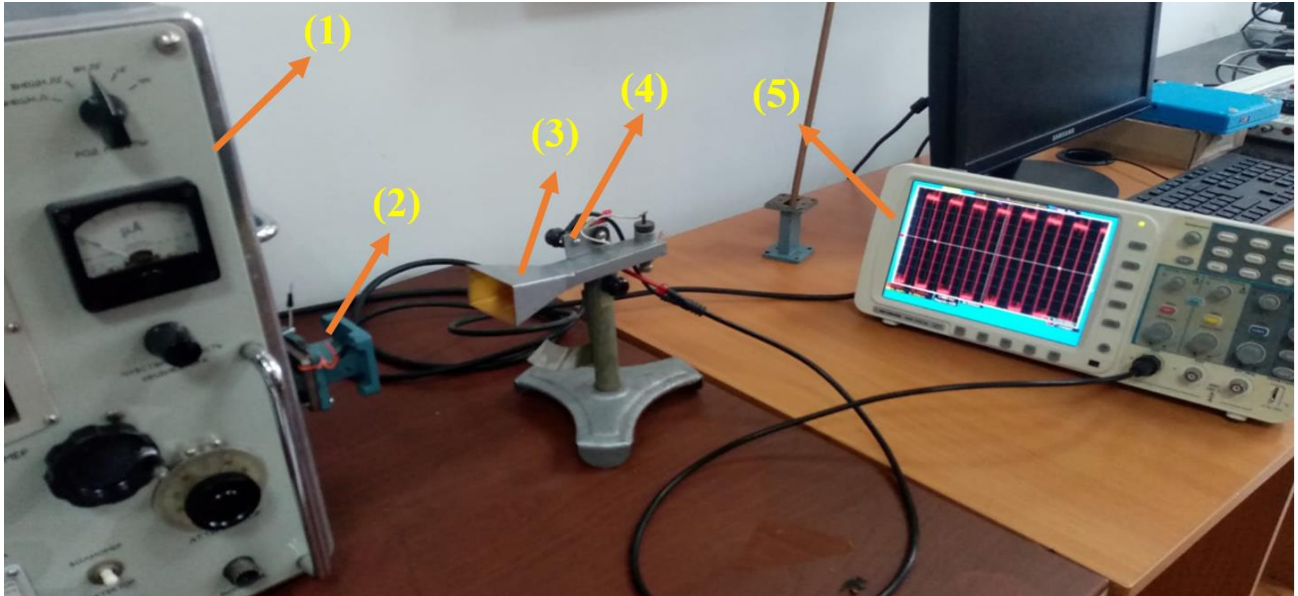


Figure 9 – Experimental setup for studying the EMI and MA properties of the prepared samples by the free-space technique. From left to right: (1) microwave generator, (2) waveguide instrument, (3) horn antenna, (4) waveguide microwave detector circuit and (5) oscilloscope



Figure 10 – Experimental setup for measuring the reflected power of the EM waves for the microwave absorption model

2.4 Sample preparation

Different methods have prepared ferrite powders and ferrite-based composites:

2.4.1 Preparation of ferrite powders

2.4.1.1 Preparation of ferrite powders by the ceramic sintering method

Ferrites were prepared by the ceramic sintering technique from metallic oxides to study the effect of substitution on radar absorption properties. The raw materials were blended with ethanol solution by a weight ratio (2:1) using the grinding balls for 8 h at 200 rpm; then, the whole mixture was transferred to the furnace for disposal of the ethanol for 24 h at 70 °C. After that, the mixture was sintered for 3 h at 1100 °C. Finally, the prepared ferrite was milled again in the presence of ethanol solution for 4 h at 200 rpm and the whole mixture was transferred to the furnace for disposal of the ethanol for 24 h at 70 °C. Table 5 and equations (2.6-2.12) show the prepared ferrites and the raw materials included in the preparation of these ferrites.

2.4.1.2 Preparation of NiZn ferrite nanoparticles by citrate precursor method

Ferrite nanoparticles were prepared by citrate precursor method. The effect of the different molar ratios of the metal ions to citrate acid (1:1, 2:1, and 3:1) and the different calcination temperatures (650, 800, and 950 °C) were studied on the ferrite properties. The flow chart for ferrite synthesis using a citrate precursor technique is shown in Figure 11. In this method, citric acid played the role of a chelating agent (chemical compound that reacts with metal ions to form stable, water-soluble metal complexes). The symbols of ferrite nanoparticle samples are detailed in Table 6. Typical images of a prepared ferrite by citrate precursor method are shown in Figure 12.

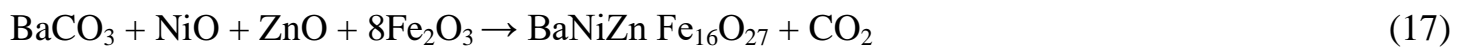
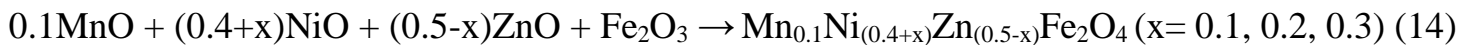
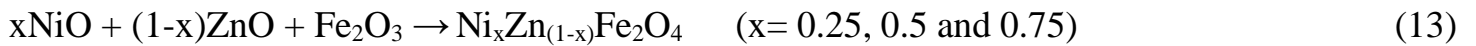
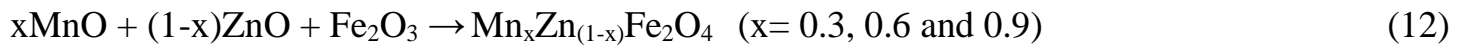


Table 5 – Prepared ferrites by the ceramic sintering technique

Ferrite	Composition
1	NiFe_2O_4
2	ZnFe_2O_4
3	MnFe_2O_4
4	CuFe_2O_4
5	$\text{Mn}_{0.3}\text{Zn}_{0.7}\text{Fe}_2\text{O}_4$
6	$\text{Mn}_{0.6}\text{Zn}_{0.4}\text{Fe}_2\text{O}_4$
7	$\text{Mn}_{0.9}\text{Zn}_{0.1}\text{Fe}_2\text{O}_4$
8	$\text{Ni}_{0.25}\text{Zn}_{0.75}\text{Fe}_2\text{O}_4$
9	$\text{Ni}_{0.5}\text{Zn}_{0.5}\text{Fe}_2\text{O}_4$
10	$\text{Ni}_{0.75}\text{Zn}_{0.25}\text{Fe}_2\text{O}_4$
11	$\text{Ni}_{0.5}\text{Zn}_{0.4}\text{Mn}_{0.1}\text{Fe}_2\text{O}_4$
12	$\text{Ni}_{0.6}\text{Zn}_{0.3}\text{Mn}_{0.1}\text{Fe}_2\text{O}_4$
13	$\text{Ni}_{0.7}\text{Zn}_{0.2}\text{Mn}_{0.1}\text{Fe}_2\text{O}_4$
14	$\text{Ni}^{3+}_{0.25}\text{Ni}^{2+}_{0.375}\text{Zn}^{2+}_{0.25}\text{Fe}_2\text{O}_4$
15	$\text{Cu}^{2+}_{0.1}\text{Ni}^{3+}_{0.15}\text{Ni}^{2+}_{0.225}\text{Zn}^{2+}_{0.45}\text{Fe}_2\text{O}_4$
16	$\text{BaNiZnFe}_{16}\text{O}_{27}$

Table 6 – Symbols of ferrite nanoparticle samples

Ferrite	Citric acid: cation	Calcination temperature (°C)	Sample symbol
$\text{Ni}_{0.5}\text{Zn}_{0.5}\text{Fe}_2\text{O}_4$	1:1	650	NZ ₁₁ - 650
	1:2		NZ ₁₂ - 650
	1:3		NZ ₁₃ - 650
	1:1	800	NZ ₁₁ - 800
	1:2		NZ ₁₂ - 800
	1:3		NZ ₁₃ - 800
	1:1	950	NZ ₁₁ - 950
	1:2		NZ ₁₂ - 950
	1:3		NZ ₁₃ - 950

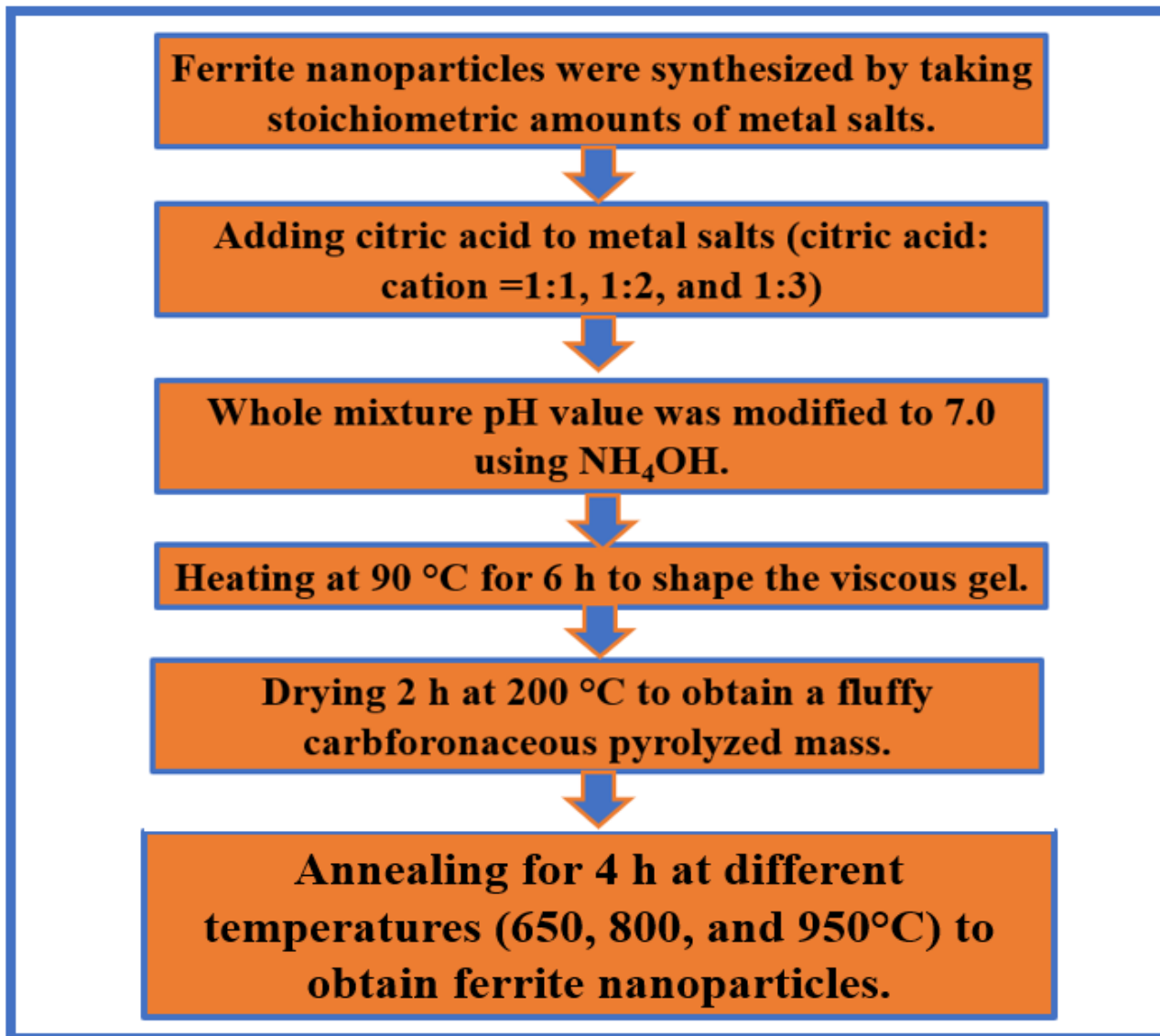


Figure 11 – Flow chart for the synthesis of ferrite utilizing a citrate precursor technique

2.4.1.3 Preparation of NiZn ferrite nanoparticles by self-combustion method

$\text{Ni}_{0.5}\text{Zn}_{0.5}\text{Fe}_2\text{O}_4$ nanoparticles were prepared by self-combustion method. Ferrite nanoparticles were synthesized by taking stoichiometric amounts of metal salts. Metal salts were blended with an aqueous sucrose solution (2 moles per metal ion). The effect of the different aqueous solutions of PVA (1%, 4%, and 6%) and the different calcination temperatures (650, 800, and 950°C) was studied on the MA properties. The flow chart for ferrite synthesis using a self-combustion technique is shown in Figure 13. In this method, sucrose played the role of fuel. The symbols of ferrite nanoparticle samples are detailed in Table 7. Typical images of a prepared ferrite by self-combustion method are shown in Figure 14.

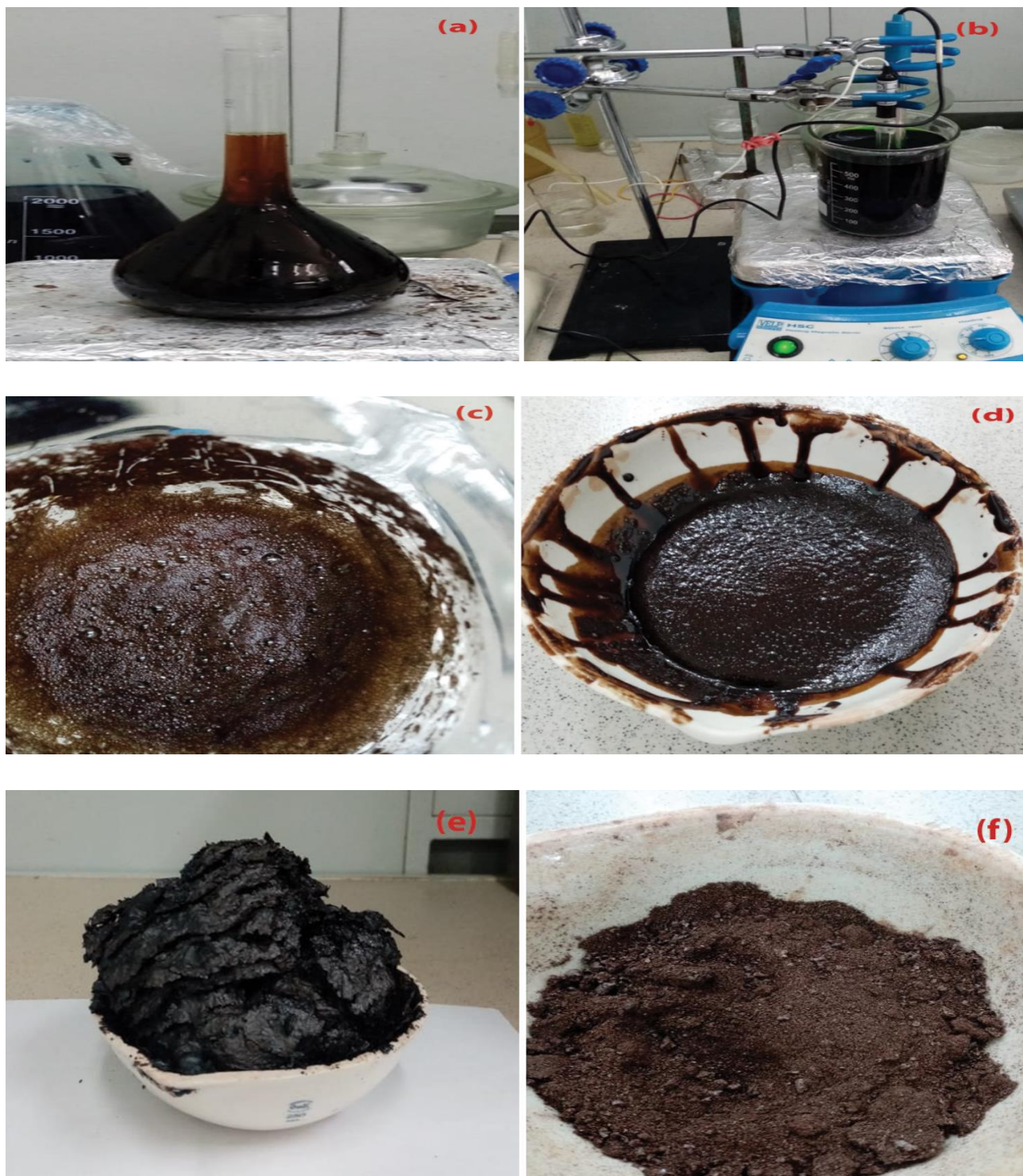


Figure 12 – Synthesis of $\text{Ni}_{0.5}\text{Zn}_{0.5}\text{Fe}_2\text{O}_4$ nanoparticles by citrate precursor method: (a) the metal salts aqueous solution in the flask, (b) using NH_4OH to maintain the pH of the solution at 7, (c) heating the solution at $90\text{ }^\circ\text{C}$ for 6 h, (d) formation the viscous gel, (e) formation a fluffy carbonaceous pyrolyzed mass and (f) obtaining nanoparticles ferrite

Table 7 – Symbols of ferrite nanoparticle samples

Ferrite	PVA concentration (%)	Calcination temperature (°C)	Sample symbol
$\text{Ni}_{0.5}\text{Zn}_{0.5}\text{Fe}_2\text{O}_4$	1	650	NSC ₁₁ - 650
	4		NSC ₁₂ - 650
	6		NSC ₁₃ - 650
	1	800	NSC ₁₁ - 800
	4		NSC ₁₂ - 800
	6		NSC ₁₃ - 800
	1	950	NSC ₁₁ - 950
	4		NSC ₁₂ - 950
	6		NSC ₁₃ - 950

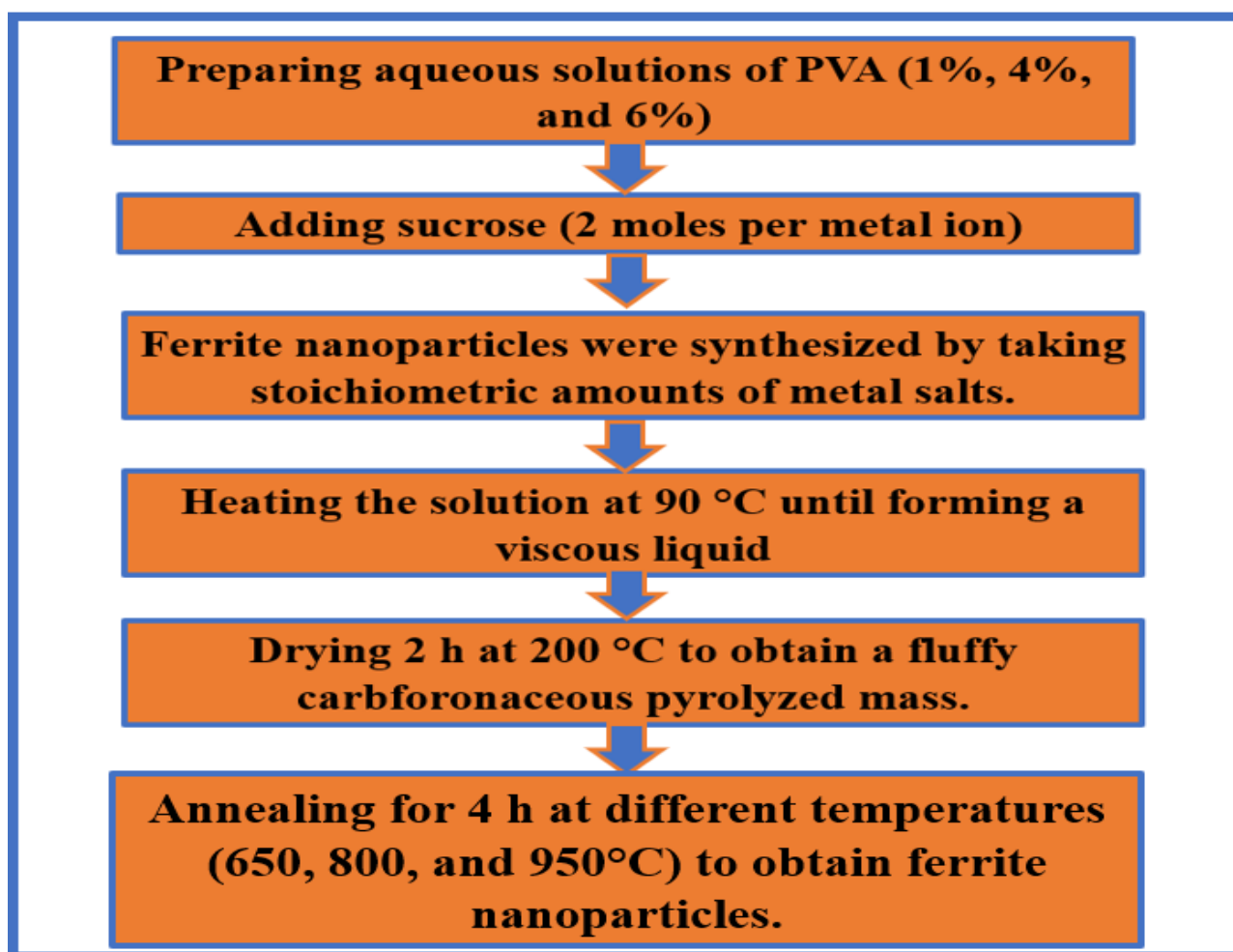


Figure 13 – Flow chart for the synthesis of ferrite utilizing self-combustion method

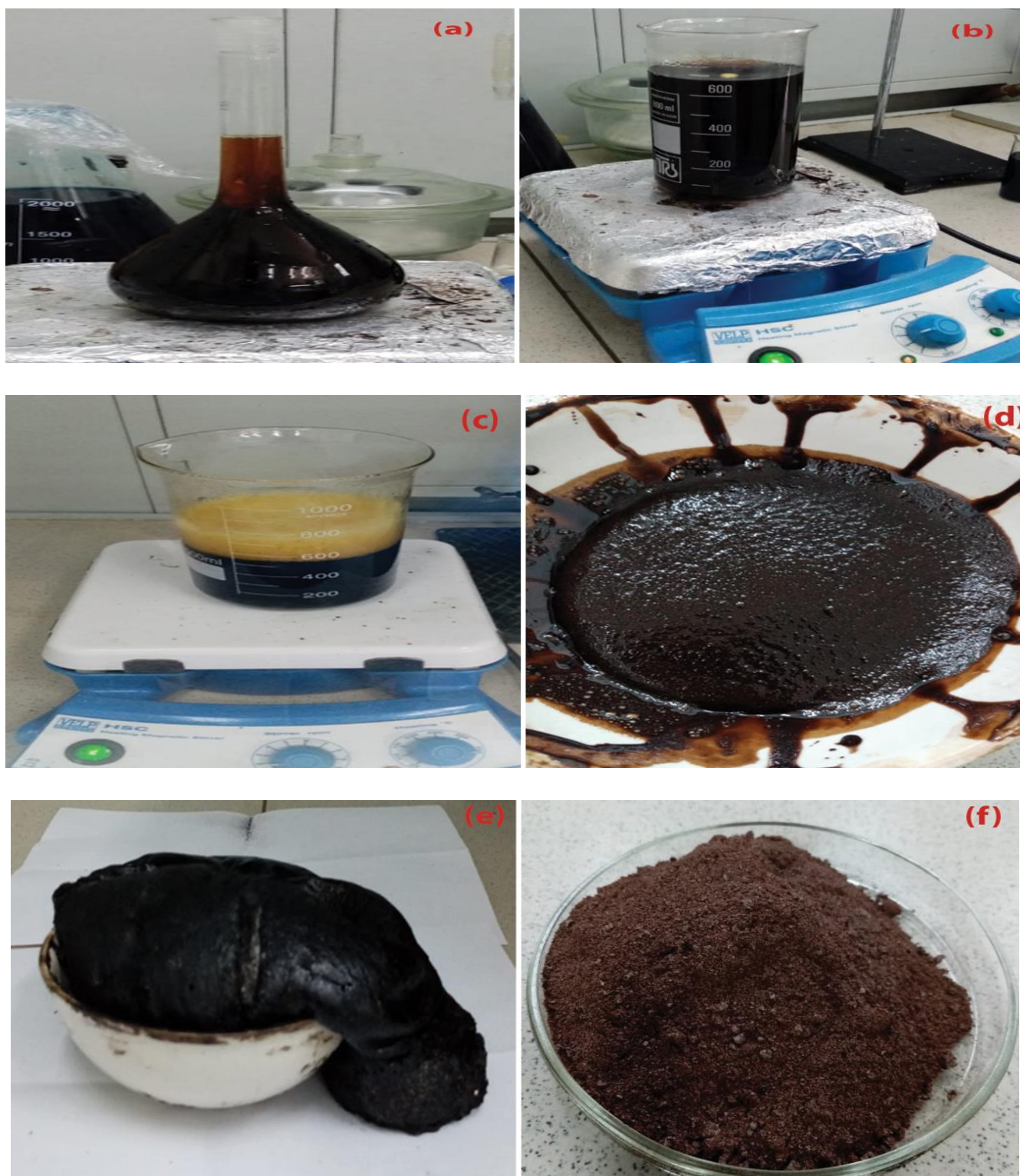


Figure 14 – Synthesis of NiZn ferrite nanoparticles by self-combustion method: (a) the metal salts aqueous solution in the flask, (b) blending the whole mixture, (c) heating the solution at 90 °C, (d) formation of a viscous liquid, (e) formation a fluffy carbonaceous pyrolyzed mass, and (f) obtaining nanoparticles ferrite

2.4.2 Preparation of microwave composites

2.4.2.1 Preparation of CB/F composites

$\text{Ni}_{0.5}\text{Zn}_{0.5}\text{Fe}_2\text{O}_4$ and $\text{Mn}_{0.1}\text{Ni}_{0.5}\text{Zn}_{0.4}\text{Fe}_2\text{O}_4$ nanoparticles were synthesized by citrate precursor and self-combustion method. Composites were synthesized by mixing ferrite nanoparticles with carbon black using a ball mill. Three different weight ratios of CB/ $\text{Ni}_{0.5}\text{Zn}_{0.5}\text{Fe}_2\text{O}_4$ and CB/ $\text{Mn}_{0.1}\text{Ni}_{0.5}\text{Zn}_{0.4}\text{Fe}_2\text{O}_4$ (1:1, 2:1, and 3:1) were prepared. The CB/F composites were ball-milled for 1 h at 300 rpm. Table 8 shows the symbols of composite samples. The practical steps of preparing the CB/F samples are shown in Figure 15.

Table 8 – Symbols of composite samples

Composite	CB: F	Calcination temperature for ferrite (°C)	Sample symbol
$\text{CB}/\text{Ni}_{0.5}\text{Zn}_{0.5}\text{Fe}_2\text{O}_4$	1:1	650	CB/F-11
	2:1		CB/F-21
	3:1		CB/F-31
$\text{CB}/\text{Mn}_{0.1}\text{Ni}_{0.5}\text{Zn}_{0.4}\text{Fe}_2\text{O}_4$	1:1	750	CB/MF-11
	2:1		CB/MF-21
	3:1		CB/MF-31

2.4.2.2 Preparation of CI/F composites

$\text{Ni}_{0.5}\text{Zn}_{0.5}\text{Fe}_2\text{O}_4$ nanoparticles were synthesized by self-combustion method. Composites were synthesized by mixing ferrite nanoparticles with carbon black using a ball mill. Three different weight ratios of CI/ $\text{Ni}_{0.5}\text{Zn}_{0.5}\text{Fe}_2\text{O}_4$ (1:1, 2:1, and 3:1) were prepared. The CI/F composites were ball-milled for 1 h at 300 rpm. Table 9 shows the symbols of composite samples.

Table 9 – Symbols of composite samples

Composite	CI: F	Calcination temperature for ferrite (°C)	Sample symbol
$\text{CI}/\text{Ni}_{0.5}\text{Zn}_{0.5}\text{Fe}_2\text{O}_4$	1:1	650	CI/F-11
	2:1		CI/F-21
	3:1		CI/F-31

2.4.2.3 Preparation of F/CI/CB composites

$\text{Ni}_{0.5}\text{Zn}_{0.5}\text{Fe}_2\text{O}_4$ nanoparticles were synthesized by self-combustion method. Composites were synthesized by mixing ferrite nanoparticles and carbonyl iron with carbon black using a ball mill. Three different weight ratios of F/CI/CB (1:1:1, 1:1:2, and 2:1:1) were prepared. The F/CI/CB composites were ball-milled for 1 h at 300 rpm. Table 10 shows the symbols of composite samples.

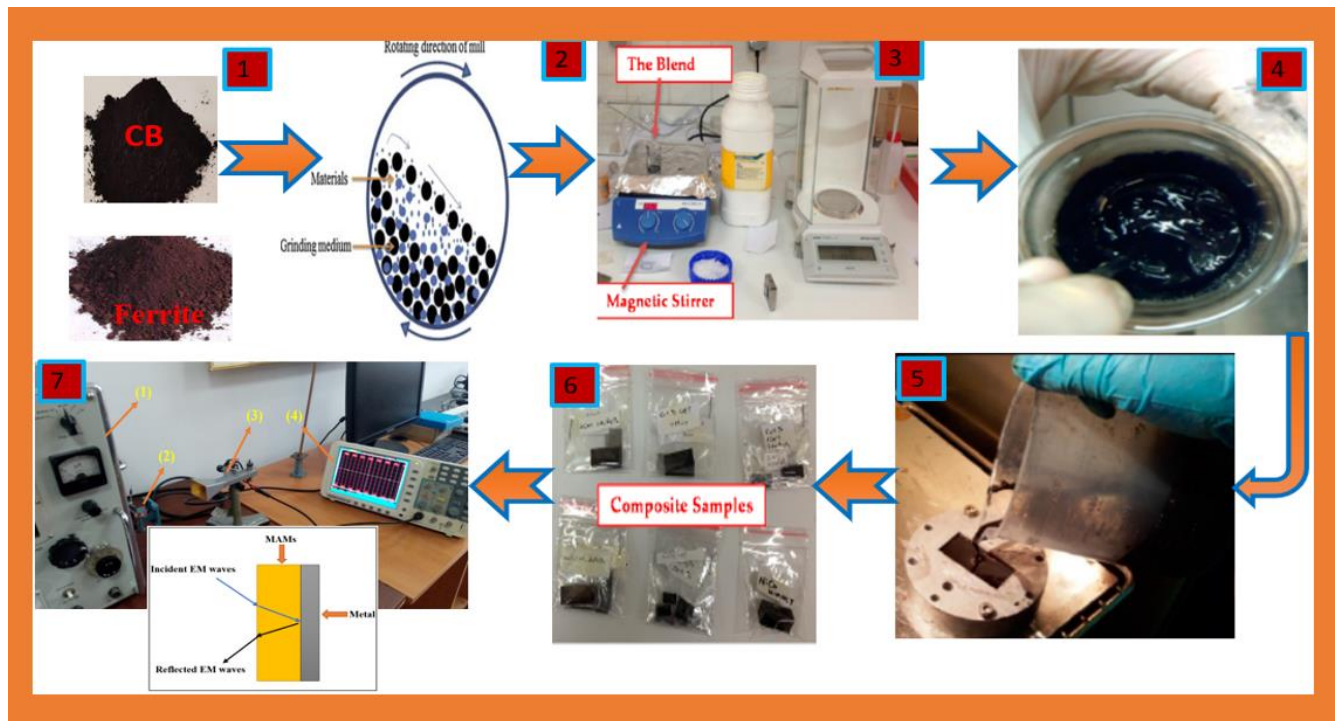


Figure 15 – Experimental steps of preparing the CB/F samples. From left to right: (1) preparing CB and F nanopowders, (2) mixing CB and F through ball mills, (3) blending CB and F with paraffin wax by a magnetic stirrer, (4) preparing mixture, (5) pouring the prepared mixture into the special mold (22.86 mm * 10.16 mm), (6) prepared samples, and (7) measuring the MA properties of the prepared samples

Table 10 – Symbols of composite samples

Sample symbols	Weight ratio		
	$\text{Ni}_{0.5}\text{Zn}_{0.5}\text{Fe}_2\text{O}_4$	CI	CB
F/CI/CB-111	1	1	1
F/CI/CB-112	1	1	2
F/CI/CB-211	2	1	1

2.4.2.4 Preparing double-layer of AC/F

$Mn_{0.1}Ni_{0.5}Zn_{0.4}Fe_2O_4$ nanoparticles were synthesized by self-combustion method. Radar absorption characteristics were studied for double-layer activated carbon/paraffin wax (AC) and $Ni_{0.5}Zn_{0.4}Mn_{0.1}Fe_2O_4$ /paraffin wax (F) composites in the frequency range of 8.8 to 12 GHz. The loading ratio of $Mn_{0.1}Ni_{0.5}Zn_{0.4}Fe_2O_4$ within a paraffin wax matrix (50% w/w). On the other hand, the loading ratio of activated carbon within a paraffin wax matrix (30% w/w). The materials were later combined into paraffin wax to manufacture double-layer composite structures with whole thicknesses of 3 and 4 mm. For a better figure and illustration of the NC structures and their naming, the layering structures are displayed in Figure 16 and Table 11.

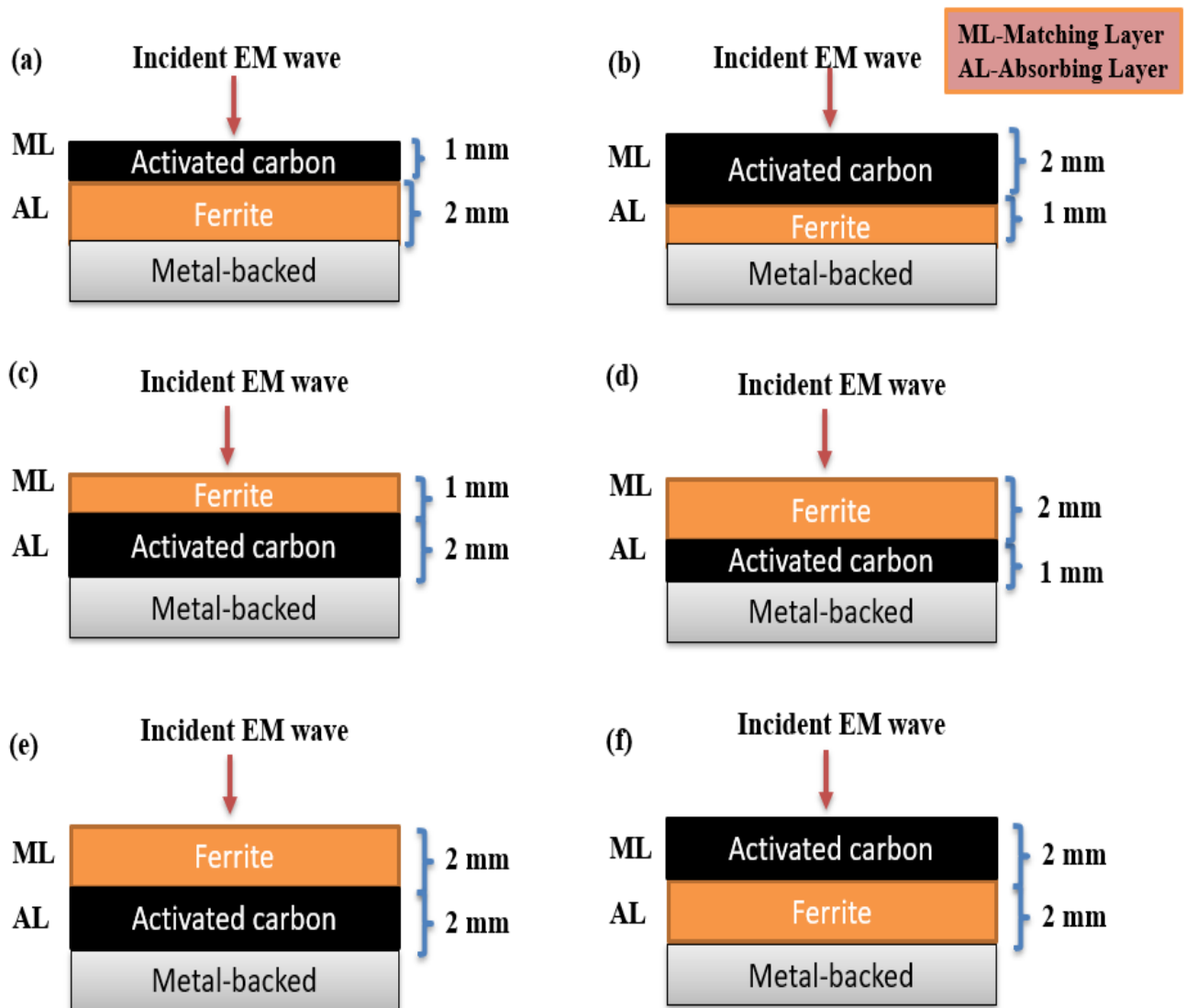


Figure 16 – DL structure of AC/F Cs with (a) 1 mm AC/1 mm F (AC/F-11), (b) 2 mm AC/1 mm F (AC/F-21), (c) 1 mm F/2 mm AC (F/AC-12), (d) 2 mm F/1 mm AC (F/AC-21), (e) 2 mm F/2 mm AC (F/AC-22), and (f) 2 mm AC/2 mm F (AC/F-22) thickness

Table 11 – Specifics on the DL structure of AC/F Cs

Sample symbols	ML	T(mm)	AL	T(mm)
AC/F-11	Activated carbon	1	Ni _{0.5} Zn _{0.4} Mn _{0.1} Fe ₂ O ₄	1
AC/F-21	Activated carbon	2	Ni _{0.5} Zn _{0.4} Mn _{0.1} Fe ₂ O ₄	1
F/AC-12	Ni _{0.5} Zn _{0.4} Mn _{0.1} Fe ₂ O ₄	1	Activated carbon	2
F/AC-21	Ni _{0.5} Zn _{0.4} Mn _{0.1} Fe ₂ O ₄	2	Activated carbon	1
F/AC-22	Ni _{0.5} Zn _{0.4} Mn _{0.1} Fe ₂ O ₄	2	Activated carbon	2
AC/F-22	Activated carbon	2	Ni _{0.5} Zn _{0.4} Mn _{0.1} Fe ₂ O ₄	2

2.4.2.5 Preparation of graphite/ferrite composites

Ni³⁺_{0.25}Ni²⁺_{0.375}Zn²⁺_{0.25}Fe₂O₄ particles were synthesized by a ceramic sintering method. composites were synthesized by mixing ferrite nanoparticles with graphite using a ball mill. Three different weight ratios of graphite/Ni³⁺_{0.25}Ni²⁺_{0.375}Zn²⁺_{0.25}Fe₂O₄ (1:1, 2:1, and 3:1) were prepared. The C/F composites were ball-milled for 1 h at 300 rpm. Table 12 shows the symbols of composite samples.

Table 12 – Symbols of composite samples

Composite	C: F	Heat treatment for ferrite (°C)	Sample symbol
C/ Ni ³⁺ _{0.25} Ni ²⁺ _{0.375} Zn ²⁺ _{0.25} Fe ₂ O ₄	1:1	1100	C/F-11
	2:1		C/F-21
	3:1		C/F-31

2.4.3 Preparation of hybrid composites

2.4.3.1 Coating NiZn spinel ferrite with PANI

The flow chart for the synthesis of PANI utilizing in-situ polymerization technique is shown in Figure 17. Firstly, sodium dodecyl sulfate and aniline were added to the distilled water while keeping mechanical stirring for 1 h. After that, HCl solution was added to the solution under stirring for 1 h. Finally, APS was dissolved in an aqueous solution utilized as an oxidizing agent and added slowly dropwise into the solution to start the polymerization. The polymerization was allowed to proceed for 6 h with stirring in an ice bath. The PANI was filtered and washed many times with distilled water and ethanol and then dried for 8 h in the furnace at 70 °C. NiZn ferrite nanoparticles were coated with polyaniline via the in-situ polymerization technique. The flow chart for the synthesis of PANI/F utilizing in-situ polymerization technique is shown in Figure 18. Three various weight ratios of aniline/Ni³⁺_{0.25}Ni²⁺_{0.375}Zn²⁺_{0.25}Fe₂O₄ (1:1, 2:1, and 3:1) were synthesized. The composite ratios of Ni³⁺_{0.25}Ni²⁺_{0.375}Zn²⁺_{0.25}Fe₂O₄ and aniline in weight

were 1:1 (PANI/F.1), 2:1 (PANI/F.2) and 3:1 (PANI/F.3), respectively. The circular samples were formed using a special 50 mm diameter mold to measure MA and EMI properties.

2.4.3.2 Preparation of PANI/CI and PANI/F/CI

PANI/CI composites were prepared using in-situ polymerization technique of PANI in the CI. The weight ratio of aniline/CI (1/1) was synthesized. On the other hand, Ternary composites of polyaniline/NiZn ferrite/carbonyl iron (PANI/F/CI) were prepared in two stages: Firstly, $\text{Ni}_{0.5}\text{Zn}_{0.5}\text{Fe}_2\text{O}_4$ were prepared using citrate precursor method. After that, PANI/90%F/10%CI composites were prepared using in-situ polymerization technique of PANI in the $\text{Ni}_{0.5}\text{Zn}_{0.5}\text{Fe}_2\text{O}_4$ and CI. The flow chart for the synthesis of PANI/F/CI utilizing in-situ polymerization technique is shown in Figure 18. The weight ratio of aniline/(F-CI) (1/1) was synthesized.

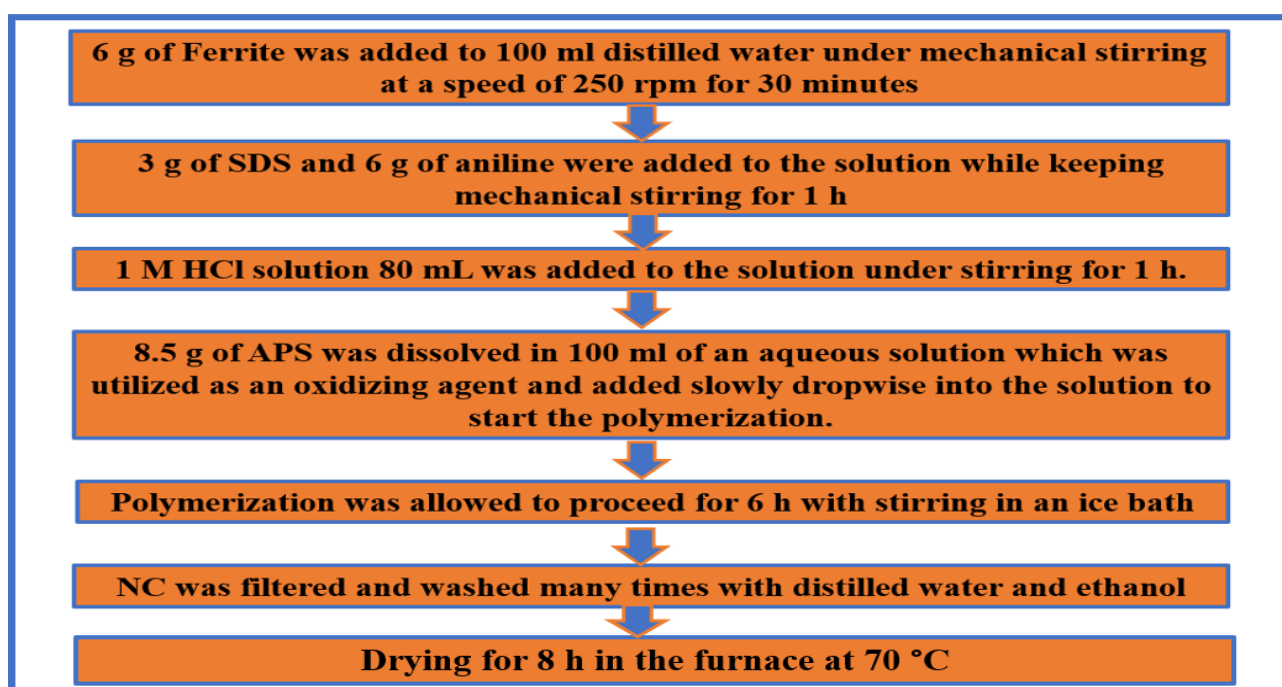


Figure 17 – Flow chart for the synthesis of PANI/F utilizing in-situ polymerization technique

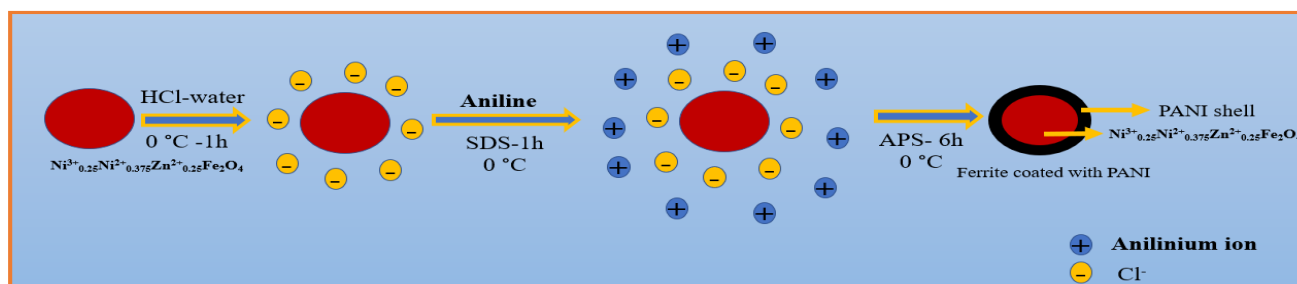


Figure 18 – Schematic diagram of a polyaniline/NiZn ferrite by the in-situ polymerization technique

2.4.3.3 Preparation of PANI/CB and PANI/F/CB

PANI/CB composites were prepared using in-situ polymerization technique of PANI in the existence of the CB. The weight ratio of aniline/CB (1/1) was synthesized. On the other hand, Ternary composites of polyaniline/NiZn ferrite/carbon black (PANI/F/CB) were prepared via two stages: Firstly, $\text{Ni}^{3+}_{0.25}\text{Ni}^{2+}_{0.375}\text{Zn}^{2+}_{0.25}\text{Fe}_2\text{O}_4$ was prepared using a ceramic sintering method. After that, PANI/F/CB composites are prepared using in-situ polymerization technique of PANI in the existence of the $\text{Ni}^{3+}_{0.25}\text{Ni}^{2+}_{0.375}\text{Zn}^{2+}_{0.25}\text{Fe}_2\text{O}_4$ and CB. The weight ratio of aniline/ (90%,70% and 50%F-10%,30% and 50%CB) (1/1) was synthesized. The flow chart for the synthesis of PANI/F/CB utilizing in-situ polymerization technique is shown in Figure 20.

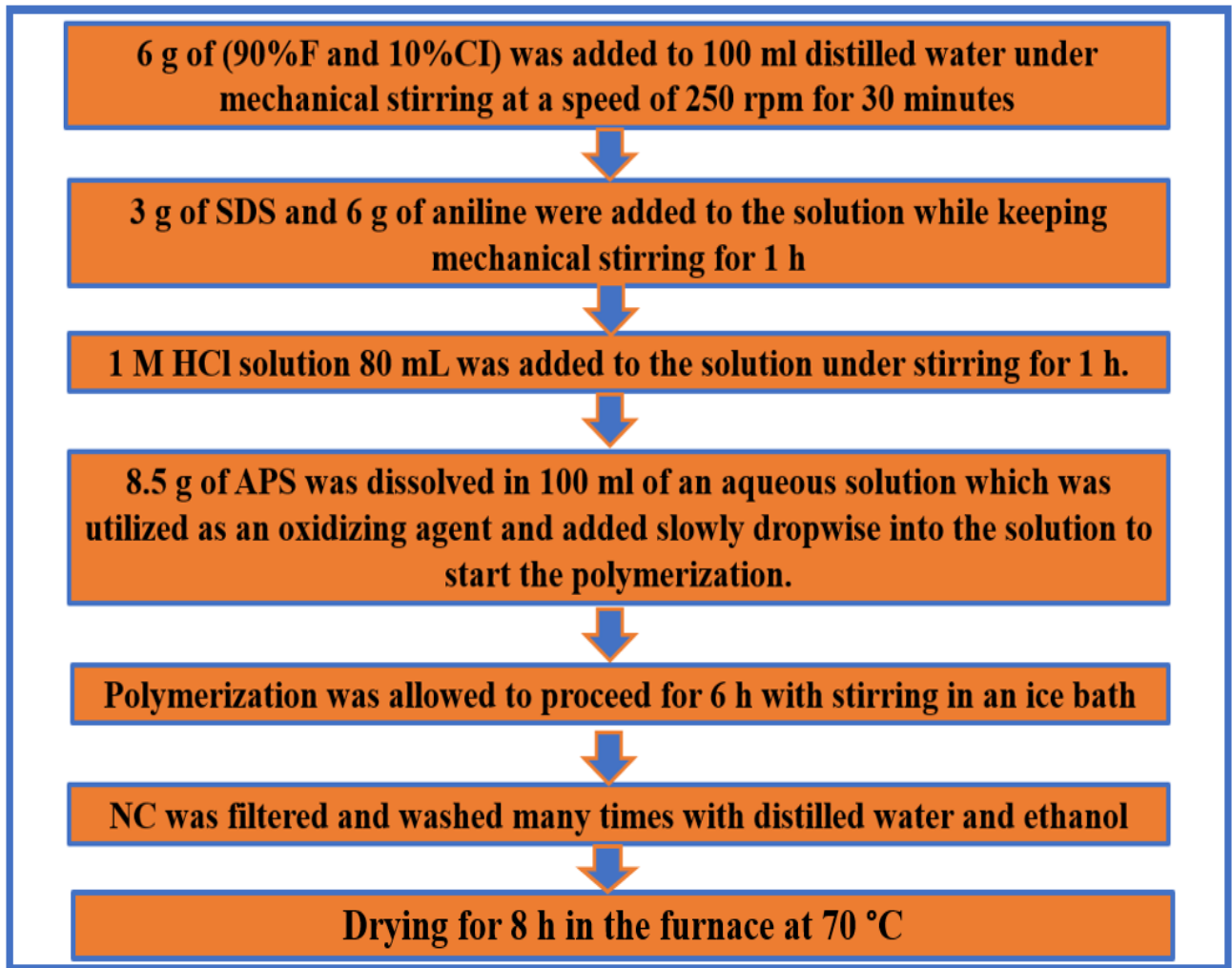


Figure 19 – Flow chart for the synthesis of PANI/F/CI utilizing in-situ polymerization technique

2.4.3.4 Coating $\text{BaNiZnFe}_{16}\text{O}_{27}$ hexagonal ferrite with PANI

$\text{BaNiZnFe}_{16}\text{O}_{27}$ particles were coated with polyaniline via the in-situ polymerization technique. The flow chart for the synthesis of PANI/HF utilizing in-situ polymerization

technique is shown in Figure 17. Three weight ratios of aniline/BaNiZnFe₁₆O₂₇ (1:1, 1:2, and 1:3) were synthesized. The composite ratios of BaNiZnFe₁₆O₂₇ and aniline in weight were 1:1 (PANI/HF.1), 1:2 (PANI/HF.2) and 1:3 (PANI/HF.3), respectively.

2.4.3.5 Preparation of PANI/SF/HF and PANI/SF/HF/CB

Ternary composites of polyaniline/Ni³⁺_{0.25}Ni²⁺_{0.375}Zn²⁺_{0.25}Fe₂O₄/BaNiZnFe₁₆O₂₇ (PANI/SF/HF) were prepared via two stages: Firstly, Ni³⁺_{0.25}Ni²⁺_{0.375}Zn²⁺_{0.25}Fe₂O₄ and BaNiZnFe₁₆O₂₇ were prepared using the ceramic sintering method. After that, PANI/50%SF/50%HF composites were prepared using in-situ polymerization technique of PANI in the existence of the Ni_{0.5}Zn_{0.5}Fe₂O₄ and BaNiZnFe₁₆O₂₇. The weight ratio of aniline/(SF-HF) (1/1) was synthesized. On the other hand, microwave absorber composite based on a combination of soft ferrite and hard ferrite incorporated with CB, namely (45%SF/45%HF/10%CB) coating with PANI have been prepared. The soft and hard ferrites are prepared using the ceramic sintering method, while the shell of PANI is deposited by the oxidative polymerization method on the ferrite.

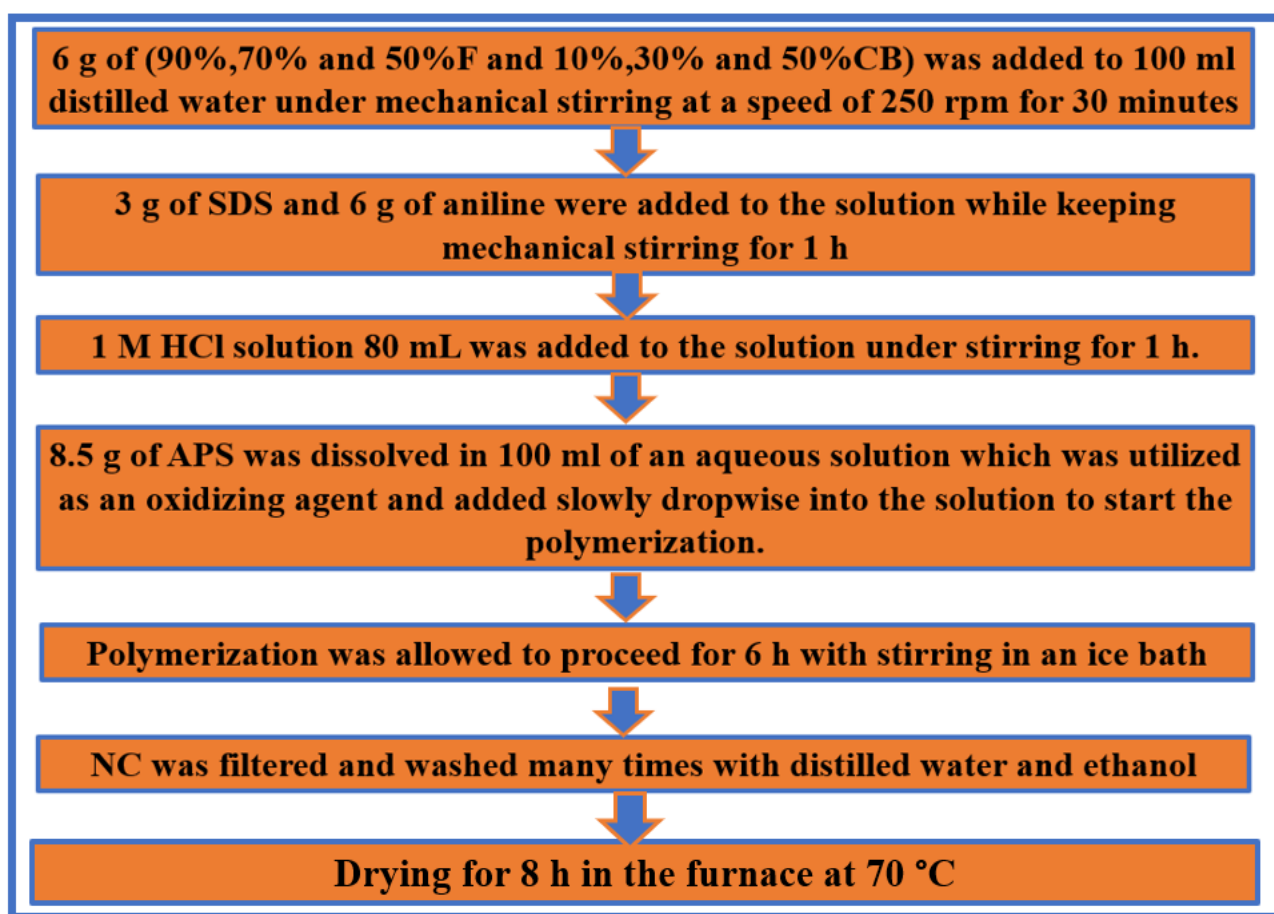


Figure 20 – Flow chart for the synthesis of PANI/F/CB utilizing in-situ polymerization technique

2.5 Statistical processing of experimental data

Four samples of each absorber were designed at different prepared thicknesses to measure the microwave absorption properties. The microwave absorbing performance of each sample was measured one time (It's due to the fact that the microwave detector circuit gives always the same result) by the free-space technique. The statistical processing of the experimental data was determined by calculating the mean value of samples (\bar{x}) and the standard deviation (S) as shown in the following equations:

$$\bar{x} = \frac{\sum_{i=1}^n x_i}{n} \quad (18)$$

$$S = \sqrt{\frac{\sum_{i=1}^n (x_i - \bar{x})^2}{n-1}} \quad (19)$$

Where x_i and n are the value of each sample, and the number of samples, respectively.

3 RESULTS AND DISCUSSION

3.1 Results and discussion of the preparation of ferrite powders by the ceramic sintering technique

3.1.1 XRD patterns

The X-ray diffraction patterns of the prepared samples were recorded at $2\theta = 10 - 90^\circ$. The crystallite size was evaluated using Scherrer's equation, $D = 0.9 \lambda / \beta \cos\theta$, where D is the crystallite size (nm), λ is the X-ray wavelength, β is the bandwidth at half-height, and θ is the diffraction angle in degree. The main peaks were fitted by the Gaussian function using Origin software to obtain 2θ and FWHM and estimated their error. As well, the error in crystallite size was determined as shown in equation (20).

$$\Delta D/D = \sqrt{\left(\frac{\Delta FWHM}{FWHM}\right)^2 + (\Delta\theta \tan\theta)^2} \quad (\Delta\theta \text{ in radian}) \quad (20)$$

3.1.1.1 X-ray diffraction of undoped ferrites

Figure 21 shows the XRD patterns of the NiFe_2O_4 , ZnFe_2O_4 , MnFe_2O_4 and CuFe_2O_4 . For undoped ferrites pattern, six diffraction peaks were detected, which conform to (hkl) planes of (220), (311), (400), (422), (511) and (440), respectively. The XRD figures of ferrites showed the formation of a single-phase cubic spinel structure with no impurity peaks. The XRD patterns of undoped ferrites were totally matched with the reference XRD patterns (JCPDS, PDF no. 01-086-2267, JCPDS, PDF. no. 00-022-012, and JCPDS, PDF. no. 00-010-0319).

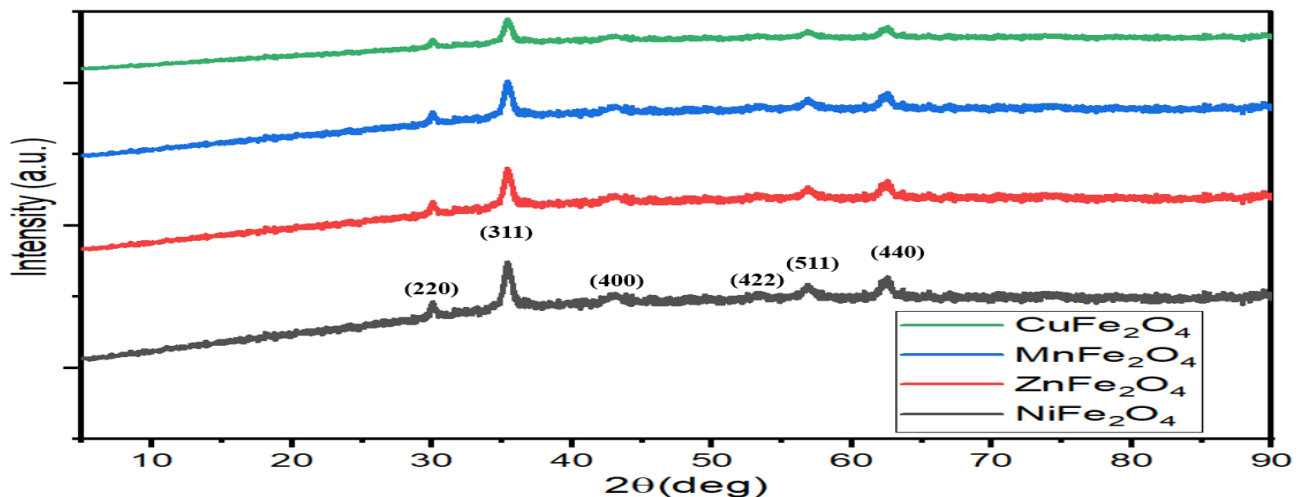


Figure 21 – XRD patterns of the NiFe_2O_4 , ZnFe_2O_4 , MnFe_2O_4 and CuFe_2O_4

3.1.1.2 X-ray diffraction of doped ferrites samples prepared by the ceramic sintering technique

Figures (22–23) show the XRD patterns of the ferrites. For $Mn_xZn_{(1-x)}Fe_2O_4$ and $Ni_xZn_{(1-x)}Fe_2O_4$ pattern, six diffraction peaks were detected, which conform to (hkl) planes of (220), (311), (400), (422), (511) and (440), respectively. On the other hand, for $Mn_{0.1}Ni_{(0.4+x)}Zn_{(0.5-x)}Fe_2O_4$, $Ni^{3+}_{0.25}Ni^{2+}_{0.375}Zn^{2+}_{0.25}Fe_2O_4$ and $Cu^{2+}_{0.1}Ni^{3+}_{0.15}Ni^{2+}_{0.225}Zn^{2+}_{0.45}Fe_2O_4$ patterns, nine diffraction peaks were noticed, which conform to (hkl) planes of (111), (220), (311), (222), (400), (422), (511), (440) and (533), respectively. The XRD figures of spinel ferrites indicated the formation of a single-phase cubic spinel structure with no impurity peaks. All the observed peaks of the spinel ferrites were matched with the standard XRD pattern (JCPDS, PDF no. 00-008-0234). For the $BaNiZnFe_{16}O_{27}$ pattern, eleven diffraction peaks were noticed, which conform to (hkil) planes of (110), (1010), (116), (0114), (107), (203), (208), (209), (2015), (2111) and (220), respectively. The hexagonal ferrites' observed peaks were matched with the standard XRD pattern (JCPDS, PDF no. 51-1877). The size of the ferrite grains (hkl (311)) has been evaluated with Scherrer's equation. Table 13 displays the calculated crystallite size of $Ni_{0.5}Zn_{0.5}Fe_2O_4$.

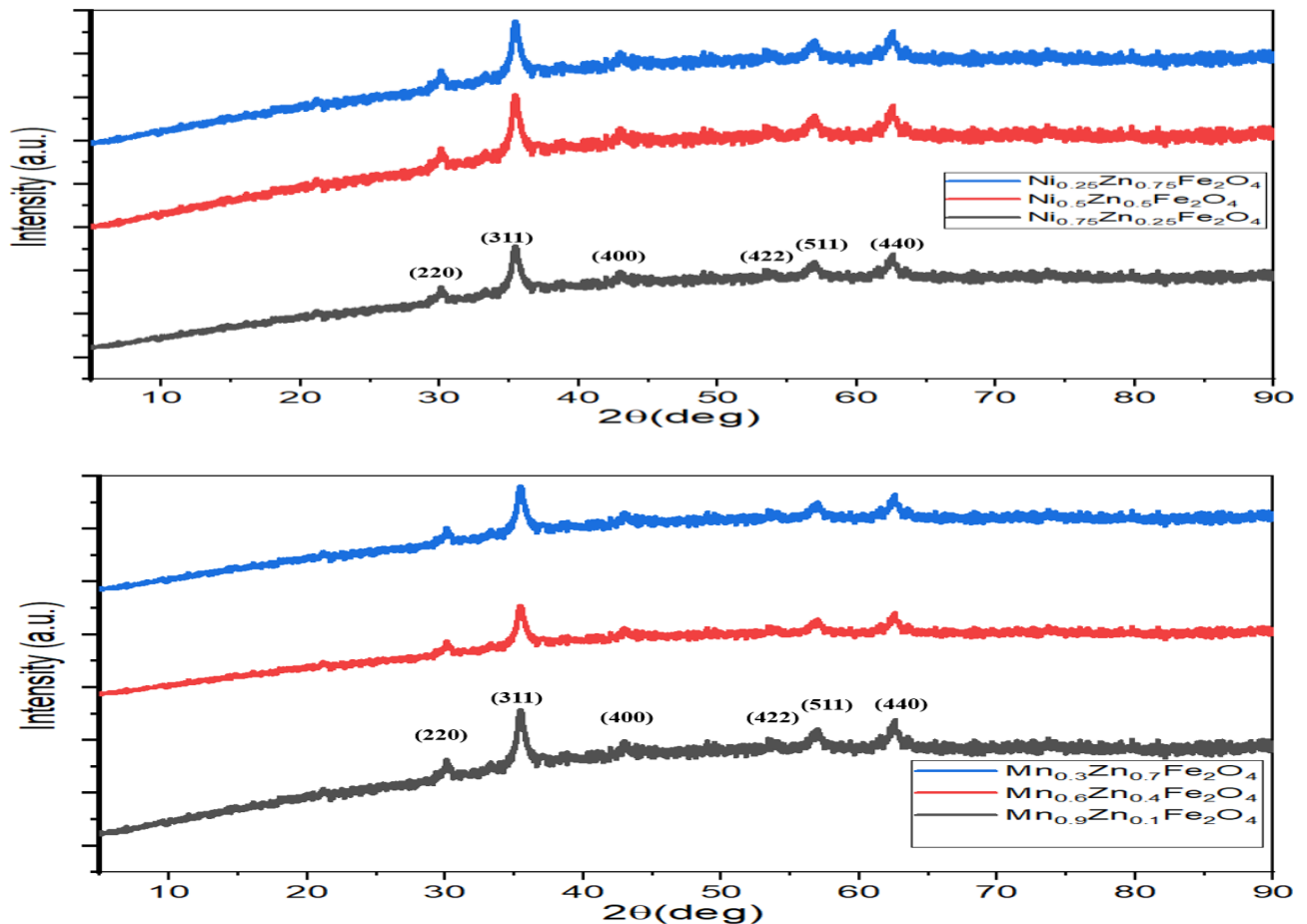


Figure 22 – XRD patterns of the $Mn_xZn_{(1-x)}Fe_2O_4$ ($x=0.3, 0.6, 0.9$) and $Ni_xZn_{(1-x)}Fe_2O_4$ ($x=0.25, 0.5, 0.75$)

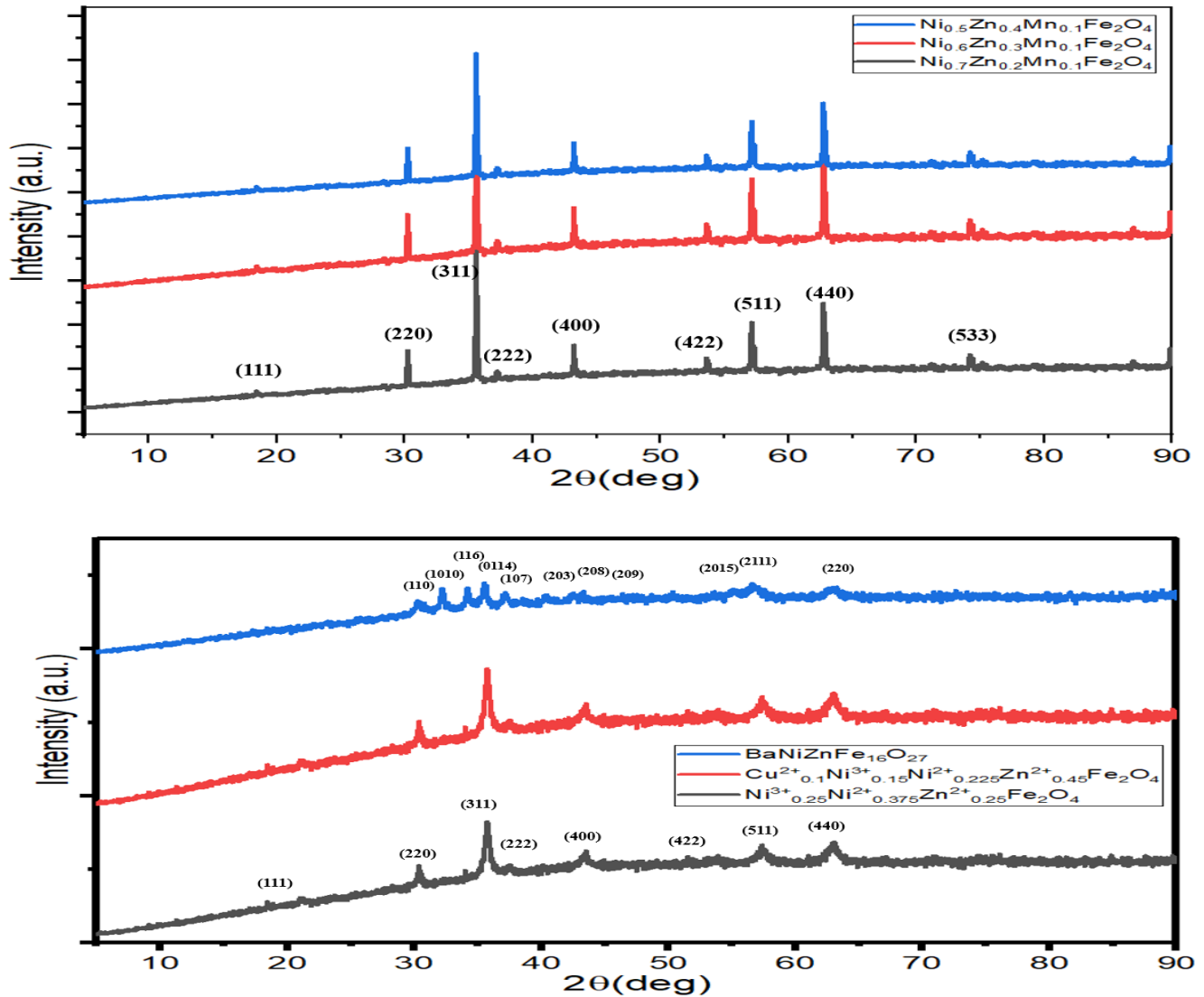


Figure 23 – XRD patterns of the $\text{Ni}^{3+}_{0.25}\text{Ni}^{2+}_{0.375}\text{Zn}^{2+}_{0.25}\text{Fe}_2\text{O}_4$, $\text{Cu}^{2+}_{0.1}\text{Ni}^{3+}_{0.15}\text{Ni}^{2+}_{0.225}\text{Zn}^{2+}_{0.45}\text{Fe}_2\text{O}_4$ and $\text{BaNiZnFe}_{16}\text{O}_{27}$

3.1.2 FTIR spectra of ferrite samples

Figures (24–25) display the FTIR spectra of the undoped and doped ferrites. The peaks within the range ($550\text{--}590\text{ cm}^{-1}$) were due to the stretching vibration of (Fe-O) at the tetrahedral sites, while the peaks located in the sites less than 460 cm^{-1} were due to the stretching vibration of (Fe-O) at the octahedral sites [86].

3.1.3 Morphology investigations for spinel and hexagonal ferrites

Figure 24 represents the SEM micrographs of the $\text{Ni}^{3+}_{0.25}\text{Ni}^{2+}_{0.375}\text{Zn}^{2+}_{0.25}\text{Fe}_2\text{O}_4$ and $\text{BaNiZnFe}_{16}\text{O}_{27}$. The grain size of the samples was analyzed by ImageJ software, as follows: a line corresponding to the scale line was drawn, then the image scale was entered into the software. The unit was selected. The matching line was drawn for grain size data. The

$\text{Ni}^{3+}_{0.25}\text{Ni}^{2+}_{0.375}\text{Zn}^{2+}_{0.25}\text{Fe}_2\text{O}_4$ and $\text{BaNiZnFe}_{16}\text{O}_{27}$ powders are almost spherical with average diameters ranging from 152–450 nm and 100–420 nm, respectively. The agglomerated powders are observed too, it's due to magneto-dipole interactions between powders. In order to gain further insight into the composition of the samples, EDX elemental mapping has been performed as demonstrated in the next section.

Table 13 – Crystallite size of doped ferrites

Sample	K	λ (Å)	2θ (°)	FWHM (°)	Crystallite size (nm)
$\text{Ni}_{0.25}\text{Zn}_{0.75}\text{Fe}_2\text{O}_4$	0.94	1.54	35.60 ± 0.01	0.16 ± 0.01	54.44 ± 3.40
$\text{Ni}_{0.5}\text{Zn}_{0.5}\text{Fe}_2\text{O}_4$	0.94	1.54	35.62 ± 0.01	0.17 ± 0.01	51.24 ± 3.01
$\text{Ni}_{0.75}\text{Zn}_{0.25}\text{Fe}_2\text{O}_4$	0.94	1.54	35.51 ± 0.01	0.18 ± 0.01	48.38 ± 2.69
$\text{Mn}_{0.3}\text{Zn}_{0.7}\text{Fe}_2\text{O}_4$	0.94	1.54	35.62 ± 0.01	0.76 ± 0.02	11.46 ± 0.32
$\text{Mn}_{0.6}\text{Zn}_{0.4}\text{Fe}_2\text{O}_4$	0.94	1.54	35.42 ± 0.01	0.75 ± 0.01	11.60 ± 0.15
$\text{Mn}_{0.9}\text{Zn}_{0.1}\text{Fe}_2\text{O}_4$	0.94	1.54	35.61 ± 0.01	0.76 ± 0.01	11.46 ± 0.23
$\text{Ni}_{0.5}\text{Zn}_{0.4}\text{Mn}_{0.1}\text{Fe}_2\text{O}_4$	0.94	1.54	35.65 ± 0.01	0.15 ± 0.01	58.08 ± 3.87
$\text{Ni}_{0.6}\text{Zn}_{0.3}\text{Mn}_{0.1}\text{Fe}_2\text{O}_4$	0.94	1.54	35.60 ± 0.01	0.16 ± 0.01	54.44 ± 3.40
$\text{Ni}_{0.7}\text{Zn}_{0.2}\text{Mn}_{0.1}\text{Fe}_2\text{O}_4$	0.94	1.54	35.55 ± 0.01	0.16 ± 0.01	54.43 ± 3.41
$\text{Ni}^{3+}_{0.25}\text{Ni}^{2+}_{0.375}\text{Zn}^{2+}_{0.25}\text{Fe}_2\text{O}_4$	0.94	1.54	35.60 ± 0.01	0.52 ± 0.01	16.75 ± 0.32
$\text{Cu}^{2+}_{0.1}\text{Ni}^{3+}_{0.15}\text{Ni}^{2+}_{0.225}\text{Zn}^{2+}_{0.45}\text{Fe}_2\text{O}_4$	0.94	1.54	35.73 ± 0.01	0.53 ± 0.02	16.44 ± 0.62

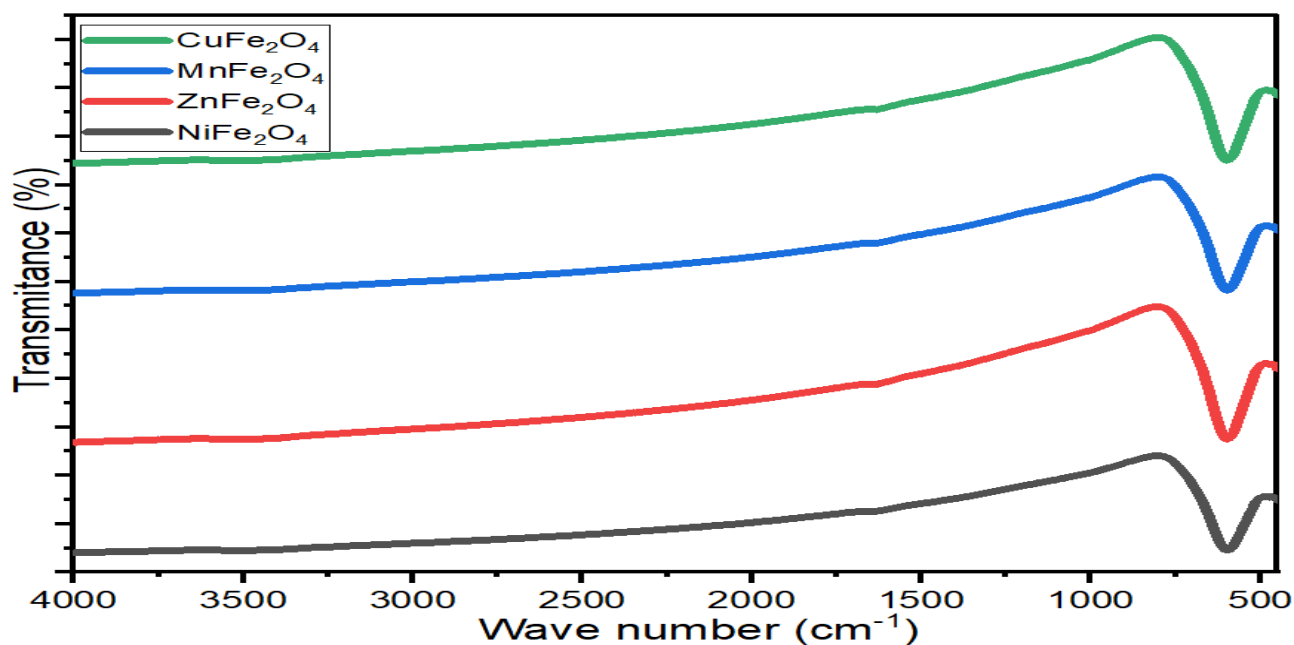


Figure 24 – FTIR spectra of undoped

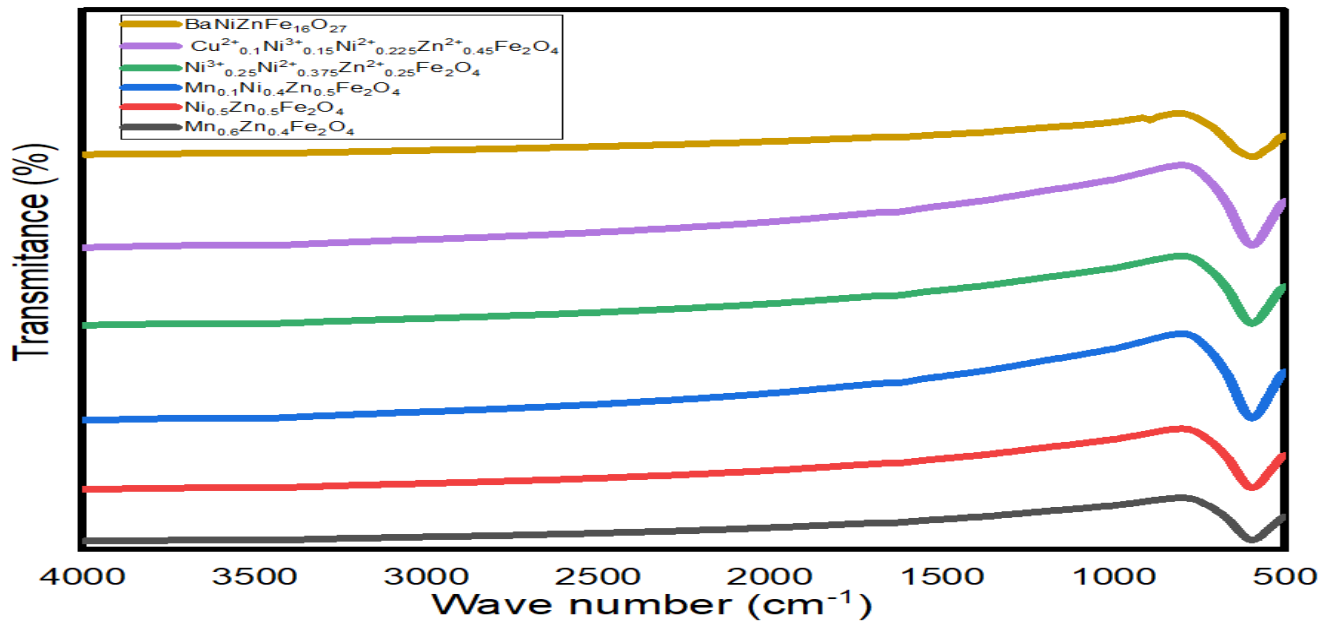


Figure 25 – FTIR spectra of doped ferrites

3.1.4 EDX analysis for spinel and hexagonal ferrites

EDX analysis of $\text{Ni}^{3+}_{0.25}\text{Ni}^{2+}_{0.375}\text{Zn}^{2+}_{0.25}\text{Fe}_2\text{O}_4$ and $\text{BaNiZnFe}_{16}\text{O}_{27}$ particles prepared by ceramic method is shown in Figure 27 and Table 14. The presence of C, O, Cl, S, Fe, Ni, Al and Zn elements in the spinel ferrite EDX spectrums was noticed. On the other hand, the presence of C, O, Ba, Cl, Fe, Ni, and Zn elements in the hexagonal ferrite EDX spectrum was found.

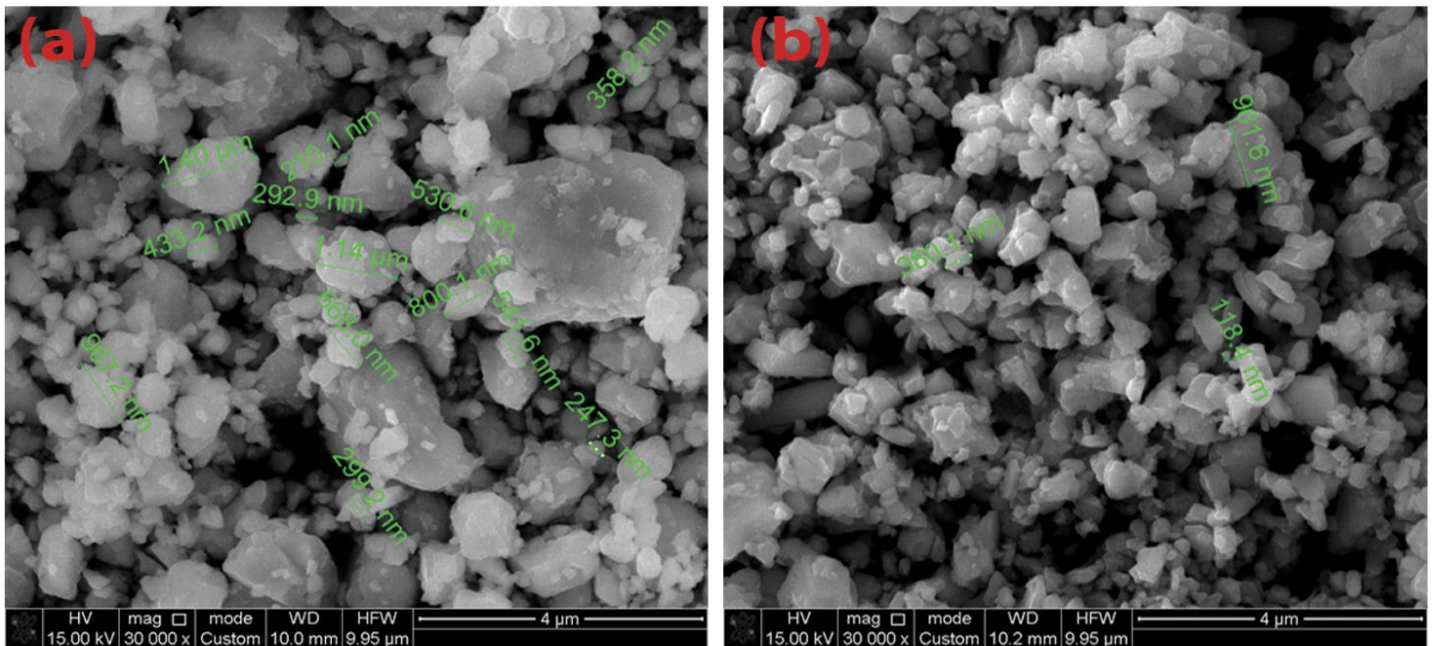


Figure 26 – SEM images of (a) $\text{Ni}^{3+}_{0.25}\text{Ni}^{2+}_{0.375}\text{Zn}^{2+}_{0.25}\text{Fe}_2\text{O}_4$, and (b) $\text{BaNiZnFe}_{16}\text{O}_{27}$

Table 14 – EDX element composition of spinel ferrites and hexagonal ferrite

Element	C	Cl	O	S	Ba	Al	Fe	Ni	Zn
$\text{Ni}^{3+}_{0.25}\text{Ni}^{2+}_{0.375}\text{Zn}^{2+}_{0.25}\text{Fe}_2\text{O}_4$ (wt%)	3.28	0.15	19.28	0.03	-	0.39	53.04	18.02	5.81
$\text{BaNiZnFe}_{16}\text{O}_{27}$ (wt%)	1.8	0.16	20.72	-	9.88	-	59.34	4.24	3.86

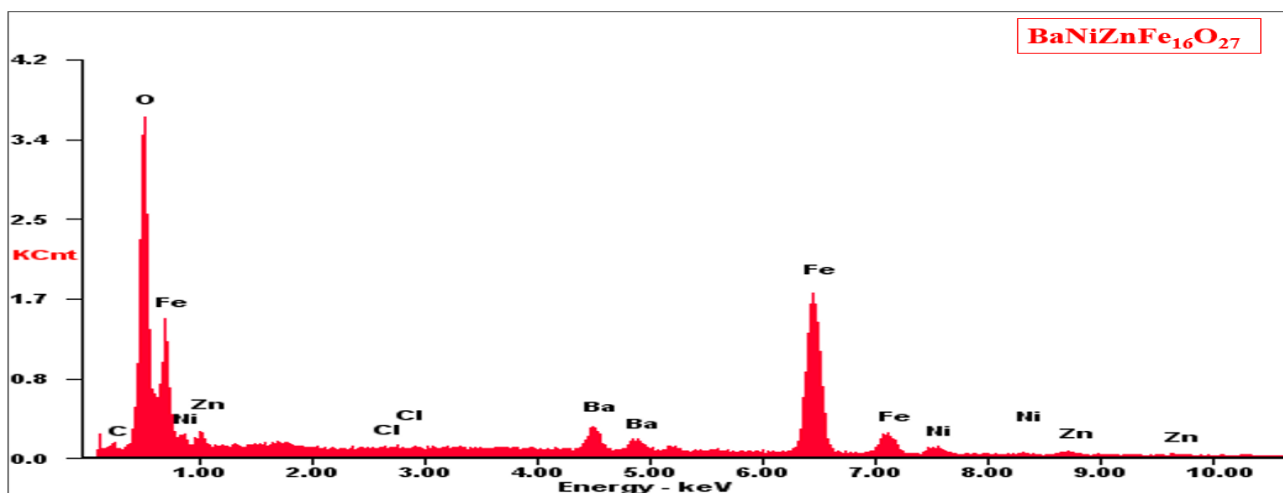
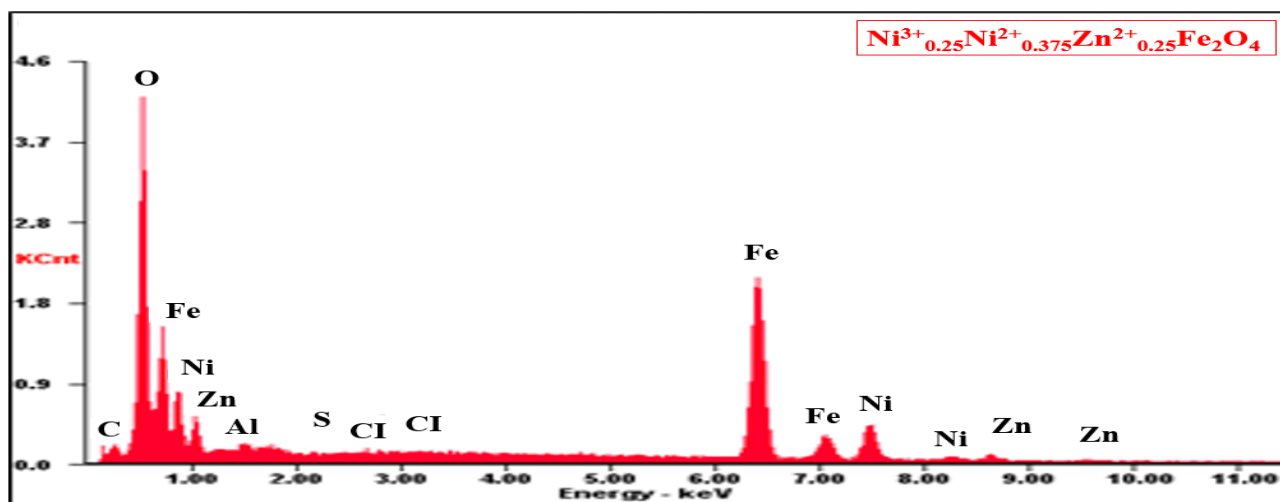


Figure 27 – EDX of spinel ferrites and hexagonal ferrite

3.1.5 Microwave absorption properties of ferrite samples prepared by the ceramic sintering technique

Several variables that affect MA properties were studied, as follows: effect of ferrite type, substitution with several metal ions, the concentration of metal ions, absorbent layer thickness, and loading percentage of ferrite in the paraffin matrix.

3.1.5.1 Microwave absorption properties of undoped ferrites

EMI shielding and MA properties of NiFe_2O_4 , ZnFe_2O_4 , MnFe_2O_4 and CuFe_2O_4 were studied. The results of this investigation are exhibited in Figure 28. The thickness of the prepared samples was 6 mm. The results showed that the absorbers with a loading percentage within a paraffin matrix of 75% w/w had weak reflection loss and low shielding efficiency. Hence, substitutions with suitable metal ions are needed to improve microwave absorption properties.

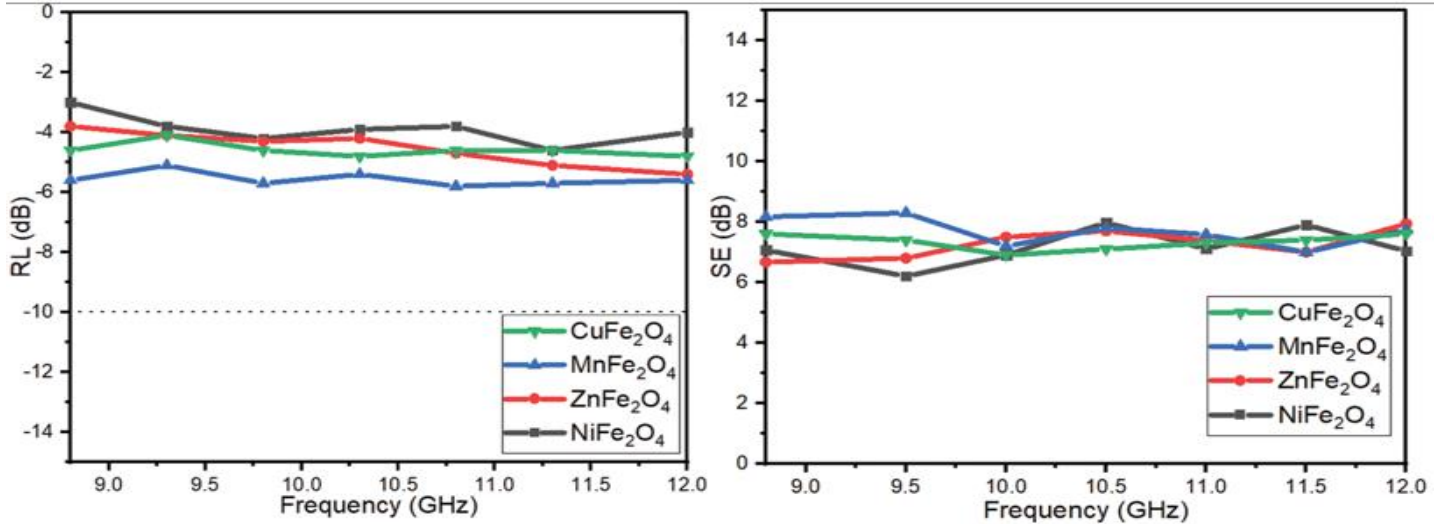


Figure 28 – RL and SE curves of NiFe_2O_4 , ZnFe_2O_4 , MnFe_2O_4 and CuFe_2O_4 at 6 mm thickness

3.1.5.2 Microwave absorption properties of doped ferrites

EMI shielding and MA properties of $\text{Mn}_x\text{Zn}_{(1-x)}\text{Fe}_2\text{O}_4$ ($x = 0.3, 0.6$ and 0.9), $\text{Ni}_x\text{Zn}_{(1-x)}\text{Fe}_2\text{O}_4$ ($x = 0.25, 0.5$ and 0.75), $\text{Ni}_{(0.4+x)}\text{Zn}_{(0.5-x)}\text{Mn}_{0.1}\text{Fe}_2\text{O}_4$ ($x = 0.1, 0.2$ and 0.3), $\text{Ni}^{3+}_{0.25}\text{Ni}^{2+}_{0.375}\text{Zn}^{2+}_{0.25}\text{Fe}_2\text{O}_4$, $\text{Cu}^{2+}_{0.1}\text{Ni}^{3+}_{0.15}\text{Ni}^{2+}_{0.225}\text{Zn}^{2+}_{0.45}\text{Fe}_2\text{O}_4$ and $\text{BaNiZnFe}_{16}\text{O}_{27}$ were investigated at a constant loading percentage of 65% w/w within a paraffin matrix with different thicknesses (3, 5 and 7 mm). The absorbers were molded to measure RL and SE at the range of 8.8–12 GHz. For $\text{Mn}_x\text{Zn}_{(1-x)}\text{Fe}_2\text{O}_4$ ($x = 0.3, 0.6$ and 0.9), the effect of Mn^{2+} ion substitution and substitution concentrations on the EMI shielding and MA properties was studied. Figures (29–30) and Table 15 show the MA properties of the prepared samples. The results displayed weak RL and low SE for $\text{Mn}_{0.3}\text{Zn}_{0.7}\text{Fe}_2\text{O}_4$ and $\text{Mn}_{0.6}\text{Zn}_{0.4}\text{Fe}_2\text{O}_4$. Also, the results indicated that a RL_{\min} was -11.7 dB at 9.2 GHz for a thickness of 5 mm, absorbing $\text{BW}_{-10\text{ dB}}$ is 0.7 GHz and the SE_{\max} was 13.3 dB at 9.6 GHz for $\text{Mn}_{0.9}\text{Zn}_{0.1}\text{Fe}_2\text{O}_4$ as shown in Figure 29 Figure 30 illustrates that the RL attenuation peaks of samples moved to lower frequencies with increasing sample thickness. This phenomenon may be defined by the quarter-wavelength ($\lambda/4$) cancellation model, as shown in equation (5) [44–46]. On the other hand, for $\text{Ni}_x\text{Zn}_{(1-x)}\text{Fe}_2\text{O}_4$ ($x = 0.25, 0.5$ and 0.75), the effect of Ni^{2+} ion substitution and substitution concentrations on the EMI shielding and MA properties

was investigated. Table 15 shows the MA properties of the absorbers. The results displayed weak RL and low SE for $\text{Ni}_{0.25}\text{Zn}_{0.75}\text{Fe}_2\text{O}_4$. As well, the results displayed that $\text{Ni}_{0.5}\text{Zn}_{0.5}\text{Fe}_2\text{O}_4$ and $\text{Ni}_{0.75}\text{Zn}_{0.25}\text{Fe}_2\text{O}_4$ exceeded the -10 dB threshold, as shown in Figure 31, which demonstrates that the RL attenuation peaks of samples moved to lower frequencies with increasing sample thickness. The results also indicate that the RL_{\min} shifted to higher frequencies by increasing the substitution with several metal ions on ferrite. The SE_{\max} was 13.7 dB at 10.4 GHz for $\text{Ni}_{0.5}\text{Zn}_{0.5}\text{Fe}_2\text{O}_4$.

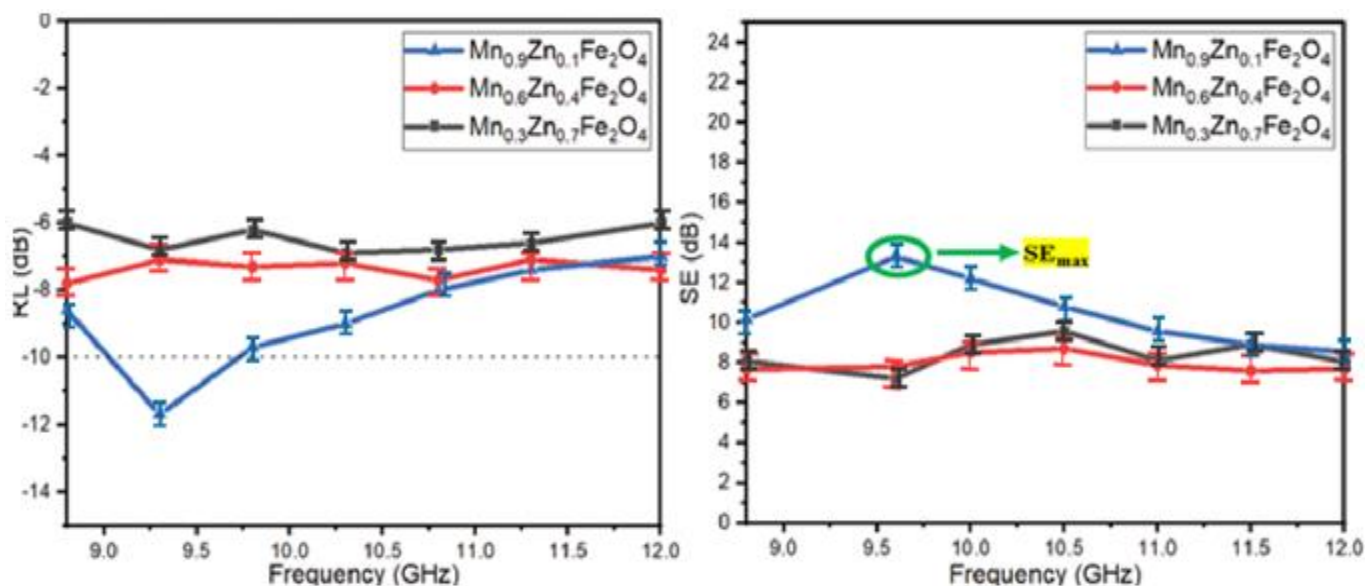


Figure 29 – RL and SE curves of $\text{Mn}_x\text{Zn}_{(1-x)}\text{Fe}_2\text{O}_4$ ($x=0.3, 0.6$ and 0.9) at 5 mm thickness

Table 16 illustrates a comparison of MA characteristics of some lately informed ferrite absorbers with different preparation methods and loading percentages. The results of the literature show these ferrites are good in the C-band and Ku-band frequencies and weak in the X-band frequency. The presently prepared ferrites display in this research better MA in the X-band frequency. The distinct of these prepared ferrites have a lower loading percentage and thickness of the absorbers compared with the other literature.

On the other hand, Ni-doped manganese zinc ferrite ($\text{Ni}_{(0.4+x)}\text{Zn}_{(0.5-x)}\text{Mn}_{0.1}\text{Fe}_2\text{O}_4$ ($x=0.1, 0.2$ and 0.3)) was studied. Table 17 demonstrate the MA properties of the prepared samples. The results indicated that the $\text{Ni}_{(0.4+x)}\text{Zn}_{(0.5-x)}\text{Mn}_{0.1}\text{Fe}_2\text{O}_4$ ($x=0.1, 0.2$ and 0.3) exceeded the -10 dB threshold, as shown in Figure 32, which illustrates that the RL attenuation peaks of samples moved to lower frequencies by increasing sample thickness. This phenomenon may be defined by the quarter-wavelength ($\lambda/4$) cancellation model, as shown in equation (1.12). The results also demonstrated that the RL_{\min} shifted to higher frequencies by increasing the substitution with several metal ions on ferrite.

Table 15 – MA behavior of doped ferrites at different thicknesses

Samples	t (mm)	RL _{min} (dB)	f _m (GHz)	BW _{-10 dB} (GHz)
Mn _{0.3} Zn _{0.7} Fe ₂ O ₄	3	-7.5±0.9	9.2±0.1	0
	5	-6.9±0.8	10.3±0.2	0
	7	-7.7±0.6	9.8±0.1	0
Mn _{0.6} Zn _{0.4} Fe ₂ O ₄	3	-7.2±0.7	10.2±0.3	0
	5	-7.8±0.9	8.2±0.1	0
	7	-7.5±0.6	9.3±0.2	0
Mn _{0.9} Zn _{0.1} Fe ₂ O ₄	3	-12.4±0.8	10.3±0.1	0.9±0.1
	5	-11.7±0.9	9.2±0.1	0.7±0.2
	7	-8.6±0.7	8.8±0.2	0
Ni _{0.25} Zn _{0.75} Fe ₂ O ₄	3	-7.5±0.8	11.0±0.3	0
	5	-7.4±0.7	12.0±0.1	0
	7	-8.2±0.6	11.4±0.3	0
Ni _{0.5} Zn _{0.5} Fe ₂ O ₄	3	-11.5±0.8	10.1±0.1	0.5±0.2
	5	-12.2±0.8	9.6±0.2	0.8±0.1
	7	-8.4±0.6	8.8±0.1	0
Ni _{0.75} Zn _{0.25} Fe ₂ O ₄	3	-12.3±0.7	11.1±0.4	0.7±0.1
	5	-13.5±0.8	10.0±0.2	0.8±0.1
	7	-11.4±0.7	9.5±0.4	0.8±0.2
Ni _{0.5} Zn _{0.4} Mn _{0.1} Fe ₂ O ₄	3	-12.2±0.9	10.7±0.1	0.9±0.1
	5	-11.8±0.6	10.2±0.3	0.8±0.2
	7	-11.1±0.6	9.4±0.1	0.8±0.1
Ni _{0.6} Zn _{0.3} Mn _{0.1} Fe ₂ O ₄	3	-11.4±0.7	11.3±0.2	0.7±0.1
	5	-13.7±0.5	10.6±0.2	1.0±0.2
	7	-12.5±0.9	10.2±0.1	1.3±0.2
Ni _{0.7} Zn _{0.2} Mn _{0.1} Fe ₂ O ₄	3	-11.7±0.3	12.0±0.3	1.0±0.1
	5	-12.5±0.6	11.3±0.3	0.9±0.2
	7	-11.8±0.2	10.7±0.1	0.5±0.1
Ni ³⁺ _{0.25} Ni ²⁺ _{0.375} Zn ²⁺ _{0.25} Fe ₂ O ₄	3	-13.3±0.7	9.8±0.4	1.3±0.1
	5	-12.7±0.4	10.3±0.1	1.2±0.2
	7	-12.5±0.8	10.7±0.2	1.3±0.1
Cu ²⁺ _{0.1} Ni ³⁺ _{0.15} Ni ²⁺ _{0.225} Zn ²⁺ _{0.45} Fe ₂ O ₄	3	-11.6±0.8	11.0±0.1	0.8±0.2
	5	-12.1±0.6	10.5±0.3	0.8±0.1
	7	-11.8±0.5	11±0.1	0.7±0.2
BaNiZnFe ₁₆ O ₂₇	3	-8.4±0.3	12.0±0.3	0
	5	-8.0±0.6	12.0±0.2	0

Table 16 – Comparison of MA properties of the present prepared ferrites with similar ferrites in the other research

Sample	method	t (mm)	f _m (GHz)	BW ₋₁₀ dB (GHz) (C-band)	BW ₋₁₀ dB (GHz) (X-band)	BW ₋₁₀ dB (GHz) (Ku-band)	LP (%)	Ref
Ni _{0.5} Zn _{0.5} Fe ₂ O ₄	Combustion	5.92	3.16	1.65	0	0	80	[87]
Ni _{0.5} Zn _{0.5} Fe ₂ O ₄	Iron oxide catalysts	5.5	6.1	3.2	0	0	70	[88]
Ni _{0.5} Zn _{0.5} Fe ₂ O ₄	Combustion	5.0	5.82	1.6	0	0	80	[89]
Mn _{0.5} Zn _{0.5} Fe ₂ O ₄	Sol-gel	20	6.0	1.2	0	0	66.66	[90]
Ni _{0.5} Zn _{0.5} Fe ₂ O ₄	-	7.10	2.19	6.0	2.0	0	73	[56]
Ni _{0.5} Zn _{0.5} Fe ₂ O ₄	nitrate-citrate precursor	5.0	8.52	-	0.41	-	80	[47]

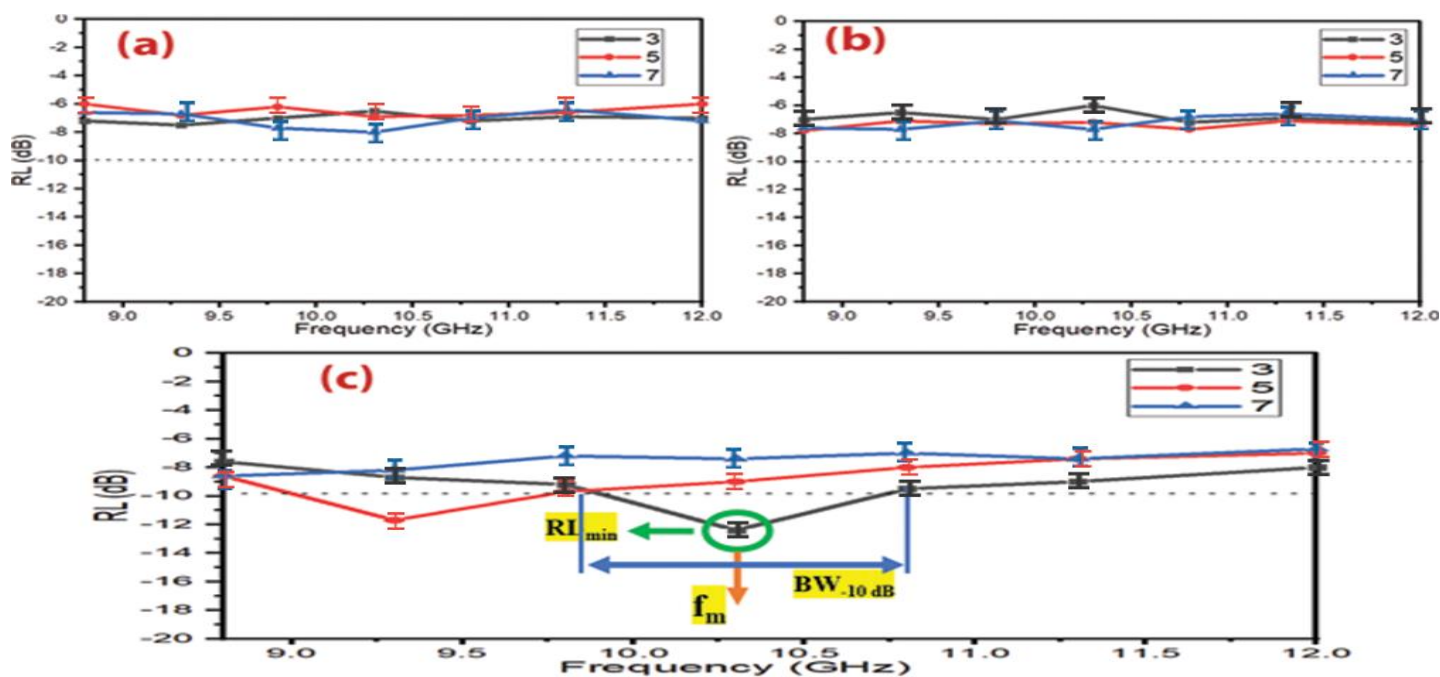


Figure 30 – RL curves of (a) Mn_{0.3}Zn_{0.7}Fe₂O₄, (b) Mn_{0.6}Zn_{0.4}Fe₂O₄ and (c) Mn_{0.9}Zn_{0.1}Fe₂O₄ at different thicknesses

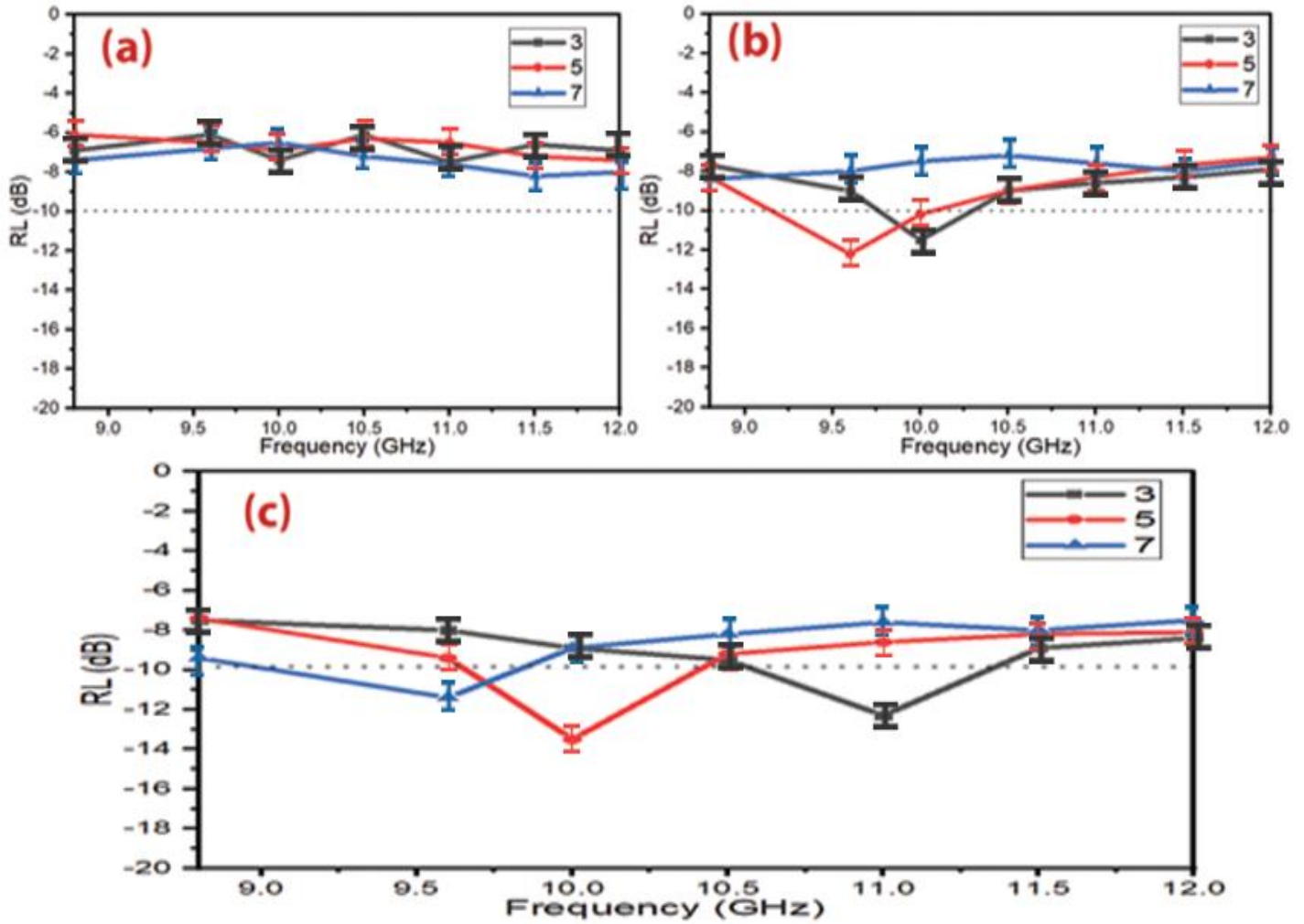


Figure 31 – RL curves of (a) $\text{Ni}_{0.25}\text{Zn}_{0.75}\text{Fe}_2\text{O}_4$, (b) $\text{Ni}_{0.5}\text{Zn}_{0.5}\text{Fe}_2\text{O}_4$ and (c) $\text{Ni}_{0.75}\text{Zn}_{0.25}\text{Fe}_2\text{O}_4$ at different thicknesses

Table 17 – MA behavior of $\text{Ni}^{3+}_{0.25}\text{Ni}^{2+}_{0.375}\text{Zn}^{2+}_{0.25}\text{Fe}_2\text{O}_4$ and $\text{Cu}^{2+}_{0.1}\text{Ni}^{3+}_{0.15}\text{Ni}^{2+}_{0.225}\text{Zn}^{2+}_{0.45}\text{Fe}_2\text{O}_4$ with different loading percentages (60% w/w, 65% w/w and 70% w/w mm) at 5 mm thickness

Samples	LP (%)	RL_{\min} (dB)	f_m (GHz)	$\text{BW}_{-10 \text{ dB}}$ (GHz)
$\text{Ni}^{3+}_{0.25}\text{Ni}^{2+}_{0.375}\text{Zn}^{2+}_{0.25}\text{Fe}_2\text{O}_4$	60	-12.3 ± 0.6	10.7 ± 0.4	1.1 ± 0.3
	65	-12.7 ± 0.8	10.3 ± 0.2	1.2 ± 0.2
	70	-12.0 ± 0.9	9.2 ± 0.3	1.0 ± 0.3
$\text{Cu}^{2+}_{0.1}\text{Ni}^{3+}_{0.15}\text{Ni}^{2+}_{0.225}\text{Zn}^{2+}_{0.45}\text{Fe}_2\text{O}_4$	60	-11.1 ± 0.9	11.5 ± 0.4	0.8 ± 0.2
	65	-12.1 ± 0.7	10.5 ± 0.2	0.9 ± 0.2
	70	-11.8 ± 0.6	10.0 ± 0.1	0.9 ± 0.1

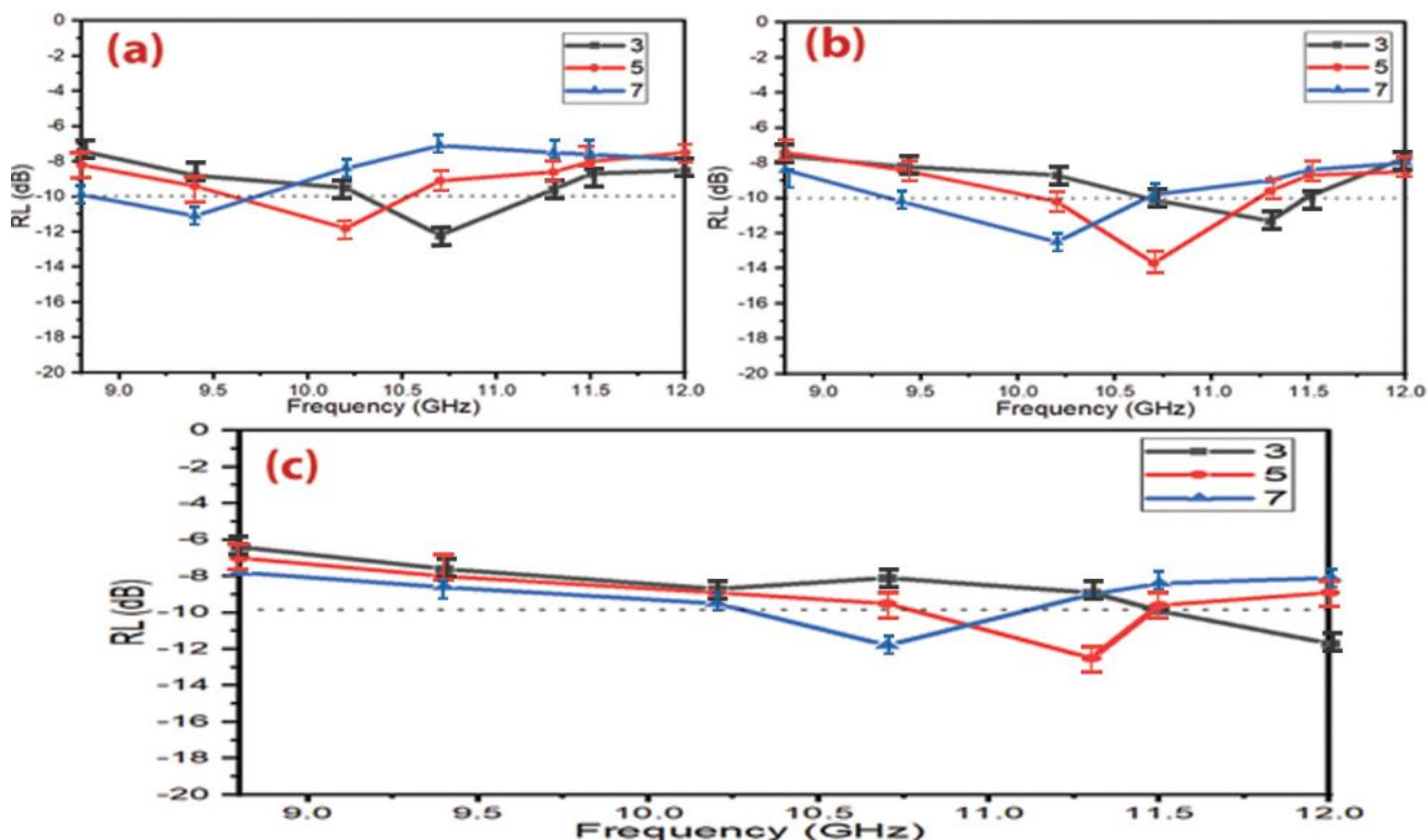


Figure 32 – RL curves of (a) $\text{Ni}_{0.5}\text{Zn}_{0.4}\text{Mn}_{0.1}\text{Fe}_2\text{O}_4$, (b) $\text{Ni}_{0.6}\text{Zn}_{0.3}\text{Mn}_{0.1}\text{Fe}_2\text{O}_4$ and (c) $\text{Ni}_{0.7}\text{Zn}_{0.2}\text{Mn}_{0.1}\text{Fe}_2\text{O}_4$ at different thicknesses

The effect of the triple nickel (Ni^{3+}) ion substitution on the EMI shielding and MA properties was investigated. Table 17 shows the prepared samples' MA properties. The absorption results demonstrate that the MA properties improved by entering the triple nickel into the nickel-zinc ferrite composition as shown in Figure 33. This substitution process increased the absorption $\text{BW}_{-10\text{ dB}}$ of the Ni-Zn ferrite and improved the RL_{min} and SE_{max} . The results indicated that the $\text{Ni}^{3+}_{0.25}\text{Ni}^{2+}_{0.375}\text{Zn}^{2+}_{0.25}\text{Fe}_2\text{O}_4$ exceeded the -10 dB threshold, which illustrates that the RL attenuation peaks of samples moved to lower frequencies by increasing sample thickness and loading percentage of absorber within a paraffin matrix.

On the other hand, Cu-doped nickel zinc ferrite ($\text{Cu}^{2+}_{0.1}\text{Ni}^{3+}_{0.15}\text{Ni}^{2+}_{0.225}\text{Zn}^{2+}_{0.45}\text{Fe}_2\text{O}_4$) was studied. Table 17 shows the prepared samples' MA properties. Figure 34 also shows a comparison of the MA curves with different loading percentages (60% w/w, 65% w/w and 70% w/w) at 5 mm thickness. The results show that the MA properties decreased by entering the Cu^{2+} into $\text{Ni}^{3+}_{0.25}\text{Ni}^{2+}_{0.375}\text{Zn}^{2+}_{0.25}\text{Fe}_2\text{O}_4$. This substitution process decreased the absorption bandwidth of $\text{Ni}^{3+}_{0.25}\text{Ni}^{2+}_{0.375}\text{Zn}^{2+}_{0.25}\text{Fe}_2\text{O}_4$, as shown in Table 17. The results indicated that the $\text{Cu}^{2+}_{0.1}\text{Ni}^{3+}_{0.15}\text{Ni}^{2+}_{0.225}\text{Zn}^{2+}_{0.45}\text{Fe}_2\text{O}_4$ exceeded the -10 dB threshold, as shown in Figure 34, which illustrates that the RL attenuation peaks of samples moved to lower frequencies by increasing sample thickness and loading percentage.

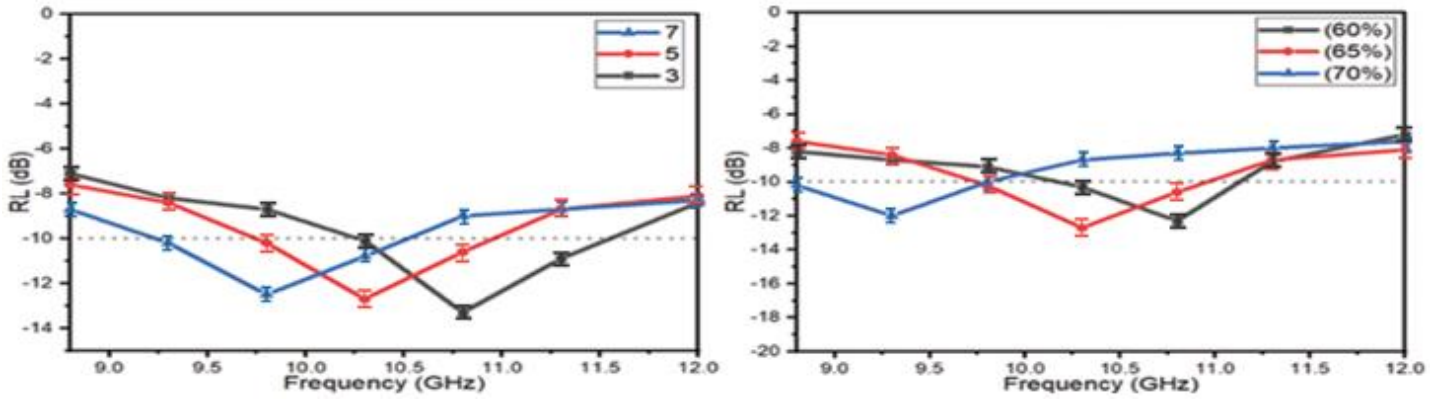


Figure 33 – RL curves of $\text{Ni}^{3+}_{0.25}\text{Ni}^{2+}_{0.375}\text{Zn}^{2+}_{0.25}\text{Fe}_2\text{O}_4$ at different thicknesses and different loading percentages (60% w/w, 65% w/w and 70% w/w mm) at 5 mm thickness

Table 18 illustrates a comparison of MA characteristics of some lately informed ferrite absorbers with different preparation methods and loading percentages. The results of the literature show these ferrites are good in the C-band and Ku-band frequencies and weak in the X-band frequency. The presently prepared ferrites display in this research better MA in the X-band frequency. The distinct of these prepared ferrites have a lower loading percentage and thickness of the absorbers compared with the other literature. The best result obtained at this stage was by using $\text{Ni}^{3+}_{0.25}\text{Ni}^{2+}_{0.375}\text{Zn}^{2+}_{0.25}\text{Fe}_2\text{O}_4$. A RL_{\min} indicated -13.3 dB at 9.8 GHz and bandwidth $\text{BW}_{-10 \text{ dB}}$ was 1.3 GHz for a thickness of 3 mm. Also, the SE_{\max} attained 15.9 dB at 10.2 GHz. However, the defect of the $\text{Ni}^{3+}_{0.25}\text{Ni}^{2+}_{0.375}\text{Zn}^{2+}_{0.25}\text{Fe}_2\text{O}_4$ that it has a low ϵ'' . This low ϵ'' of $\text{Ni}^{3+}_{0.25}\text{Ni}^{2+}_{0.375}\text{Zn}^{2+}_{0.25}\text{Fe}_2\text{O}_4$ can be attributed to the non-dielectric properties of ferrite, therefore the EM wave absorption capability largely results from the magnetic loss (natural resonance and exchange resonance are the main factors for the loss of the magnetic field energy [91]).

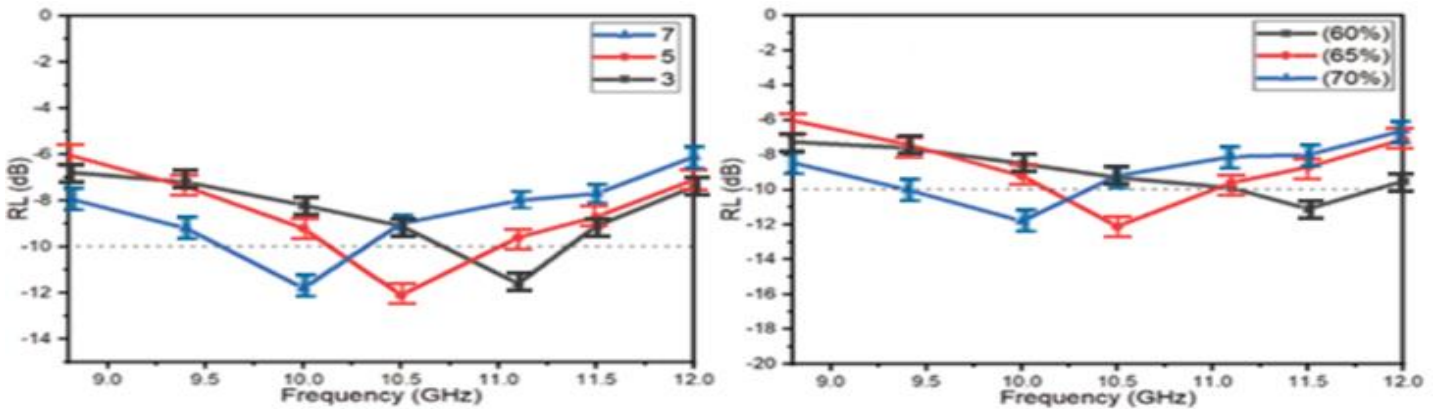


Figure 34 – RL curves of $\text{Cu}^{2+}_{0.1}\text{Ni}^{3+}_{0.15}\text{Ni}^{2+}_{0.225}\text{Zn}^{2+}_{0.45}\text{Fe}_2\text{O}_4$ at different thicknesses and different loading percentages (60% w/w, 65% w/w and 70% w/w mm) at 5 mm thickness

Table 18 – Comparison of MA properties of the present prepared ferrites with similar ferrites in the other research

Sample	method	t (mm)	BW _{-10 dB} (GHz) (C-band)	BW _{-10 dB} (GHz) (X-band)	BW _{-10 dB} (GHz) (Ku-band)	LP (%)	Ref
Mn _{0.5} Zn _{0.5} Fe ₂ O ₄	Sol-gel	20	1.2	0	0	66.66	[90]
Cu _{0.2} Ni _{0.45} Zn _{0.35} Fe ₂ O ₄	Co-Precipitation	7.35	1.1	0	0	100	[92]
Cu _{0.3} Ni _{0.2} Zn _{0.5} Fe ₂ O ₄	Nitrate-citrate precursor	6.2	0	0.6	0	70	[93]
Ni _{0.4} Zn _{0.4} Mn _{0.2} Fe ₂ O ₄	Nitrate-citrate precursor	5.0	-	0.8	-	80	[47]
Ni _{0.4} Zn _{0.4} Cu _{0.2} Fe ₂ O ₄			-	1.2	-		
Ni _{0.4} Zn _{0.4} Mg _{0.2} Fe ₂ O ₄			-	0.7	-		
Ni _{0.4} Cu _{0.2} Zn _{0.4} Tb _{0.8} Fe _{1.2} O ₄	Sonochemical	8.0	2.1	-	-	70	[51]
Ni _{0.4} Cu _{0.2} Zn _{0.4} Eu _{0.8} Fe _{1.2} O ₄	Sol-gel	7.0	1.5	-	-	70	[52]
Cu _{0.2} Ni _{0.4} Zn _{0.4} Fe ₂ O ₄	Ceramic	9.2	1.5	0	0	85	[94]

3.2 Results and discussion of the preparation of ferrite powders by citrate precursor technique

3.2.1 X-ray diffraction of ferrite samples

Figure 35 displays the XRD patterns of Ni_{0.5}Zn_{0.5}Fe₂O₄. The effect of the different molar ratios of the metal ion/citrate acid (1:1, 2:1 and 3:1) and the different calcination temperatures (650, 800 and 950°C) was investigated on the ferrite properties. The XRD Figures of ferrites showed the formation of a single-phase cubic spinel structure with no impurity peaks [95]. All the observed peaks of the NiZn ferrite were matched with the standard XRD pattern (JCPDS, PDF no. 08–0234). The size of the NiZn ferrite grains (hkl (311)) has been evaluated with Scherrer's equation, $D=0.9 \lambda/\beta \cos\theta$. The XRD patterns showed that the crystallite size of

nickel-zinc ferrite increased by increasing the calcination temperature, as shown in Figure 36. One can observe that the crystallite size of nickel-zinc ferrite increased by increasing the metal ion concentrations during the preparation process of the ferrite, regardless of the calcination temperature, which will impact its EMI shielding and MA properties, as will be clarified later.

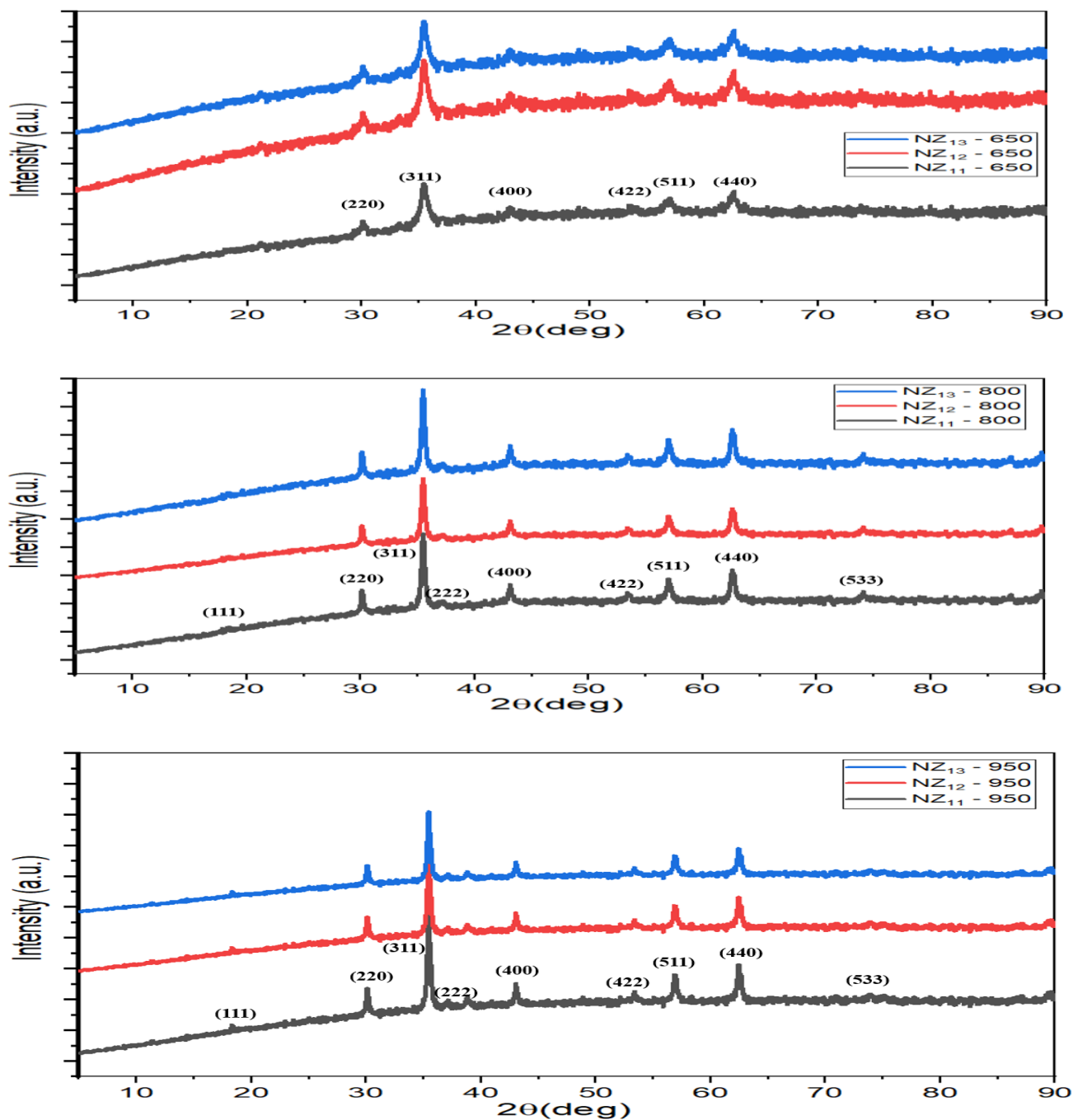


Figure 35 – XRD patterns at $\text{Ni}_{0.5}\text{Zn}_{0.5}\text{Fe}_2\text{O}_4$ of the different molar ratios of the metal ion/citrate acid (1:1, 2:1, and 3:1) at the different calcination temperatures (650, 800, and 950°C)

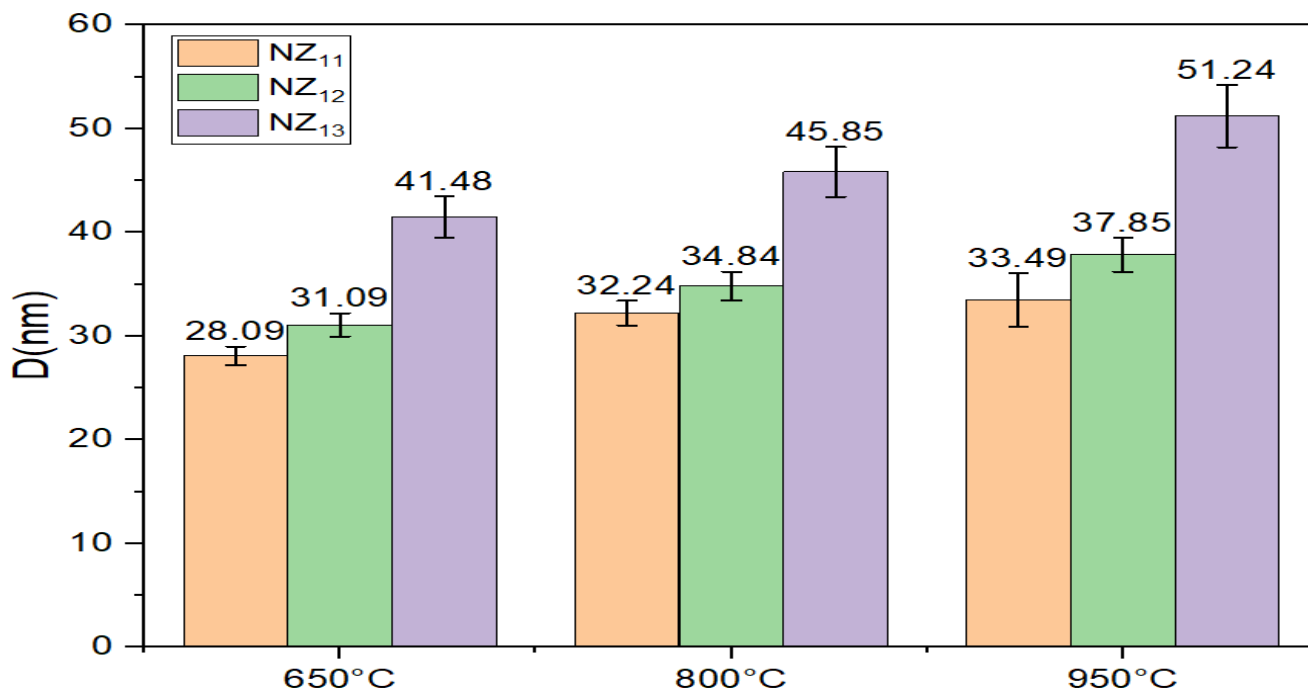


Figure 36 – Change of crystallite size of nickel-zinc ferrite prepared by citrate precursor method by changing the preparation conditions (calcination temperatures, metal ion concentrations)

3.2.2 FTIR spectra of ferrite samples

Figure 37 shows the FTIR spectra of $\text{Ni}_{0.5}\text{Zn}_{0.5}\text{Fe}_2\text{O}_4$ prepared by citrate precursor technique. The peaks within the range ($560\text{--}590\text{ cm}^{-1}$) were due to the stretching vibration of (Fe-O) at the tetrahedral sites, while the peaks located in the sites less than 460 cm^{-1} were due to the stretching vibration of (Fe-O) at the octahedral sites [86]. In addition, the peaks within the range ($1630\text{--}1640\text{ cm}^{-1}$) were due to the stretching vibration of C=O and the peaks at 2348 cm^{-1} and 3452 cm^{-1} referred to O-H stretching vibration [96,97].

3.2.3 Morphology investigations for spinel ferrite sample

Figure 38 represents the SEM micrographs of the $\text{Ni}_{0.5}\text{Zn}_{0.5}\text{Fe}_2\text{O}_4$ nanoparticles (NZ₁₁-650) prepared by the citrate precursor method on the scale bar of $10\text{ }\mu\text{m}$ and $2\text{ }\mu\text{m}$. The agglomerated spherical particles of spinel ferrite are noticed, it's due to magneto-dipole interactions between particles. In order to gain further insight into the composition of the sample, EDX elemental mapping has been performed as demonstrated in the next section.

3.2.4 EDX analysis for spinel ferrite sample

EDX analysis of $\text{Ni}_{0.5}\text{Zn}_{0.5}\text{Fe}_2\text{O}_4$ nanoparticles prepared by citrate precursor method is shown in Figure 39 and Table 19. The presence of C, O, Cl, S, Fe, Ni, Al and Zn elements in the spinel ferrite EDX spectrums was noticed.

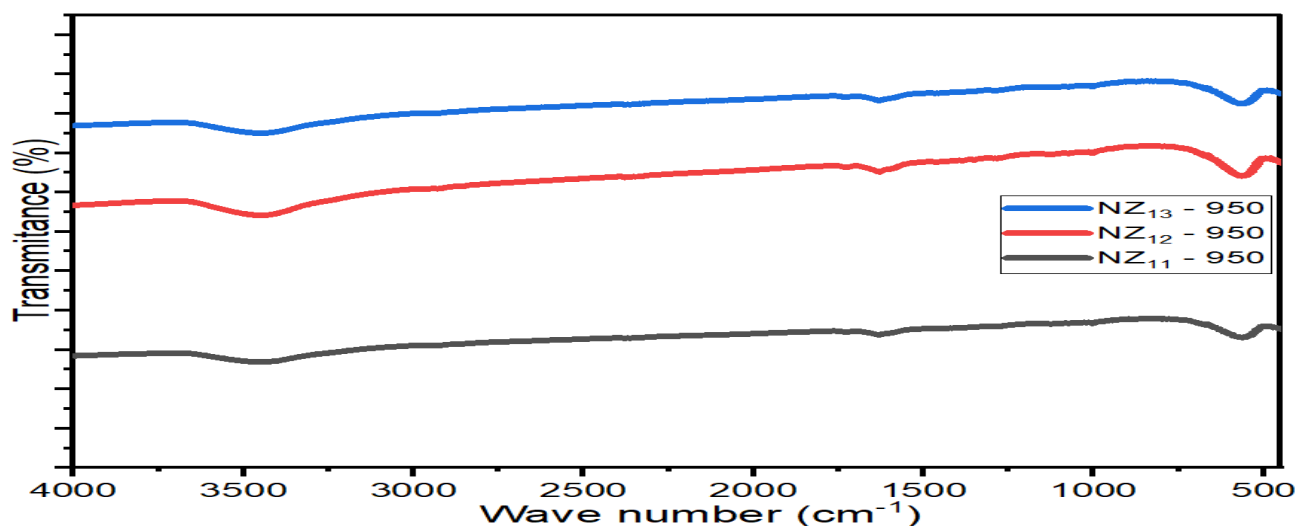
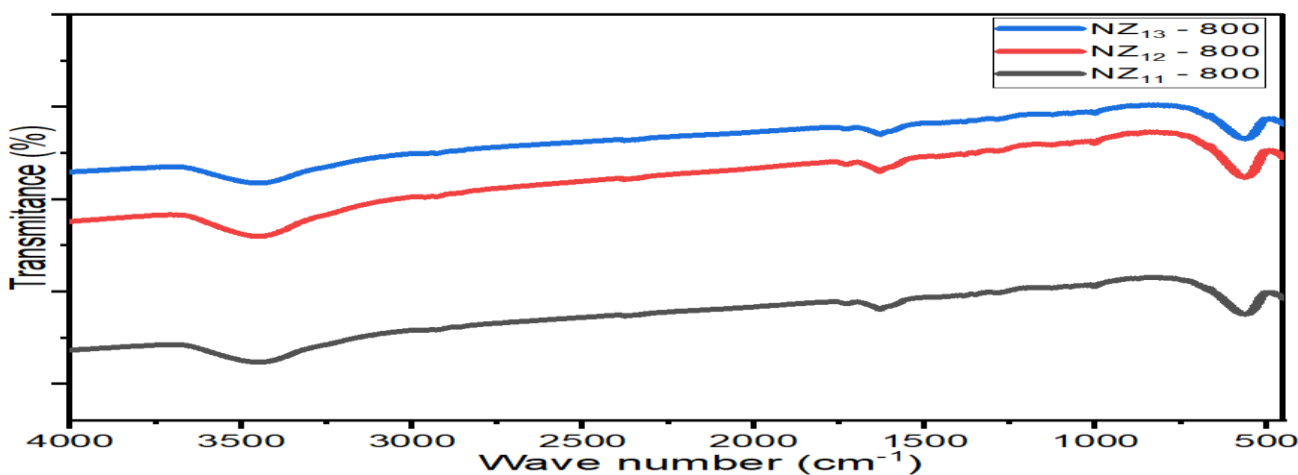
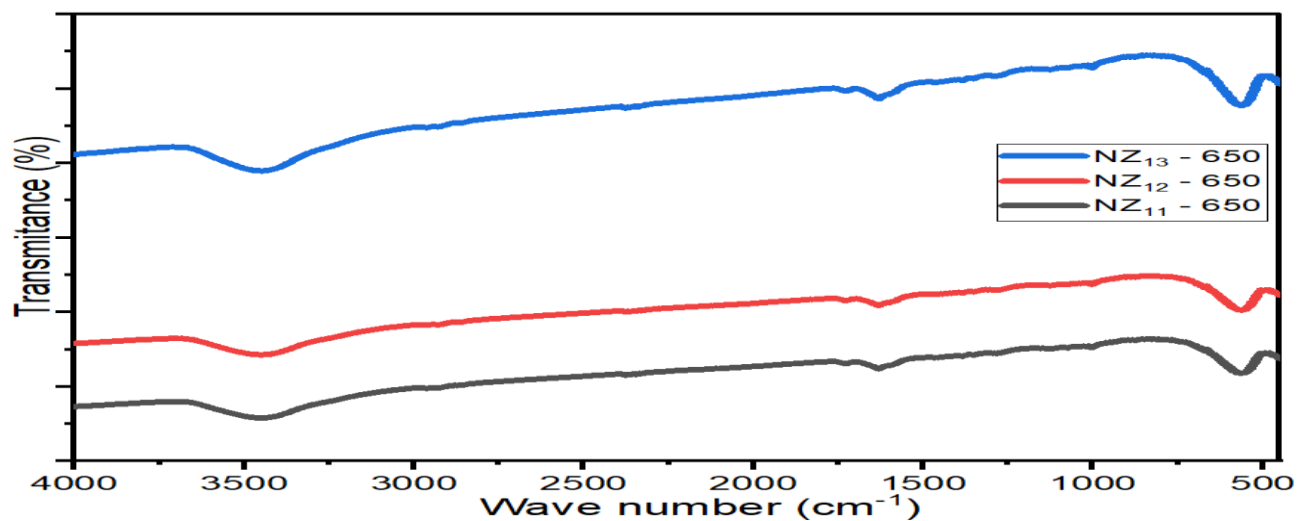


Figure 37 – FTIR spectra of $\text{Ni}_{0.5}\text{Zn}_{0.5}\text{Fe}_2\text{O}_4$ at the different molar ratios of the metal ion/citrate acid (1:1, 2:1 and 3:1) at the different calcination temperatures (650, 800 and 950°C)

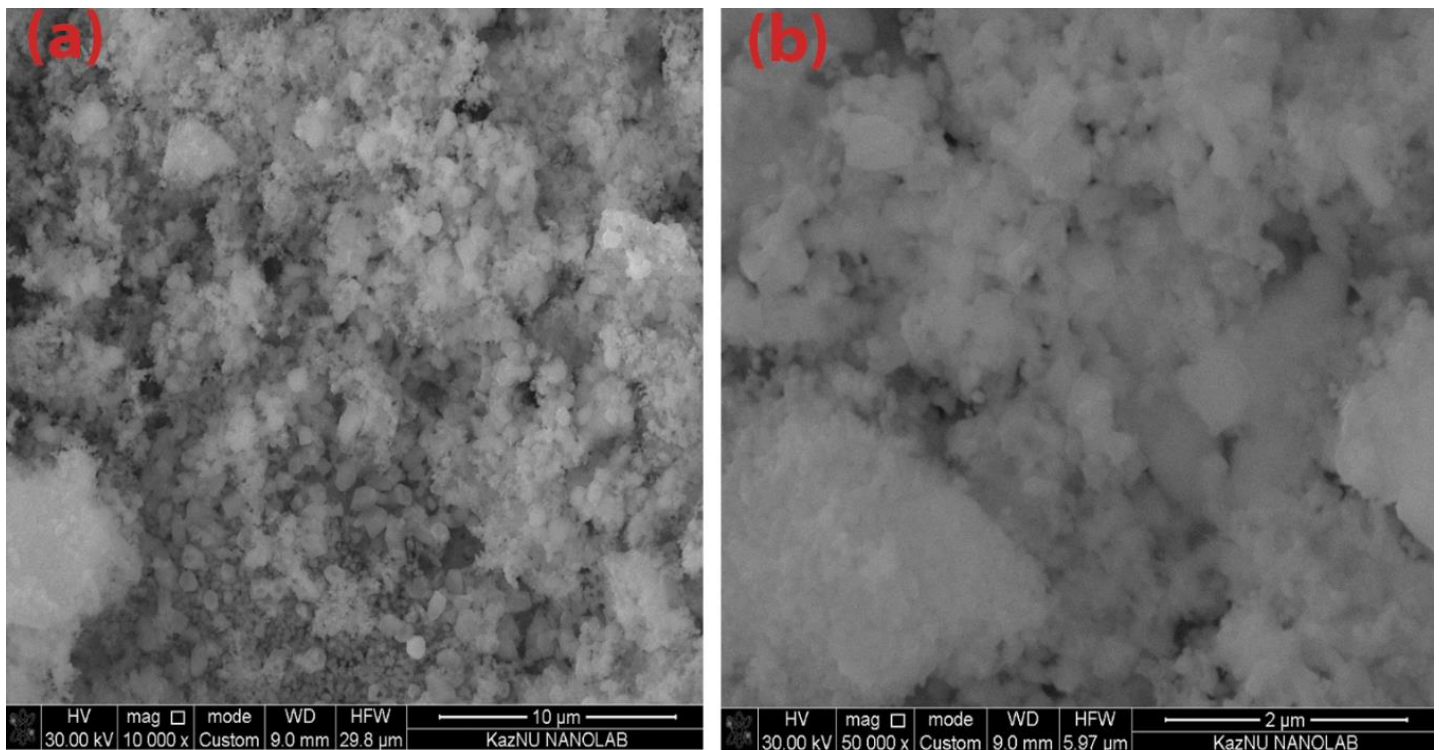


Figure 38 – SEM images of spinel ferrite on the scale bar of (a) 10 μm and (b) 2 μm

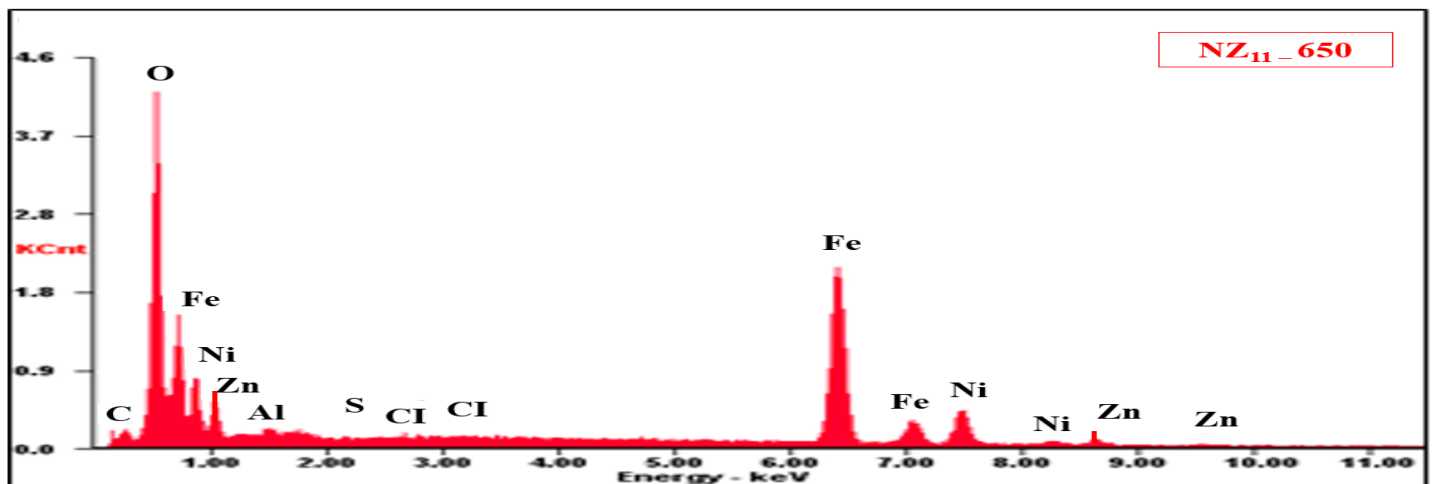


Figure 39 – EDX of spinel ferrite

Table 19 – EDX element composition of spinel ferrites and hexagonal ferrite

Element	C	Cl	O	S	Ba	Al	Fe	Ni	Zn
NZ ₁₁ -650 (wt%)	3.30	0.13	19.26	0.02	-	0.41	53.02	13.04	10.82

3.2.5 Microwave absorption properties of ferrite samples prepared by citrate precursor technique

Several variables that affect MA properties were studied: molar ratio of the metal ion to citrate acid, calcination temperature, absorber thickness and loading percentage.

3.2.5.1 Microwave absorption properties of $\text{Ni}_{0.5}\text{Zn}_{0.5}\text{Fe}_2\text{O}_4$ nanoparticles

The effect of the different molar ratios of the metal ions to citrate acid (1:1, 2:1, and 3:1) and calcination temperatures (650, 800, and 950°C) on the properties of $\text{Ni}_{0.5}\text{Zn}_{0.5}\text{Fe}_2\text{O}_4$ was studied. Samples were prepared with a thickness of 5 mm and a loading percentage of 65%. The results indicated that the RL attenuation peaks of samples moved to lower frequencies with increasing the metal ions to citrate acid and calcination temperature as shown in Figure 40. This may be due to the change in the crystallite size of the ferrite nanoparticles. The results of XRD patterns indicated that the crystallite size of nickel-zinc ferrite increased by increasing the calcination temperature and the metal ion concentration. The best result obtained at this stage was by using $\text{NZ}_{11}-650$ as shown in Figure 41 and Table 20.

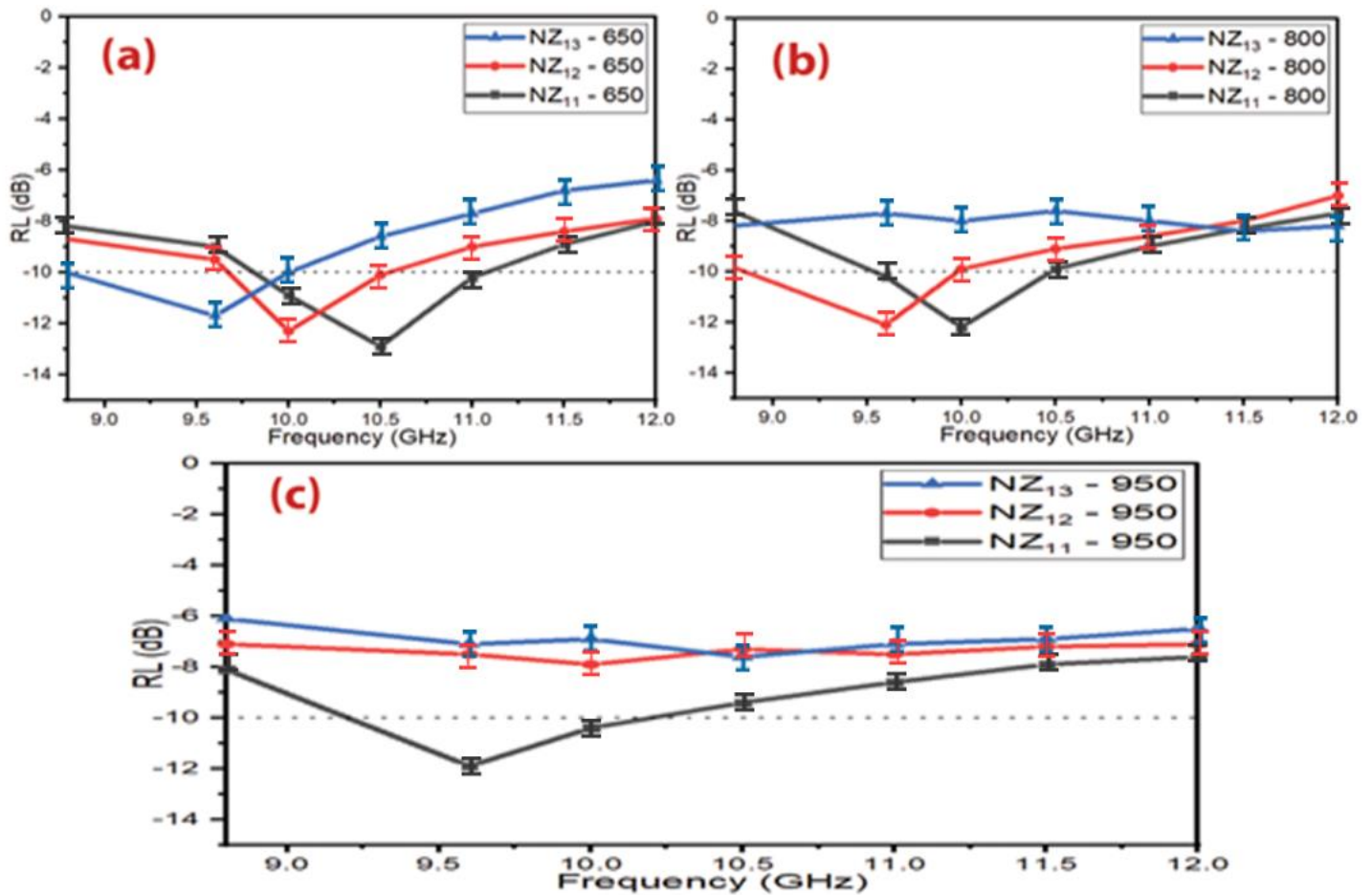


Figure 40 – RL curves of $\text{Ni}_{0.5}\text{Zn}_{0.5}\text{Fe}_2\text{O}_4$ nanoparticles at (a) 650 °C, (b) 800 °C and (c) 950 °C

Table 20 – MA behavior of $\text{Ni}_{0.5}\text{Zn}_{0.5}\text{Fe}_2\text{O}_4$ nanoparticles

Samples	T (°C)	RL _{min} (dB)	f _m (GHz)	BW _{-10 dB} (GHz)
NZ ₁₁ - 650	650	-12.9±0.5	10.5±0.3	1.3±0.3
NZ ₁₂ - 650		-12.3±0.8	10.0±0.2	0.8±0.3
NZ ₁₃ - 650		-11.7±0.7	9.5±0.2	1.2±0.1
NZ ₁₁ - 800	800	-12.2±0.4	10.1±0.1	1.1±0.2
NZ ₁₂ - 800		-12.0±0.7	9.5±0.1	0.9±0.1
NZ ₁₃ - 800		-8.4±0.8	11.4±0.3	0
NZ ₁₁ - 950	950	-11.9±0.4	9.6±0.1	0.8±0.2
NZ ₁₂ - 950		-7.9±0.9	9.9±0.1	0
NZ ₁₃ - 950		-7.7±0.7	110.4±0.2	0

3.2.5.1 Influence of sample thickness and loading percentage on the f_m

The influence of the different loading percentages and thicknesses on NZ11 – 650 properties were investigated. Figure 42 shows that the RL moved gradually to a lower frequency with the increased loading percentage. Also, the same phenomenon was noticed by increasing the thickness of an absorber. These results may be defined by the quarter-wavelength ($\lambda/4$) cancellation model, as shown in equation (5) [44–46]. From the above studies, we found the f_m position controllability of ferrite nanoparticles prepared with the citrate precursor technique.

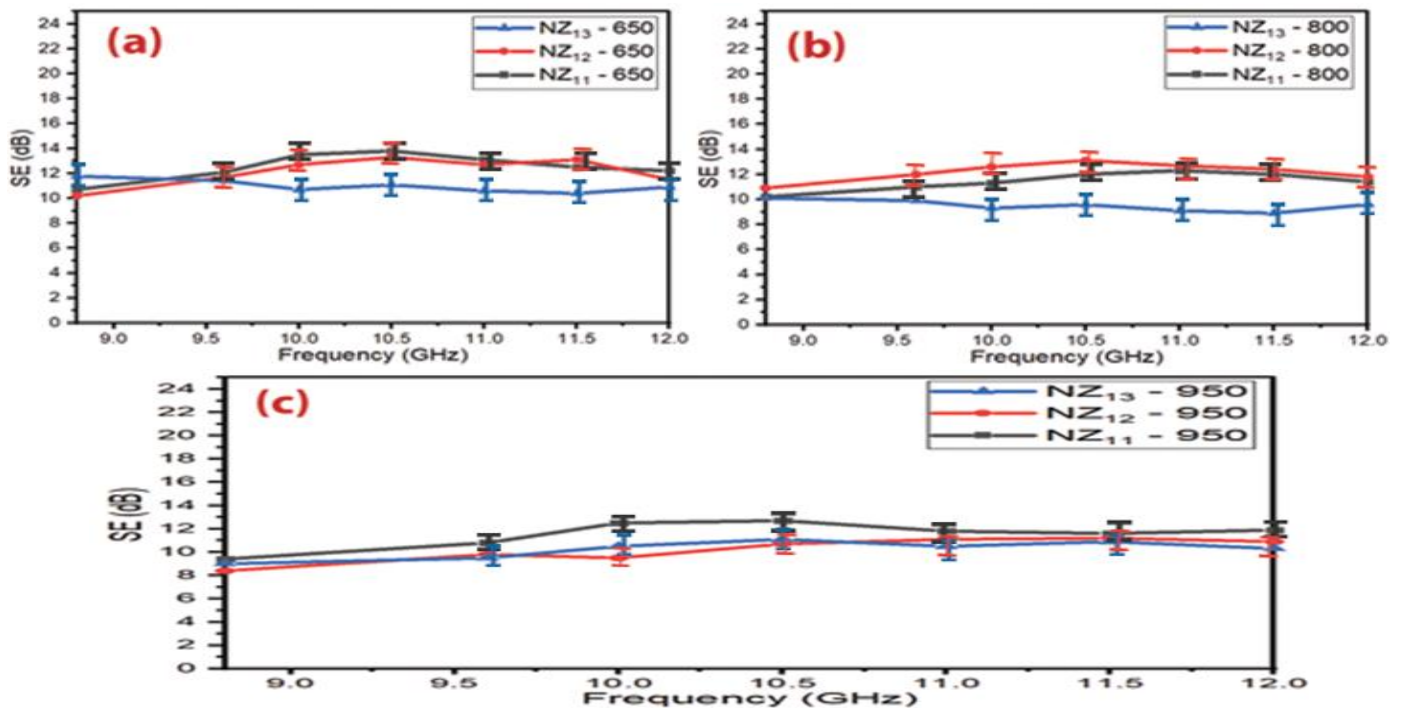


Figure 41 – SE curves of $\text{Ni}_{0.5}\text{Zn}_{0.5}\text{Fe}_2\text{O}_4$ nanoparticles (a) 650 °C, (b) 800 °C and (c) 950 °C.

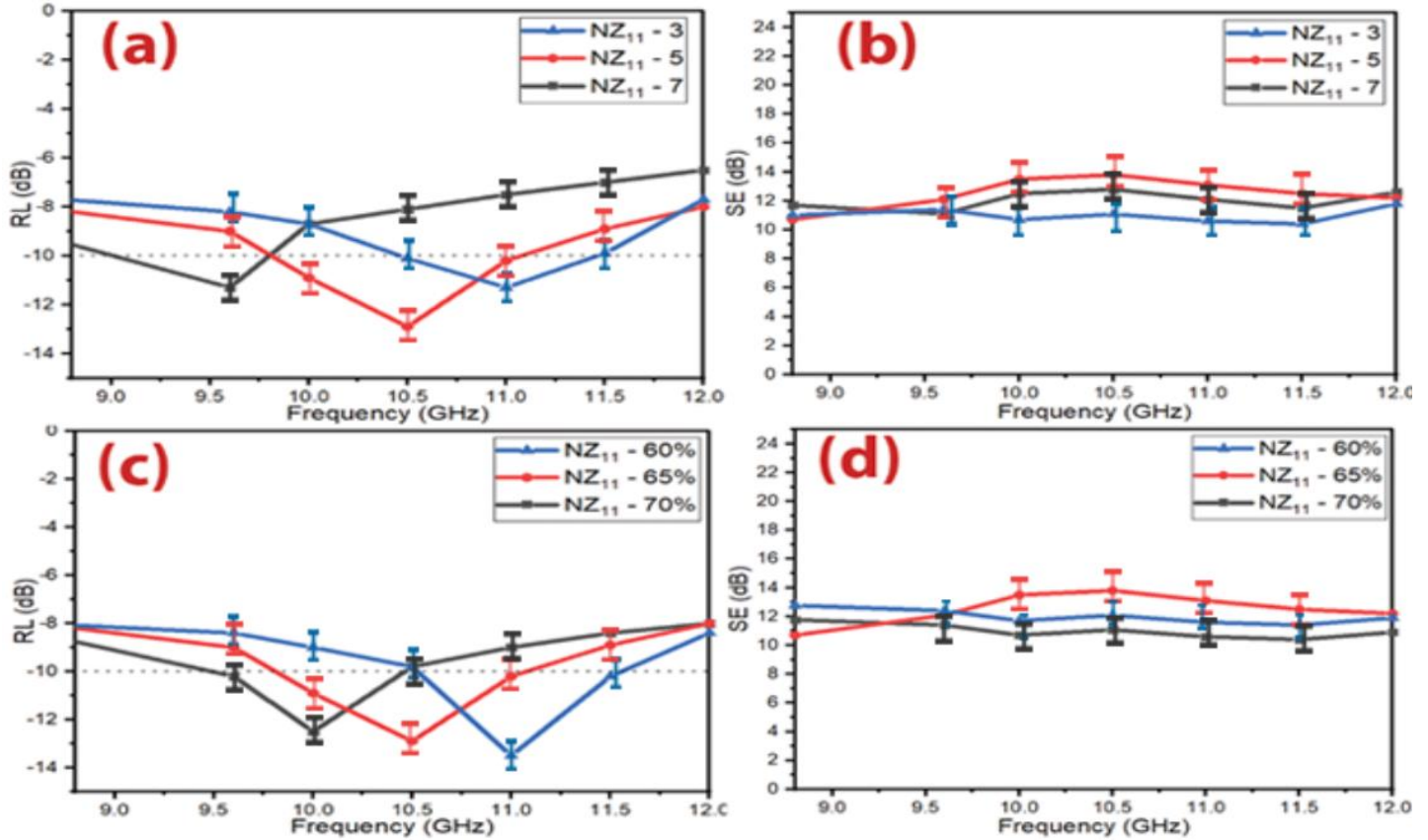


Figure 42 – (a,b) RL and SE curves of $\text{Ni}_{0.5}\text{Zn}_{0.5}\text{Fe}_2\text{O}_4$ nanoparticles at different thicknesses and (d,c) RL and SE curves of $\text{Ni}_{0.5}\text{Zn}_{0.5}\text{Fe}_2\text{O}_4$ nanoparticles with varying percentages of loading (60% w/w, 65% w/w and 70% w/w mm) at 5 mm thickness

3.3 Results and discussion of the preparation of ferrite powders by self-combustion technique

3.3.1 X-ray diffraction of ferrite samples

Figure 43 displays the XRD patterns of $\text{Ni}_{0.5}\text{Zn}_{0.5}\text{Fe}_2\text{O}_4$. The effect of the different aqueous solutions of PVA (1%, 4% and 6%) and the different calcination temperatures (650, 800 and 950°C) were studied on the ferrite properties. The XRD Figures of ferrites showed the formation of a single-phase cubic spinel structure with no impurity peaks [95]. All the observed peaks of the NiZn ferrite were matched with the standard XRD pattern (JCPDS, PDF no. 08–0234). The size of the NiZn ferrite grains (hkl (311)) has been evaluated with Scherrer’s equation. The XRD patterns results showed that the crystallite size of nickel-zinc ferrite increased by increasing the calcination temperature, as shown in Figure 44. One can notice that the crystallite size of nickel-zinc ferrite increased by increasing the PVA concentrations during the preparation process of the ferrite, regardless of calcination temperature, which will affect its EMI shielding and MA properties, as will be explained later.

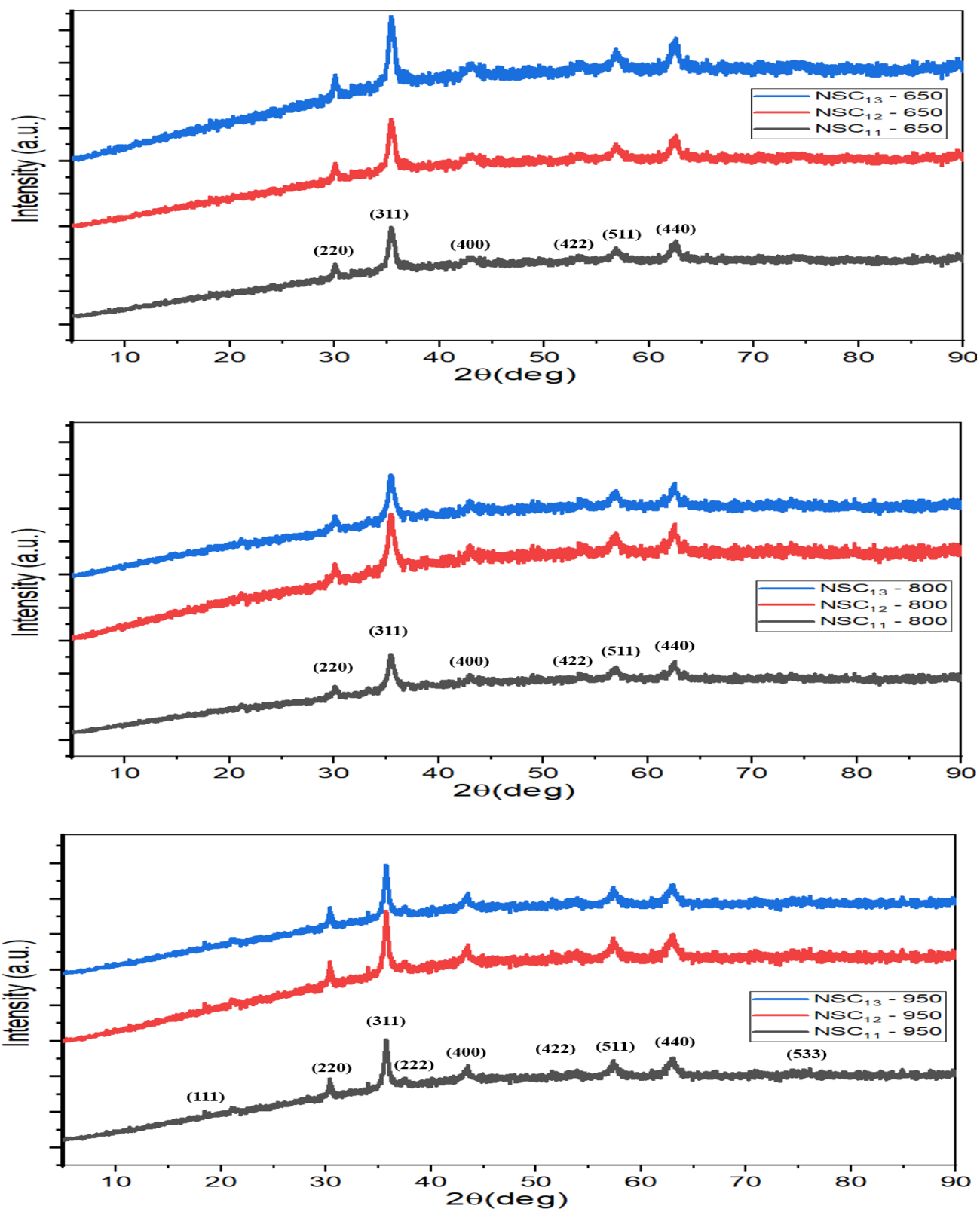


Figure 43 – XRD patterns of $\text{Ni}_{0.5}\text{Zn}_{0.5}\text{Fe}_2\text{O}_4$ at the different aqueous solutions of PVA (1%, 4%, and 6%) at the different calcination temperatures (650, 800, and 950°C)

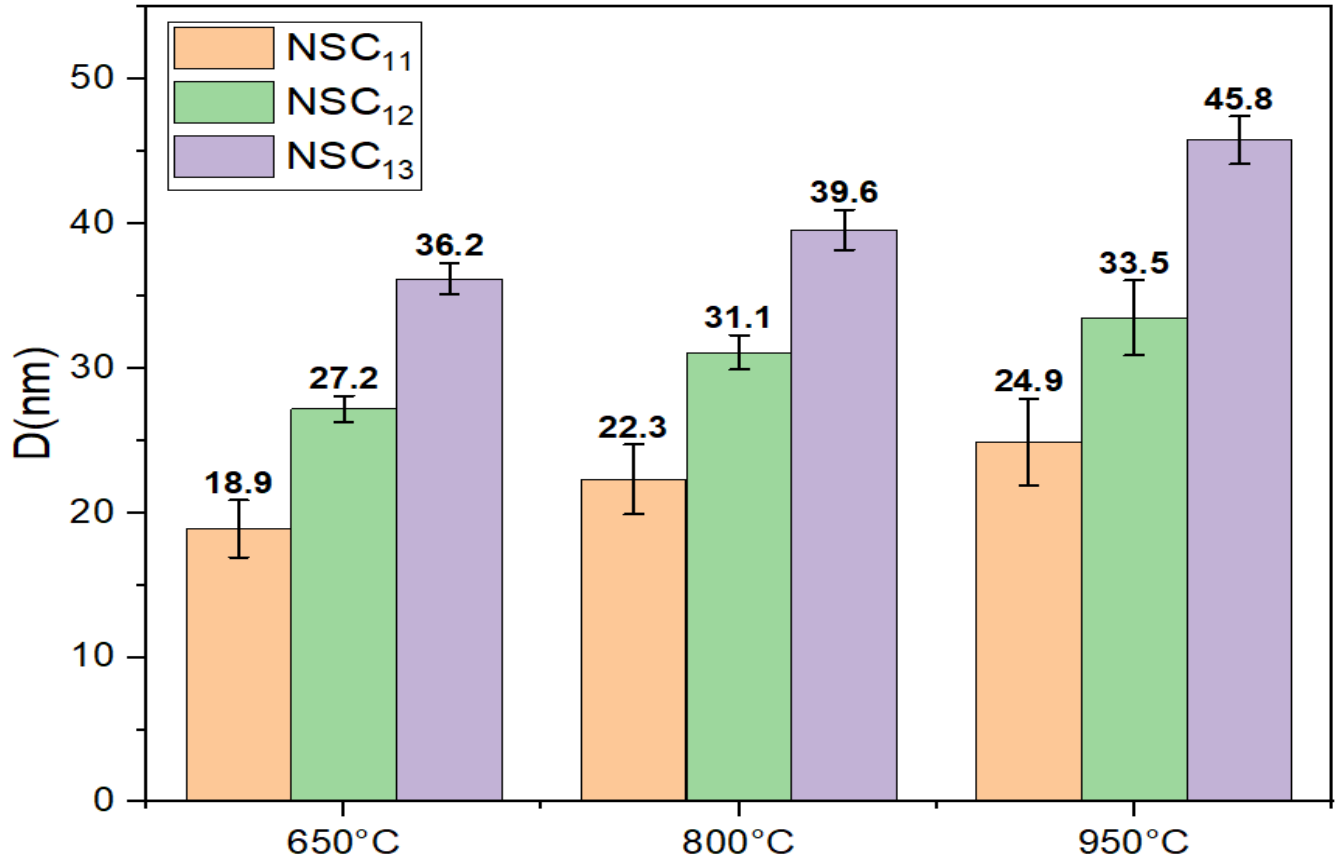


Figure 44 – Change of crystallite size of ferrites prepared by self-combustion method by changing the preparation conditions (calcination temperatures, PVA concentrations)

3.3.2 FTIR spectra of ferrite samples

Figure 45 shows the FTIR spectra of $\text{Ni}_{0.5}\text{Zn}_{0.5}\text{Fe}_2\text{O}_4$ prepared by the self-combustion technique. The peaks within the range ($560\text{--}590\text{ cm}^{-1}$) were due to the stretching vibration of (Fe-O) at the tetrahedral sites, while the peaks located in the sites less than 460 cm^{-1} were due to the stretching vibration of (Fe-O) at the octahedral sites [86]. In addition, the peaks within the range ($1630\text{--}1640\text{ cm}^{-1}$) were due to the stretching vibration of C=O and the peaks at 2348 cm^{-1} and 3452 cm^{-1} referred to O-H stretching vibration [96,97]. The effects of increasing PVA concentration haven't appeared in the FTIR spectra of $\text{Ni}_{0.5}\text{Zn}_{0.5}\text{Fe}_2\text{O}_4$. This is due to the evaporation of PVA by heat treatment at different temperatures ($650, 800$ and $950\text{ }^\circ\text{C}$).

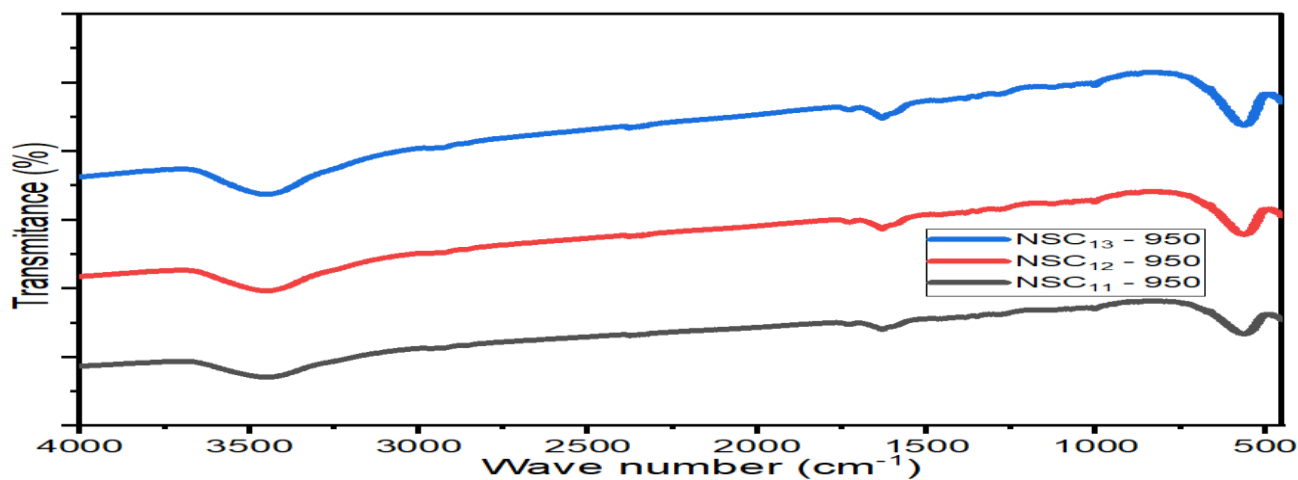
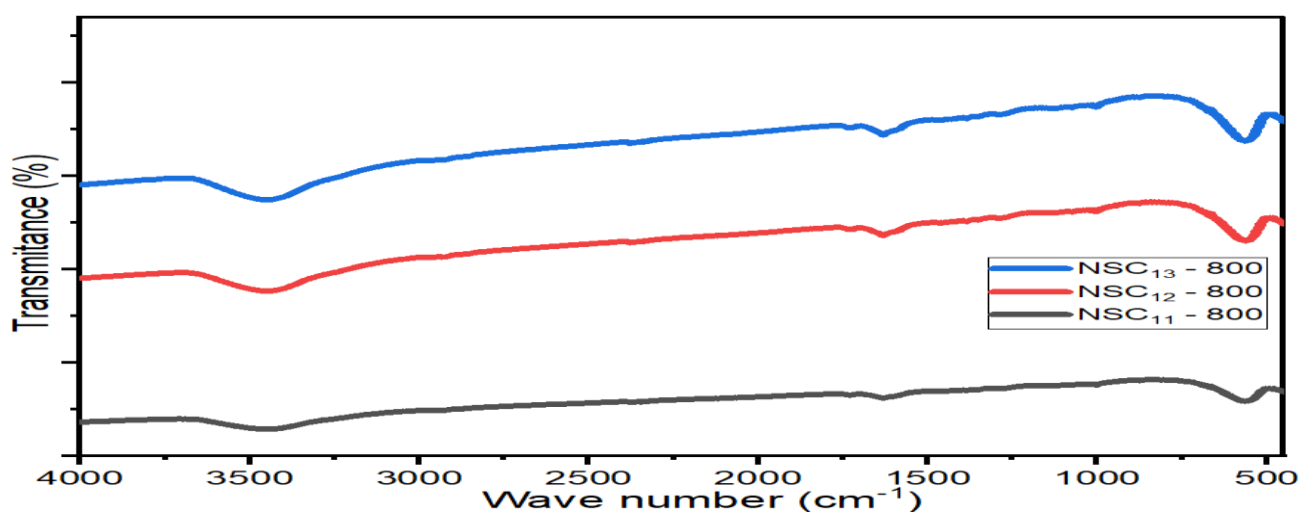
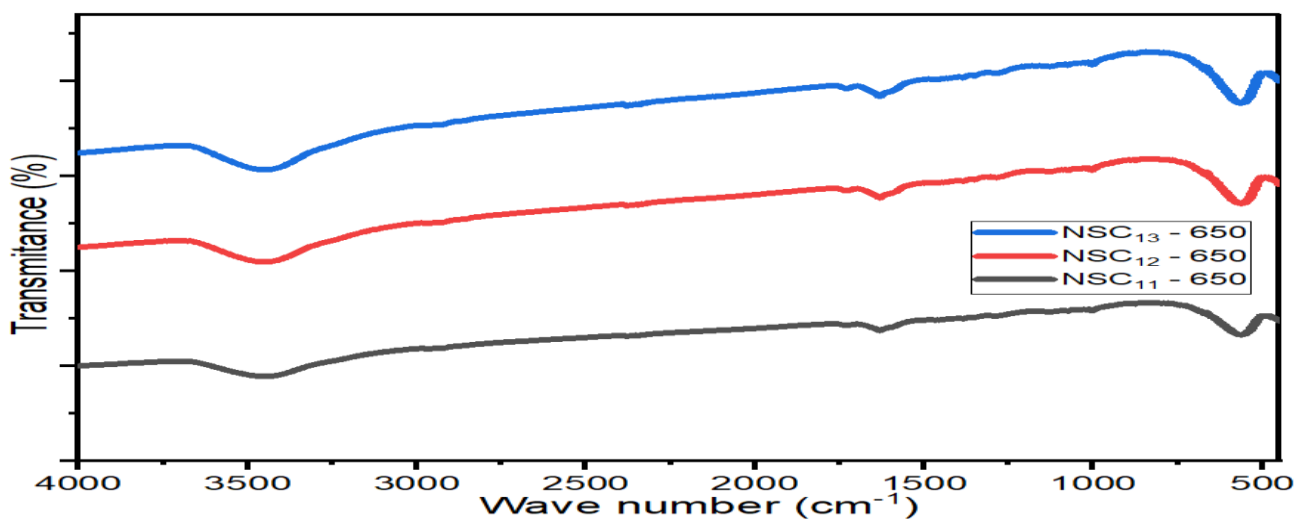


Figure 45 – FTIR spectra of $\text{Ni}_{0.5}\text{Zn}_{0.5}\text{Fe}_2\text{O}_4$ at the different aqueous solutions of PVA (1%, 4% and 6%) at the different calcination temperatures (650, 800 and 950°C)

3.3.3 Morphology investigations for spinel ferrite sample

Figure 46 represents the SEM micrographs of the $\text{Ni}_{0.5}\text{Zn}_{0.5}\text{Fe}_2\text{O}_4$ nanoparticles (NSC₁₁₋₆₅₀) prepared by self-combustion technique on the scale bar of 20 μm and 2 μm . The agglomerated spherical particles of spinel ferrite are noticed, it's due to magneto-dipole interactions between particles. EDX was used to know the chemical composition of the spinel ferrite sample as shown below.

3.3.4 EDX analysis for spinel ferrite sample

EDX analysis of $\text{Ni}_{0.5}\text{Zn}_{0.5}\text{Fe}_2\text{O}_4$ nanoparticles prepared by self-combustion method is shown in Figure 47 and Table 21. The presence of C, O, Cl, S, Fe, Ni, Al and Zn elements in the spinel ferrites EDX spectrums was noticed.

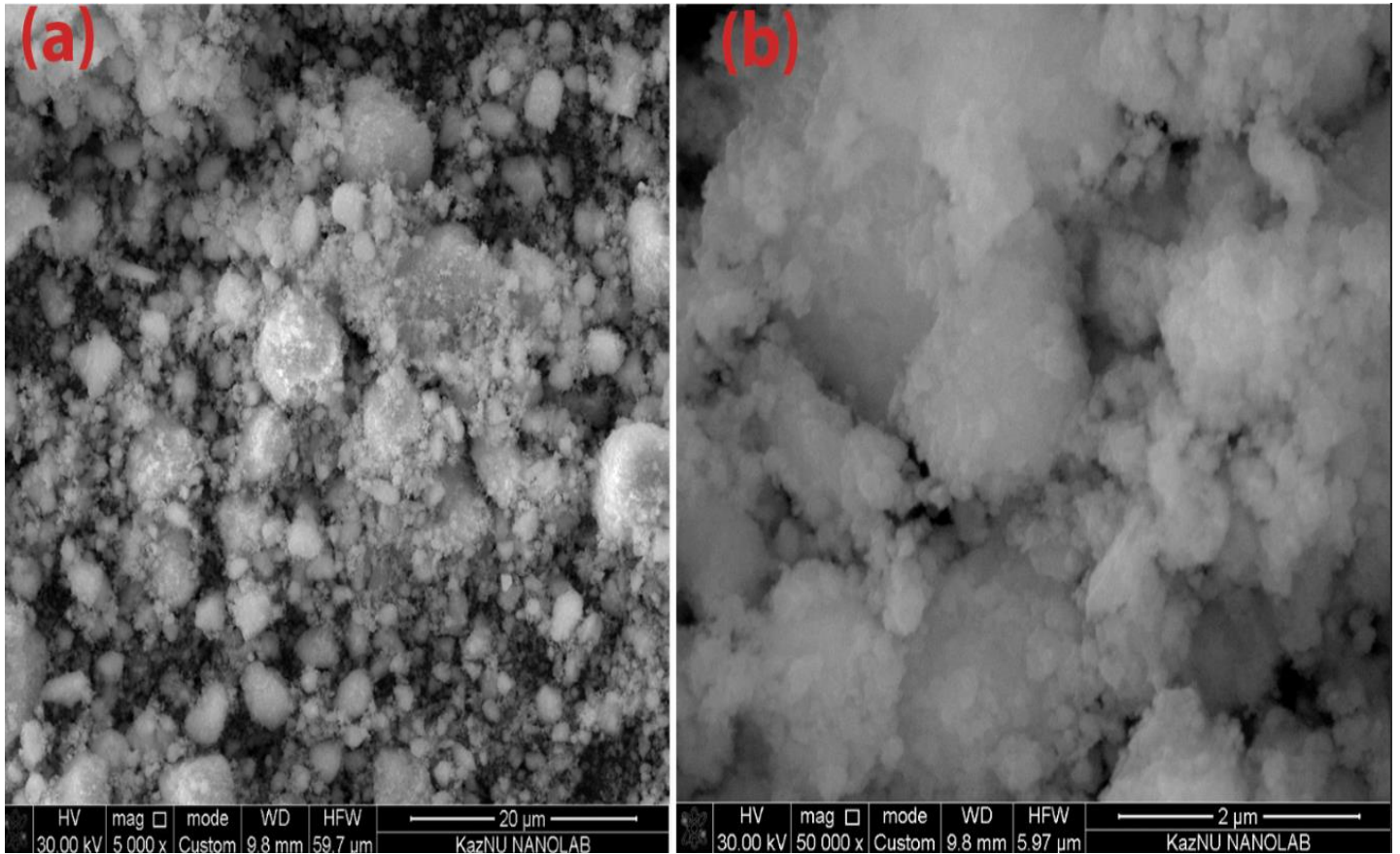


Figure 46 – SEM images of spinel ferrite on the scale bar of (a) 20 μm and (b) 2 μm

Table 21 – EDX element composition of spinel ferrites and hexagonal ferrite

Element	C	Cl	O	S	Ba	Al	Fe	Ni	Zn
NSC ₁₁₋₆₅₀ (wt%)	3.50	0.17	18.92	0.01	-	0.39	54.01	12.79	10.21

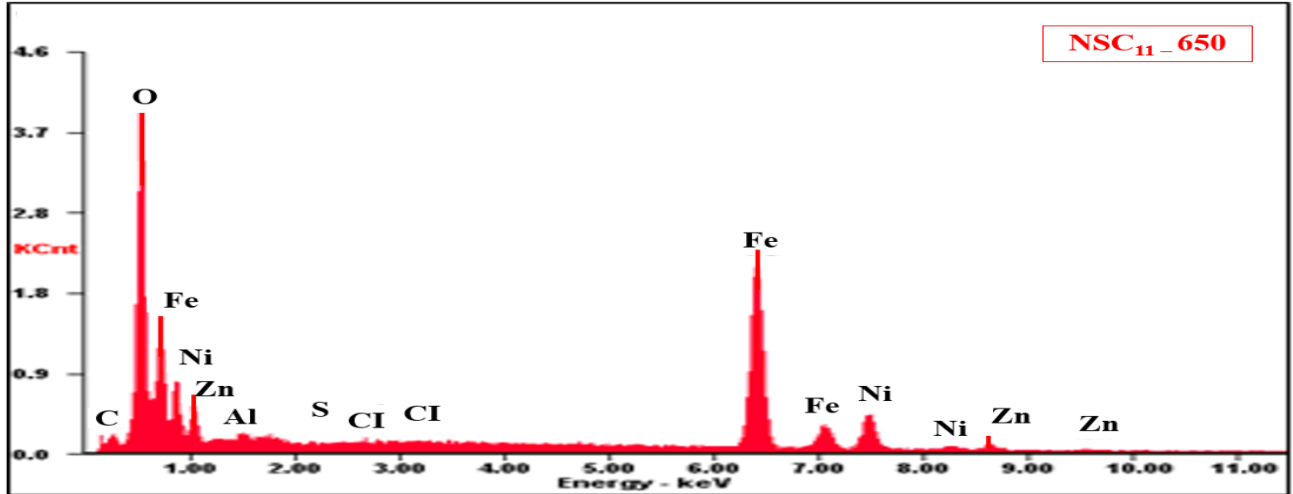


Figure 47 – EDX of spinel ferrite

3.3.5 Microwave absorption properties of ferrite samples prepared by the self-combustion technique

Several variables that affect MA properties were studied: PVA concentration, calcination temperature, absorber thickness and loading percentage of ferrite in the host matrix.

3.3.5.1 Microwave absorption properties of $\text{Ni}_{0.5}\text{Zn}_{0.5}\text{Fe}_2\text{O}_4$ nanoparticles

The effect of the different aqueous solutions of PVA (1%, 4%, and 6%) and calcination temperatures (650, 800, and 950°C) on the properties of $\text{Ni}_{0.5}\text{Zn}_{0.5}\text{Fe}_2\text{O}_4$ was studied. Samples were prepared with a thickness of 5 mm and a loading percentage of 65%. The results indicated that the RL attenuation peaks of samples shifted to lower frequencies with increasing PVA concentration and calcination temperature as shown in Figure 48. This may be due to the change in the crystallite size of the ferrite nanoparticles. The results of XRD patterns indicated that the crystallite size of nickel-zinc ferrite increased by increasing the calcination temperature and PVA concentration. The best result obtained was by using NSC₁₁–800 as shown in Figure 48 and Table 22.

3.3.5.1 Influence of sample thickness and loading percentage on the f_m

The influence of the different loading percentages (60, 65 and 70% w/w) and thicknesses (3, 5 and 6 mm) on NZ11 – 650 properties were investigated. Figure 49 shows that the RL moved gradually to a lower frequency with the increased loading percentage. Also, the same phenomenon was noticed by increasing the thickness of an absorber. These results may be defined by the quarter-wavelength ($\lambda/4$) cancellation model, as shown in equation (5) [44–46]. The results indicated a RL_{\min} of -12.9 dB at 10.0 GHz and absorption $\text{BW}_{-10\text{ dB}}$ of 0.7 GHz for 5 mm thickness for NSC₁₁–70%. The SE_{\max} was 14.4 dB at 8.8 GHz. From the above studies, we found the f_m position controllability of ferrite nanoparticles prepared with the self-combustion.

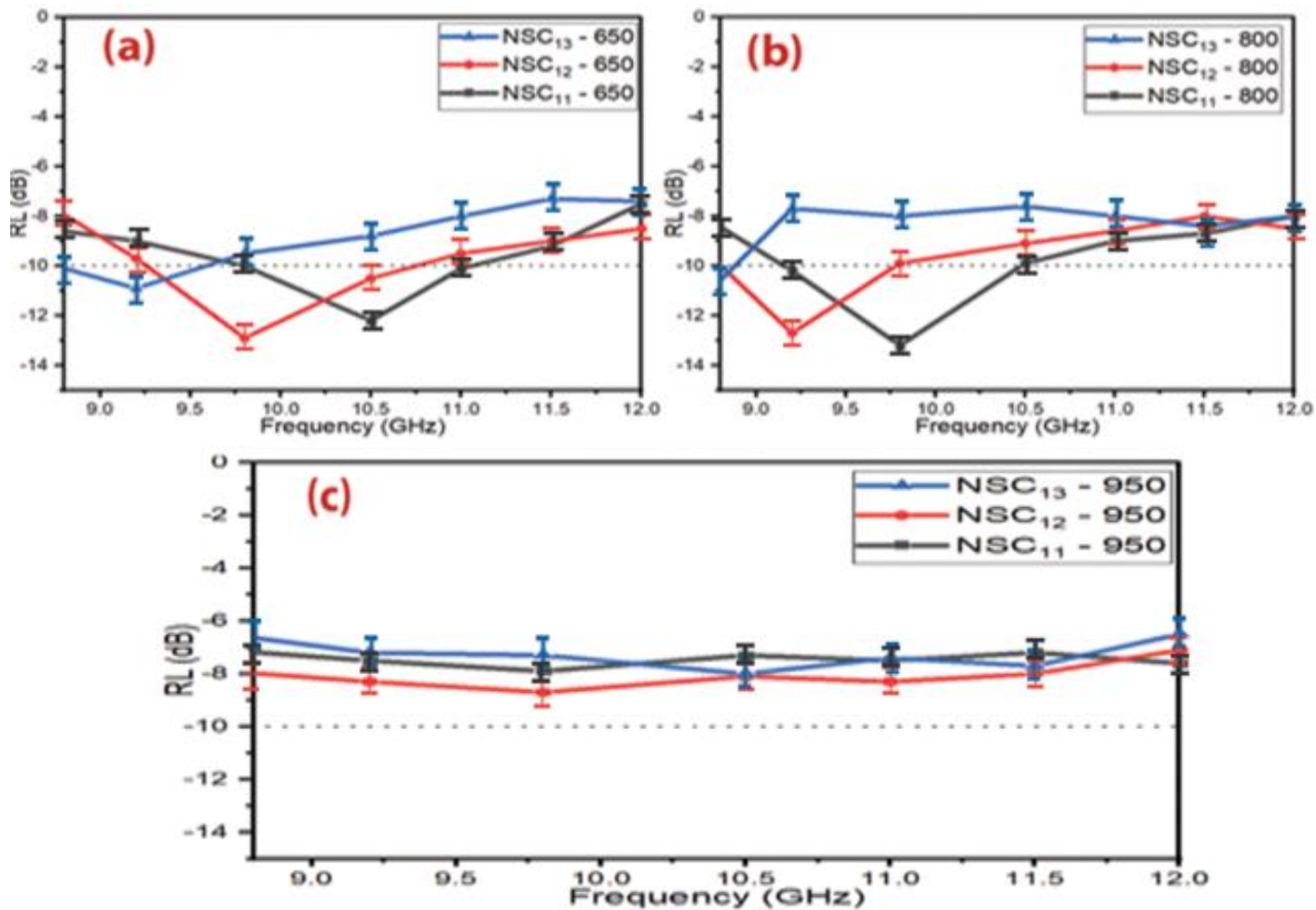


Figure 48 – RL curves of $\text{Ni}_{0.5}\text{Zn}_{0.5}\text{Fe}_2\text{O}_4$ nanoparticles at (a) 650 °C, (b) 800 °C and (c) 950 °C

Table 22 – MA behavior of $\text{Ni}_{0.5}\text{Zn}_{0.5}\text{Fe}_2\text{O}_4$ nanoparticles

Samples	T (°C)	RL _{min} (dB)	f _m (GHz)	BW _{-10 dB} (GHz)
NSC ₁₁ - 650	650	-12.2±0.7	10.5±0.3	1.3±0.1
NSC ₁₂ - 650		-12.9±0.9	9.8±0.1	1.5±0.3
NSC ₁₃ - 650		-10.9±0.6	9.2±0.1	0.8±0.1
NSC ₁₁ - 800	800	-13.2±0.8	9.7±0.1	1.2±0.2
NSC ₁₂ - 800		-12.7±0.7	9.3±0.2	1.0±0.1
NSC ₁₃ - 800		-11.3±0.8	8.8±0.1	0.2±0.1
NSC ₁₁ - 950	950	-7.9±0.8	9.5±0.1	0
NSC ₁₂ - 950		-8.0±0.6	11.0±0.3	0
NSC ₁₃ - 950		-8.1±0.7	10.5±0.2	0

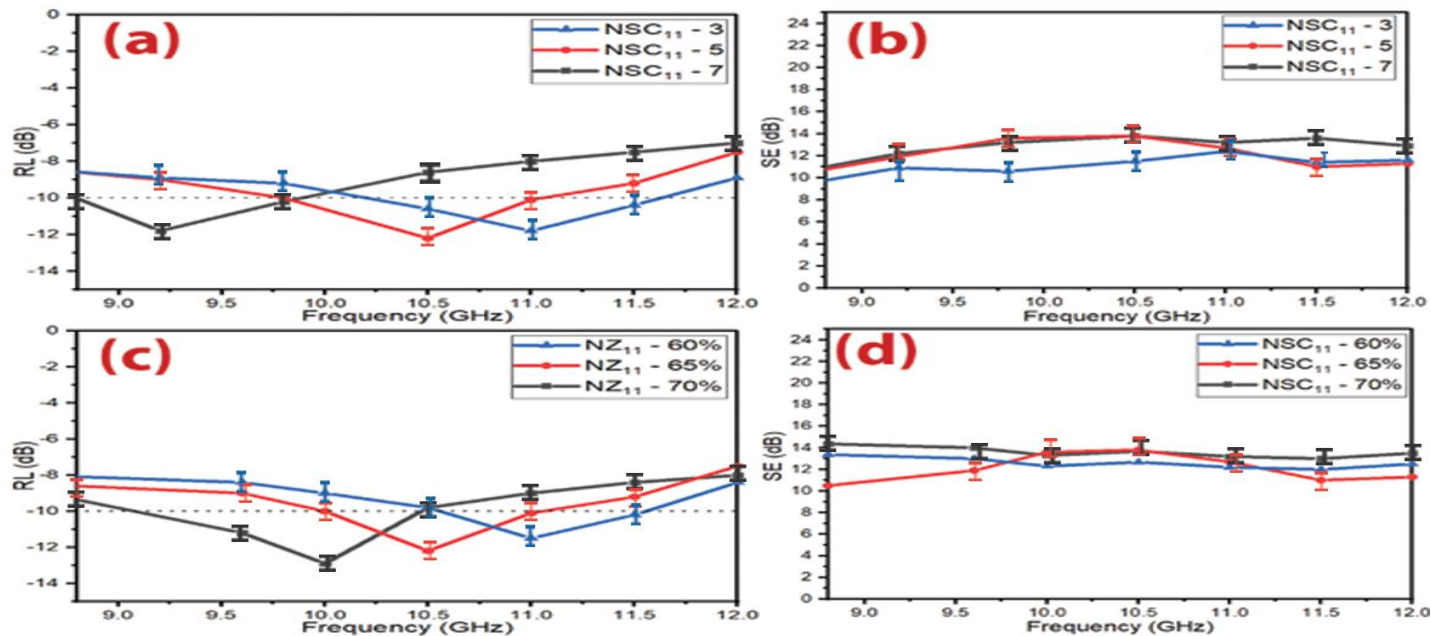


Figure 49 – (a,b) RL and SE curves of $\text{Ni}_{0.5}\text{Zn}_{0.5}\text{Fe}_2\text{O}_4$ nanoparticles at different thicknesses and (c,d) RL and SE curves of $\text{Ni}_{0.5}\text{Zn}_{0.5}\text{Fe}_2\text{O}_4$ nanoparticles with different loading percentages (60% w/w, 65% w/w and 70% w/w mm) at 5 mm thickness

From the above studies, One can notice that MA properties were changed with the variation of the synthesis method. The best result was obtained by using the $\text{Ni}_{0.5}\text{Zn}_{0.5}\text{Fe}_2\text{O}_4$ nanoparticles with a loading percentage of 60% at a constant calcination temperature of 650°C prepared by the citrate precursor method. However, the defects of these prepared absorbers are that they have a limited absorption $\text{BW}_{-10\text{ dB}}$ and high loading percentage. This necessitated working to decrease the loading percentage and increase the absorption $\text{BW}_{-10\text{ dB}}$ of the absorbers to cover most of the X-band frequency by incorporating magnetic loss and dielectric loss materials.

3.4 Results and discussion of microwave composites

3.4.1 X-ray diffraction of CB, AC, C and CI samples

Figure 50 shows the XRD patterns of carbon black, activated carbon, graphite and carbonyl iron. For the CB pattern, two diffraction peaks were detected at 2θ values of 22.88° and 43.22° . As well, for the AC pattern, two diffraction peaks were noticed at 2θ values of 22.85° and 43.19° , which conform to (hkl) planes of (002) and (100), respectively [98]. On the other hand, for the graphite pattern, five characteristic peaks were detected at 2θ values of 26.36° , 42.65° , 54.17° , 77.52° , and 82.94° , which conform to (hkl) planes of (002), (100), (004), (110) and (112), respectively. Finally, for the carbonyl iron pattern, three characteristic peaks were noticed at 2θ values of 44.61° , 64.26° and 82.33° , which conform to (hkl) planes of (100), (200), and (211), respectively. The XRD pattern of carbonyl iron resembles crystallites in which the sample

mainly contains the α -Fe phase [99]. All the observed peaks of CI were matched with the standard XRD pattern (JCPDS, PDF no. 06-0696).

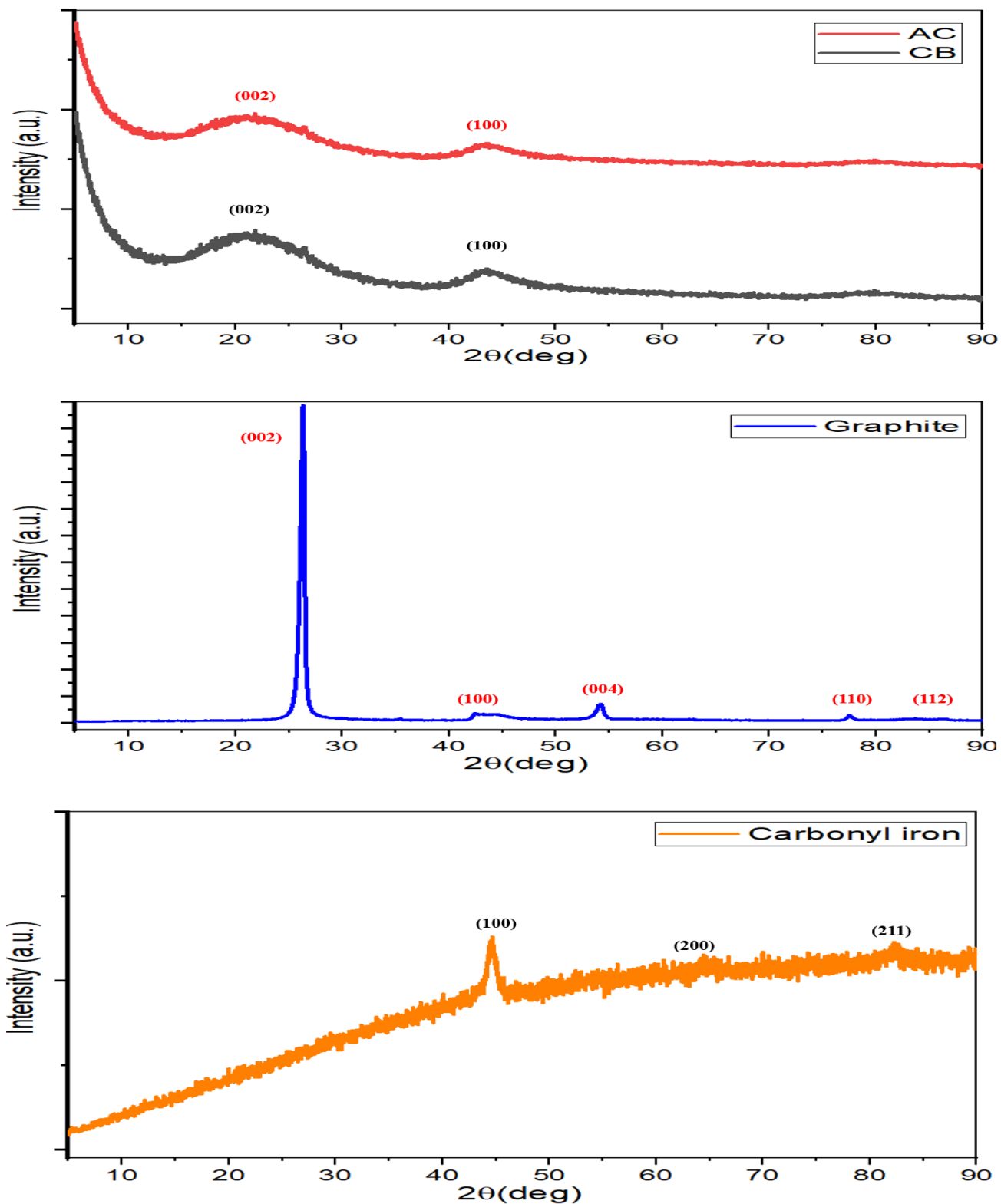


Figure 50 – XRD patterns of CB, AC, C and CI

3.4.2 FTIR spectra of CB, AC, C and CI samples

Figure 51 exhibits the FTIR spectra of CB, AC, C and CI. The peak at 1630.4 cm^{-1} was due to the stretching vibration of C=O, while the peaks at 2348 cm^{-1} and 3452 cm^{-1} were due to the stretching vibration of O-H [96,97].

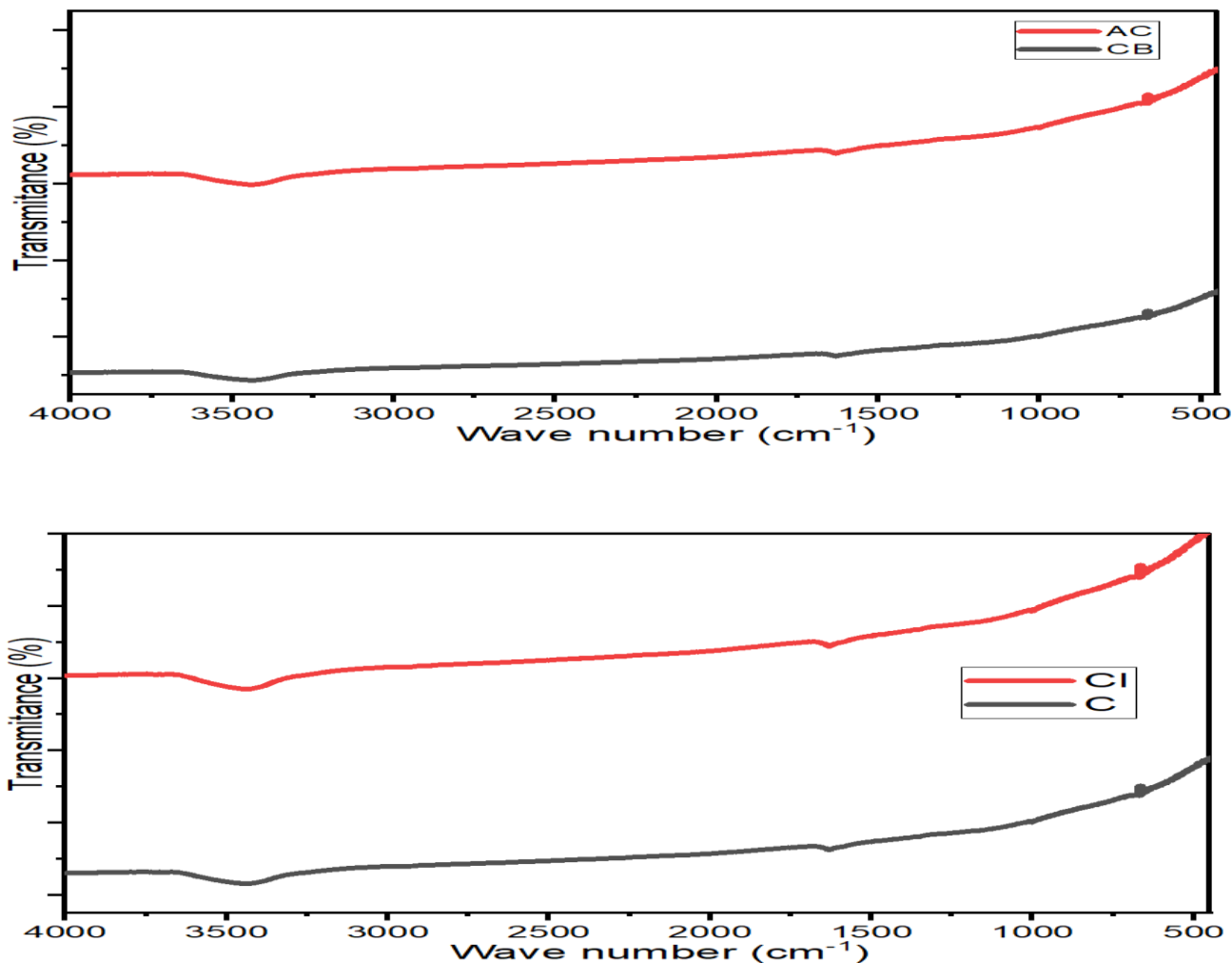


Figure 51 – FTIR spectra of CB and AC, C and CI

3.4.3 Microwave absorption properties of ferrite composites

Several variables that affect MA properties were studied, as follows: ferrite composite type, the weight ratio of CB/ $\text{Ni}_{0.5}\text{Zn}_{0.5}\text{Fe}_2\text{O}_4$, CB/ $\text{Mn}_{0.1}\text{Ni}_{0.5}\text{Zn}_{0.4}\text{Fe}_2\text{O}_4$, C/ $\text{Ni}^{3+}_{0.25}\text{Ni}^{2+}_{0.375}\text{Zn}^{2+}_{0.25}\text{Fe}_2\text{O}_4$ and $\text{Ni}_{0.5}\text{Zn}_{0.5}\text{Fe}_2\text{O}_4$ /CI/CB, and loading percentage.

3.4.3.1 Microwave absorption properties of carbon black/NiZn ferrite composites

MA properties of CB/ $\text{Ni}_{0.5}\text{Zn}_{0.5}\text{Fe}_2\text{O}_4$ composites were studied at a loading percentage of 45% w/w with the different weight ratios of CB/ $\text{Ni}_{0.5}\text{Zn}_{0.5}\text{Fe}_2\text{O}_4$ (1:1, 2:1, and 3:1). Figure 52

displays the RL of the prepared samples with different thicknesses (2–4–6 mm). The results show that the RL attenuation peaks of samples moved to lower frequencies with increasing sample thickness. This phenomenon may be defined by the quarter-wavelength ($\lambda/4$) cancellation model, as shown in equation (5). The results demonstrated that the absorber of 3.2 GHz bandwidth had a RL_{\min} of -18.2 dB at the f_m of 9.9 GHz with a thickness of 6 mm for CB/F-21. The defect of the $Ni_{0.5}Zn_{0.5}Fe_2O_4$ that it has a low ϵ'' . This low ϵ'' of $Ni_{0.5}Zn_{0.5}Fe_2O_4$ can be attributed to the non-dielectric properties of ferrite, therefore the EM wave absorption capability largely results from the magnetic loss (natural resonance and exchange resonance are the main factors for the loss of the magnetic field energy [91]). On the other hand, the defect of the CB is that it has low μ'' . This low μ'' of CB can be attributed to the non-magnetism properties of CB, therefore the EM wave absorption capability largely results from the dielectric loss [100]. This is explained by the increase of the imaginary part of the permittivity explained by the conductive nature of CB. The results revealed the impact of incorporating $Ni_{0.5}Zn_{0.5}Fe_2O_4$ (magnetic loss material) and CB (dielectric loss material) on the SD, RL_{\min} and $BW_{-10\text{ dB}}$ of the prepared absorber. The same result is observed for other prepared ferrite composites (CB/ $Mn_{0.1}Ni_{0.5}Zn_{0.4}Fe_2O_4$, C/ $Ni^{3+}_{0.25}Ni^{2+}_{0.375}Zn^{2+}_{0.25}Fe_2O_4$, and $Ni_{0.5}Zn_{0.5}Fe_2O_4/CI/CB$). Table 23 shows the MA behavior of CB/ $Ni_{0.5}Zn_{0.5}Fe_2O_4$ composites and pure CB powder at different thicknesses (2–4–6 mm).

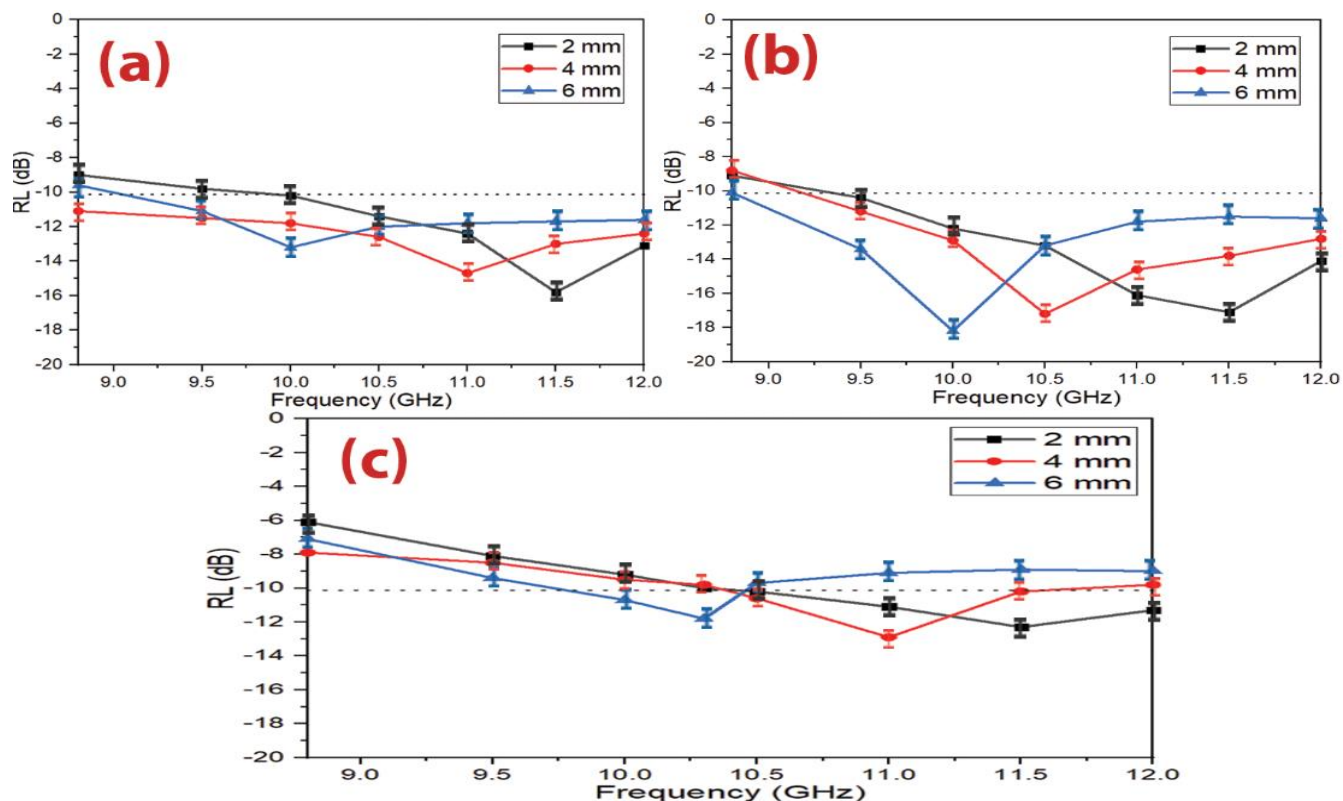


Figure 52 – RL curves of (a) CB/F-11 composite, (b) CB/F-21 composite and (c) CB/F-31 composite at different thicknesses (2–4–6 mm)

Table 23 – MA behavior of CB/Ni_{0.5}Zn_{0.5}Fe₂O₄ composites and pure CB powder at different thicknesses (2–4–6 mm)

Composite samples	t (mm)	RL _{min} (dB)	f _m (GHz)	BW _{-10 dB} (GHz)	SD (kg/m ²)
CB	2.0	-11.6±0.6	10.9±0.1	0.7±0.1	2.91±0.09
	4.0	-12.5±0.7	10.4±0.2	0.8±0.2	2.92±0.06
	6.0	-11.3±0.8	9.8±0.1	0.3±0.1	2.94±0.08
CB/F-11	2.0	-15.8±0.9	11.6±0.3	2.1±0.2	3.72±0.06
	4.0	-14.7±0.8	10.9±0.2	3.2±0.1	3.74±0.04
	6.0	-13.2±0.8	10.2±0.2	2.8±0.1	3.75±0.06
CB/F-21	2.0	-17.1±0.7	11.4±0.2	2.6±0.1	3.49±0.07
	4.0	-17.2±0.7	10.5±0.3	2.8±0.1	3.50±0.04
	6.0	-18.2±0.7	9.9±0.1	3.2±0.4	3.52±0.06
CB/F-31	2.0	-11.9±0.8	11.6±0.1	1.6±0.1	3.18±0.04
	4.0	-11.8±0.7	11.1±0.3	1.8±0.1	3.20±0.06
	6.0	-11.2±0.8	10.3±0.2	2.3±0.3	3.21±0.08

3.4.3.2 Microwave absorption properties of carbon black/MnNiZn ferrite composites

EMI shielding and MA properties of CB/Mn_{0.1}Ni_{0.5}Zn_{0.4}Fe₂O₄ composites were studied at a constant loading percentage of 40% w/w with the different weight ratios of CB/Mn_{0.1}Ni_{0.5}Zn_{0.4}Fe₂O₄ (1:1, 2:1, and 3:1). Figure 53 illustrates the RL of the prepared samples with different thicknesses (2–4–6 mm). The results demonstrated the RL attenuation peaks of samples moved to lower frequencies with increasing sample thickness. Table 24 shows the results of all the prepared absorbers. The best result obtained at this stage was by using CB/MF-21 composite.

From the above studies, One can notice that the RL_{min} and BW_{-10 dB} were changed with the variation of the ferrite type used with carbon black. The best result was obtained by using the CB/Mn_{0.1}Ni_{0.5}Zn_{0.4}Fe₂O₄ composite (1:1) with a thickness of 2 mm. This improvement is due to the fact that these processes will affect the MA capacity by changing the complex permeability and permittivity.

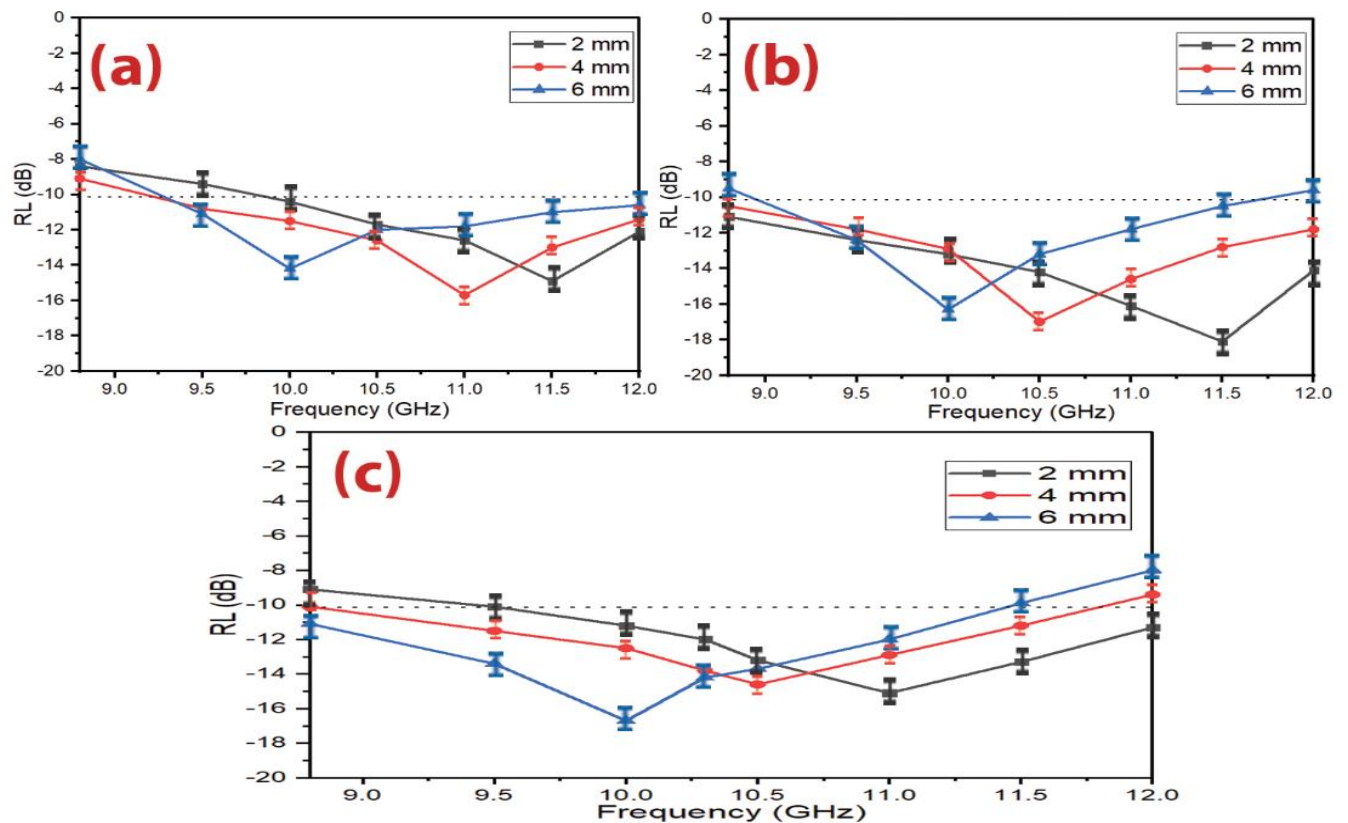


Figure 53 – RL curves of (a) CB/MF-11 composite, (b) CB/MF-21 composite, and (c) CB/MF-31 composite at various thicknesses (2–4–6 mm)

3.4.3.1 Microwave absorption properties of graphite/NiZn ferrite composites

EMI shielding and MA properties of $C/Ni^{3+}_{0.25}Ni^{2+}_{0.375}Zn^{2+}_{0.25}Fe_2O_4$ composites were studied at a constant loading percentage of 45% w/w with the different weight ratios of $C/Ni^{3+}_{0.25}Ni^{2+}_{0.375}Zn^{2+}_{0.25}Fe_2O_4$ (1:1, 2:1, and 3:1). Figure 54 displays the RL of the prepared samples with different thicknesses (2–4–6 mm). The results demonstrated the RL attenuation peaks of samples moved to lower frequencies with increasing sample thickness. Table 25 and Figure 55 show the results of all the prepared absorbers. The defect of the $Ni^{3+}_{0.25}Ni^{2+}_{0.375}Zn^{2+}_{0.25}Fe_2O_4$ that it has a low ϵ'' . This low ϵ'' of $Ni^{3+}_{0.25}Ni^{2+}_{0.375}Zn^{2+}_{0.25}Fe_2O_4$ can be attributed to the non-dielectric properties of ferrite, therefore the EM wave absorption capability largely results from the magnetic loss (natural resonance and exchange resonance are the main factors for the loss of the magnetic field energy [91]). On the other hand, the defect of the C is that it has low μ'' . This low μ'' of C can be attributed to the non-magnetism properties of C, therefore the EM wave absorption capability largely results from the dielectric loss [100]. This is explained by the increase of the imaginary part of the permittivity explained by the conductive nature of C. The results revealed the impact of incorporating $Ni^{3+}_{0.25}Ni^{2+}_{0.375}Zn^{2+}_{0.25}Fe_2O_4$ and C on the SD, RL_{min} , SE_{max} , and $BW_{-10\text{ dB}}$ of the prepared absorber. The best result obtained at this stage was by using the C/F-31 composite.

Table 24 – MA behavior of CB/Mn_{0.1}Ni_{0.5}Zn_{0.4}Fe₂O₄ composites at various thicknesses (2–4–6 mm)

Composite samples	t (mm)	RL _{min} (dB)	f _m (GHz)	BW _{-10 dB} (GHz)	SD (kg/m ²)
CB	2.0	-11.6±0.7	10.9±0.2	0.7±0.1	2.91±0.05
	4.0	-12.5±0.6	10.4±0.1	0.8±0.1	2.92±0.08
	6.0	-11.3±0.5	9.8±0.1	0.3±0.1	2.94±0.06
CB/MF-11	2.0	-14.7±0.9	11.5±0.2	2.0±0.3	3.63±0.05
	4.0	-15.8±0.7	11.0±0.2	3.2±0.3	3.65±0.07
	6.0	-13.9±0.7	10.1±0.1	2.9±0.1	3.66±0.05
CB/MF-21	2.0	-18.3±0.8	11.4±0.2	3.2±0.1	3.40±0.06
	4.0	-17.2±0.7	10.5±0.2	3.2±0.2	3.41±0.04
	6.0	-17.1±0.8	10.0±0.1	2.8±0.2	3.43±0.06
CB/MF-31	2.0	-15.1±0.8	11.0±0.1	2.5±0.1	3.09±0.04
	4.0	-14.6±0.7	10.6±0.2	2.9±0.1	3.11±0.06
	6.0	-16.7±0.8	9.9±0.1	2.6±0.2	3.12±0.07

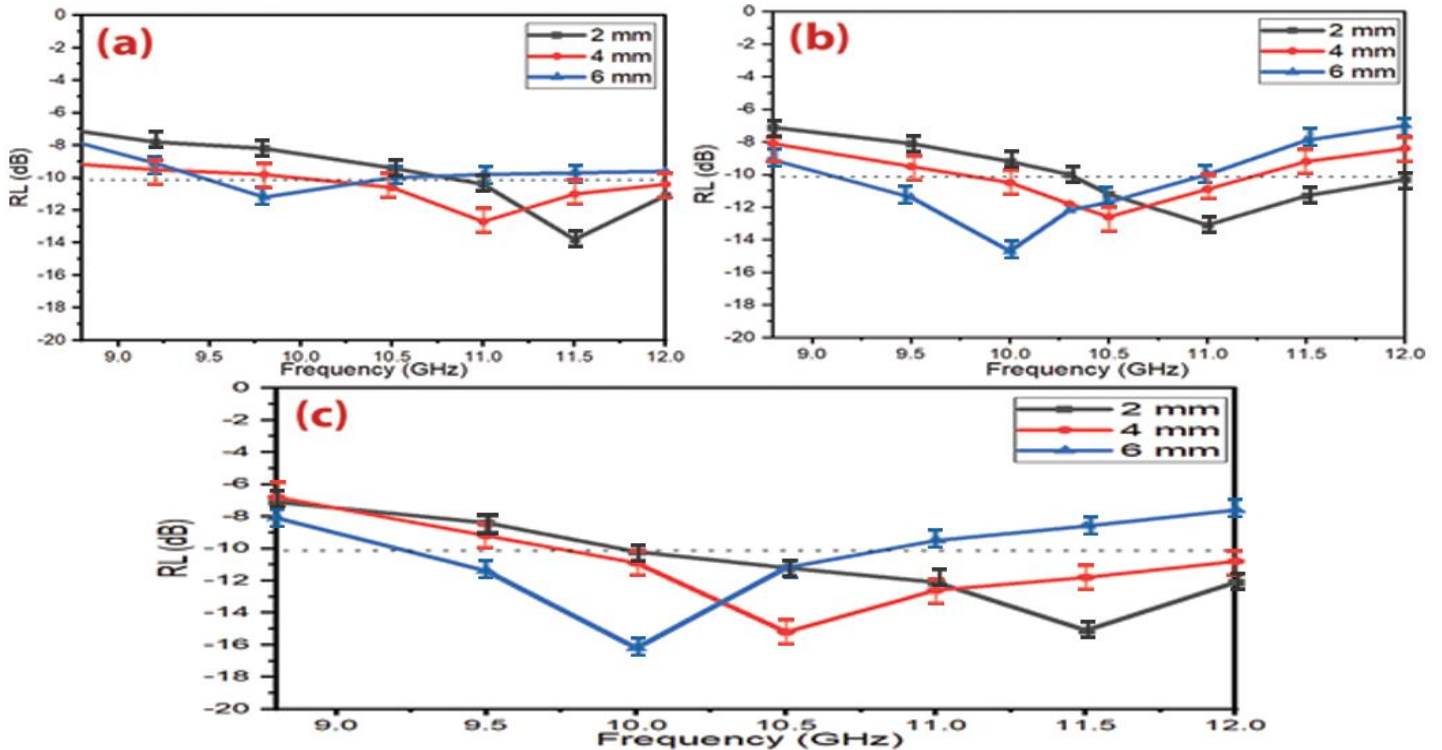


Figure 54 – RL curves of (a) C/F-11 composite, (c) C/F-21 composite, and (d) C/F-31 composite at various thicknesses (2–4–6 mm)

Table 25 – MA behavior of $C/Ni^{3+}_{0.25}Ni^{2+}_{0.375}Zn^{2+}_{0.25}Fe_2O_4$ composites at different thicknesses (2–4–6 mm)

Composite samples	t (mm)	RL _{min} (dB)	f _m (GHz)	BW _{-10 dB} (GHz)	SD (kg/m ²)
C/F-11	2.0	-13.8±0.7	11.5±0.3	1.1±0.2	3.71±0.04
	4.0	-12.7±0.7	11.0±0.3	1.8±0.3	3.73±0.08
	6.0	-11.2±0.6	9.8±0.2	1.3±0.2	3.74±0.05
C/F-21	2.0	-13.1±0.9	11.0±0.3	1.9±0.1	3.51±0.08
	4.0	-12.7±0.7	10.6±0.1	1.6±0.1	3.52±0.04
	6.0	-14.8±0.6	10.1±0.2	2.2±0.2	3.54±0.05
C/F-31	2.0	-15.1±0.7	11.5±0.1	1.6±0.1	3.17±0.04
	4.0	-15.2±0.8	10.5±0.1	2.3±0.2	3.19±0.08
	6.0	-16.2±0.9	10.0±0.1	2.0±0.1	3.21±0.05

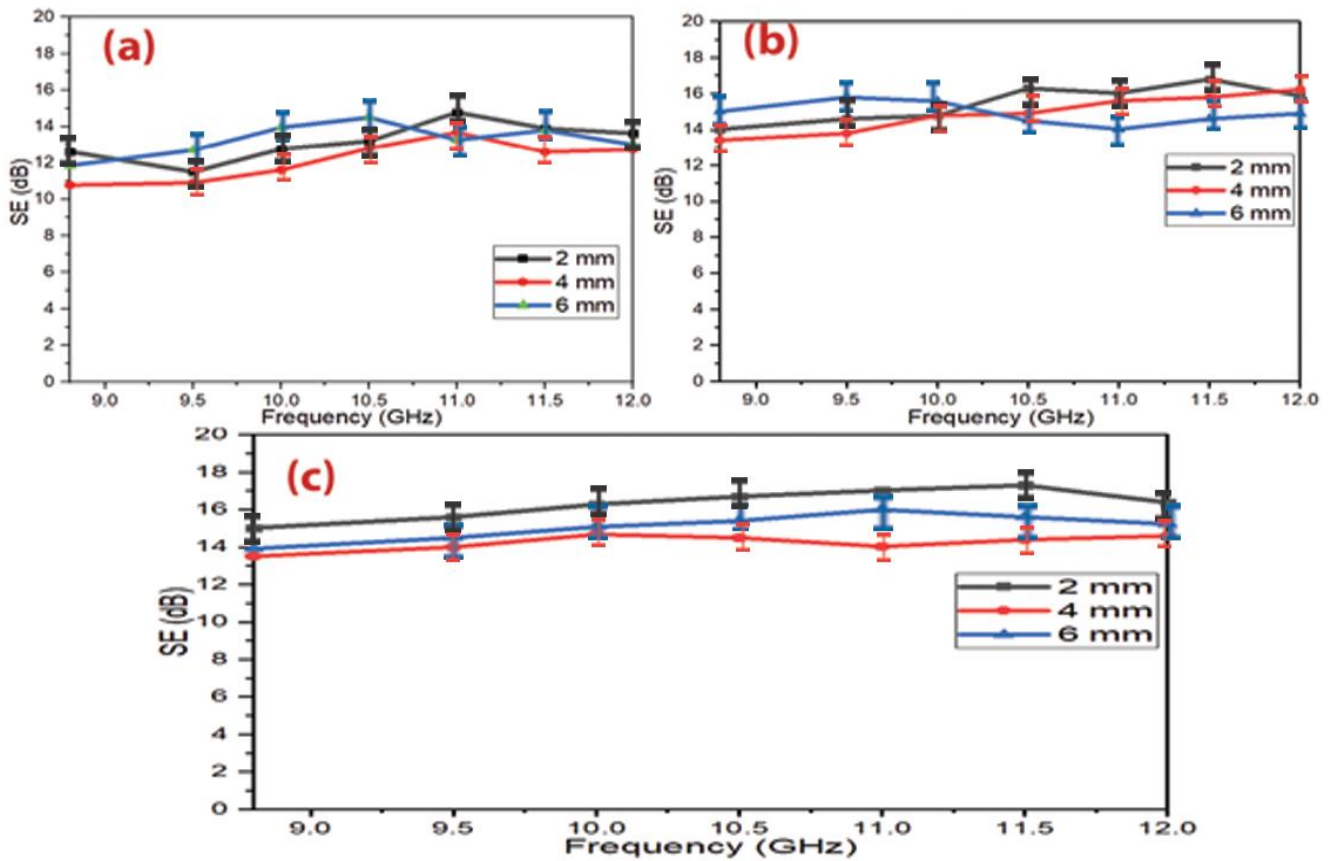


Figure 55 – SE curves of (a) C/F-11 composite, (b) C/F-21 composite, and (c) C/F-31 composite at various thicknesses (2–4–6 mm)

3.4.3.2 Microwave absorption properties of carbonyl iron/NiZn ferrite composites

EMI shielding and MA properties of CI/Ni_{0.5}Zn_{0.5}Fe₂O₄ composites were investigated at a loading percentage of 45% w/w with the different weight ratios of C/Ni³⁺_{0.25}Ni²⁺_{0.375}Zn²⁺_{0.25}Fe₂O₄ (1:1, 2:1, and 3:1). Figure 56 displays the RL of the prepared samples with different thicknesses (2–4–6 mm). The results demonstrated the RL attenuation peaks of samples moved to lower frequencies with increasing sample thickness. Table 26 and Figure 57 represent the results of all the prepared absorbers. The results indicated a RL_{min} of -16.1 dB at 9.8 GHz for a thickness of 6 mm for the CI/F-21 composite sample. The SE_{max} was 16.5 dB at 11.2 GHz for the CI/F-21 composite sample. The results revealed the impact of incorporating Ni_{0.5}Zn_{0.5}Fe₂O₄ (magnetic loss material) and CI (magnetic loss material) on the SD, RL_{min}, SE_{max}, and BW_{-10 dB} of the prepared absorber. The defects of these absorbers are that they have a limited absorption BW_{-10 dB}. This is due to the fact that the absorbers have a high complex relative permeability and low complex relative permittivity. This necessitated working to add CB to NiZn ferrite/carbonyl iron to increase the absorption BW_{-10 dB} to cover most of the X-band frequency and low the SD.

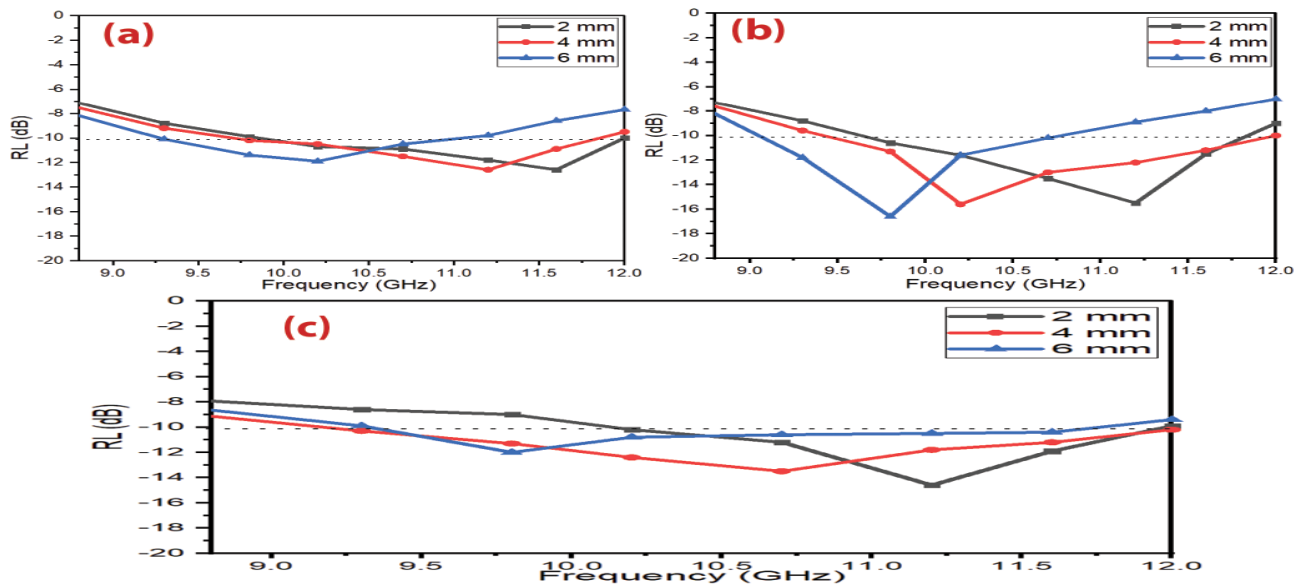


Figure 56 – RL curves of (a) CI/F-11 composite, (b) CI/F-21 composite and (c) CI/F-31 composite at different thicknesses (2–4–6 mm)

3.4.3.3 Microwave absorption properties of ternary composites of NiZn ferrite/carbonyl iron/carbon black

MA properties of Ni_{0.5}Zn_{0.5}Fe₂O₄/CI/CB composites were investigated at a loading percentage of 40% w/w with the different weight ratios of Ni_{0.5}Zn_{0.5}Fe₂O₄/CI/CB (1:1:1, 1:1:2, and 2:1:1). Figure 58 displays the RL of the prepared samples with different thicknesses (2–4–6 mm). The results demonstrated the RL attenuation peaks of samples moved to lower

frequencies with increasing sample thickness. Table 27 and Figure 58 represent the results of all the prepared absorbers. The defect of the $\text{Ni}_{0.5}\text{Zn}_{0.5}\text{Fe}_2\text{O}_4$ and CI that they have low ϵ'' . This low ϵ'' of $\text{Ni}_{0.5}\text{Zn}_{0.5}\text{Fe}_2\text{O}_4$ and CI can be attributed to the non-dielectric properties of $\text{Ni}_{0.5}\text{Zn}_{0.5}\text{Fe}_2\text{O}_4$ and CI, therefore the EM wave absorption capability largely results from the magnetic loss (natural resonance and exchange resonance are the main factors for the loss of the magnetic field energy [91]). On the other hand, the defect of the CB is that it has low μ'' . This low μ'' of CB can be attributed to the non-magnetism properties of CB, therefore the EM wave absorption capability largely results from the dielectric loss [100]. This is explained by the increase of the imaginary part of the permittivity explained by the conductive nature of CB. The results reveal that the incorporation of these three components with their different loss mechanisms has a synergistic effect that enhances the attenuation properties of the final composite. This incorporation leads to obtaining a wider $\text{BW}_{-10\text{ dB}}$, lower SD absorber, and loading percentage compared to the $\text{Ni}_{0.5}\text{Zn}_{0.5}\text{Fe}_2\text{O}_4/\text{CI}$ absorber. The best result was obtained by using the F/CI/CB-211 composite sample. In order to evaluate the beneficial impact of adding CB to the F/CI on the microwave properties, Table 28 shows a comparison of the radar absorption properties of some lately reported carbon-based materials. The results of the literature show these composites are good in the C-band and Ku-band frequencies and limited in the X-band frequency. The presently prepared composites display in this research better MA in the X-band frequency. The distinct of these prepared composites have a lower loading percentage and thickness of the absorbers compared with the other literature. As a result, one can notice by tuning the different parameters of the fabrication and properly combining magnetic loss and dielectric loss components, a lightweight microwave absorber can be obtained with broad absorption bandwidth at the range of 8.8–12.0 GHz. These prepared composites are promising candidates for applications such as EMI shielding and stealth technology.

Table 26 – MA behavior of $\text{CI}/\text{Ni}_{0.5}\text{Zn}_{0.5}\text{Fe}_2\text{O}_4$ composites at different thicknesses (2–4–6 mm)

Composite samples	t (mm)	RL_{\min} (dB)	f_m (GHz)	$\text{BW}_{-10\text{ dB}}$ (GHz)	SD (kg/m^2)
CI/F-11	2.0	-12.6 ± 0.6	11.6 ± 0.3	2.2 ± 0.1	4.52 ± 0.05
	4.0	-12.5 ± 0.7	11.2 ± 0.1	2.0 ± 0.2	4.54 ± 0.07
	6.0	-11.9 ± 0.8	10.2 ± 0.4	1.8 ± 0.1	4.55 ± 0.08
CI/F-21	2.0	-15.5 ± 0.7	11.2 ± 0.3	2.1 ± 0.3	4.76 ± 0.04
	4.0	-15.6 ± 0.7	10.2 ± 0.3	2.5 ± 0.2	4.77 ± 0.06
	6.0	-16.1 ± 0.8	9.8 ± 0.2	1.8 ± 0.1	4.79 ± 0.08
CI/F-31	2.0	-14.6 ± 0.7	11.2 ± 0.1	1.8 ± 0.3	4.91 ± 0.08
	4.0	-13.5 ± 0.9	10.7 ± 0.2	2.8 ± 0.1	4.92 ± 0.05
	6.0	-12.0 ± 0.7	9.8 ± 0.1	2.2 ± 0.4	4.94 ± 0.06

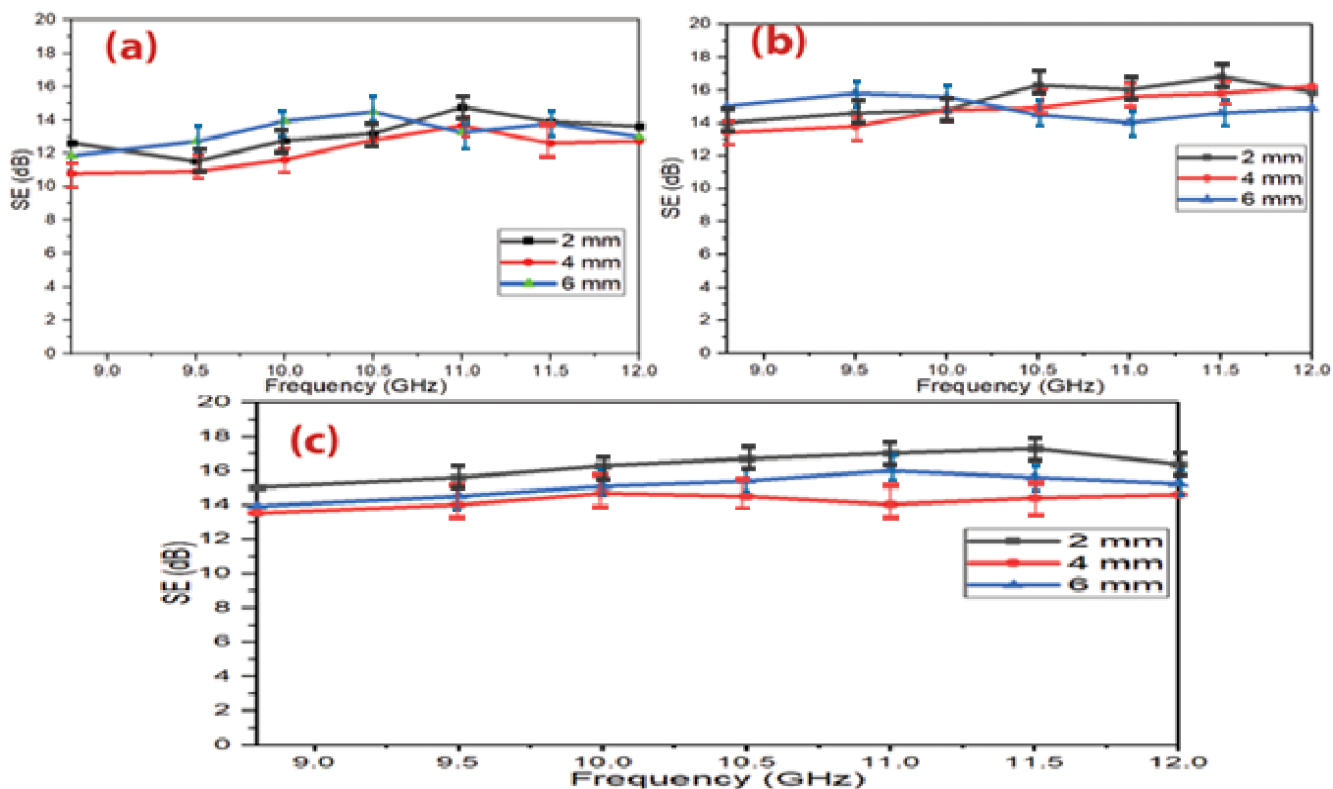


Figure 57 – SE curves of (a) CI/F-11 composite, (b) CI/F-21 composite and (c) CI/F-31 composite at different thicknesses (2–4–6 mm)

Table 27 – MA behavior of $\text{Ni}_{0.5}\text{Zn}_{0.5}\text{Fe}_2\text{O}_4/\text{CI}/\text{CB}$ composites at various thicknesses (2–4–6 mm)

Composite samples	t (mm)	RL_{\min} (dB)	f_m (GHz)	$\text{BW}_{-10 \text{ dB}}$ (GHz)
F/CI/CB-111	2.0	-18.3 ± 0.9	11.5 ± 0.2	3.2 ± 0.1
	4.0	-18.5 ± 0.7	10.3 ± 0.3	3.2 ± 0.1
	6.0	-19.4 ± 0.8	9.9 ± 0.1	3.2 ± 0.1
F/CI/CB-112	2.0	-17.3 ± 0.6	11.3 ± 0.3	3.2 ± 0.1
	4.0	-16.3 ± 0.8	10.4 ± 0.2	2.9 ± 0.1
	6.0	-15.5 ± 0.7	9.8 ± 0.2	2.8 ± 0.1
F/CI/CB-211	2.0	-18.4 ± 0.7	11.7 ± 0.1	3.2 ± 0.1
	4.0	-17.3 ± 0.8	10.9 ± 0.4	3.2 ± 0.1
	6.0	-15.8 ± 0.6	10.0 ± 0.3	3.2 ± 0.1

3.4.3.1 Microwave absorption properties of double-layer of AC/F

Microwave absorption characteristics were studied for double-layer activated carbon/paraffin wax (AC) and $\text{Mn}_{0.1}\text{Ni}_{0.5}\text{Zn}_{0.4}\text{Fe}_2\text{O}_4/\text{paraffin wax}$ (F) composites as shown in

Figure 59. The AC/F-21 (activated carbon as a matching layer with a thickness of 1 mm and activated carbon as an absorbing layer with a thickness of 2 mm) exhibited a minimal reflection loss of -21.4 dB at 10.35 GHz and the absorption $BW_{-10\text{ dB}}$ of 2.3 GHz. While the F/AC-12 (MnNiZn ferrite as a matching layer with a thickness of 1 mm and activated carbon as an absorbing layer with a thickness of 2 mm) exhibited a minimal reflection loss of -16.2 dB at 10.2 GHz and the absorption $BW_{-10\text{ dB}}$ of 1.9 GHz. The results showed the significant effects of the layer positions of the absorbers on their MA characteristics are systematically studied by adjusting the matching and absorbing layers.

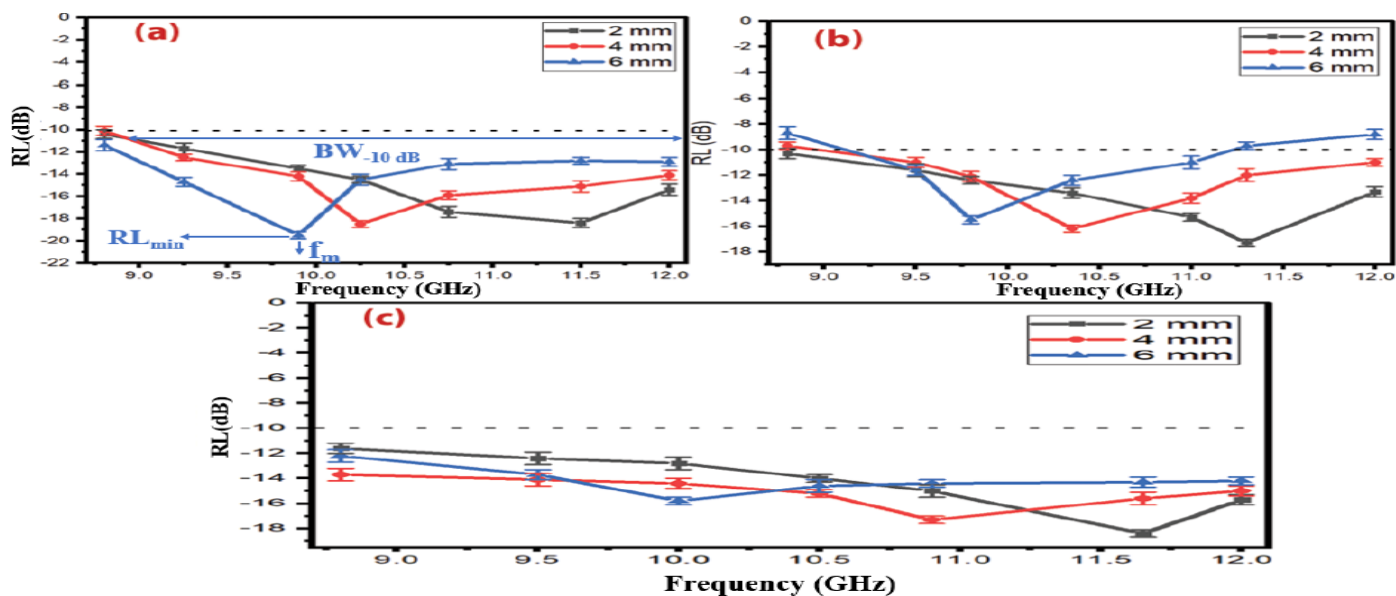


Figure 58 – RL curves of (a) F/CI/CB-111 composite, (b) F/CI/CB-112 composite and (c) F/CI/CB-211 composite at various thicknesses (2–4–6 mm)

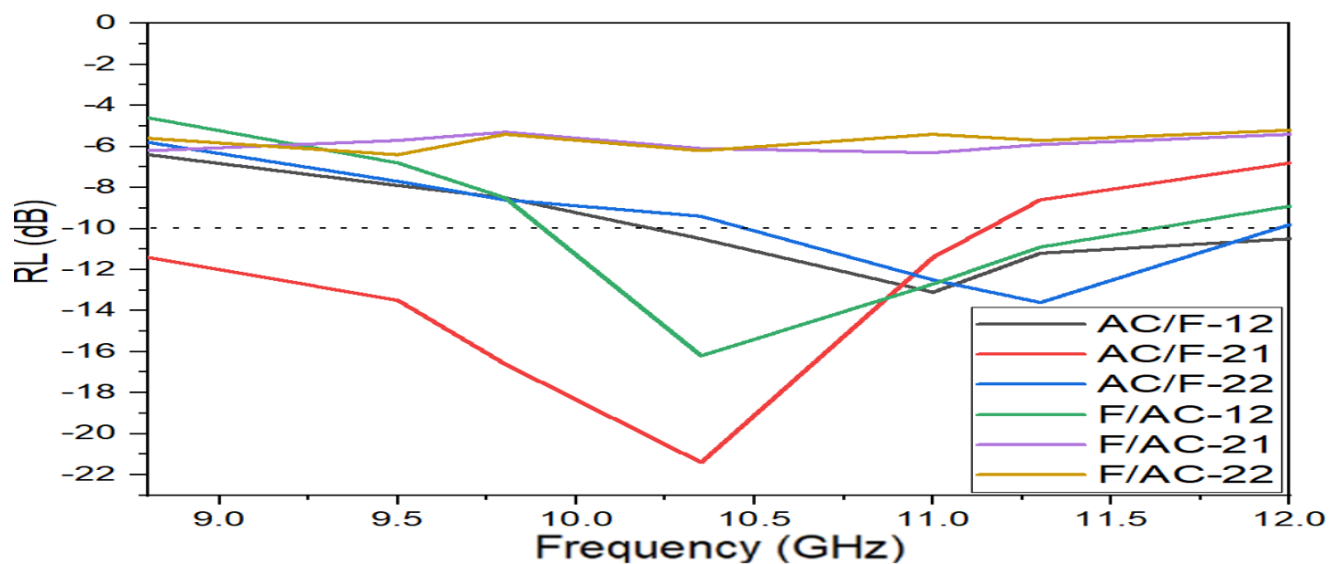


Figure 59 – RL curves of double-layer of AC/F composites

Table 28 – Radar absorption properties of carbon-based materials

Sample	t (mm)	f (GHz)	BW _{-10 dB} (GHz) _(C-band)	BW _{-10 dB} (GHz) _(X-band)	BW _{-10 dB} (GHz) _(Ku-band)	Ref
ZnFe ₂ O ₄ /rGO	2.5	9.3	1.6	1.0	0	[101]
NiFe ₂ O ₄ /rGO	1.9	14.5	0	1.4	3.8	[102]
CoFe ₂ O ₄ /rGO	1.6	14.7	0	0	4.5	[103]
MWCNT/Ni _{0.5} Zn _{0.5} Fe ₂ O ₄	2.0	10.4	0.08	0	0	[104]
CF/Fe ₃ O ₄ /BN	3.0	12.5	0	0.8	3.4	[105]
Ni/MWNT	4.0	7.2	2.2	1.2	0	[106]
Sm ₂ O ₃ /MWCNT	2.0	9.4	1.1	0.5	0	[107]
Fe/Fe ₃ C/MWCNT	2.0	9.0	1.6	0.8	0	[108]
	3.5	4.6	2.3	0	0	
Fe/CNTs	3.5	11.4	0	2.9	0	[109]
CoNC/CNTs	4.7	5.2	2.2	0	0	[110]
FeCo@CFs	1.6	16.6	0	3.5	0.9	[111]

Table 29 shows the radar absorption properties of double-layer activated carbon/paraffin wax (AC) and Mn_{0.1}Ni_{0.5}Zn_{0.4}Fe₂O₄/paraffin wax (F) composites. As a result, one can observe the effect of combining Mn_{0.1}Ni_{0.5}Zn_{0.4}Fe₂O₄ (magnetic loss material) and AC (dielectric loss material) on the EMI and MA properties of the prepared absorber. This incorporation leads to an effective and low-thickness absorber with a wide bandwidth. This is due to the fact that layer positions of the absorbers will affect the MA capacity by changing the complex permeability and permittivity.

Table 29 – Radar absorption properties of double-layer of AC/F composites

Sample symbols	t (mm)	RL _{min} (dB)	f _m (GHz)	BW _{-10 dB} (GHz)
AC/F-12	3.0	-13.1±0.6	11.0±0.1	1.9±0.1
AC/F-21	3.0	-21.4±0.5	10.3±0.2	2.3±0.2
AC/F-22	4.0	-13.6±0.5	11.2±0.1	1.4±0.1
F/AC12	3.0	-16.2±0.8	10.2±0.3	1.9±0.2
F/AC-21	3.0	-6.5±0.7	10.8±0.2	0
F/AC-22	4.0	-6.9±0.5	9.6±0.1	0

3.5 Results and discussion of the preparation of Hybrid composites

3.5.1 X-ray diffraction of PANI-based composites

Figure 60 displays the XRD patterns of the $\text{Ni}^{3+}_{0.25}\text{Ni}^{2+}_{0.375}\text{Zn}^{2+}_{0.25}\text{Fe}_2\text{O}_4$, PANI/F composites and PANI. The characteristic peaks of PANI/F hybrid composites matched the characteristic peaks of $\text{Ni}^{3+}_{0.25}\text{Ni}^{2+}_{0.375}\text{Zn}^{2+}_{0.25}\text{Fe}_2\text{O}_4$ core as mentioned above. This revealed when the $\text{Ni}^{3+}_{0.25}\text{Ni}^{2+}_{0.375}\text{Zn}^{2+}_{0.25}\text{Fe}_2\text{O}_4$ magnetic core was coated with PANI, the spinel structure of the $\text{Ni}^{3+}_{0.25}\text{Ni}^{2+}_{0.375}\text{Zn}^{2+}_{0.25}\text{Fe}_2\text{O}_4$ magnetic core remained intact. As shown in Figure 60, the XRD pattern of the pure PANI displayed an amorphous structure with two characteristic peaks at 20.22° and 25.36° , which were attributed to the periodicity parallel to the polymer chains of PANI [112,113]. The XRD patterns of the PANI/ $\text{Ni}^{3+}_{0.25}\text{Ni}^{2+}_{0.375}\text{Zn}^{2+}_{0.25}\text{Fe}_2\text{O}_4$ composites displayed crystalline peaks because of the existence of NiZn ferrite in these composites. The two characteristic peaks of the PANI disappeared due to the $\text{Ni}^{3+}_{0.25}\text{Ni}^{2+}_{0.375}\text{Zn}^{2+}_{0.25}\text{Fe}_2\text{O}_4$ particles [114,115].

The XRD patterns of $\text{Ni}_{0.5}\text{Zn}_{0.5}\text{Fe}_2\text{O}_4$, CI, PANI/CI and PANI/F/CI composite are shown in Figure 61. The characteristic peaks of the PANI/F/CI hybrid composite showed matching the characteristic peaks of $\text{Ni}_{0.5}\text{Zn}_{0.5}\text{Fe}_2\text{O}_4$ as cited above. The XRD patterns of the PANI/F/CI hybrid composite showed crystalline peaks because of the existence of NiZn ferrite in this composite.

Figure 62 displays the XRD patterns of the PANI/CB, PANI/90%F/10%CB, PANI/70%F/30%CB and PANI/50%F/50%CB hybrid composite. For the PANI/F/CB patterns, eight diffraction peaks were detected, which conform to (hkl) planes of (111), (220), (311), (222), (400), (422), (511) and (440), respectively. The characteristic peaks of PANI/F/CB composites matched the characteristic peaks of $\text{Ni}^{3+}_{0.25}\text{Ni}^{2+}_{0.375}\text{Zn}^{2+}_{0.25}\text{Fe}_2\text{O}_4$ as mentioned above. For PANI/CB pattern, two diffraction peaks were noticed, which conform to (hkl) planes of (002) and (100), respectively. The characteristic peaks of PANI/CB composites matched the characteristic peaks of carbon black, as cited above.

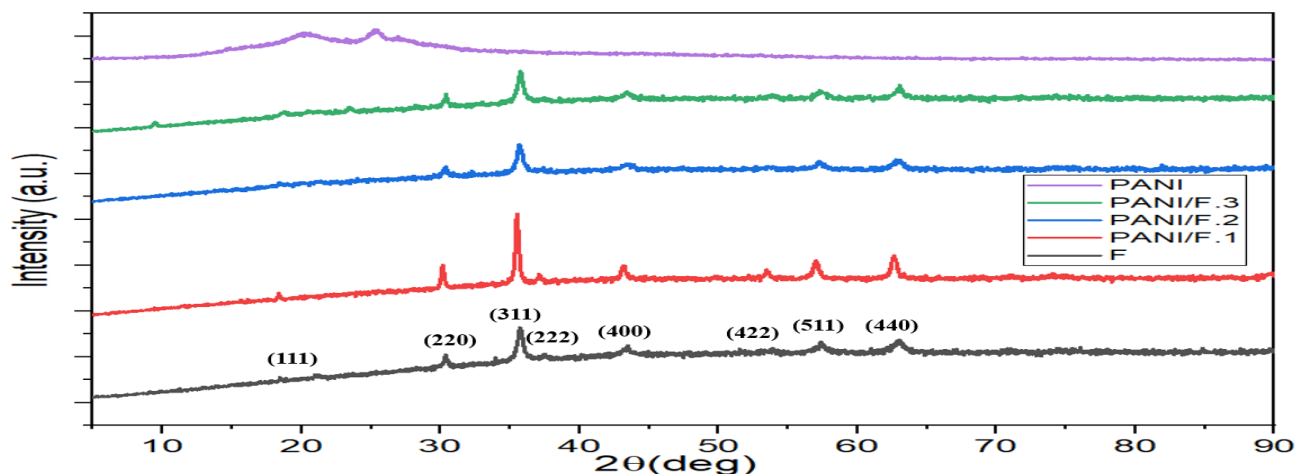


Figure 60 – XRD patterns of $\text{Ni}^{3+}_{0.25}\text{Ni}^{2+}_{0.375}\text{Zn}^{2+}_{0.25}\text{Fe}_2\text{O}_4$, PANI/ $\text{Ni}^{3+}_{0.25}\text{Ni}^{2+}_{0.375}\text{Zn}^{2+}_{0.25}\text{Fe}_2\text{O}_4$ composites and pure PANI

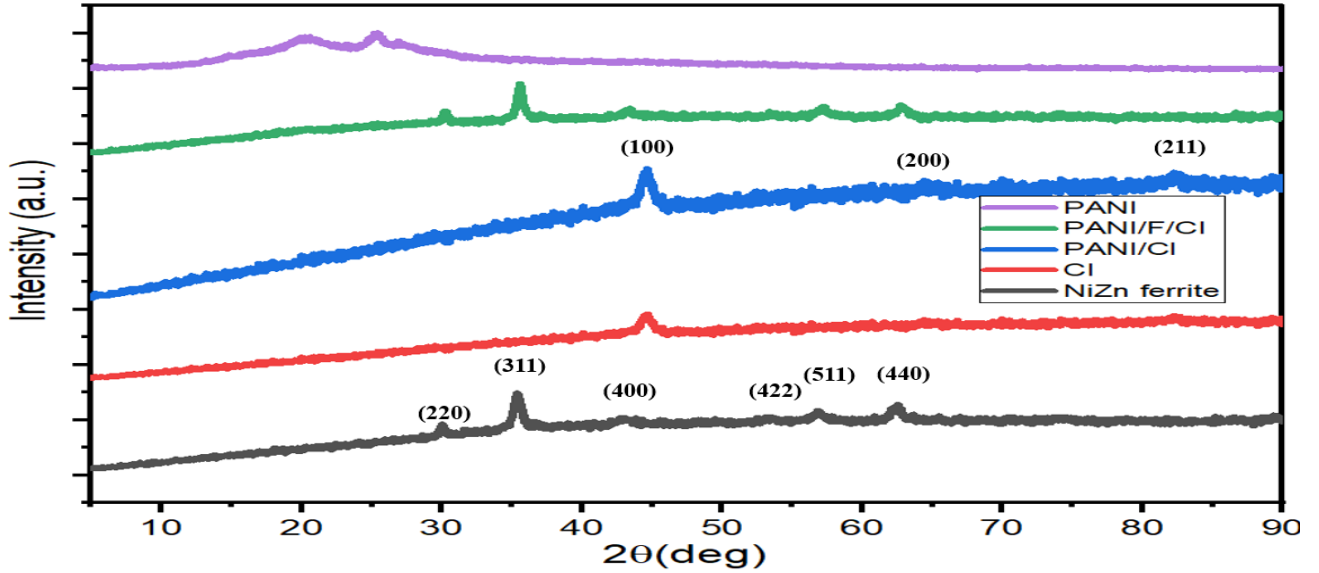


Figure 61 – XRD patterns of $\text{Ni}_{0.5}\text{Zn}_{0.5}\text{Fe}_2\text{O}_4$, CI, PANI/F/CI, PANI/F/CI composites and pure PANI

Figure 63 shows the XRD patterns of the HF and PANI/HF composites. The characteristic peaks of PANI/HF composites showed matching the characteristic peaks of the $\text{BaNiZnFe}_{16}\text{O}_{27}$ core as cited above. This was shown when the $\text{BaNiZnFe}_{16}\text{O}_{27}$ magnetic core was coated with PANI. The hexagonal structure of the $\text{BaNiZnFe}_{16}\text{O}_{27}$ magnetic core remained intact. The XRD patterns of the PANI/ $\text{BaNiZnFe}_{16}\text{O}_{27}$ composites displayed crystalline peaks because of the existence of $\text{BaNiZnFe}_{16}\text{O}_{27}$ in these composites. The XRD patterns of PANI/SF/HF and PANI/SF/HF/CB hybrid composite are shown in Figure 61. For the PANI/SF/HF and PANI/SF/HF/CB patterns, eleven diffraction peaks were detected, which conform to (110), (1010), (116), (0114), (107), (203), (208), (209), (2015), (2111) and (220), respectively.

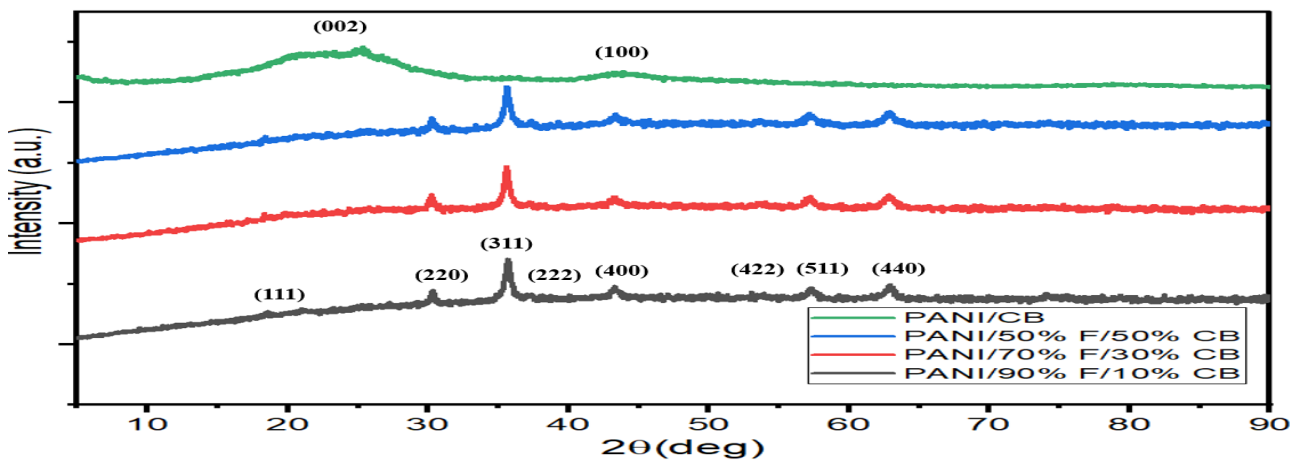


Figure 62 – XRD patterns of PANI/F/CB and PANI/CB hybrid composites

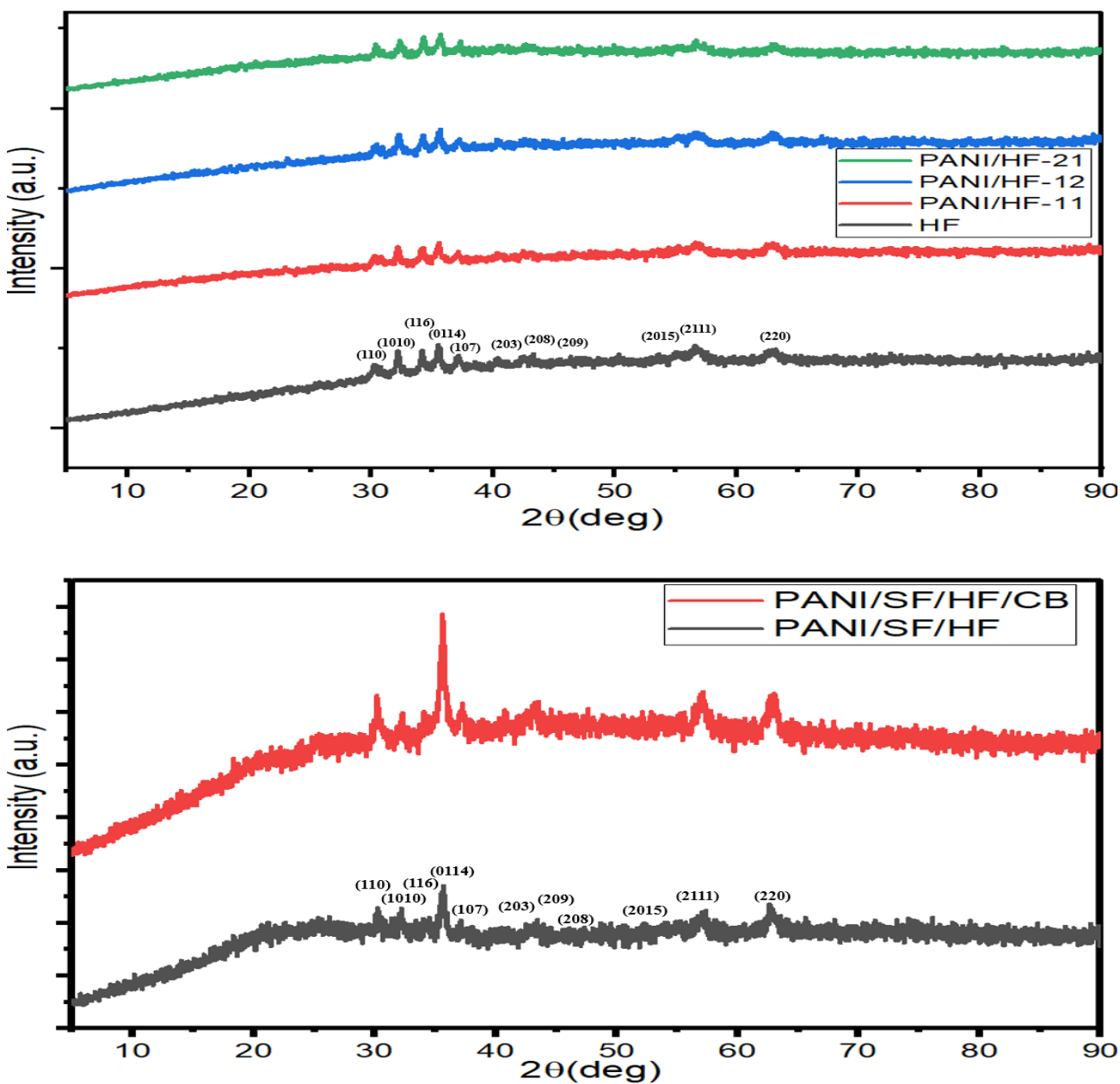


Figure 63 – XRD patterns of HF, PANI/HF, PANI/SF/HF and PANI/SF/HF/CB

3.5.2 FTIR spectra of PANI-based composites

Figure 64 exhibits the FTIR spectra of the PANI-based composites. The peaks within the range ($1568\text{--}1580\text{ cm}^{-1}$) and ($1475\text{--}1489\text{ cm}^{-1}$) were due to the C=N and C=C stretching modes of vibration for the quinonoid and benzenoid units of the polymer, while the peaks within the range ($1290\text{--}1298\text{ cm}^{-1}$) and ($1475\text{--}1489\text{ cm}^{-1}$) were due to N-H bending and asymmetric C-H stretching of the benzenoid ring, respectively [116,117]. Finally, the peaks within the range ($1113\text{--}1125\text{ cm}^{-1}$) and ($790\text{--}800\text{ cm}^{-1}$) were due to N-H bending and asymmetric C-H stretching of the benzenoid ring, respectively [65,114]. In addition, the characteristic peaks within the range ($563\text{--}585\text{ cm}^{-1}$) of the PANI-based composites matched the characteristic peak of ferrite,

as cited above. This indicates the stretching vibration of (Fe-O), which confirms the formation of the metal-oxygen in the PANI-based composites.

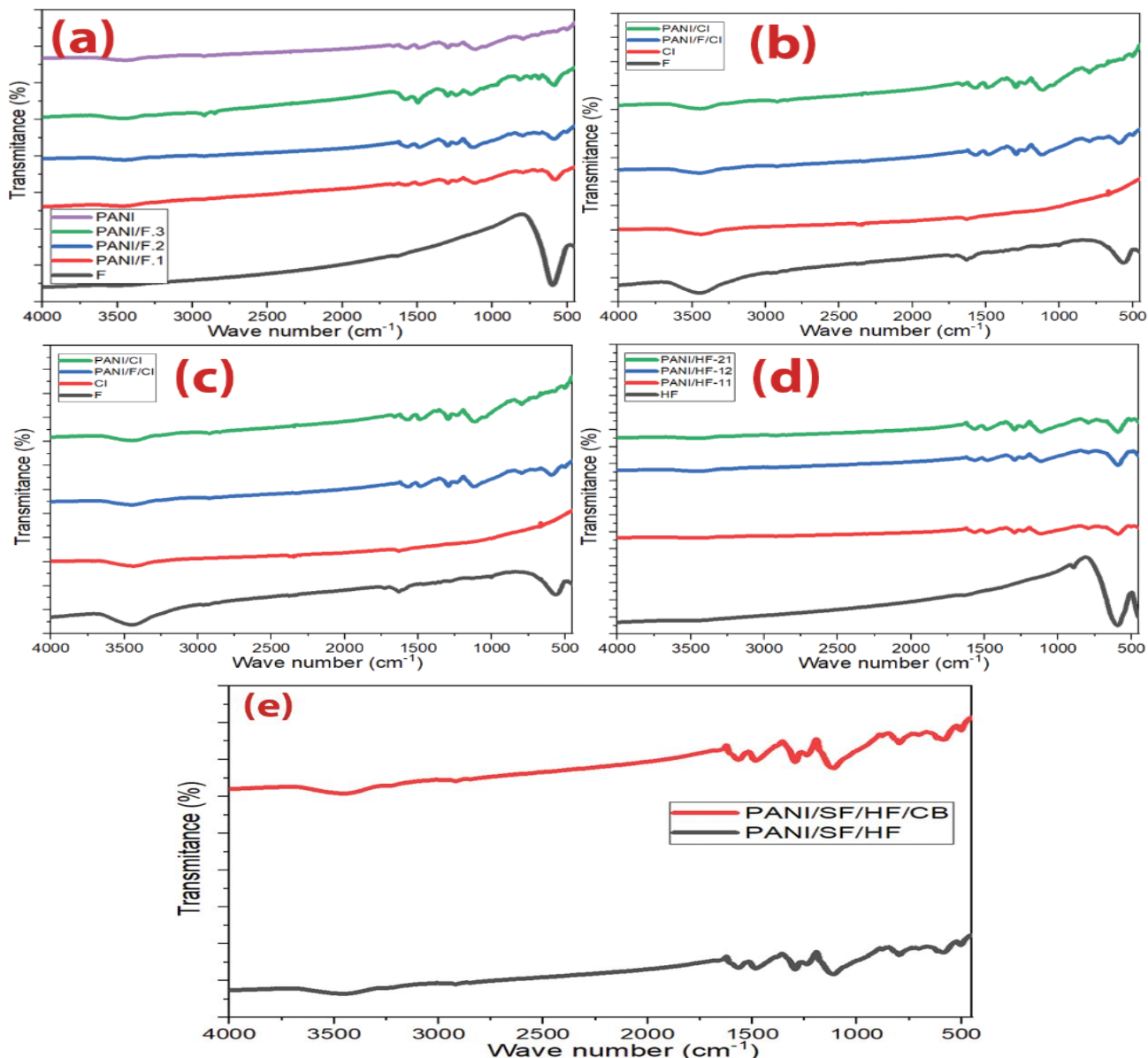


Figure 64 – FTIR spectra of (a) $\text{Ni}^{3+}_{0.25}\text{Ni}^{2+}_{0.375}\text{Zn}^{2+}_{0.25}\text{Fe}_2\text{O}_4$, PANI/ $\text{Ni}^{3+}_{0.25}\text{Ni}^{2+}_{0.375}\text{Zn}^{2+}_{0.25}\text{Fe}_2\text{O}_4$ composites and pure PANI, (b) $\text{Ni}_{0.5}\text{Zn}_{0.5}\text{Fe}_2\text{O}_4$, CI, PANI/CI and PANI/F/CI composites, (c) PANI/CB and PANI/F/CB composites, (d) HF and PANI/HF composites and (e) PANI/SF/HF and PANI/SF/HF/CB hybrid composites

3.5.3 Morphology investigations of PANI-based composites

Figure 65 represents the SEM micrographs of the PANI and PANI/F composites. The grain size of the samples was analyzed by the ImageJ software. The combination of rough surface sheets and short rods of PANI was noticed. After coating by polyaniline, a continued overlayer

of PANI was created on the $\text{Ni}^{3+}_{0.25}\text{Ni}^{2+}_{0.375}\text{Zn}^{2+}_{0.25}\text{Fe}_2\text{O}_4$ particles. The $\text{Ni}^{3+}_{0.25}\text{Ni}^{2+}_{0.375}\text{Zn}^{2+}_{0.25}\text{Fe}_2\text{O}_4$ composites images exhibit that the $\text{Ni}^{3+}_{0.25}\text{Ni}^{2+}_{0.375}\text{Zn}^{2+}_{0.25}\text{Fe}_2\text{O}_4$ particles were coated with PANI to create the composite structure. The average diameters for PANI/F.1, PANI/F.2 and PANI/F.3 ranging from 164–652 nm, 145–360 nm and 132–345 nm, respectively. In addition to that, agglomerated rod-like particle formation was noticed in the PANI/F composites, and this was due to the increased percentage of PANI content in the composites. In order to gain further insight into the composition of the samples, EDX elemental mapping has been performed as demonstrated in the next section. The morphology of the CI and PANI/F/CI composite is shown in Figure 66. The spherical particles of carbonyl iron are observed. On the other hand, after coating with polyaniline, a continued overlayer of PANI is created on the CI and $\text{Ni}_{0.5}\text{Zn}_{0.5}\text{Fe}_2\text{O}_4$ particles' surface. The average diameters for CI and PANI/F/CI composite ranging from 0.4–4.6 μm and 132–315 nm, respectively. A particle size distribution histogram was determined from the SEM image for PANI/F1 and CI (Figure 67).

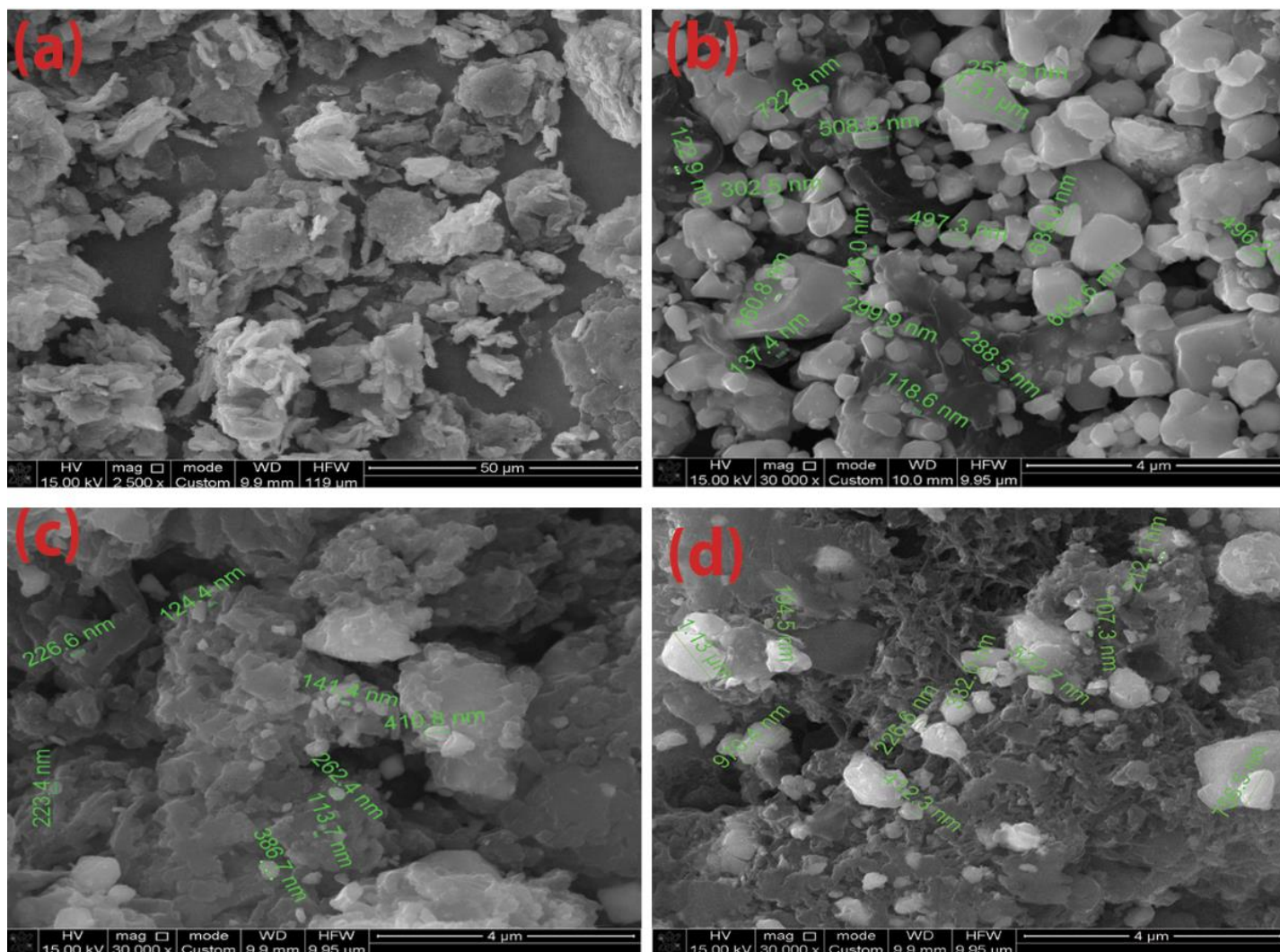


Figure 65 – SEM images of (a) PANI, (b) PANI/F.1, (c) PANI/F.2 and (d) PANI/F.3

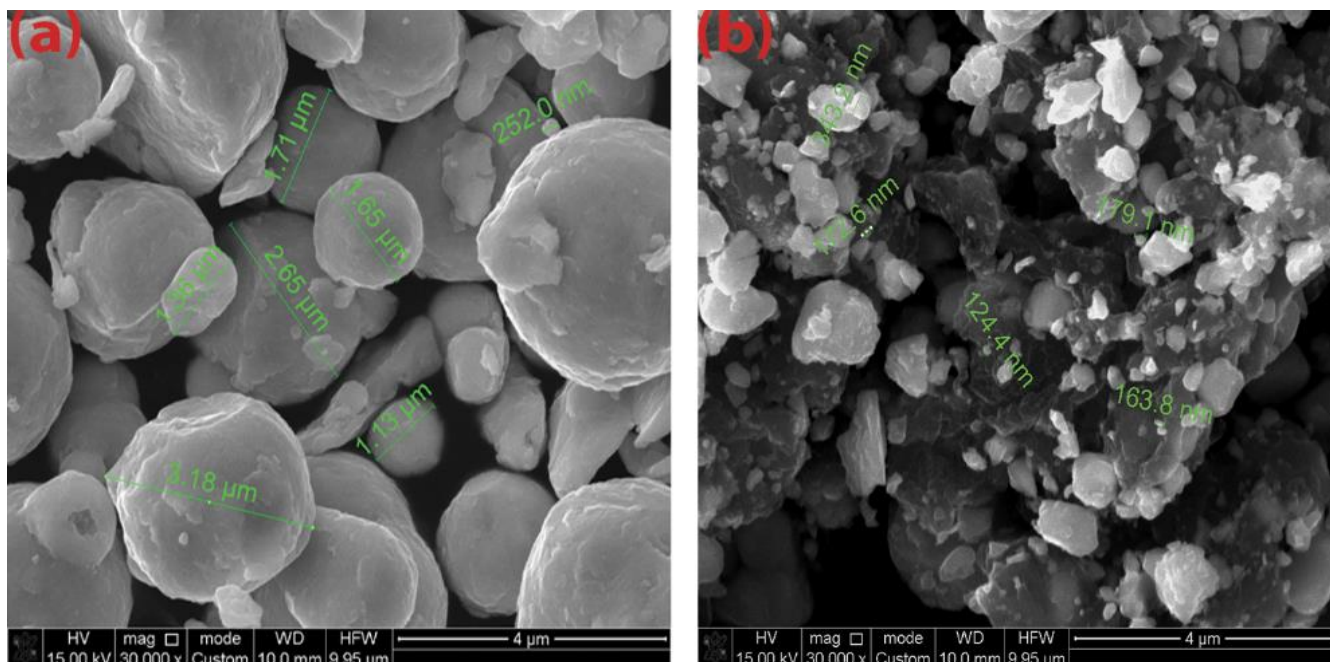


Figure 66 – SEM images of (a) CI and (b) PANI/F/CI composite

Figures (68–69) depict SEM micrographs of the PANI/HF, PANI/SF/HF and PANI/SF/HF/CB composites. After the in-situ polymerization of aniline, one can readily notice the deposition of fine particles of PANI on spinel and hexagonal ferrite particles. EDX was used to know the chemical composition of the PANI/HF, PANI/SF/HF and PANI/SF/HF/CB samples as shown below.

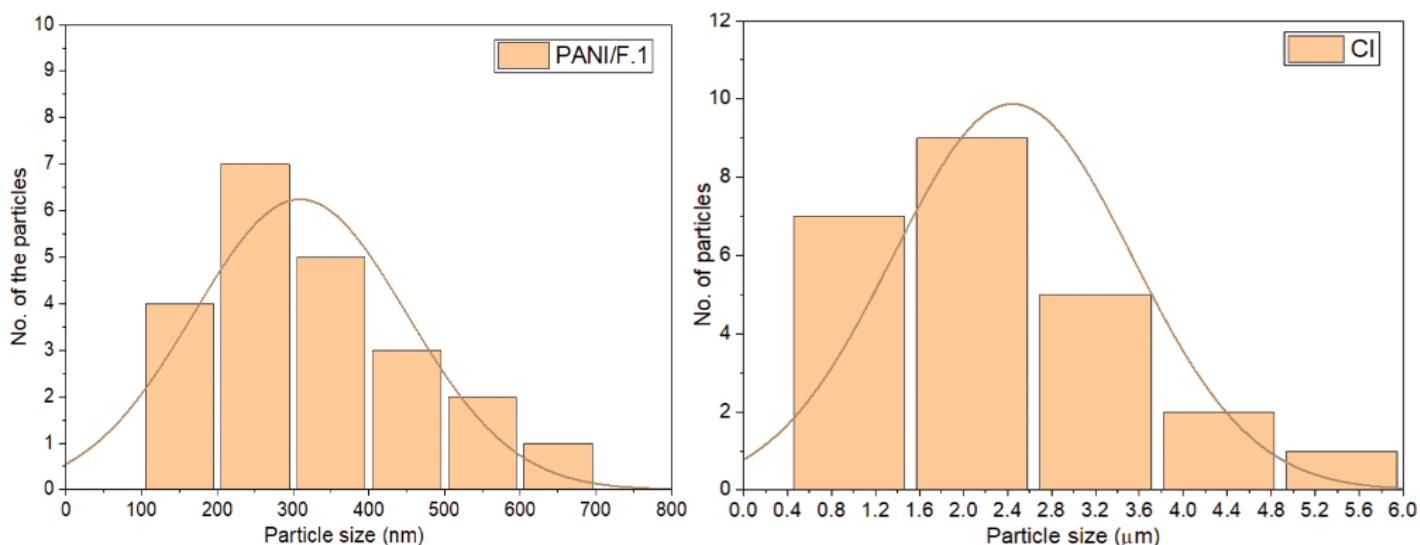


Figure 67 – A particle size distribution histogram determined from the SEM image for PANI/F1 and CI

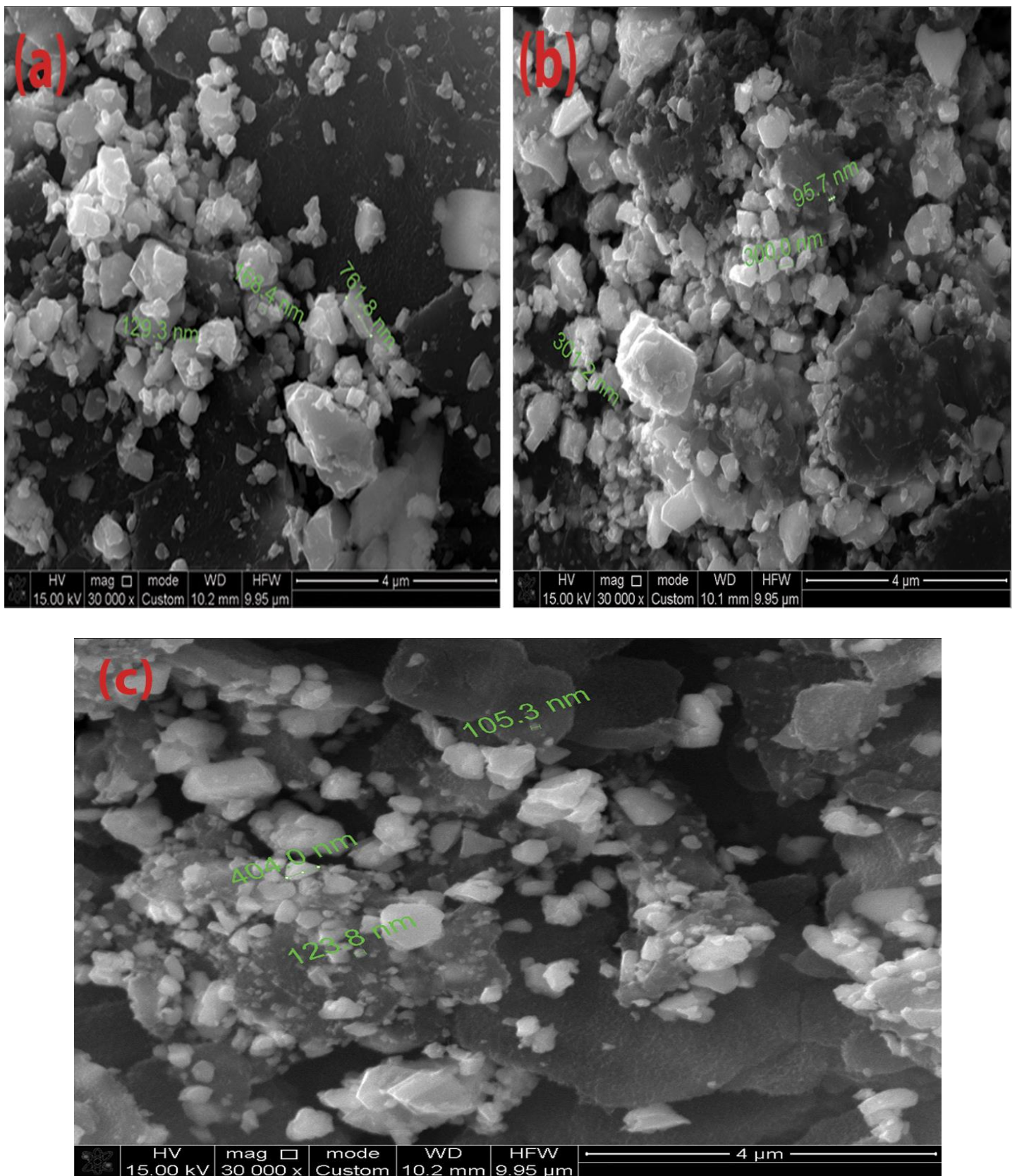


Figure 68 – SEM images of (a) PANI/HF.1, (b) PANI/HF. 2 and (c) PANI/HF.3 composites

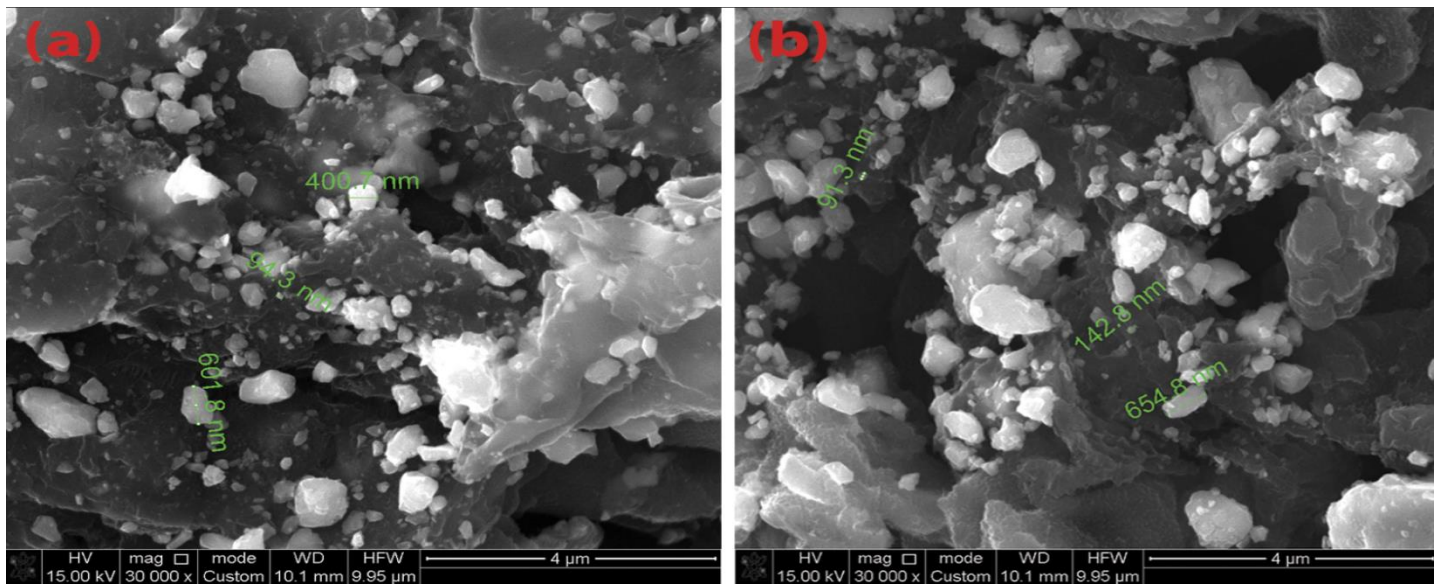


Figure 69 – SEM images of (a) PANI/SF/HF and (b) PANI/SF/HF/CB composites

3.5.4 EDX analysis of PANI-based composites

EDX analysis of PANI and PANI-based composites are shown in Figures (70-72) and Table 30. The presence of C, O, S and Cl elements in the PANI EDX spectrum is found. The elemental Cl and S presence can be attributed to doping agents' hydrochloric acid and sodium dodecyl sulfate. On the other hand, the presence of C, O, Cl, S, Fe, Ba, Zn, Al and Ni elements in the PANI-based composites EDX spectrum was observed. One can observe with increasing the PANI in composites, the carbon will increase and iron will decrease inside them, which will impact its EMI shielding and MA properties, as will be clarified later.

Table 30 – EDX element composition of PANI and PANI-based composites

Element	C	Cl	O	S	Al	Fe	Ni	Zn	Ba
PANI (wt%)	84.52	0.45	11.81	3.17	0.05	0	0	0	0
PANI/F.1 (wt%)	37.29	0.32	15.2	1.75	0.12	28.6	7.67	9.05	0
PANI/F.2 (wt%)	51.76	0.22	19.27	2.42	0.08	17.95	6.32	1.98	0
PANI/F.3 (wt%)	63.01	0.18	17.30	2.93	0.08	11.17	3.96	1.37	0
PANI/F/Cl (wt%)	51.72	0.51	19.23	2.02	0.08	17.15	5.32	3.97	0
PANI/HF.1 (wt%)	53.44	0.30	14.63	2.63	0	21.02	2.63	1.60	3.75
PANI/HF.2 (wt%)	59.02	0.67	15.31	3.14	0	15.69	2.29	1.09	2.79
PANI/HF.3 (wt%)	66.91	0.18	15.94	2.91	0	9.65	1.61	0.59	2.21
PANI/SF/HF (wt%)	61.27	0.73	12.42	4.51	0	13.97	4.64	1.42	1.04
PANI/SF/HF/CB (wt%)	75.44	0.85	12.44	3.65	0	4.45	2.31	0.47	0.39

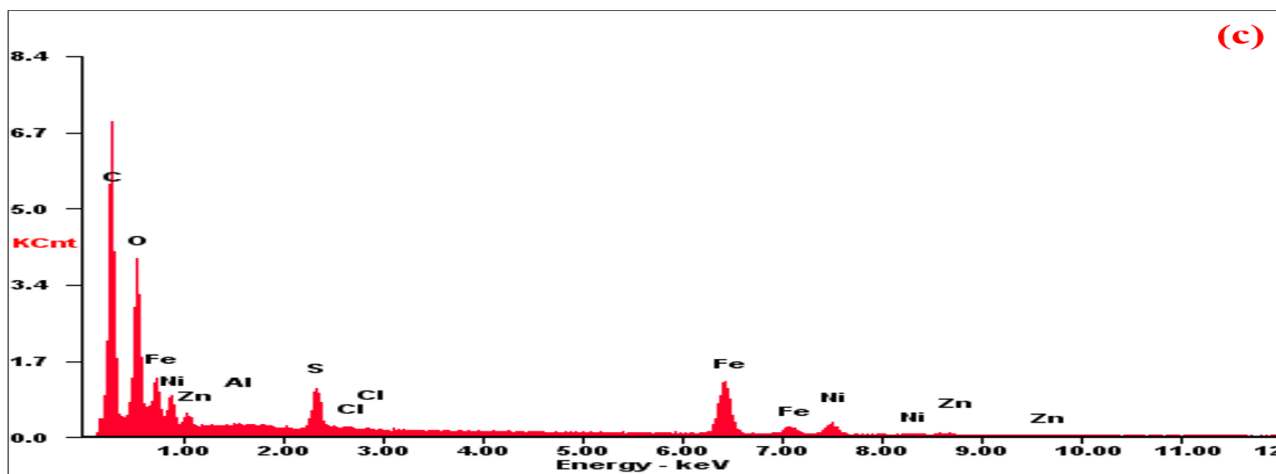
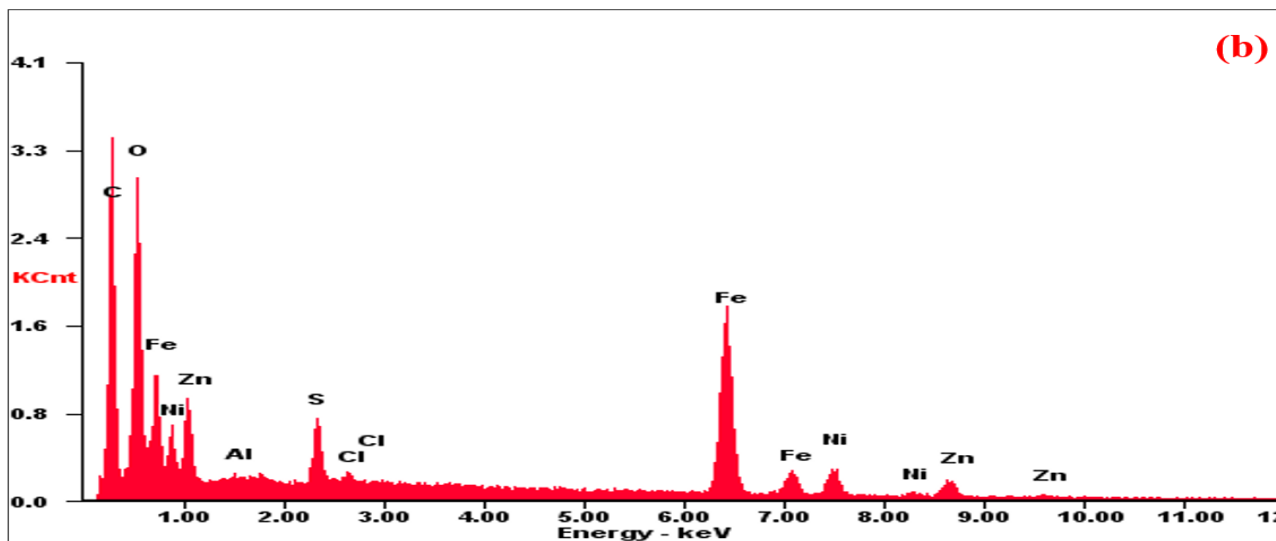
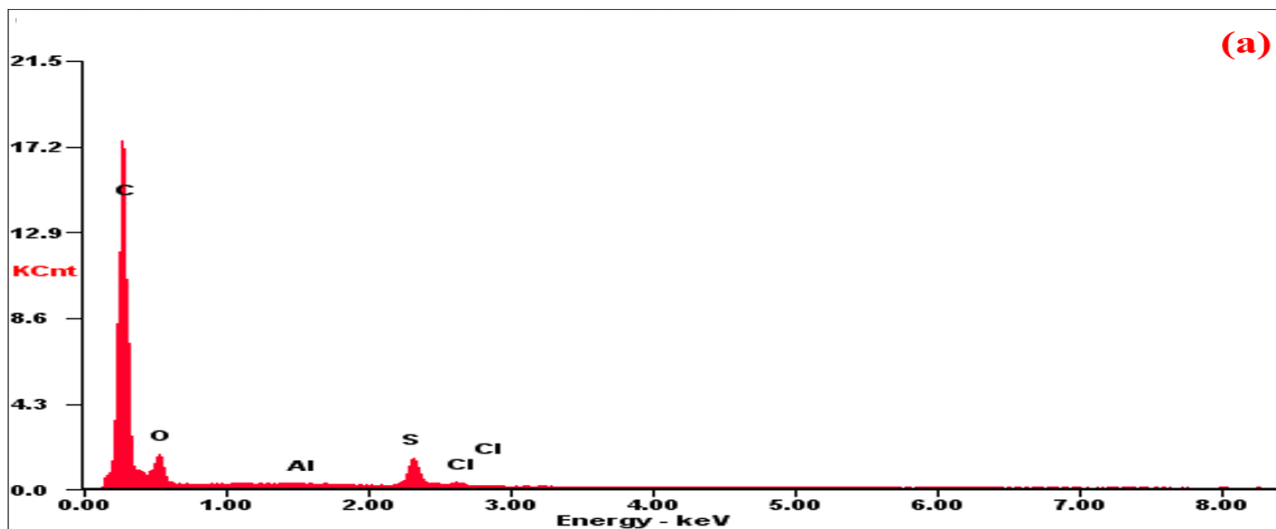


Figure 70 – EDX of (a) PANI, (b) PANI/F.1 and (c) PANI/F.2 hybrid composites

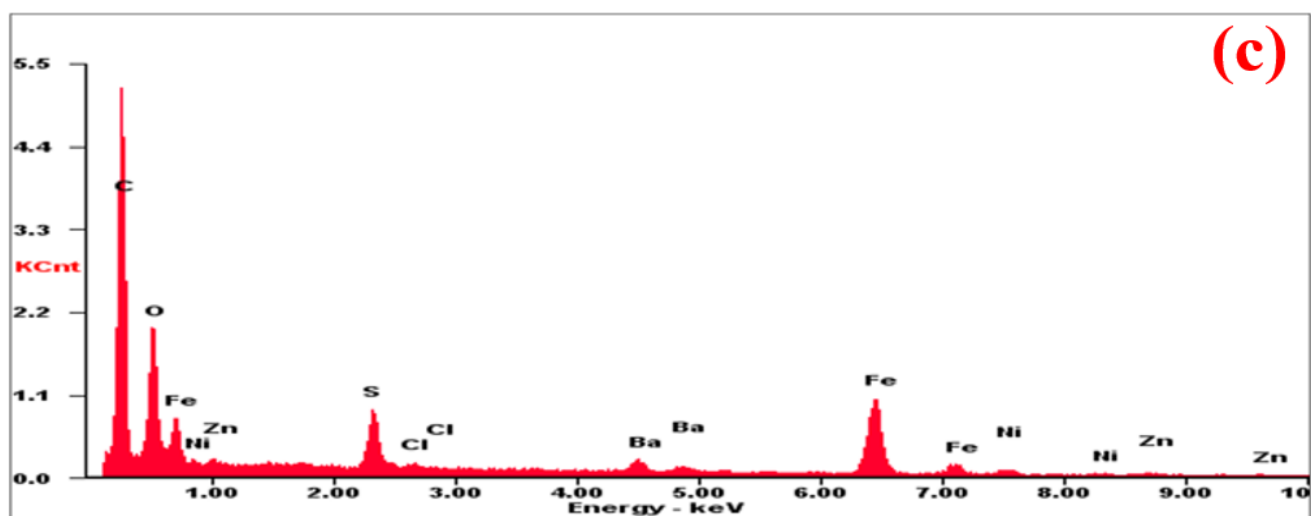
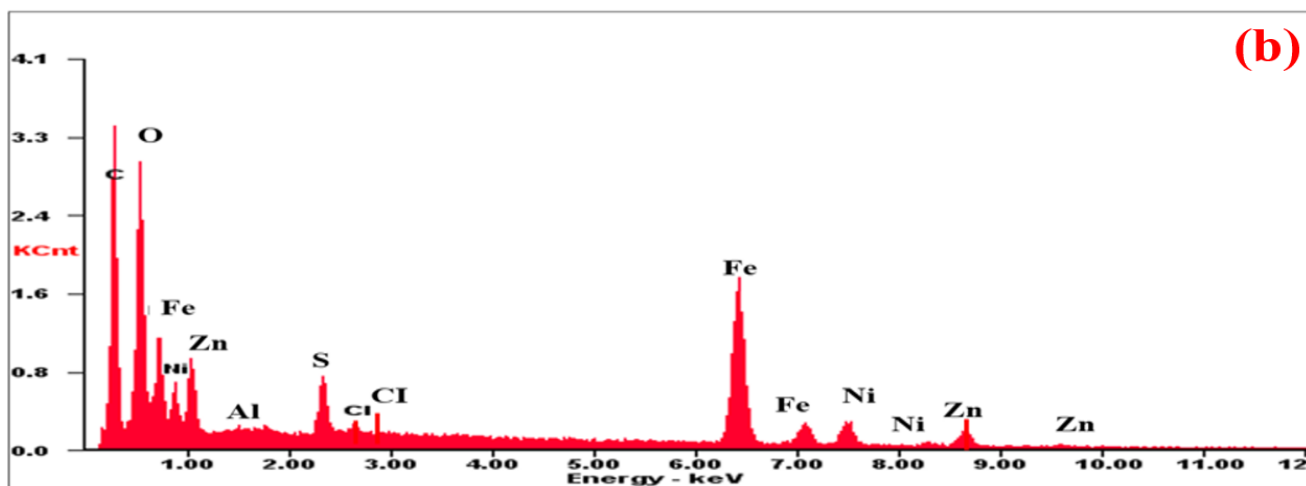
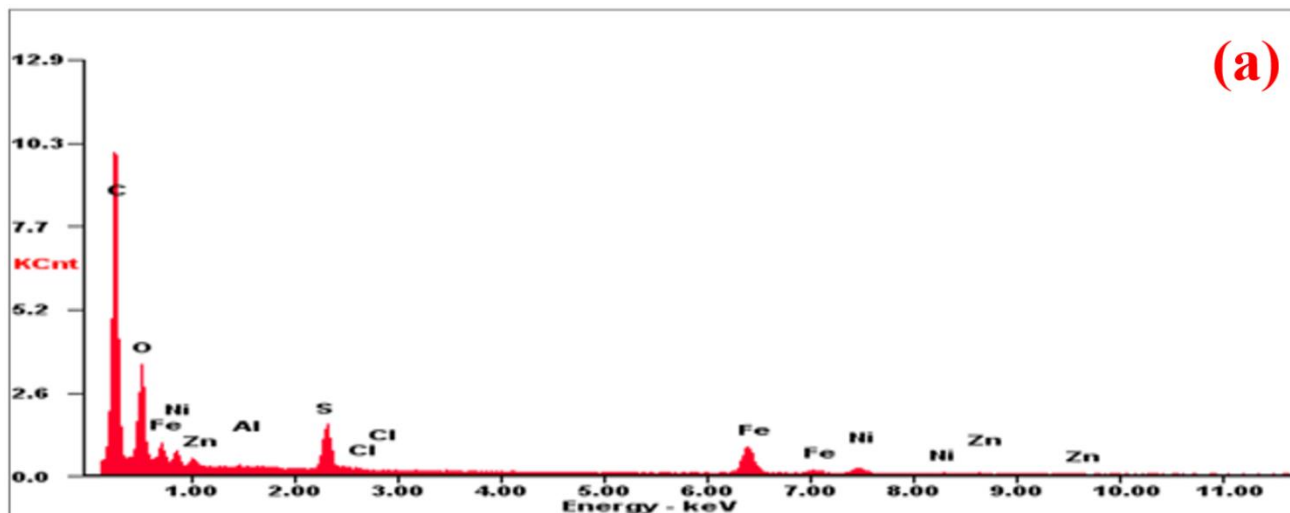


Figure 71 – EDX of (a) PANI/F.3, (b) PANI/F/Cl and (c) PANI/HF-11 hybrid composites

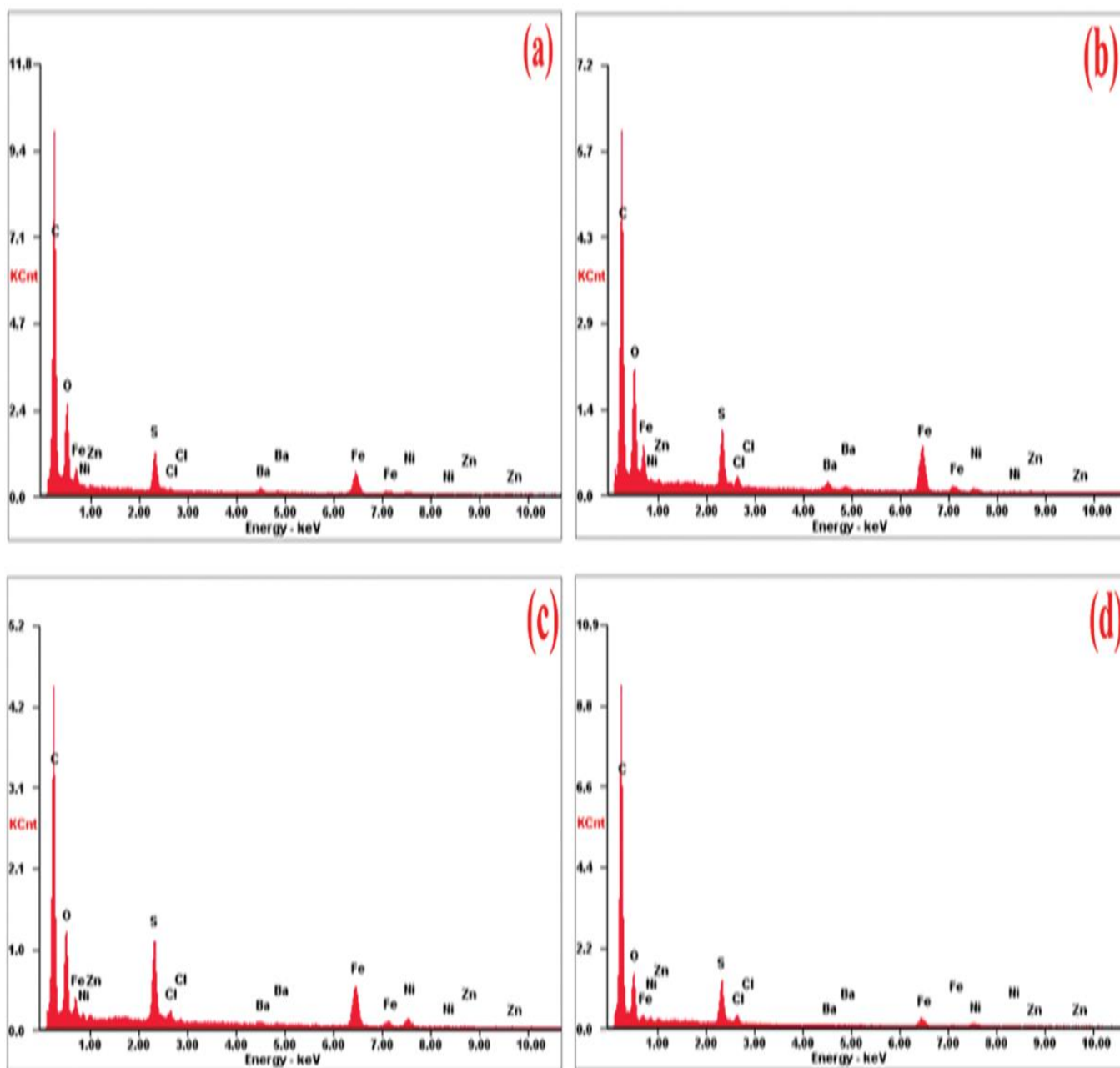


Figure 72 – EDX of (a) PANI/HF-21, (b) PANI/HF-12, (c) PANI/SF/HF and (d) PANI/SF/HF/CB hybrid composites

3.5.5 TGA analysis of PANI-based composites

The TGA curves of the $\text{Ni}^{3+}_{0.25}\text{Ni}^{2+}_{0.375}\text{Zn}^{2+}_{0.25}\text{Fe}_2\text{O}_4$, $\text{Ni}_{0.5}\text{Zn}_{0.5}\text{Fe}_2\text{O}_4$, $\text{BaNiZnFe}_{16}\text{O}_{27}$, PANI/ $\text{Ni}^{3+}_{0.25}\text{Ni}^{2+}_{0.375}\text{Zn}^{2+}_{0.25}\text{Fe}_2\text{O}_4$, PANI/CB, PANI/F/CB, PANI/F/Cl, PANI/ $\text{BaNiZnFe}_{16}\text{O}_{27}$, PANI/SF/HF and PANI/SF/HF/CB are shown in Figure 73. $\text{Ni}^{3+}_{0.25}\text{Ni}^{2+}_{0.375}\text{Zn}^{2+}_{0.25}\text{Fe}_2\text{O}_4$, $\text{Ni}_{0.5}\text{Zn}_{0.5}\text{Fe}_2\text{O}_4$, and $\text{BaNiZnFe}_{16}\text{O}_{27}$ particles, no mass loss is noticed over the whole temperature range. PANI loses 4.87% of its weight in the field of 110–130 °C, which is due to the evaporation of moisture in the PANI. The thermal decomposition of the PANI is shown in

the range of 230–1000 °C and had a big weight loss of 65.12%. On the other hand, PANI-based composites can be evaluated from the TGA curves, as shown in Table 31.

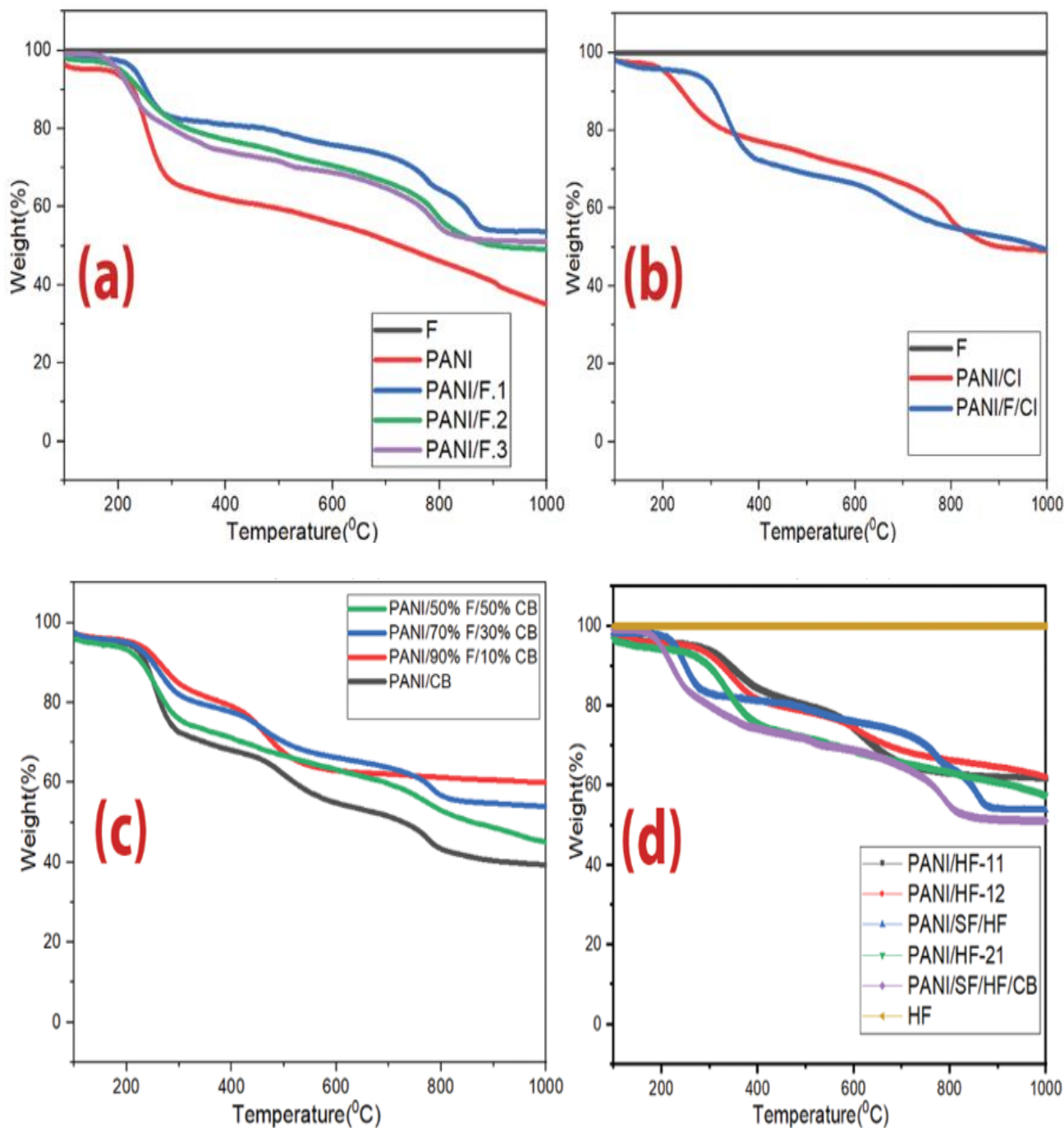


Figure 73 – TGA thermograms of (a) $\text{Ni}^{3+}_{0.25}\text{Ni}^{2+}_{0.375}\text{Zn}^{2+}_{0.25}\text{Fe}_2\text{O}_4$, $\text{PANI}/\text{Ni}^{3+}_{0.25}\text{Ni}^{2+}_{0.375}\text{Zn}^{2+}_{0.25}\text{Fe}_2\text{O}_4$ composites and pure PANI, (b) $\text{Ni}_{0.5}\text{Zn}_{0.5}\text{Fe}_2\text{O}_4$, PANI/CI and PANI/F/CI composites, (c) PANI/CB and PANI/F/CB hybrid composites and (d) HF, PANI, PANI/SF/HF and PANI/SF/HF/CB composites

Table 31 – TGA measurements of the PANI-based composites

Sample	Calculated PANI percentage	Evaluated PANI percentage utilizing TGA
PANI/F.1	50%	53.8%
PANI/F.2	66.7%	49.5%
PANI/F.3	75%	51.2%
PANI/CI	50%	49.0%
PANI/F/CI	50%	49.5%
PANI/CB	50%	39.7%
PANI/90%F/10%CB	50%	45.4%
PANI/70%F/30%CB	50%	54.3%
PANI/50%F/50%CB	50%	60.1%
PANI/HF-11	50%	61.7%
PANI/HF-12	33.3%	62.4%
PANI/HF-21	66.7%	58.5%
PANI/SF/HF	50%	53.8%
PANI/SH/HF/CB	50%	51.3%

3.5.6 Microwave absorption properties of PANI-based composites

Several variables that affect microwave absorption properties were studied, as follows: PANI-based composites type (PANI/Ni³⁺_{0.25}Ni²⁺_{0.375}Zn²⁺_{0.25}Fe₂O₄, PANI/BaNiZnFe₁₆O₂₇, PANI/Ni³⁺_{0.25}Ni²⁺_{0.375}Zn²⁺_{0.25}Fe₂O₄/CB, PANI/Ni³⁺_{0.25}Ni²⁺_{0.375}Zn²⁺_{0.25}Fe₂O₄/CI, PANI/SF/HF, PANI/SF/HF/CB, PANI/CB, PANI/CI), weight ratios of PANI/Ni³⁺_{0.25}Ni²⁺_{0.375}Zn²⁺_{0.25}Fe₂O₄, and PANI/BaNiZnFe₁₆O₂₇, and adding CB and CI to hybrid composites.

3.5.6.1 Role of the incorporation of dielectric loss and magnetic loss materials to enhance EM wave absorption performance:

Microwave absorption behaviors of the absorbent substances are determined by complex permittivity ($\epsilon_r = \epsilon' - i\epsilon''$) which describes the interaction of the electric field with the absorbent substance and complex permeability ($\mu_r = \mu' - i\mu''$) which describes the interaction of the magnetic field with the absorbent substance. The interaction of the electric and magnetic field with the absorbent substance occurs in two ways: stored power of the external electric and magnetic field in the substance (real parts ϵ' , μ'), lost power because of the external electric and magnetic field (imaginary parts ϵ'' , μ'') [21–23]. In addition to that, dielectric loss tangent ($\tan\delta_\epsilon = \frac{\epsilon''}{\epsilon'}$) can be represented as the ratio of both ϵ' and ϵ'' , and in the same way for the magnetic loss tangent ($\tan\delta_\mu = \frac{\mu''}{\mu'}$). The dielectric loss tangent can be originated by polarization relaxation and conductance loss as given in the free-electron theory $\epsilon'' \approx \frac{1}{2\pi\rho f \epsilon_0}$

[118]. Where ρ and ϵ_0 are the resistivity and the dielectric constant of free space, respectively. The mechanism of polarizability that instigates microwave absorption contains rotation and orientation of the dipoles. Ionic polarization, electronic polarization, dipole polarization, and interfacial polarization are the main source of polarization relaxation. On the other hand, the magnetic loss tangent can be originated from hysteresis, natural resonance, domain wall resonance and eddy current loss. Hysteresis losses usually occur even at D.C. or low frequencies, and domain wall resonance occurs at less than 0.1 GHz. When the reflection loss only comes from the eddy current effect, the value of $\mu'' \mu'^{-2} f^{-1}$ will be constant as the frequency changes [119].

EMI shielding and MA properties of the $\text{Ni}^{3+}_{0.25}\text{Ni}^{2+}_{0.375}\text{Zn}^{2+}_{0.25}\text{Fe}_2\text{O}_4$, PANI, and PANI/F composites were investigated. The results of this investigation are exhibited in Figure 74 and Table 32. Figure 74 illustrates the changing of the RL and SE as a function of the EM wave frequency for $\text{Ni}^{3+}_{0.25}\text{Ni}^{2+}_{0.375}\text{Zn}^{2+}_{0.25}\text{Fe}_2\text{O}_4$, PANI and PANI/F composites. The thickness of the prepared samples was 2.9 mm. As illustrated in Figure 74, for the $\text{Ni}^{3+}_{0.25}\text{Ni}^{2+}_{0.375}\text{Zn}^{2+}_{0.25}\text{Fe}_2\text{O}_4$, weak RL and low SE were observed. The defect of the $\text{Ni}^{3+}_{0.25}\text{Ni}^{2+}_{0.375}\text{Zn}^{2+}_{0.25}\text{Fe}_2\text{O}_4$ is that it has low ϵ'' . This low ϵ'' of $\text{Ni}^{3+}_{0.25}\text{Ni}^{2+}_{0.375}\text{Zn}^{2+}_{0.25}\text{Fe}_2\text{O}_4$ can be attributed to the non-dielectric properties of ferrite, therefore the EM wave absorption capability largely results from the magnetic loss (natural resonance and exchange resonance are the main factors for the loss of the magnetic field energy [91]). On the other hand, for the pure PANI, the RL was between 6.2–8.1 dB and the SE was between 9.6–12.5 dB. The defect of the PANI is that it has low μ'' . This low μ'' of PANI can be attributed to the non-magnetism properties of polyaniline, therefore the EM wave absorption capability largely results from the dielectric loss [100]. This is explained by the increase of the imaginary part of the permittivity explained by the conductive nature of PANI, and the increase of the real part is a feature of the Maxwell-Wagner polarization effect [120] that occurs in an insulating medium (wax) loaded with conductive particles (PANI). The underlying mechanism to improve the microwave absorption performance of an absorber is believed to be linked to the interfacial polarization between the different components [60].

The polymerization of aniline monomers on the external surface of F leads to the interface polarization charges. From Figure 74, it can be readily seen that the core/shell (F/PANI) structure shows better microwave absorption characteristics compared with F and PANI absorbers. This result indicates that the synergistic effect of combining magnetic and dielectric lossy materials is not exalted until they are in a core/shell structure where the interfacial polarizations become more important and play a primordial role. The same result is observed for other prepared hybrid composites (PANI/BaNiZnFe₁₆O₂₇, PANI/CI, PANI/F/CI, PANI/F/CB, PANI/50%SF/50%HF, and PANI/45%SF/45%HF/10%CB).

3.5.6.2 Effect of sample thickness on the RL

Figure 75 illustrates the RL of PANI/F.2 composite with different thicknesses at the loading percentage of 25% w/w. Figure 75 illustrates that the RL attenuation peaks of samples moved

to lower frequencies with increasing sample thickness. This phenomenon may be defined by the quarter-wavelength ($\lambda/4$) cancellation model, as shown in equation (5).

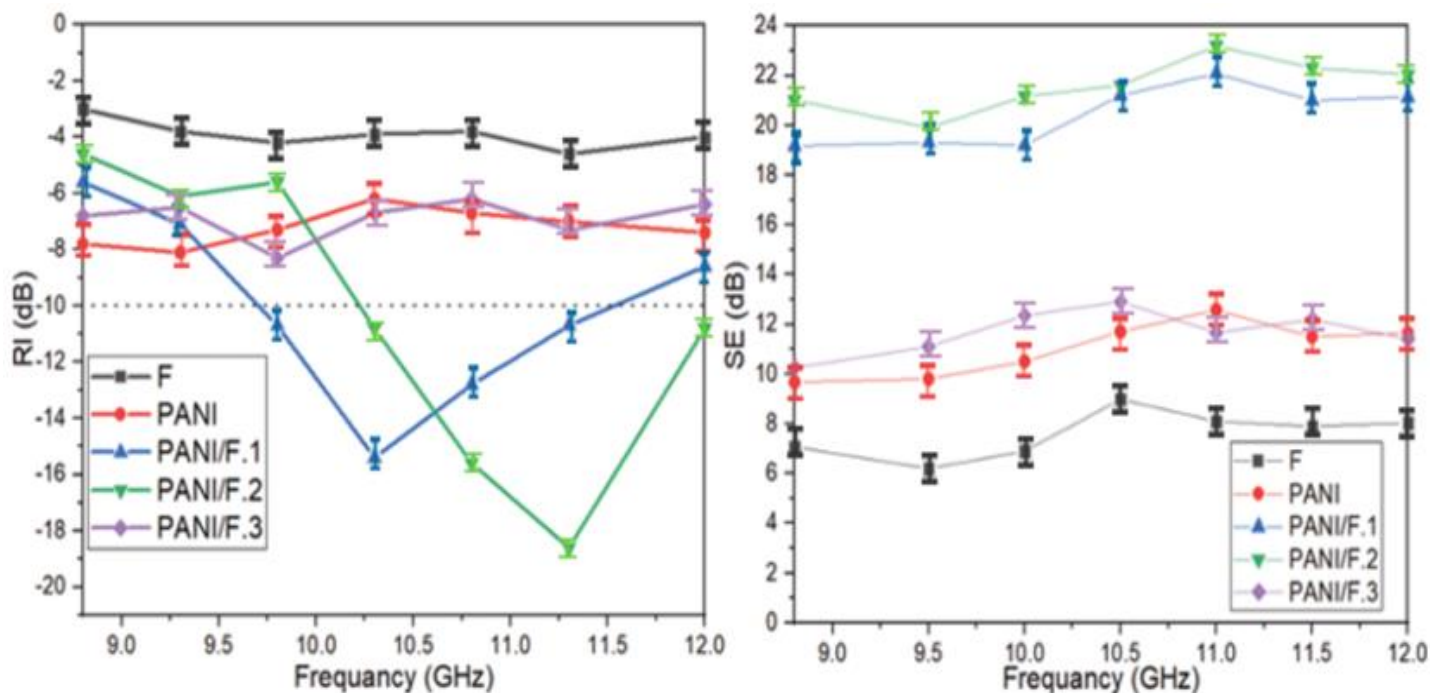


Figure 74 – RL and SE curves of $\text{Ni}^{3+}_{0.25}\text{Ni}^{2+}_{0.375}\text{Zn}^{2+}_{0.25}\text{Fe}_2\text{O}_4$, $\text{PANI}/\text{Ni}^{3+}_{0.25}\text{Ni}^{2+}_{0.375}\text{Zn}^{2+}_{0.25}\text{Fe}_2\text{O}_4$ composites and pure PANI at 2.9 mm thickness

Table 32 – MA behavior of $\text{Ni}^{3+}_{0.25}\text{Ni}^{2+}_{0.375}\text{Zn}^{2+}_{0.25}\text{Fe}_2\text{O}_4$, $\text{PANI}/\text{Ni}^{3+}_{0.25}\text{Ni}^{2+}_{0.375}\text{Zn}^{2+}_{0.25}\text{Fe}_2\text{O}_4$ composites and pure PANI at 2.9 mm thickness

Samples	RL_{\min} (dB)	f_m (GHz)	$\text{BW}_{-10 \text{ dB}}$ (GHz)	SD (kg/m^2)
$\text{Ni}^{3+}_{0.25}\text{Ni}^{2+}_{0.375}\text{Zn}^{2+}_{0.25}\text{Fe}_2\text{O}_4$	-4.2 ± 0.5	-	-	4.53 ± 0.05
PANI	-8.1 ± 0.7	-	-	2.21 ± 0.08
PANI/F.1	-15.4 ± 0.8	10.2 ± 0.3	1.9 ± 0.3	3.22 ± 0.07
PANI/F.2	-18.6 ± 0.7	11.3 ± 0.2	1.8 ± 0.6	3.04 ± 0.05
PANI/F.3	-8.3 ± 0.5	-	-	2.96 ± 0.04

It can be noticed from equation (5) that the f_m is inversely proportionate to the thickness of an absorber. One can conclude that the optimal matching and absorption can be accomplished by modifying the thickness of an absorber (Table 33).

Table 33 – MA behavior of PANI/F.2 hybrid composite at various thicknesses

PANI/F.2	t (mm)	RL _{min} (dB)	f _m (GHz)	BW _{-10dB} (GHz)	SD (kg/m ²)
	2.90	-18.6±0.8	11.3±0.1	1.8±0.2	3.04±0.05
	3.12	-19.8±0.7	10.8±0.2	2.2±0.2	3.07±0.08
	3.46	-15.7±0.5	10.2±0.1	2.7±0.1	3.09±0.06
	3.62	-16.9±0.9	9.3±0.2	1.7±0.3	3.12±0.06

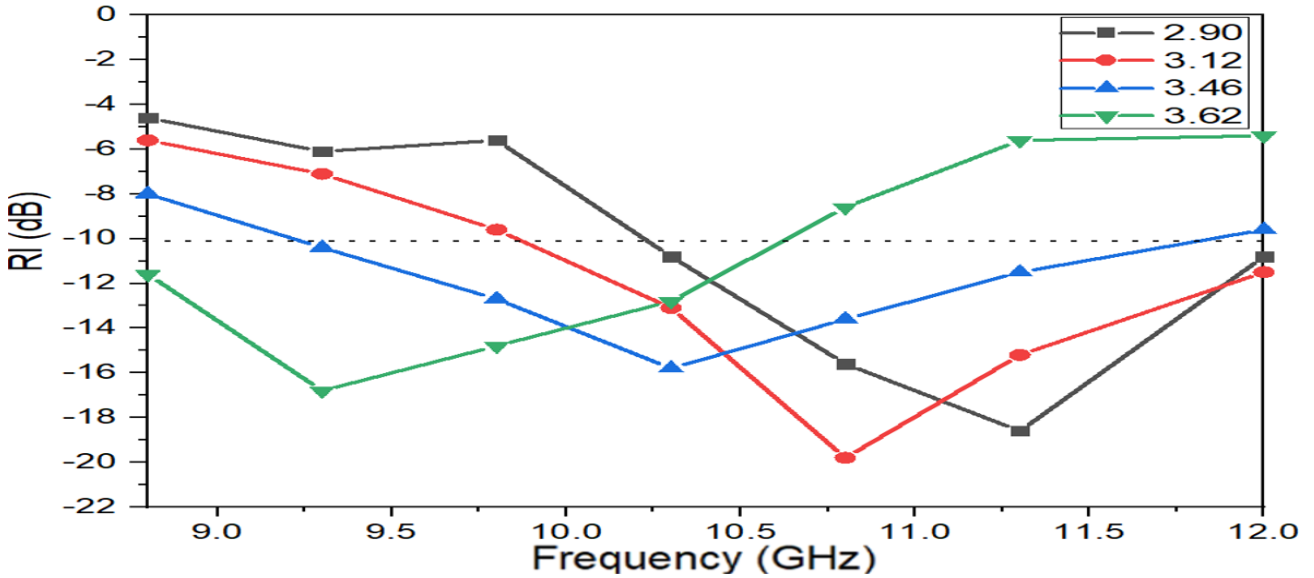


Figure 75 – RL curves of PANI/F.2 hybrid composite at various thicknesses

3.5.6.3 Influence of the incorporation of Ni_{0.5}Zn_{0.5}Fe₂O₄, CI and PANI on the RL and the SE

EMI shielding and MA properties of the Ni_{0.5}Zn_{0.5}Fe₂O₄, CI, PANI, PANI/CI and PANI/F/CI nanocomposite were investigated. The results of this investigation are exhibited in Figure 76 and Table 34. Figure 76 illustrates the changing of the RL and SE as a function of the EM wave frequency for Ni_{0.5}Zn_{0.5}Fe₂O₄, CI, PANI, PANI/CI and PANI/F/CI nanocomposite. The thickness of the prepared samples was 3.2 mm. As illustrated in Figure 76, for the Ni_{0.5}Zn_{0.5}Fe₂O₄ and CI, weak RL and low SE were observed. The defect of the Ni_{0.5}Zn_{0.5}Fe₂O₄ and CI are that they have low complex relative permittivity. On the other hand, for the pure PANI, the RL was between 6.6–8.5 dB and the SE was between 9.8–12.9 dB. The defect of the PANI is that it has low complex relative permeability. Furthermore, when PANI was incorporated with ferrite, which was mixed with carbonyl iron, the RL increased to -25.7 dB at 11.3 GHz for PANI/F/CI composite and the SE increased to 30.12 dB at 11.0 GHz. As a result, the underlying mechanism to improve the microwave absorption performance of an absorber is believed to be linked to the interfacial polarization between the different components [60].

The polymerization of aniline monomers on the external surface of $\text{Ni}_{0.5}\text{Zn}_{0.5}\text{Fe}_2\text{O}_4$ and CI leads to the interface polarization charges. From Figure 76, it can be readily seen that the PANI/F/CI structure shows better microwave absorption characteristics compared with $\text{Ni}_{0.5}\text{Zn}_{0.5}\text{Fe}_2\text{O}_4$, CI and PANI absorbers. This result indicates that the synergistic effect of combining magnetic and dielectric lossy materials where the interfacial polarizations become more important and play a primordial role. These prepared composites are promising candidates for applications such as EMI shielding and stealth technology.

Table 34 – MA behavior of $\text{Ni}_{0.5}\text{Zn}_{0.5}\text{Fe}_2\text{O}_4$, CI, PANI, PANI/CI and PANI/F/CI composite at 3.2 mm thickness

Samples	RL_{\min} (dB)	f_m (GHz)	$\text{BW}_{-10 \text{ dB}}$ (GHz)	SD (kg/m^2)
$\text{Ni}_{0.5}\text{Zn}_{0.5}\text{Fe}_2\text{O}_4$	-4.6 ± 0.7	-	-	4.56 ± 0.07
CI	-6.5 ± 0.5	-	-	5.21 ± 0.05
PANI	-8.5 ± 0.6	-	-	2.25 ± 0.04
PANI/CI	-21.3 ± 0.9	10.2 ± 0.3	2.7 ± 0.2	3.36 ± 0.07
PANI/F/CI	-25.7 ± 0.7	11.3 ± 0.1	2.6 ± 0.1	3.31 ± 0.08

3.5.6.4 Influence of sample thickness and loading ratio of the absorption material within paraffin on the RL

Figure 77 illustrates the RL of PANI/F/CI composite with various thicknesses (3.2, 3.4 and 3.6 mm) at the various loading percentages (30% w/w and 35% w/w). Figure 77 shows that the RL attenuation peaks of samples moved to lower frequencies with increasing sample thickness.

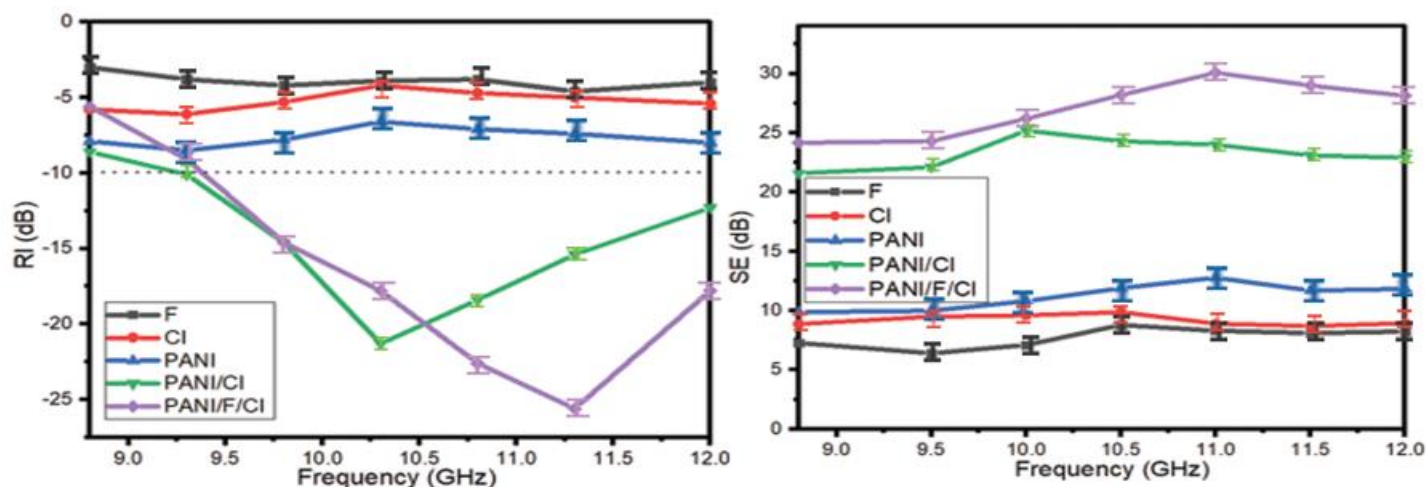


Figure 76 – RL and SE curves of $\text{Ni}_{0.5}\text{Zn}_{0.5}\text{Fe}_2\text{O}_4$, CI, PANI, PANI/CI and PANI/F/CI composite at 3.2 mm thickness. SE curves of $\text{Ni}_{0.5}\text{Zn}_{0.5}\text{Fe}_2\text{O}_4$, CI, PANI and PANI/F/CI composite at 3.2 mm thickness

On the other hand, one can notice the RL_{\min} moves gradually to a lower frequency with the increase in the loading percentage within a paraffin matrix. Furthermore, Table 35 shows the PANI/F/CI composites have reasonable SD, ranging from 3.31 to 3.40 kg/m², and wide BW_{-10dB} extending from 2.5 to 3.0 GHz. The absorption percentage of microwaves reached about 99.9% with a loading percentage of 30%. One can conclude that optimal absorption can be accomplished by modifying the absorber thickness and the loading percentage.

Table 35 – MA behavior of PANI/F/CI composite at various thicknesses and various loading ratios within a paraffin matrix

Loading ratio %	t (mm)	RL_{\min} (dB)	f_m (GHz)	BW_{-10dB} (GHz)	SD (kg/m ²)
30%	3.2	-25.7±0.7	11.3±0.3	2.6±0.1	3.31±0.04
	3.4	-28.5±0.9	10.8±0.1	3.0±0.2	3.35±0.07
	3.6	-26.8±0.6	9.8±0.2	2.9±0.1	3.37±0.06
35%	3.2	-28.6±0.7	10.8±0.2	2.5±0.1	3.33±0.05
	3.4	-30.8±0.8	10.3±0.1	2.8±0.2	3.38±0.06
	3.6	-28.4±0.8	9.3±0.2	2.6±0.1	3.40±0.05

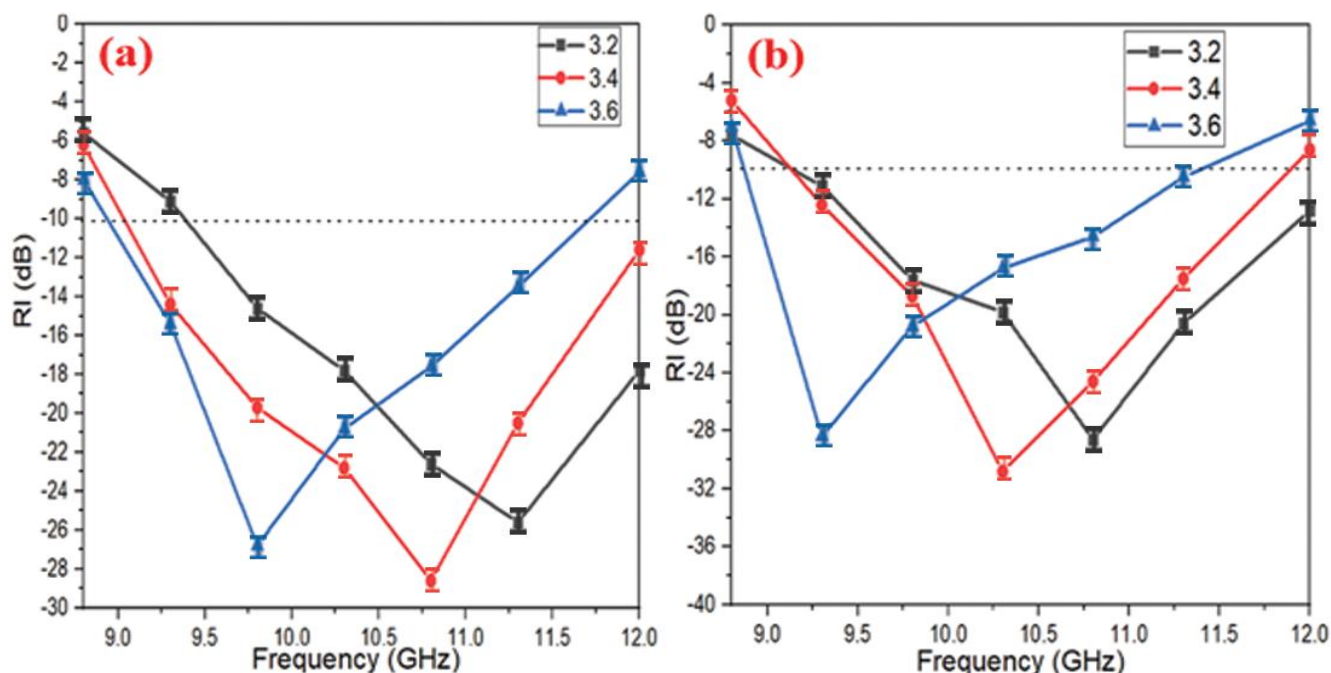


Figure 77 – RL curves of PANI/F/CI composite with various thicknesses (3.2, 3.4, 3.6 mm) at the various weight ratios of the absorber within a paraffin matrix (a) 30% and (b) 35%

3.5.6.5 Influence of the incorporation of $\text{Ni}^{3+}_{0.25}\text{Ni}^{2+}_{0.375}\text{Zn}^{2+}_{0.25}\text{Fe}_2\text{O}_4$, CB and PANI on the RL and the SE

EMI shielding and MA properties of the PANI/CB and PANI/F/CB composites were studied. The results of this investigation are exhibited in Figure 78 and Table 36. Figure 78 illustrates the changing of the RL and SE as a function of the EM wave frequency for PANI/CB and PANI/F/CB composites at the loading percentage of 30% w/w. The thickness of the prepared samples was 3.0 mm. As illustrated in Figure 78, for the PANI/CB, weak RL and medium SE were observed. The defect of the PANI/CB is that it has low complex relative permeability. On the other hand, when PANI/CB was incorporated with ferrite, the RL increased to -17.2 dB at 9.9 GHz for PANI/70%F/30%CB composite and the SE increased to 19.7 dB at 11.1 GHz. As a result, one can notice by tuning the different parameters of the fabrication and properly combining magnetic loss and dielectric loss components, a lightweight microwave absorber can be obtained with broad absorption bandwidth at the range of 8.8–12.0 GHz. These prepared composites are promising candidates for applications such as EMI shielding and stealth technology.

Table 36 – MA behavior of PANI/CB and PANI/F/CB composites at 3.0 mm thickness

Samples	RL _{min} (dB)	f _m (GHz)	BW _{-10 dB} (GHz)	SD (kg/m ²)
PANI/CB	-8.4 ± 0.3	10.5 ± 0.2	0	2.62 ± 0.09
PANI/50%F/50%CB	-15.6 ± 0.8	11.0 ± 0.2	2.8 ± 0.1	2.91 ± 0.05
PANI/70%F/30%CB	-17.2 ± 0.7	9.9 ± 0.1	2.8 ± 0.1	3.02 ± 0.08
PANI/90%F/10%CB	-15.1 ± 0.8	10.5 ± 0.1	3.2 ± 0.1	3.15 ± 0.07

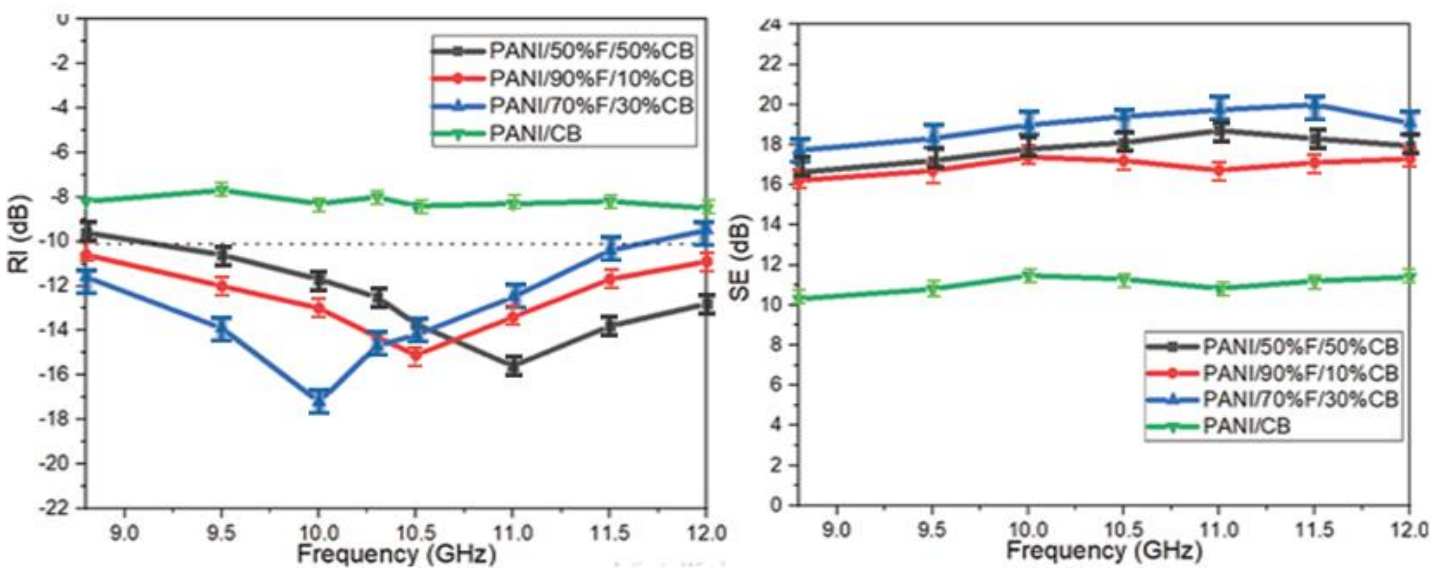


Figure 78– RL and SE curves of PANI/CB and PANI/F/CB composites at 3.0 mm thickness

3.5.6.6 Effect of PANI/BaNiZnFe₁₆O₂₇ hybrid composites morphology on the RL and the SE

EMI shielding and MA properties of the HF and PANI/HF composites were investigated. The results of this investigation are exhibited in Figure 79 and Table 37. Figure 79 illustrates the changing of the RL and SE as a function of the EM wave frequency for various weight ratios of PANI/HF at the loading percentage of 30% w/w. The thickness of the prepared samples was 3.0 mm. As illustrated in Figure 79, for the BaNiZnFe₁₆O₂₇ particles, weak RL and low SE were noticed. That is due to low complex relative permittivity. To improve the RL and SE of BaNiZnFe₁₆O₂₇. That requires incorporation with PANI. As a result, the RL increased to -17.0 dB at 11.6 GHz for PANI/HF.2 composite and the SE increased to 17.9 dB at 10.2 GHz. This refers to the MA and EMI shielding properties being related to the morphology of the composite. In reality, the mixture of agglomerated particles and rod-like morphology appears to show the best MA and EMI shielding properties. As a result, the underlying mechanism to improve the microwave absorption performance of an absorber is believed to be linked to the interfacial polarization between the different components [60]. The polymerization of aniline monomers on the external surface of HF leads to the interface polarization charges. From Figure 79, it can be readily seen that the core/shell (HF/PANI) structure shows better microwave absorption characteristics compared with HF and PANI absorbers. This result indicates that the synergistic effect of combining magnetic and dielectric lossy materials is not exalted until they are in a core/shell structure where the interfacial polarizations become more important and play a primordial role.

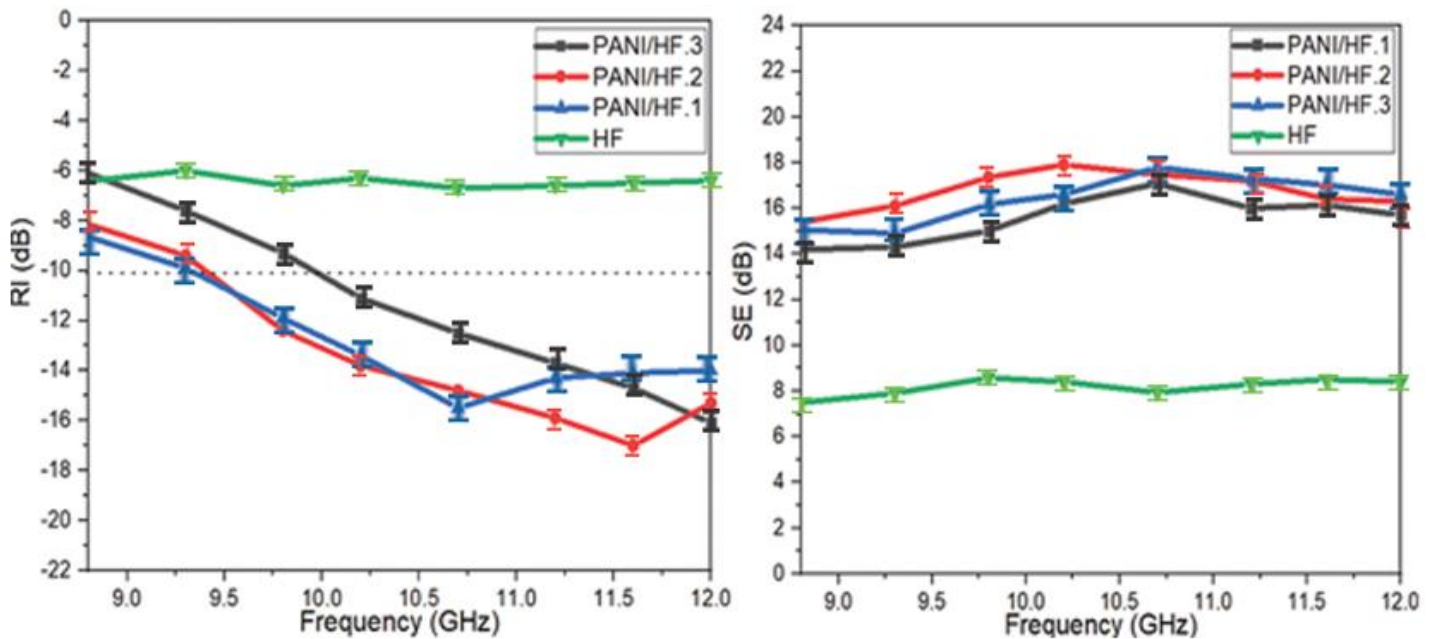


Figure 79 – RL and SE curves of PANI/HF composites at 3.0 mm thickness. SE curves of PANI/HF composites at 3.0 mm thickness

Table 37 – MA behavior of HF and PANI/HF composites at 3.0 mm thickness

Samples	RL _{min} (dB)	f _m (GHz)	BW _{-10 dB} (GHz)	SD (kg/m ²)
HF	-6.7±0.6	10.6±0.2	0	4.61±0.07
PANI/HF.1	-15.6±0.7	10.7±0.1	2.7±0.1	3.74±0.09
PANI/HF.2	-17.0±0.8	11.6±0.2	2.6±0.1	3.57±0.06
PANI/HF.3	-16.1±0.8	12.0±0.1	2.5±0.1	3.16±0.07

3.5.6.7 Microwave absorption properties of PANI/SF/HF and PANI/SF/HF/CB composites

EMI shielding and MA properties of the PANI/SF/HF and PANI/SF/HF/CB composites were studied. The results of this investigation are exhibited in Figure 80 and Table 38. Figure 80 illustrates the changing of the RL and SE as a function of the EM wave frequency for PANI/SF/HF and PANI/SF/HF/CB composites at the loading percentage of 30% w/w. As illustrated in Figure 80, the results illustrate that the PANI/SF/HF with a RL_{min} of -27.1 dB at 11.5 GHz with the SD 3.21 kg/m². The SE_{max} was 29.0 dB at 10.2 GHz for a thickness of 3 mm. On the other hand, the results illustrate that the PANI/SF/HF/CB with a RL_{min} of -25.2 dB at 10.5 GHz with the SD 3.14 kg/m². The SE_{max} was 26.1 dB at 10.2 GHz for a thickness of 3 mm. This refers to the MA and EMI shielding properties related to the composite morphology. As a result, this improvement is due to the fact that this incorporation will affect the MA capacity by changing the complex permeability and permittivity. This incorporation leads to an effective and low-thickness absorber with a wide BW_{-10dB}. These prepared composites are promising candidates for applications such as EMI shielding and stealth technology.

Table 38 – MA behavior of PANI/SF/HF and PANI/SF/HF/CB composites at 3.0 mm thickness

Samples	RL _{min} (dB)	f _m (GHz)	BW _{-10 dB} (GHz)	SD (kg/m ²)
PANI/50%SF/50%HF	-27.1±0.8	11.5±0.1	3.2±0.1	3.21±0.08
PANI/45%SF/45%HF/10%CB	-25.2±0.9	10.5±0.1	3.2±0.1	3.14±0.06

Figure 81 illustrates the RL of PANI/SF/HF composites with various thicknesses (3.0, 3.22 and 3.45 mm). Figure 81 shows that the RL attenuation peaks of samples moved to lower frequencies with increasing sample thickness. On the other hand, one can notice the RL_{min} moves gradually to a lower frequency with the increase in loading percentage. Furthermore, Table 39 shows the PANI/SF/HF composites have low SD, ranging from 3.21 to 3.26 kg/m². The absorption percentage of microwaves reached about 99.9%. One can conclude that optimal absorption can be accomplished by modifying the absorber thickness and the loading percentage. The best result was obtained by using the PANI/SF/HF composite sample. Figure

82 shows the relationship between the number of research that studied the radar absorption properties of PANI/F within the range of 8.0-12.0 GHz and the absorption bandwidth under -10 dB. It turns out that the number of these research (22), and only four research were able to cover most of the range (8.0-12.0 GHz). In order to evaluate the beneficial impact of the combination of PANI with SF/HF on the radar absorption properties, Table 40 shows a comparison of radar absorption properties of some lately reported PANI/NiZn ferrite absorbers with various loading ratios of the composites in the host matrix. The results of the literature show these composites have an elevated loading percentage in the host matrix. This leads to a high surface density and heavy weight of the absorbers. This confirms the distinctiveness of prepared composites in terms of lower loading percentage compared with this literature.

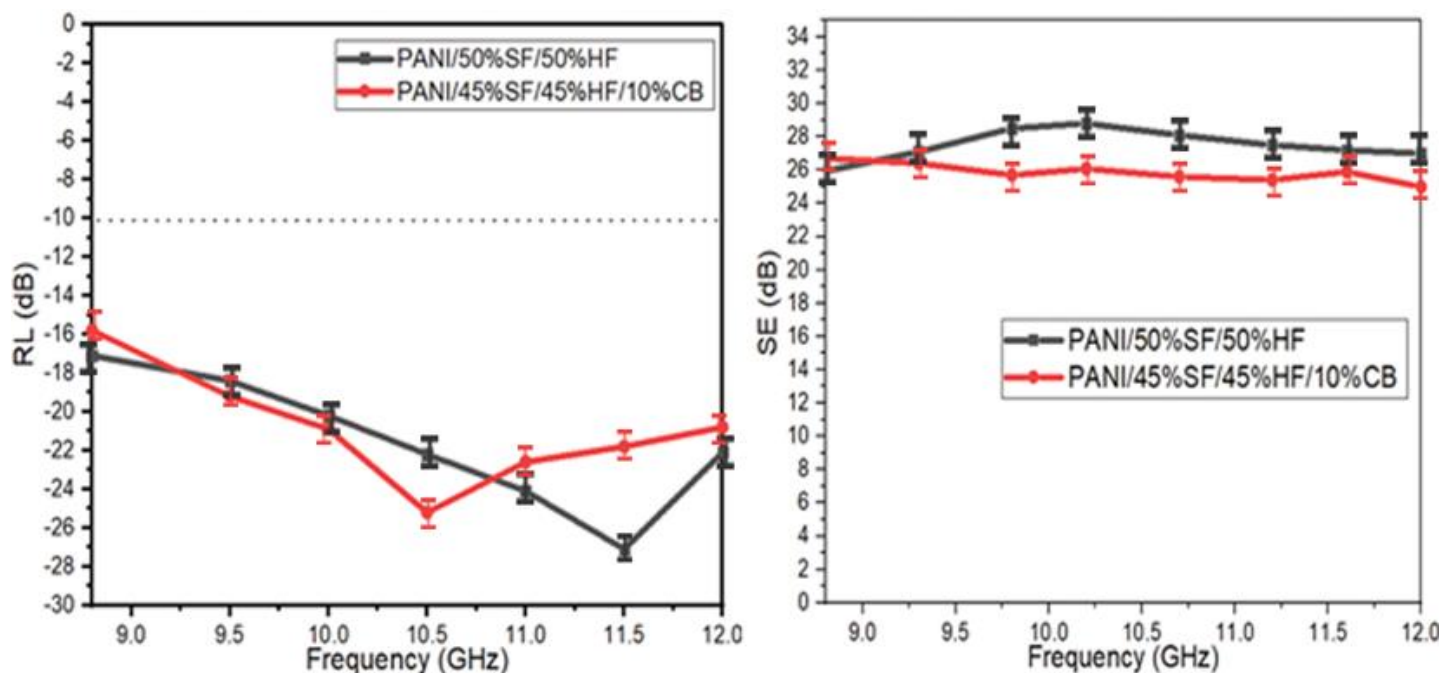


Figure 80 – RL and SE curves of PANI/SF/HF and PANI/SF/HF/CB composites at 3.0 mm thickness

Table 39 – MA behavior of PANI/SF/HF composites at various thicknesses (3.0, 3.22, 3.45 mm)

Loading ratio %	t (mm)	RL _{min} (dB)	f _m (GHz)	BW _{-10dB} (GHz)	SD (kg/m ²)
30%	3.00	-27.1±0.7	11.5±0.2	3.2±0.1	3.21±0.06
	3.22	-25.4±0.9	11.0±0.1	3.2±0.2	3.23±0.07
	3.45	-24.3±0.9	10.6±0.2	3.2±0.1	3.26±0.05

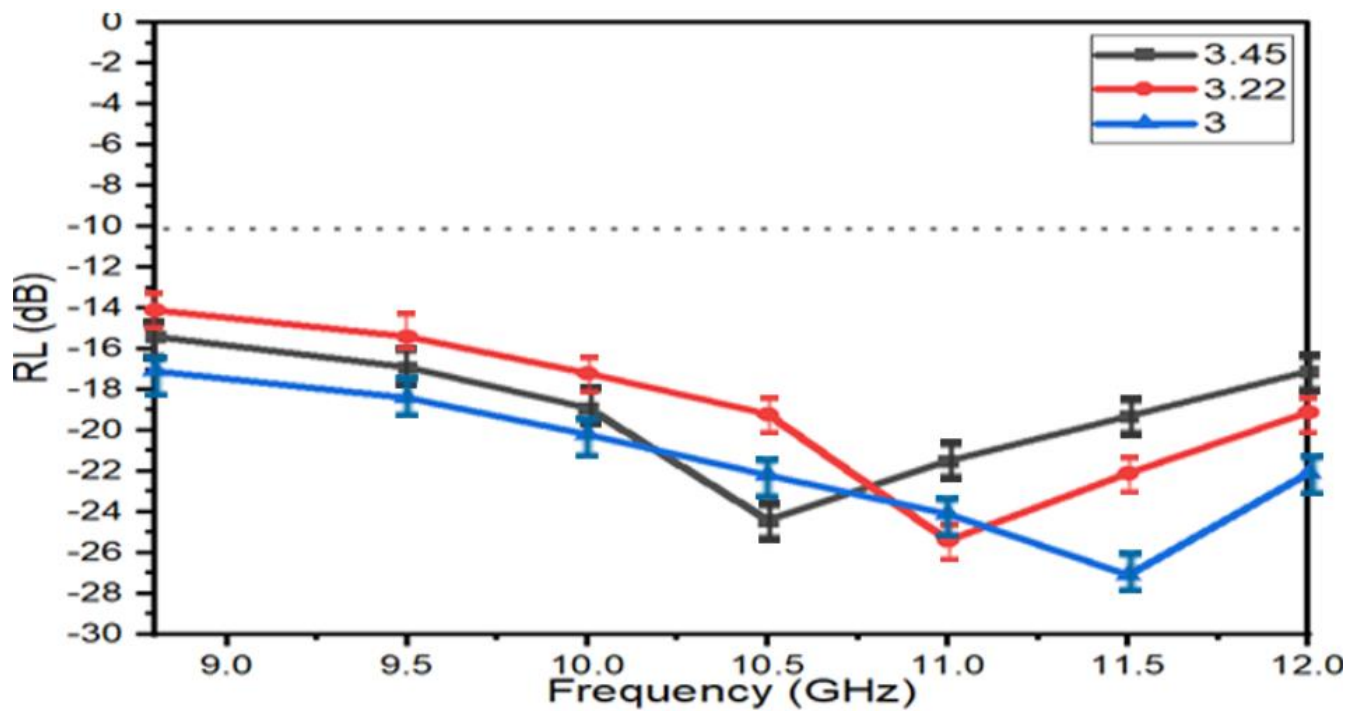


Figure 81 – RL curves of PANI/SF/HF with various thicknesses (3.0, 3.22, 3.45 mm)

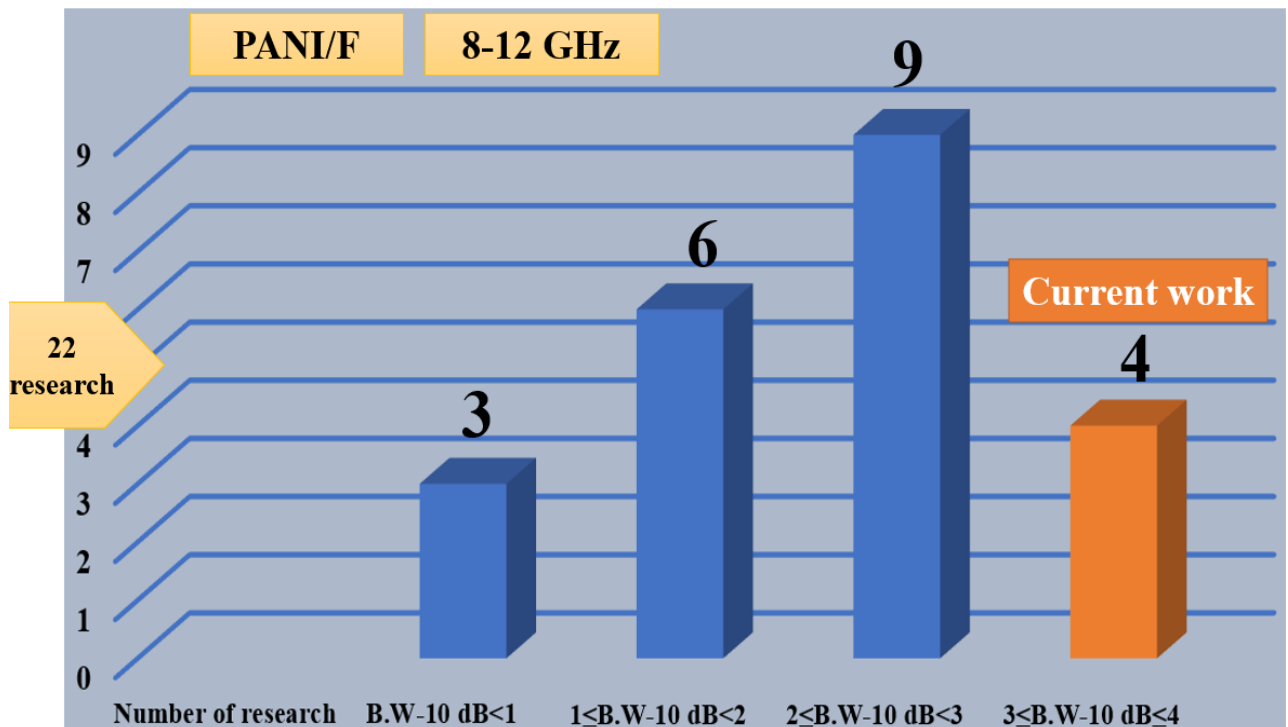


Figure 82 – Relationship between the number of research that studied the radar absorption properties of PANI/F and the absorption bandwidth under -10 dB

Table 40 – Radar absorption properties of PANI-based materials

Specimen (relative weight ratio)/host matrix	LP (%)	t (mm)	RL _{min} (dB)	f _m (GHz)	BW _{-10dB} (GHz)	Ref
NiZn ferrite-PANI(50:50)/Epoxy	67	2.00	-14	11.0	2.6	[63]
NiZn ferrite-PANI(35:65)/Epoxy	20	2.00	-20	9.1	0.5	[121]
NiZn ferrite-PANI(1:3)/Paraffin	75	3.50	-32	9.5	3.8	[65]
NiZn ferrite-PANI(2:1)/Paraffin	70	2.00	-27.5	6.0	3.0	[64]
NiZn ferrite-PANI/Epoxy	67	3.00	-17	11.1	2.8	[66]

CONCLUSION

1. The impact of ferrite type, substitution with metal ions, the concentration of metal ions, and loading percentage of ferrite in the host matrix on EMI and MA properties were exhibited. The best result obtained was by using $\text{Ni}^{3+}_{0.25}\text{Ni}^{2+}_{0.375}\text{Zn}^{2+}_{0.25}\text{Fe}_2\text{O}_4$. A RL_{\min} indicated -13.3 dB at 9.8 GHz and absorption $\text{BW}_{-10\text{ dB}}$ was 1.3 GHz for a thickness of 3 mm. Also, the SE_{\max} attained 15.9 dB at 10.2 GHz. However, the defect of the $\text{Ni}^{3+}_{0.25}\text{Ni}^{2+}_{0.375}\text{Zn}^{2+}_{0.25}\text{Fe}_2\text{O}_4$ that it has a low ε'' . This low ε'' of $\text{Ni}^{3+}_{0.25}\text{Ni}^{2+}_{0.375}\text{Zn}^{2+}_{0.25}\text{Fe}_2\text{O}_4$ can be attributed to the non-dielectric properties of ferrite, therefore the EM wave absorption capability largely results from the magnetic loss (natural resonance and exchange resonance are the main factors for the loss of the magnetic field energy).

2. Received ferrite absorbers from magnetic loss materials. It was found that the RL attenuation peaks of samples were shown to move to lower frequencies with increasing the metal ions to citrate acid, PVA concentration and calcination temperature. This may be due to the change in the crystallite size of the ferrite nanoparticles. The results of XRD patterns indicated that the crystallite size of nickel-zinc ferrite increased by increasing the calcination temperature. As well, the XRD patterns results revealed that the crystallite size of nickel-zinc ferrite increased by increasing the metal ions and PVA concentrations during the preparation process of the ferrite, regardless of the calcination temperature.

3. The effect of ferrite composite type, the weight ratio of $\text{CB}/\text{Ni}_{0.5}\text{Zn}_{0.5}\text{Fe}_2\text{O}_4$, $\text{CB}/\text{Mn}_{0.1}\text{Ni}_{0.5}\text{Zn}_{0.4}\text{Fe}_2\text{O}_4$, $\text{C}/\text{Ni}^{3+}_{0.25}\text{Ni}^{2+}_{0.375}\text{Zn}^{2+}_{0.25}\text{Fe}_2\text{O}_4$ and $\text{Ni}_{0.5}\text{Zn}_{0.5}\text{Fe}_2\text{O}_4/\text{CI}/\text{CB}$, and loading percentage were displayed. The results reveal that the combination of dielectric and magnetic components in a beneficial way has a synergistic effect that enhances the attenuation properties of the final composite. The best result obtained was by using F/CI/CB-211 composite. A RL_{\min} indicated -18.4 dB at 11.7 GHz and $\text{BW}_{-10\text{ dB}}$ was 4.0 GHz for a thickness of 2 mm with a SD of 4.01 kg/m^2 .

4. The underlying mechanism to improve the microwave absorption performance of a hybrid composite is believed to be linked to the interfacial polarization between the different components. The results of the hybrid composites revealed that the RL_{\min} and SE_{\max} improved by obtaining -19.8 dB and 23.18 dB, respectively for PANI/F.2 composite with a loading percentage in the host matrix of 25% reached. This result indicates that the synergistic effect of combining magnetic and dielectric lossy materials is not exalted until they are in a core/shell structure where the interfacial polarizations become more important and play a primordial role. The same result is observed for other prepared hybrid composites ($\text{PANI}/\text{BaNiZnFe}_{16}\text{O}_{27}$, PANI/CI , $\text{PANI}/\text{F}/\text{CI}$, $\text{PANI}/\text{F}/\text{CB}$, $\text{PANI}/50\%\text{SF}/50\%\text{HF}$, and $\text{PANI}/45\%\text{SF}/45\%\text{HF}/10\%\text{CB}$).

5. It was detected that PANI/SF/HF and PANI/SF/HF/CB composites had the best results to absorb EM waves. The absorption percentage of EM waves reached about 99.9% with a loading percentage of 30%.

Assessment of technical efficiency proposed in the thesis

The results obtained in the framework of this thesis can be suggested for producing microwave absorbers synthesized based on magnetic loss and dielectric loss materials. An advantage of the work is that obtained absorbers can attenuate about 99.9% of EM waves with low SD and wide absorption BW₋₁₀. These microwave absorbers can be used to cover the walls of anechoic chambers and to prevent or reduce EM reflections from large bodies.

Assessment of the scientific level and economic efficiency of the work

Nowadays, most international companies work to fabricate MAMs for reducing the noise produced by electronic circuits and smartphones, removing the noise from the original images on screens and manufacturing protective shields in microwave ovens. As well as fabricating these materials for military applications to reduce the radar cross-section of some military systems in order to keep them away from the eyes of hostile radars. MAMs consider expensive materials from a commercial point of view (1 Kg of MAMs costs between 900-1200\$). This work opens up prospects for the production of effective absorbers in the laboratory as affordable, cheap (e.g., 1 Kg of raw materials of CB/Mn_{0.1}Ni_{0.5}Zn_{0.4}Fe₂O₄, PANI/Ni³⁺_{0.25}Ni²⁺_{0.375}Zn²⁺_{0.25}Fe₂O₄/CB and PANI/SF/HF cost between 25-40 \$, 75-100\$, and 90-110\$, respectively) with the required international quality. The results obtained are of practical interest for obtaining new improved composites for absorbing EM waves at the X-band frequency. In addition, the scientific level of the presented thesis complies with international standards for research conducted in the selected field. This is evidenced by a good level of publications, the presentation and the discussion of the results of work at international conferences.

REFERENCES

1. Zhang J. et al. Preparation and Microwave Absorbing Characteristics of Multi-Walled Carbon Nanotube/Chiral-Polyaniline Composites // *Open J. Polym. Chem.* - 2014. - Vol. 04, № 03. - P. 62–72.
2. Hosseini S.H., Asadnia A., Moloudi M. Preparation and electromagnetic wave absorption hard-soft Ba ferrite/polypyrrole core-shell nanocomposites // *Mater. Res. Innov.*- 2015. - Vol. 19, № 2. - P. 107–112.
3. Lv H. et al. A Flexible Microwave Shield with Tunable Frequency-Transmission and Electromagnetic Compatibility // *Adv. Funct. Mater.* - 2019. - Vol. 29, № 14. - P. 1–8.
4. Liang C. et al. Ultra-light MXene aerogel/wood-derived porous carbon composites with wall-like “mortar/brick” structures for electromagnetic interference shielding // *Sci. Bull. Science China Press.* - 2020. - Vol. 65, № 8. - P. 616–622.
5. Chen X. et al. Capacitive behavior of MoS₂ decorated with FeS₂@carbon nanospheres // *Chem. Eng. J.* - 2020. - Vol. 379, № 4.
6. Chen S. et al. Asymmetric alicyclic amine-polyether amine molecular chain structure for improved energy storage density of high-temperature crosslinked polymer capacitor // *Chem. Eng. J. Elsevier B.V.*- 2020. - Vol. 387. - P. 123662.
7. Cheng C. et al. Simultaneously improving mode I and mode II fracture toughness of the carbon fiber/epoxy composite laminates via interleaved with uniformly aligned PES fiber webs // *Compos. Part A Appl. Sci. Manuf. Elsevier Ltd.* - 2020. - Vol. 129. - P. 105696.
8. Xu H. et al. Lightweight Ti₂CT x MXene/Poly(vinyl alcohol) Composite Foams for Electromagnetic Wave Shielding with Absorption-Dominated Feature // *ACS Appl. Mater. Interfaces.* - 2019. - Vol. 11, № 10. - P. 10198–10207.
9. Xie X.B. et al. Spinel structured MFe₂O₄ (M = Fe, Co, Ni, Mn, Zn) and their composites for microwave absorption: A review // *Chem. Eng. J. Elsevier B.V.*- 2022. -Vol. 428, № 5. - P. 131160.
10. Bera P. et al. Solution combustion synthesis, characterization, magnetic, and dielectric properties of CoFe₂O₄ and Co_{0.5}M_{0.5}Fe₂O₄ (M = Mn, Ni, and Zn) // *Phys. Chem. Chem. Phys.*- 2020. -Vol. 22, № 35. - P. 20087–20106.
11. Wang X.X. et al. Assembling Nano–Microarchitecture for Electromagnetic Absorbers and Smart Devices // *Adv. Mater.* - 2020. Vol. 32, № 36. - P. 1–22.
12. Ari Adi W. et al. Metamaterial: Smart Magnetic Material for Microwave Absorbing Material // *Electromagn. Fields Waves.* - 2019. - P. 1–18.
13. Griffiths H. et al. Radar spectrum engineering and management: Technical and regulatory issues // *Proc. IEEE. IEEE.* - 2015. - Vol. 103, № 1. - P. 85–102.
14. Adebayo L.L. et al. Investigation of the broadband microwave absorption of citric acid coated Fe₃O₄/PVDF composite using finite element method // *Appl. Sci.* 2019. -Vol. 9, № 18.
15. McDowell A.J., Hubing T.H. Analysis and comparison of plane wave shielding effectiveness decompositions // *IEEE Trans. Electromagn. Compat.* - 2014. - Vol. 56, № 6. P.

1711–1714.

16. Wang Y. et al. Recent advances in conjugated polymer-based microwave absorbing materials // *Polymers (Basel)*. - 2017. - Vol. 9, № 1.

17. Zhao B. et al. Recent Advances on the Electromagnetic Wave Absorption Properties of Ni Based Materials // *Eng. Sci.* - 2018. - P. 5–40.

18. Drab M. et al. Electric double layer and orientational ordering of water dipoles in narrow channels within a modified Langevin Poisson-Boltzmann model // *Entropy*. - 2020. - Vol. 22, № 9.

19. Raju G. Dielectric Loss and Relaxation-I. Dielectrics in Electric Fields, Second Edition, 2016. - 83–136 p.

20. Mohamed M.A. et al. The field of an electric dipole and the polarizability of a conducting object embedded in the interface between dielectric materials // *Prog. Electromagn. Res. B.* - 2009. - № 16. - P. 1–20.

21. Green M. et al. Dielectric, magnetic, and microwave absorption properties of polyoxometalate-based materials // *J. Magn. Magn. Mater. Elsevier B.V.* - 2020. - Vol. 497, № 9. - P. 165974.

22. Pratap V. et al. Electromagnetic and microwave absorbing properties of U-type barium hexaferrite / polyaniline-epoxy composites Electromagnetic and Microwave Absorbing Properties of U- type Barium Hexaferrite // *Polyaniline-Epoxy Composites*. - 2020. - Vol. 080003, № 5. - P. 1–6.

23. Du S., Chen H., Hong R. Preparation and electromagnetic properties characterization of reduced graphene oxide/strontium hexaferrite nanocomposites // *Nanotechnol. Rev.* - 2020. - Vol. 9, № 1. - P. 105–114.

24. Srivastava R., Yadav B.C. Ferrite materials: Introduction, synthesis techniques, and applications as sensors // *Int. J. Green Nanotechnol. Biomed.* - 2012. - Vol. 4, № 2. - P. 141–154.

25. Jadhav V. V. et al. Properties of ferrites. Spinel Ferrite Nanostructures for Energy Storage Devices. - Elsevier Inc.- 2020. - № 5. - 35–50 p.

26. Arora A. Optical and electric field control of magnetism. - Univ. Potsdam. 2018. - P. 11–20.

27. Dehghan R., Seyyed Ebrahimi S.A., Badiei A. Investigation of the effective parameters on the synthesis of Ni-ferrite nanocrystalline powders by coprecipitation method // *J. Non. Cryst. Solids. Elsevier B.V.* - 2008. - Vol. 354, № 47–51. - P. 5186–5188.

28. Hankare P.P. et al. Synthesis, characterization and effect of sintering temperature on magnetic properties of MgNi ferrite prepared by co-precipitation method // *J. Alloys Compd.* - 2009. - Vol. 475, № 1–2. - P. 926–929.

29. Vadivel M. et al. Synthesis, structural, dielectric, magnetic and optical properties of Cr substituted CoFe₂O₄ nanoparticles by co-precipitation method // *J. Magn. Magn. Mater. Elsevier*. - 2014. - Vol. 362. - P. 122–129.

30. Jacob B.P. et al. Influence of preparation method on structural and magnetic properties of

nickel ferrite nanoparticles // Bull. Mater. Sci. - 2011. - Vol. 34, № 7. - P. 1345–1350.

31. Padmanaban R. et al. Recent Trends in Materials Science (RTMS-2011) // Recent Trends Mater. Sci. Appl. - 2017. № 10. - P. 2011.

32. Ding Z. et al. Synthesis and Characterization of Co-Zn Ferrite Nanoparticles by Hydrothermal Method: A Comparative Study // IEEE Trans. Magn. - 2015. - Vol. 51, № 11. - P. 2–5.

33. Zalite I. et al. Hydrothermal synthesis of cobalt ferrite nanosized powders // IOP Conf. Ser. Mater. Sci. Eng. - 2015. - Vol. 77, № 1.

34. Praveena K. et al. Microwave absorption studies of magnetic sublattices in microwave sintered Cr³⁺ doped SrFe₁₂O₁₉ // J. Magn. Magn. Mater. Elsevier. - 2017. - Vol. 426, №7. - P. 604–614.

35. Mallesh S. et al. Structure and magnetic properties of ZnO coated MnZn ferrite nanoparticles // J. Magn. Magn. Mater. Elsevier. - 2016. - Vol. 418. - P. 112–117.

36. Jia P.Y. et al. Sol-gel synthesis and characterization of SiO₂@CaWO₄, SiO₂@CaWO₄:Eu³⁺/Tb³⁺ core-shell structured spherical particles // Nanotechnology.-2006. - Vol. 17, № 3. - P. 734–742.

37. Sulaiman N.H. et al. Superparamagnetic calcium ferrite nanoparticles synthesized using a simple solgel method for targeted drug delivery // Biomed. Mater. Eng. - 2015. - Vol. 26. - P. 103–110.

38. Panchal N.R., Jotania R.B. Cobalt ferrite nano particles by microemulsion route // Nanotechnology. - 2010. - Vol. 1, № 1. - P. 17–18.

39. Saini P., Aror M. Microwave Absorption and EMI Shielding Behavior of Nanocomposites Based on Intrinsically Conducting Polymers, Graphene and Carbon Nanotubes // New Polym. Spec. Appl. - 2012.- Vol. 18, № 3.

40. Folgueras L. de C., Alves M.A., Rezende M.C. Microwave absorbing paints and sheets based on carbonyl iron and polyaniline: Measurement and simulation of their properties // J. Aerosp. Technol. Manag. - 2010. - Vol. 2, № 1. - P. 63–70.

41. Boeva Z.A., Sergeev V.G. Polyaniline: Synthesis, properties, and application // Polym. Sci. Ser. C. - 2014. - Vol. 56, № 1. - P. 144–153.

42. Yusuf J.Y. et al. Recent advances and prospect of cobalt based microwave absorbing materials // Ceram. Int. Elsevier Ltd and Techna Group S.r.l.. - 2020. - Vol. 46, № 17. - P. 26466–26485.

43. Chen N., Gu M. Microstructure and Microwave Absorption Properties of Y-Substituted Ni-Zn Ferrites // Open J. Met. - 2012. - Vol. 02, № 02. - P. 37–41.

44. Wang S. et al. Synthesis of porous nitrogen-doped graphene decorated by γ -Fe₂O₃ nanorings for enhancing microwave absorbing performance // Ceram. Int. Elsevier Ltd and Techna Group S.r.l.- 2020. - Vol. 46, № 1. - P. 1002–1010.

45. Shu R. et al. Facile synthesis of nitrogen-doped reduced graphene oxide/nickel-zinc ferrite composites as high-performance microwave absorbers in the X-band // Chem. Eng. J. Elsevier. - 2020. - Vol. 384, № 7. - P. 123266.

46. Jaiswal R. et al. EMI and microwave absorbing efficiency of polyaniline-functionalized reduced graphene oxide/ γ -Fe₂O₃/epoxy nanocomposite // *Soft Matter*. - 2020. - Vol. 16, № 28.- P. 6643–6653.
47. Bueno A.R., Gregori M.L., Nóbrega M.C.S. Microwave-absorbing properties of Ni_{0.50-x}Zn_{0.50-x}Me_{2x}Fe₂O₄ (Me=Cu, Mn, Mg) ferrite-wax composite in X-band frequencies // *J. Magn. Magn. Mater.* - 2008. - Vol. 320, № 6. - P. 864–870.
48. Zinc N. et al. Synthesis and Microwave Absorbing Properties of Cu-Doped. - 2013. - Vol. 2013.
49. Chen B.Y. et al. Preparation and microwave absorption properties of Ni-Co nanoferrites // *J. Alloys Compd. Elsevier B.V.*- 2015. - Vol. 618. - P. 222–226.
50. Almessiere M.A. et al. Effect of Nd-Y co-substitution on structural, magnetic, optical and microwave properties of NiCuZn nanospinel ferrites // *J. Mater. Res. Technol. Korea Institute of Oriental Medicine.*- 2020. - Vol. 9, № 5. - P. 11278–11290.
51. Almessiere M.A. et al. Microstructure, dielectric and microwave features of [Ni_{0.4}Cu_{0.2}Zn_{0.4}](Fe_{2-x}Tbx)O₄ ($x \leq 0.1$) nanospinel ferrites // *J. Mater. Res. Technol. Korea Institute of Oriental Medicine.*- 2020. - Vol. 9, № 5. - P. 10608–10623.
52. Almessiere M.A. et al. Impact of Eu³⁺ ion substitution on structural, magnetic and microwave traits of Ni–Cu–Zn spinel ferrites // *Ceram. Int. Techna Group S.r.l.*- 2020. -Vol. 46, № 8. - P. 11124–11131.
53. Almessiere M.A. et al. Strong correlation between Dy³⁺ concentration, structure, magnetic and microwave properties of the [Ni_{0.5}Co_{0.5}](DyxFe_{2-x})O₄ nanosized ferrites // *J. Ind. Eng. Chem. The Korean Society of Industrial and Engineering Chemistry.* - 2020. -Vol. 90.- P. 251–259.
54. Goel S. et al. Effect of neodymium doping on microwave absorption property of barium hexaferrite in X-band // *Mater. Res. Express. IOP Publishing.* - 2020. - Vol. 7, № 1.
55. Ghasemi A. et al. Microwave absorption properties of Mn-Co-Sn doped barium ferrite nanoparticles // *IEEE Trans. Magn.* -2009. -Vol. 45, № 6. - P. 2456–2459.
56. Houbi A. et al. Microwave absorbing properties of ferrites and their composites: A review // *J. Magn. Magn. Mater. Elsevier B.V.*- 2021. -Vol. 529, №9. - P. 167839.
57. Harris V.G. Modern microwave ferrites // *IEEE Trans. Magn.* - 2012. - Vol. 48, № 3. -P. 1075–1104.
58. Cui G. et al. Excellent microwave absorption properties derived from the synthesis of hollow Fe₃O₄@reduced graphene oxide (RGO) nanocomposites // *Nanomaterials.* - 2019. - Vol. 9, № 2. - P. 1–12.
59. Luo J. et al. Excellent microwave absorption properties by tuned electromagnetic parameters in polyaniline-coated Ba_{0.9}La_{0.1}Fe_{11.9}Ni_{0.1}O₁₉/reduced graphene oxide nanocomposites // *RSC Adv. Royal Society of Chemistry.* - 2017. - Vol. 7, № 58. - P. 36433–36443.
60. Ali N.N. et al. Lightweight broadband microwave absorbers of core–shell (polypyrrole/NiZn ferrite) nanocomposites in the X-band: insights on interfacial polarization //

J. Mater. Sci. Mater. Electron. Springer US.- 2019. -Vol. 30, № 7. - P. 6876–6887.

61. Hosseini S.H., Asadnia A. Synthesis, characterization, and microwave-absorbing properties of polypyrrole/MnFe₂O₄ nanocomposite // J. Nanomater. - 2012. - Vol. 20.

62. Mostafa N.Y., Hessien M.M., Shaltout A.A. Hydrothermal synthesis and characterizations of Ti substituted Mn-ferrites // J. Alloys Compd. - 2012. -Vol. 529. - P. 29–33.

63. Ting T.H., Yu R.P., Jau Y.N. Synthesis and microwave absorption characteristics of polyaniline/NiZn ferrite composites in 2-40 GHz // Mater. Chem. Phys. - 2011. - Vol. 126, № 1–2. - P. 364–368.

64. Wang C.P. et al. Novel one-dimensional polyaniline/Ni_{0.5}Zn_{0.5}Fe₂O₄ hybrid nanostructure: Synthesis, magnetic, and electromagnetic wave absorption properties // J. Nanoparticle Res. - 2014. - Vol. 16, № 3.

65. Wang M. et al. Controlled synthesis and microwave absorption properties of Ni_{0.6}Zn_{0.4}Fe₂O₄/PANI composite via an in-situ polymerization process // J. Magn. Magn. Mater. Elsevier. - 2015.- Vol. 377. - P. 52–58.

66. Wang C. et al. Synthesis of novel NiZn-ferrite/Polyaniline nanocomposites and their microwave absorption properties // Mater. Sci. Semicond. Process. Elsevier.- 2013. -Vol. 16, № 1. - P. 77–82.

67. Ma R.T., Zhao H.T., Zhang G. Preparation, characterization and microwave absorption properties of polyaniline/Co_{0.5}Zn_{0.5}Fe₂O₄ nanocomposite // Mater. Res. Bull. - 2010. - Vol. 45, № 9. - P. 1064–1068.

68. Sun J. et al. Preparation of copper-cobalt-nickel ferrite/graphene oxide/polyaniline composite and its applications in microwave absorption coating // Prog. Org. Coatings. Elsevier. - 2020. - Vol. 141, № 10. - P. 105552.

69. Manna K., Srivastava S.K. Fe₃O₄@Carbon@Polyaniline Trilaminar Core-Shell Composites as Superior Microwave Absorber in Shielding of Electromagnetic Pollution // ACS Sustain. Chem. Eng. - 2017. - Vol. 5, № 11. - P. 10710–10721.

70. Xiong P., Huang H., Wang X. Design and synthesis of ternary cobalt ferrite/graphene/polyaniline hierarchical nanocomposites for high-performance supercapacitors This work is dedicated to Professor MIN Enze on the occasion of his 90th birthday. // J. Power Sources. Elsevier B.V. - 2014. -Vol. 245. - P. 937–946.

71. Mondal K. et al. Carbon Nanostructures for Energy and Sensing Applications // J. Nanotechnol. - 2019. -Vol. 2019. - P. 10–13.

72. Kwiatkowski M. et al. Evaluation of CO₂ interactions with S-doped nanoporous carbon and its composites with a reduced GO: Effect of surface features on an apparent physical adsorption mechanism // Carbon N. Y.- 2016. -Vol. 98. - P. 250–258.

73. Anh L.T.Q., Van Dan N. A microwave-absorbing property of super-paramagnetic zinc–nickel ferrite nanoparticles in the frequency range of 8–12 GHz // Appl. Phys. A Mater. Sci. Process. Springer Berlin Heidelberg.- 2020. - Vol. 126, № 1. - P. 1–6.

74. Mahmood H. et al. Spinel ferrite-hexaferrite nanocomposites: Synthesis and characterization for high frequency devices fabrication // Dig. J. Nanomater. Biostructures.-

2019. -Vol. 14, № 3. - P. 711–720.

75. Che R. et al. Microwave Absorption Enhancement and Complex Permittivity and Permeability of Fe Encapsulated within Carbon Nanotubes // *Adv. Mater.* - 2004. - Vol. 16, № 5.- P. 401–405.

76. Lin H. et al. Investigation of the microwave-absorbing properties of Fe-filled carbon nanotubes // *Mater. Lett.* - 2007. - Vol. 61, № 16. - P. 3547–3550.

77. Wu N. et al. Strengthened electromagnetic absorption performance derived from synergistic effect of carbon nanotube hybrid with Co@C beads // *Adv. Compos. Hybrid Mater. Advanced Composites and Hybrid Materials.*- 2018. - Vol. 1, № 1. - P. 149–159.

78. Yang B. et al. Surface-oxidized FeCo/carbon nanotubes nanorods for lightweight and efficient microwave absorbers // *Mater. Des. Elsevier Ltd.* - 2017. - Vol. 136. - P. 13–22.

79. Feng A. et al. Synthesis of a hierarchical carbon fiber@cobalt ferrite@manganese dioxide composite and its application as a microwave absorber // *RSC Adv. Royal Society of Chemistry.*- 2020. - Vol. 10, № 18. - P. 10510–10518.

80. Gholampoor M., Movassagh-Alanagh F., Salimkhani H. Fabrication of nano-Fe₃O₄ 3D structure on carbon fibers as a microwave absorber and EMI shielding composite by modified EPD method // *Solid State Sci. Elsevier Masson SAS.* - 2017. - Vol. 64. - P. 51–61.

81. Liu Y. et al. Preparation and properties of cobalt oxides coated carbon fibers as microwave-absorbing materials // *Appl. Surf. Sci. Elsevier B.V.* - 2011. - Vol. 257, № 17. - P. 7678–7683.

82. Meng X. et al. The electrochemical preparation and microwave absorption properties of magnetic carbon fibers coated with Fe₃O₄ films // *Appl. Surf. Sci. Elsevier B.V.*- 2011. - Vol. 257, № 24. - P. 10808–10814.

83. Verma P. et al. Electromagnetic interference shielding performance of carbon nanostructure reinforced, 3D printed polymer composites // *J. Mater. Sci. Springer US.* - 2021. - Vol. 56, № 20. - P. 11769–11788.

84. Bayat M. et al. Electromagnetic interference shielding effectiveness of hybrid multifunctional Fe₃O₄/carbon nanofiber composite // *Polymer (Guildf).* - 2014. -Vol. 55, № 3.- P. 936–943.

85. Hong Y.K. et al. Method and apparatus to measure electromagnetic interference shielding efficiency and its shielding characteristics in broadband frequency ranges // *Rev. Sci. Instrum.* - 2003. - Vol. 74. - № 2. - P. 1098–1102.

86. Kondawar S.B., Nandapure A.I. Magnetic and electrical properties of zinc-substituted nickel ferrite reinforced conducting polyaniline nanocomposites // *J. Chinese Adv. Mater. Soc.*- 2014. - Vol. 2, № 3. - P. 186–198.

87. Peng C.H. et al. Microwave-absorbing characteristics for the composites of thermal-plastic polyurethane (TPU)-bonded NiZn-ferrites prepared by combustion synthesis method // *Mater. Sci. Eng. B Solid-State Mater. Adv. Technol.* - 2005. - Vol. 117, № 1. - P. 27–36.

88. Hwang Y. Microwave absorbing properties of NiZn-ferrite synthesized from waste iron oxide catalyst // *Mater. Lett.* - 2006. - Vol. 60, № 27. - P. 3277–3280.

89. Kim D.Y. et al. Dependence of microwave absorbing property on ferrite volume fraction in MnZn ferrite-rubber composites // *IEEE Trans. Magn.* - 1996. - Vol. 32, № 2. - P. 555–558.
90. Diniz V.C.S. et al. Effects of Mn_{1-x}Zn_xFe₂O₄ Nanoparticles Concentration in a Silicone Matrix on Complex Permeability and Permittivity in the 1-10 GHz Range // *Mater. Res.* - 2022. - Vol. 25. - P. 1–9.
91. Xiang J. et al. Magnetic carbon nanofibers containing uniformly dispersed Fe/Co/Ni nanoparticles as stable and high-performance electromagnetic wave absorbers // *J. Mater. Chem. A. Royal Society of Chemistry.* - 2014. - Vol. 2, № 40. - P. 16905–16914.
92. Lee J. et al. Absorber for 1 GHz Application // 2009. - Vol. 45, № 10. - P. 4230–4233.
93. Lima U.R. et al. Synthesis of NiCuZn ferrite nanoparticles and microwave absorption characterization // *Mater. Sci. Eng. B Solid-State Mater. Adv. Technol.* - 2008. - Vol. 151, № 3. - P. 238–242.
94. Zhao D.L., Lv Q., Shen Z.M. Fabrication and microwave absorbing properties of Ni-Zn spinel ferrites // *J. Alloys Compd.* - 2009. - Vol. 480, № 2. - P. 634–638.
95. El Nahrawy A.M. et al. Crystallographic and magnetic properties of Al₃₊-co-doped NiZnFe₂O₄ nano-particles prepared by sol-gel process // *Egypt. J. Chem.* - 2019. - Vol. 62, № 3. - P. 925–932.
96. Figueroa Ramírez S.J., Miranda-Hernández M. Carbon film electrodes as support of metallic particles // *Int. J. Electrochem. Sci.* - 2012. - Vol. 7, № 1. - P. 150–166.
97. Kim S.Y. et al. Core-shell-structured cross-linked poly(glycidyl methacrylate)-coated carbonyl iron microspheres and their magnetorheology // *J. Mater. Sci.* - 2014. - Vol. 49, № 3. - P. 1345–1352.
98. Hu E. et al. The role of soot particles in the tribological behavior of engine lubricating oils // *Wear. Elsevier.* - 2013. - Vol. 304, № 1–2. - P. 152–161.
99. Bahri-Laleh N. et al. Microwave Absorption Properties of Polyaniline/Carbonyl Iron Composites // *Silicon. Silicon.* - 2018. - Vol. 10, № 4. - P. 1337–1343.
100. Cheng Y. et al. Rationally regulating complex dielectric parameters of mesoporous carbon hollow spheres to carry out efficient microwave absorption // *Carbon N. Y. Elsevier Ltd.* - 2018. - Vol. 127. - P. 643–652.
101. Shu R. et al. Synthesis and high-performance microwave absorption of reduced graphene oxide/zinc ferrite hybrid nanocomposite // *Mater. Lett. Elsevier B.V.* - 2018. - Vol. 215. - P. 229–232.
102. Zong M. et al. One-step hydrothermal synthesis and microwave electromagnetic properties of RGO/NiFe₂O₄ composite // *Ceram. Int. Elsevier.* - 2014. - Vol. 40, № 5. - P. 6821–6828.
103. Zong M., Huang Y., Zhang N. Reduced graphene oxide-CoFe₂O₄ composite: Synthesis and electromagnetic absorption properties // *Appl. Surf. Sci. Elsevier B.V.* - 2015. - Vol. 345. - P. 272–278.
104. Mustaffa M.S. et al. An investigation of microstructural, magnetic and microwave absorption properties of multi-walled carbon nanotubes/Ni_{0.5}Zn_{0.5}Fe₂O₄ // *Sci. Rep.* - 2019.-

Vol. 9, № 1. - P. 3–9.

105. Ye W. et al. Preparation and properties of CF-Fe₃O₄-BN composite electromagnetic wave-absorbing materials // RSC Adv. Royal Society of Chemistry. - 2020. Vol. 10, № 19. - P. 11121–11131.

106. Zou T. et al. Electromagnetic and microwave absorbing properties of multi-walled carbon nanotubes filled with Ni nanowire // J. Alloys Compd. - 2010. - Vol. 496, № 1–2. - P. 22–24.

107. Zhang L., Zhu H. Dielectric, magnetic, and microwave absorbing properties of multi-walled carbon nanotubes filled with Sm₂O₃ nanoparticles // Mater. Lett. Elsevier B.V. - 2009. - Vol. 63, № 2. - P. 272–274.

108. Xu P. et al. A study of the magnetic and electromagnetic properties of γ -Fe₂O₃-multiwalled carbon nanotubes (MWCNT) and Fe/Fe₃C-MWCNT composites // Mater. Chem. Phys. - 2009. - Vol. 114, № 2–3. - P. 556–560.

109. Zhao D.L., Li X., Shen Z.M. Preparation and electromagnetic and microwave absorbing properties of Fe-filled carbon nanotubes // J. Alloys Compd. - 2009. - Vol. 471, № 1–2. - P. 457–460.

110. Xu X. et al. Cactus-Inspired Bimetallic Metal-Organic Framework-Derived 1D-2D Hierarchical Co/N-Decorated Carbon Architecture toward Enhanced Electromagnetic Wave Absorbing Performance // ACS Appl. Mater. Interfaces. - 2019. - Vol. 11, № 14. - P. 13564–13573.

111. Xiang J. et al. Synthesis and characterization of FeCo/C hybrid nanofibers with high performance of microwave absorption // Mater. Res. Bull. Elsevier Ltd. - 2014. - Vol. 60. - P. 589–595.

112. Ezzati S.N. et al. Conducting, magnetic polyaniline/Ba_{0.25}Sr_{0.75}Fe₁₁(Ni_{0.5}Mn_{0.5})O₁₉ nanocomposite: Fabrication, characterization and application // J. Alloys Compd. Elsevier Ltd. - 2015. - Vol. 646. - P. 1157–1164.

113. Meng X. et al. Facile synthesis of shell-core polyaniline/SrFe₁₂O₁₉ composites and magnetic properties // RSC Adv. Royal Society of Chemistry. - 2016. - Vol. 6, № 6. - P. 4946–4949.

114. Ali N.N. et al. Comparative study of microwave absorption characteristics of (Polyaniline/NiZn ferrite) nanocomposites with different ferrite percentages // Mater. Chem. Phys. Elsevier B.V. - 2018. - Vol. 211. - P. 79–87.

115. Elsayed A.H. et al. Synthesis and Properties of Polyaniline / ferrites// Nanocomposites. - 2011. - Vol. 6. - P. 206–221.

116. Gairola S.P. et al. Enhanced microwave absorption properties in polyaniline and nano-ferrite composite in X-band // Synth. Met. Elsevier B.V. - 2010. - Vol. 160, № 21–22. - P. 2315–2318.

117. Li G. et al. Preparation of magnetic and conductive NiZn ferrite-polyaniline nanocomposites with core-shell structure // Colloids Surfaces A Physicochem. Eng. Asp. - 2006. - Vol. 276, № 1–3. - P. 40–44.

118. Xie P. et al. Tunneling-induced negative permittivity in Ni/MnO nanocomposites by a bio-gel derived strategy // *J. Mater. Chem. C.* - 2020. - Vol. 8, № 9. - P. 3029–3039.
119. He L. et al. Preparation of reduced graphene oxide coated flaky carbonyl iron composites and their excellent microwave absorption properties // *RSC Adv. Royal Society of Chemistry.* - 2018. - Vol. 8, № 6. - P. 2971–2977.
120. Prodromakis T., Papavassiliou C. Engineering the Maxwell-Wagner polarization effect // *Appl. Surf. Sci.* - 2009. - Vol. 255, № 15. - P. 6989–6994.
121. Didehban K. et al. Radar Absorption Properties of Ni_{0.5}Zn_{0.5}Fe₂O₄/PANI/epoxy nanocomposites // *J. Chinese Chem. Soc.* - 2015. - Vol. 62, № 9. - P. 826–831.